

Backbone Curve Analysis of Nonlinear Mechanical Systems



The
University
Of
Sheffield.

Xuanang Liu

Department of Mechanical Engineering
University of Sheffield

This thesis is submitted for the degree of
Doctor of Philosophy

Supervisor

Prof. David Wagg

March, 2018

I would like to dedicate this thesis to:

My wife, Lynn, for loving and supporting me.

My parents, J. Liu and X. Ling, for absolutely everything.

Declaration

I hereby declare that except where specific reference is made to the work of others, the contents of this thesis are original and have not been submitted in whole or in part for consideration for any other degree or qualification in this, or any other university. This thesis is my own work and contains nothing which is the outcome of work done in collaboration with others, except as specified in the text and Acknowledgements.

Xuanang Liu
March, 2018

Acknowledgements

First of all, I would like to my deepest gratitude to my supervisor, Professor David Wagg, for his guidance, encouragement and support throughout this project. If this work is any worth, it is mainly because of him.

I am grateful to Prof. Simon Neild and Dr Tom Hill from the University of Bristol and Dr Andrea Cammarano from the University of Glasgow for the advice about nonlinear modal interactions, and Dr Nikoloas Dervilis from the University of Sheffield for the help of the self-adaptive differential evolution algorithm.

Many thanks to my colleagues and friends in the Dynamics Research Group for useful discussions and everyday funny jokes.

Abstract

Nonlinear dynamic behaviour has become increasingly significant due to the performance demands on modern mechanical structures that are increasingly lightweight and flexible, e.g. the geometric nonlinearity caused by the large deflection. Also, numerous traditional mechanical applications are found to be able to achieve better performance when nonlinear characteristics are exploited. However, the application of any traditional linear analysis to nonlinear systems can only provide, at best, suboptimal solutions as the well-established linear techniques fail to capture the unique nonlinear features, e.g. modal interactions and bifurcations.

This thesis aims to improve the theoretical understanding of the smooth nonlinear dynamic behaviours of mechanical systems and apply the findings to develop innovative approaches for practical use. Backbone curve analysis is employed throughout the thesis as a tool to develop this understanding.

The resonant interactions only involving two modes of a three-lumped-mass nonlinear oscillator are investigated. It is demonstrated that the backbone curves of this example system can provide an interpretation of the underlying nonlinear dynamic behaviours, including stability and bifurcations. Then we consider two kinds of triple-mode resonant interactions in other 3-DoF systems, including $1 : 1 : 1$ and $1 : 2 : 3$ modal interactions. The effects of these multi-mode resonant interactions, e.g. the non-existent of single- and double-mode responses and the resonance between ‘non-resonant’ modes after involving extra modes, are demonstrated, and the mechanism is explored using backbone curves.

A nonlinear dynamic phenomenon, resonant frequency shift, is also considered. The power spectrum density results of a thin plate under multi-mode-multi-frequency excitations are used to demonstrate this nonlinear behaviour, which shows that the frequency shift can be caused by an interaction between any non-resonant modes. Based on a nonlinear reduced-order model, backbone curves are used to explain the mechanism of the non-resonant modal interaction, which is caused by the unconditionally resonant mixed-mode nonlinear terms. The understanding of the non-resonant modal interaction is then used to develop a practical approach for nonlinear system identification which employs the backbone curves as the parametric model. The proposed identification approach is applied to the example plate to demonstrate its accuracy and advantages.

Table of contents

Table of contents	xi
List of figures	xv
List of tables	xix
1 Introduction	1
1.1 Research motivations	3
1.2 Thesis outline	3
2 Literature review	7
2.1 Nonlinear dynamic behaviours in mechanical systems	7
2.1.1 Nonlinear dynamic characteristics	7
2.1.2 Effects of the nonlinearity in mechanical systems	8
2.2 Methods for analysing nonlinear dynamics	10
2.2.1 Numerical methods	10
2.2.2 Approximate analytical methods	12
2.2.3 Modal analysis	15
2.3 Nonlinear system identification	18
2.4 Summary	20
3 Analysis tools for nonlinear systems	23
3.1 Introduction	23
3.2 Direct normal form method	25
3.2.1 Linear modal transform	26
3.2.2 Forcing transform	27
3.2.3 Nonlinear near-identity transform	29
3.2.4 Discussion of limitations	36

3.3	Stability analysis of the steady-state solution	38
3.4	Backbone curves	40
3.5	Application to an example system	43
3.5.1	Forced response approximation	44
3.5.2	Stability analysis	48
3.5.3	Backbone curve calculation	50
3.6	Summary	51
4	$N - i$ modal interaction of nonlinear multi-degree-of-freedom systems	55
4.1	Introduction	55
4.2	Nonlinear 3-DoF system with bilateral symmetry	57
4.3	Backbone curves	61
4.3.1	Calculation of backbone curves	61
4.3.2	Stability of the backbone curves	70
4.4	Forced response	73
4.4.1	Relation between forced response and backbone curves	73
4.4.2	Relation between modal interactions and force amplitudes	78
4.5	Summary	82
5	N modal interaction of nonlinear multi-degree-of-freedom systems	85
5.1	Introduction	85
5.2	Backbone curve model of the generic 3-DoF system with cubic nonlinear springs	87
5.3	1 : 1 : 1 modal interaction	91
5.3.1	Calculation of backbone curves	98
5.3.2	Forced response	107
5.4	Auto-parametric modal interaction	109
5.4.1	Design of the underlying linear structure	111
5.4.2	Backbone curves	112
5.5	Summary	118
6	Resonant frequency shift	121
6.1	Introduction	121
6.2	Frequency shift of an example pinned-pinned plate	123
6.3	Nonlinear reduced-order model	128
6.3.1	Development of a nonlinear reduced-order model	128

6.3.2	Simulation results	131
6.4	Effect of the nonlinear coupled-mode terms explanation	138
6.4.1	Non-resonant interaction	138
6.4.2	Backbone curves and forced response results	143
6.5	Summary	146
7	System identification based on backbone curve models	151
7.1	Introduction	151
7.2	Backbone curve measurement from transient free-decay data	153
7.2.1	Short-time Fourier transform with size-varying windows	154
7.2.2	Estimation of the instantaneous frequencies and amplitudes	155
7.2.3	Application	157
7.3	Stiffness parameters identification	164
7.3.1	Differential evolution algorithm	164
7.3.2	Self-adaptive differential evolution algorithm	166
7.3.3	Application	169
7.4	Summary	174
8	Conclusion and future work	177
8.1	Conclusions	177
8.2	Suggestions for potential future work	184
	References	187
	Appendix A Order selection criteria for AR modelling	195
A.1	AR modelling	195
A.2	Order selection criteria	195
	Appendix B An example system with resonant and non-resonant modal interactions	197
B.1	Resonant modal interaction	198
B.1.1	Hardening nonlinearity	199
B.1.2	Softening nonlinearity	201
B.2	Non-resonant modal interaction	201

List of figures

1.1	Example nonlinear mechanical structures.	2
2.1	A schematic diagram of an in-line, 2-DoF oscillator.	15
3.1	A schematic diagram of a forced, 1-DoF Duffing oscillator.	43
3.2	The responses of a forced, 1-DoF Duffing oscillator.	47
3.3	The response stability of a forced, 1-DoF Duffing oscillator.	50
3.4	The backbone curve of a 1-DoF Duffing oscillator.	52
4.1	A schematic diagram of an in-line, 3-DoF system with a bilaterally symmetric structure and cubic nonlinear springs.	57
4.2	The projection diagrams of modal displacement responses on the backbone curves of a bilaterally symmetric, 3-DoF system.	64
4.3	The backbone curves of a bilaterally symmetric, 3-DoF system with hardening nonlinearity and no bifurcation on the backbone curves	67
4.4	The backbone curves of a bilaterally symmetric, 3-DoF system with softening nonlinearity and bifurcations on the single-mode backbone curves.	69
4.5	The forced displacement response curves of a bilaterally symmetric, 3-DoF system with hardening nonlinearity and no modal interaction.	75
4.6	The forced response curves of a bilaterally symmetric, 3-DoF system with softening nonlinearity when the force is applied in its second mode only.	76
4.7	The intersections between the forced response curve and the corresponding stability boundary of a bilaterally symmetric, 3-DoF system with softening nonlinearity when only its second mode is forced.	81
4.8	The intersections between the forced response curve and the corresponding stability boundary of a bilaterally symmetric, 3-DoF system with softening nonlinearity when only its third mode is forced.	83

5.1	A schematic diagram of the generic, in-line, 3-DoF system with cubic nonlinear springs.	87
5.2	A schematic diagram of an in-line, 3-DoF system with a mistuned periodically symmetric structure and cubic nonlinear springs.	91
5.3	The projection diagrams of modal displacement responses on the triple-mode backbone curves of a mistuned periodically symmetric, 3-DoF system.	103
5.4	The backbone curves of a mistuned periodically symmetric, 3-DoF system with hardening nonlinearity and no triple-mode modal interaction.	104
5.5	The backbone curves of a mistuned periodically symmetric, 3-DoF system with softening nonlinearity and triple-mode modal interactions.	106
5.6	The forced response curves of a mistuned periodically symmetric, 3-DoF system with softening nonlinearity when the force is applied in its second mode only.	108
5.7	The forced response curves of a mistuned periodically symmetric, 3-DoF system with softening nonlinearity when the force is applied in its first or third mode only.	109
5.8	A schematic diagram of an in-line, 3-DoF system with cubic nonlinear springs.	109
5.9	The variation of the linear natural frequencies with the linear stiffness of the system depicted in Fig. 5.8	112
5.10	The variation of the linear modeshapes with the linear stiffness of the system depicted in Fig. 5.8	113
5.11	The backbone curves of the 3-DoF system depicted in Fig. 5.8 with 1 : 2 : 3 linear natural frequencies.	118
6.1	A schematic diagram of a thin, rectangular plate with the edges simply supported.	123
6.2	The linear modeshape configurations of the first four bending modes of a thin, rectangular plate with the edges simply supported, computed using Abaqus®.	125
6.3	The power spectral density of the response of a thin, rectangular plate with the edges simply supported to random excitations, computed using finite element model simulation data.	126
6.4	The power spectral density of the response of a thin, rectangular plate with the edges simply supported to a hybrid excitation, computed using finite element model simulation data.	127

6.5	The linear modeshape configurations of the first four modes of a thin, rectangular plate with the edges simply supported, used in the Galerkin decomposition.	133
6.6	The power spectral density of the response of a thin, rectangular plate with the edges simply supported to random excitations in the first four modes, computed using nonlinear reduced-order model simulation data.	135
6.7	The power spectral density of the response of a thin, rectangular plate with the edges simply supported to a hybrid excitation in the first four modes, computed using nonlinear reduced-order model simulation data.	136
6.8	The power spectral density of the response of a thin, rectangular plate with the edges simply supported to random or hybrid excitations in Mode I and III, computed using nonlinear reduced-order model simulation data.	137
6.9	The backbone curves of a thin, rectangular plate with the edges simply supported, with considering the effect of the non-resonant modal interaction.	144
6.10	The forced response curves of a thin, rectangular plate with the edges simply supported when its first mode is forced to respond at a constant amplitude and the third mode is harmonically forced.	148
6.11	The forced response curves of a thin, rectangular plate with the edges simply supported when its first and third modes are harmonically forced simultaneously.	149
7.1	A schematic representation of a free-decay response of the example plate depicted in Fig. 6.1.	159
7.2	A schematic representation of the Hanning windows of a varying size with time.	160
7.3	A schematic representation of the Fourier transfer coefficient results of the free-decay response of the example plate depicted in Fig. 6.1.	160
7.4	A schematic representation of the instantaneous response amplitudes and frequencies of the example plate depicted in Fig. 6.1.	161
7.5	The backbone curves of the example plate depicted in Fig. 6.1, measured from nonlinear reduced-order model simulation data.	162
7.6	The force configurations used in finite element analysis simulations of the example plate depicted in Fig. 6.1.	163
7.7	The backbone curves of the example plate depicted in Fig. 6.1, measured from finite element model simulation data.	163

7.8	A schematic diagram of the differential evolution algorithm.	167
7.9	A schematic representation of the convergence map of the self-adaptive differential evolution algorithm processing nonlinear reduced-order model simulation data.	172
7.10	A schematic representation of the convergence map of the self-adaptive differential evolution algorithm processing finite element computational model simulation data.	173
7.11	A comparison between the true and estimated backbone curves of the example plate depicted in Fig. 6.1, using nonlinear reduced-order model simulation data.	174
7.12	A comparison between the estimated backbone curves of the example plate depicted in Fig. 6.1, using finite element model simulation data for the single-mode- and double-mode-forced situations.	175
B.1	The backbone curves of the 3-DoF system depicted in Fig. 5.8 with 1 : 2 : 2 linear natural frequencies and hardening nonlinearity.	200
B.2	The backbone curves of the 3-DoF system depicted in Fig. 5.8 with 1 : 2 : 2 linear natural frequencies and softening nonlinearity.	202

List of tables

6.1	Properties of the example plate.	124
6.2	Linear natural frequencies and nonlinear parameters for the first four modes of the example plate.	132
6.3	Expressions of the parameters in the descriptions of the double-mode backbone curves of the example plate.	141
6.4	Expressions of the extra parameters in the descriptions of the double-mode backbone curves of the example plate depicted, with non-resonant interactions considered.	143
7.1	The true and estimated values of the linear natural frequencies and nonlinear parameters of the example plate, using nonlinear reduced-order model simulation data.	171
7.2	The estimated values of the linear natural frequencies and nonlinear parameters of the example plate, using finite element model simulation data.	173

Nomenclature

N	The number of degrees of freedom of a system
\mathbf{C}	An $\{N \times N\}$ damping matrix, see Eq. (3.1)
$\mathbf{\Gamma}_x$	An $\{N \times 1\}$ vector of nonlinear terms in physical coordinates x , see Eq. (3.1)
\mathbf{K}	An $\{N \times N\}$ stiffness matrix, see Eq. (3.1)
\mathbf{M}	An $\{N \times N\}$ mass matrix, see Eq. (3.1)
\mathbf{x}	An $\{N \times 1\}$ vector of physical displacements, see Eq. (3.1)
ε	A bookkeeping parameter denoting the smallness
$\dot{}$	The first-order derivative with respect to time
$\ddot{}$	The second-order derivative with respect to time
$\bar{\mathbf{P}}_x$	An $\{N \times 1\}$ vector of force amplitudes in physical coordinates x , see Eq. (3.2)
\mathbf{P}_x	An $\{N \times 2\}$ matrix of force amplitudes in physical coordinates x , see Eq. (3.2)
\mathbf{r}	A $\{2 \times 1\}$ vector of complex exponential functions expressing the sinusoidal component of external force, Eq. (3.2)
Ω	The external force frequency, see Eq. (3.2)
e	Euler's number

\mathbf{i}	Imaginary unit, i.e. $\mathbf{i} = \sqrt{-1}$
t	Time
r_p	The positive complex component of the sinusoidal forcing, see Eq. (3.2)
r_m	The negative complex component of the sinusoidal forcing, see Eq. (3.2)
\mathbf{N}_x	An $\{N \times 1\}$ vector of nonlinear terms and linear damping terms in physical coordinates x , see Eq. (3.3)
Φ	An $\{N \times N\}$ matrix of linear modeshapes, see Eq. (3.4)
Λ	A diagonal $\{N \times N\}$ matrix of the square of linear natural frequencies, see Eq. (3.6)
ω_{ni}	The i^{th} linear natural frequency, see Eq. (3.6)
\mathbf{N}_q	An $\{N \times 1\}$ vector of nonlinear terms and linear damping terms in modal coordinates q , see Eq. (3.8)
\mathbf{P}_q	An $\{N \times 2\}$ matrix of excitation amplitudes in modal coordinates q , see Eq. (3.8)
$\mathbf{P}_{q,i}$	An $\{1 \times 2\}$ vector representing the i^{th} row of matrix \mathbf{P}_q
\mathbf{q}	An $\{N \times 1\}$ vector of modal displacements, see Eq. (3.8)
\mathbf{I}_N	An $\{N \times N\}$ identity matrix
\mathbf{P}_v	An $\{N \times 2\}$ matrix of excitation amplitudes in forcing-transformed modal coordinates v , see Eq. (3.14)
$\mathbf{P}_{v,i}$	An $\{1 \times 2\}$ vector representing the i^{th} row of matrix \mathbf{P}_v
\mathbf{v}	An $\{N \times 1\}$ vector of forcing-transformed modal displacements, see Eq. (3.14)

W	An $\{2 \times 2\}$ matrix of diagonal elements $+\mathbf{i}\Omega$ and $-\mathbf{i}\Omega$, see Eq. (3.13)
e	An $\{N \times 2\}$ matrix for removing non-resonant forcing terms, see Eq. (3.11)
e_i	A $\{1 \times 2\}$ vector representing the i^{th} row of matrix e
N_v	An $\{N \times 1\}$ vector of nonlinear terms and linear damping terms in forcing-transformed modal coordinates v , see Eq. (3.14)
P_u	An $\{N \times 2\}$ matrix of excitation amplitudes in resonant coordinates u , see Eq. (3.26)
u	An $\{N \times 1\}$ vector of the fundamental components of modal displacements, Eq. (3.26)
Y	A diagonal $\{N \times N\}$ matrix of the square of fundamental response frequencies, see Eq. (3.24)
N_u	An $\{N \times 1\}$ vector of resonant nonlinear terms and linear damping terms, Eq. (3.26)
n_{u(j)}	An $\{N \times 1\}$ vector of the resonant components in the j^{th} homological equation, see Eq. (3.30)
[n_{u(j)}]	An $\{N \times L_j\}$ matrix of the coefficients of the components in n_{u(j)} , corresponding to the terms in u_(j)[*] , see Eq. (3.40b)
N_{u,i}	The i^{th} term of vector N_u
N_{ui}⁺	The time-invariant complex component of the i^{th} term of N_u corresponding to the positive conjugate of the resonating term, see Eq. (3.54)
N_{ui}⁻	The time-invariant complex component of the i^{th} term of N_u corresponding to the negative conjugate of the resonating term, see Eq. (3.54)

H	An $\{N \times 1\}$ vector of harmonic components of the modal displacements, see Eq. (3.22)
$\mathbf{h}_{(j)}$	An $\{N \times 1\}$ vector of the harmonic components in the j^{th} homological equation, see Eq. (3.31)
$[h_{(j)}]$	An $\{N \times L_j\}$ matrix of the coefficients of the components in $\mathbf{h}_{(j)}$, corresponding to the terms in $\mathbf{u}_{(j)}^*$, see Eq. (3.40c)
\mathbf{N}_v	An $\{N \times 1\}$ vector of nonlinear terms and linear damping terms in forcing-transformed coordinates v , see Eq. (3.14)
$\mathbf{n}_{v(j)}$	An $\{N \times 1\}$ vector of nonlinear and damping, including both resonant and harmonic, components in the j^{th} homological equation
$[n_{v(j)}]$	An $\{N \times L_j\}$ matrix of the coefficients of the components in $\mathbf{N}_{v(j)}$, corresponding to the terms in $\mathbf{u}_{(j)}^*$, see Eq. (3.40a)
L_j	The number of unique combinations of the variables in the j^{th} homological equation
$\mathbf{u}_{(j)}^*$	An $\{L_j \times 1\}$ vector of unique combinations of the variables in the j^{th} homological equation
ω_{ri}	The fundamental response frequency of the i^{th} mode, see Eq. (3.39)
ϕ_i	The phase of the fundamental response component of the i^{th} mode, see Eq. (3.39)
U_i	The amplitude of the fundamental response component of the i^{th} mode, see Eq. (3.39)
u_i	The i^{th} term of vector \mathbf{u} , representing the displacement of the fundamental component of the i^{th} mode, Eq. (3.39)
u_{ip}	The positive component of the complex conjugate pair that forms u_i , Eq. (3.39)

- u_{im} The negative component of the complex conjugate pair that forms u_i , Eq. (3.39)
- \mathbf{u}_p An $\{N \times 1\}$ vector whose i^{th} term is u_{ip}
- \mathbf{u}_m An $\{N \times 1\}$ vector whose i^{th} term is u_{im}
- $\boldsymbol{\beta}_{(j)}$ An $\{N \times L_j\}$ matrix for identifying the resonant terms in the j^{th} homological equation

Chapter 1

Introduction

Real-life mechanical systems are inherently nonlinear to some extent, and the sources of nonlinearity are diverse: geometric, material and contact/boundary conditions. Nonlinearity is often viewed to be problematic as it may cause unwanted vibration motions and sometimes even catastrophic failure of mechanical structures. One of the typical devastating incidents is the collapse of the first Tacoma Narrows Bridge (Fig. 1.1(a)) whose failure is due to the catastrophic vibrations caused by the nonlinear fluid-structure interaction. Therefore, traditionally most structures are designed to operate within regions where their behaviour is approximately linear. However, linearity is an idealisation. The existence of structural nonlinearities is often inevitable, especially for these recent advanced mechanical applications which are required to perform more cleanly and efficiently. For example, in the aerodynamic field, to enhance fuel economy and prevent climate change, *high-aspect-ratio* wings (Fig. 1.1(b)) are employed to increase the lift-to-drag ratio, and a lot of composite material components of nonlinear mechanical properties replace the traditional metal ones to reduce weight. All of these will eventually result in nonlinearities of aeroplane systems.

In fact, the occurrence of nonlinearities is not always negative. On the contrary, nonlinearities can also bring advantages, e.g. with the concept of nonlinear design, the application context or performance may be significantly improved. One example may be that about the nonlinear improvement of tuned mass dampers (TMDs), a vibration reduction device widely used in engineering structures. One significant drawback of linear TMDs is that they have a small operating frequency range. This suggests that linear TMDs are not suitable for applications where the excitation has several dominant frequencies and systems possess nonlinear components. In this context, the nonlinear characteristics may be exploited to address this limitation. By replacing the linear springs and damping with nonlinear ones in TMDs, their effective frequency range was proved to be significantly enhanced [80].

(a) The collapse of the Tacoma Narrows Bridge¹(b) An ASH 31 glider with very high aspect ratio²

Fig. 1.1 Example nonlinear mechanical structures.

About the well-established linear techniques for designing and optimising the dynamic performance of mechanical structures, most of them adopt the approach of *modal analysis*, which is based on the concept of *linear normal modes*. In the modal analysis, the equation of motion (EoM) of a dynamic system can be decoupled using linear normal modes and then system (free or forced) response can be expressed as the superposition of individual linear normal mode responses. This decomposition is based on an important property of linear normal modes, i.e. *orthogonality*, which means that the modes are uncoupled. More specifically, the response of one mode is not affected by the change of other modes. Due to the uncoupling property, linear modes are to be considered individually.

Undeniably, with the useful properties of linear normal modes, the linear techniques have achieved numerous implementation successes, e.g. reduced-order modelling and system identification. However, these linear techniques are obviously limited for nonlinear systems. One simple reason is that the principle of superposition does not hold for nonlinear systems due to the presence of nonlinearities. Therefore, considering the (positive and negative) significance of the nonlinearity, the lack of tools suited to dealing with nonlinearity in dynamic structures presents a challenge of developing novel techniques and methodologies for nonlinear dynamic systems. This expectation can only be achieved by better understanding and interpreting nonlinear system behaviours.

This thesis aims to further improve the theoretical understanding of the smooth nonlinear dynamic behaviours of mechanical systems, and apply the findings to develop innovative approaches for the practical use.

¹[https://en.wikipedia.org/wiki/Tacoma_Narrows_Bridge_\(1940\)](https://en.wikipedia.org/wiki/Tacoma_Narrows_Bridge_(1940))

²https://en.wikipedia.org/wiki/Schleicher_ASH_31

1.1 Research motivations

The overall objective of the project is

- To advance understanding and develop techniques for dynamic analysis of nonlinear mechanical systems.

The specific objectives are

- To further explore modal interactions within nonlinear systems with a low number of degrees of freedom.
- To demonstrate that backbone curves offer a valuable tool for interpreting the nonlinear dynamic behaviours of mechanical systems.
- To investigate an alternative approach for the identification of nonlinear mechanical systems using backbone curves.

1.2 Thesis outline

- In Chapter 2, a brief literature review is presented, related to the dynamic characteristics of nonlinear systems, e.g. modal interaction. Two main approaches for solving nonlinear mathematical models, i.e. numerical and approximate analytical approaches, are discussed. Additionally, the modal analysis for nonlinear systems, i.e. normal form analysis and nonlinear normal modes, is briefly introduced. Lastly, the techniques for the identification of nonlinear systems are compared.
- In Chapter 3, the derivation of the application of the direct normal form technique to a general nonlinear system under damped and single-frequency forcing is presented, in which its implementation assumptions and corresponding limitations are discussed. The companion approach for the stability assessment of the direct normal form solutions is introduced to complete the framework for the nonlinear solution approximation. This approximation framework is shown to be able to compute the backbone curves of nonlinear systems by considering its underlying conservative system, i.e. without damping and forcing terms. The objective of this chapter is to introduce the implementation procedure of the direct normal form technique in detail, which is the primary technique used throughout this thesis.

- In Chapter 4, the research of dynamic characteristics, especially the resonant modal interaction, of a nonlinear 3-degree-of-freedom (DoF) system is presented. The structure of this system is specifically designed to make one of its vibration modes linearly independent and the other two, with similar linear natural frequencies, nonlinearly coupled. The direct normal form method is first applied to approximate the time-invariant equations governing the forced resonances of this system under the harmonic excitation at a frequency in the vicinity of its linear natural frequencies. However, to reveal the relationship between the modal interaction and the physical system parameters, the governing equations without the forcing and damping terms are considered to compute backbone curves. These backbone curves are demonstrated to be able to interpret different kinds of resonant modal interaction between the two nonlinearly interacting modes. Based on the observation of the relationship between forced response and backbone curves, these backbone curves are found to be useful to predict the occurrence of response bifurcations caused by resonant modal interaction for the forced and damped situation. The purpose of this chapter is to demonstrate the resonant modal interaction involving a subset of vibration modes of systems of multiple degrees of freedom and show the ability of backbone curves to interpret and predict nonlinear bifurcations caused by the resonant internal interaction.
- In Chapter 5, the resonant modal interaction among three nonlinearly coupled modes is considered. Firstly, the derivation of the direct normal form technique applied to a generic conservative 3-DoF system with cubic stiffness nonlinearity is introduced. The results are later used to compute backbone curves of specific examples for demonstrating different kinds of potential internal interaction. For the first example, its three vibration modes are designed to be nonlinearly coupled, and their linear natural frequencies are tuned to be closed such that the three modes may potentially, resonantly interact with each other. The second example has three nonlinearly coupled modes of commensurable linear natural frequencies, i.e. $\omega_{n1} : \omega_{n2} : \omega_{n3} \approx 1 : 2 : 3$. The backbone curves solutions of both examples are discussed respectively, and the backbone curve bifurcations are considered to interpret the resonant interaction happening among multiple nonlinear modes. The objective of this chapter is to demonstrate the resonant internal interaction involving all modes of systems of multiple degrees of freedom and show the backbone curves can be further applied to interpret these more complex nonlinear phenomena.
- In Chapter 6, the resonant frequency shift of systems under multi-frequencies exci-

tations due to the non-resonant modal interaction is considered. This nonlinear phenomenon is shown by the power spectral density results of finite element computational models of a thin rectangular plate under random and random plus harmonic excitations at relatively high power levels. Two nonlinear reduced-order models consisting of the first four vibration modes of the example plate are employed to simulate the response under the identical excitations of interest, and the results are qualitatively compared with the finite element analysis results. The difference between the two nonlinear mathematical models is that one includes the nonlinear coupled-mode terms and the other one does not. The comparison results show that the nonlinear coupled-mode terms associated non-resonant modes contribute to the resonant frequency shift. The backbone curves are again employed to interpret the mechanism of these nonlinear coupled-mode terms affecting resonant frequencies, which is because of the non-resonant modal interaction occurring for the situation when multiple modes are simultaneously and externally excited. The objective of this chapter is to show the effect of the non-resonant interaction for multi-mode excitation situations and the significance of the nonlinear coupled-mode terms of non-resonant modes to be included in the mathematical model for such situations.

- In Chapter 7, an approach for nonlinear system identification is investigated. This approach is inspired by the findings in Chapter 6 and its main advantages are: estimating parameters of multiple modes through applying a single test and determining parameters related to non-resonant mixed-mode nonlinear terms. The idea of resonant decay is employed to estimate backbone curves, in which multiple modes of the system under consideration are initially forced and then freely decay after the excitation is removed. The short-time Fourier transform with time-varying windows is employed to measure backbone curves from the free-decay response. Then the backbone curve model with the consideration of non-resonant modal interaction is used to determine the parameters of the mathematical model.
- In Chapter 8, the conclusions and potential further work are discussed.

Chapter 2

Literature review

In this chapter, a brief literature review is presented, related to nonlinear dynamic characteristics, analysis approaches for studying nonlinear systems and nonlinear system identification.

2.1 Nonlinear dynamic behaviours in mechanical systems

In Chapter 1, the importance of the role of nonlinearities in mechanical systems has been briefly introduced. In this section, the dynamic characteristics of nonlinear mechanical systems and their corresponding effects are discussed. Since nonlinear dynamics is a popular research area studied for decades, plenty of relating literature is available. For example, in the books [8, 30, 39, 56, 92], much of the early literature and background to nonlinear dynamics have been summarised.

2.1.1 Nonlinear dynamic characteristics

Compared with that of linear systems, the dynamic behaviour of nonlinear systems presents numerous unique features. One example is the initial condition sensitivity: contrary to linear systems the steady-state response of a nonlinear system may not be unique and may depend on the initial conditions. Besides, when subject to a harmonic input the major component of the output of a nonlinear system may not be at the input frequency, i.e. a subharmonic or a superharmonic of the input frequency. These unique characteristics may cause nonlinear dynamic phenomena including multiple solutions, jump phenomena, harmonics, resonance distortion, quasi-periodic motions, etc. However, the most significant dynamic characteristic of nonlinear systems, more specifically for nonlinear multi-DoF discrete systems and

continuous systems, may be *modal interactions* [66, 67]. Unlike a linear system whose vibration modes are uncoupled and behave independently, the modes of a nonlinear system may be nonlinearly coupled and interact, which is the main reason that the superposition principle does not hold for nonlinear systems.

The modal interaction can cause energy exchanges between/among modes, one of whose results is that the externally unforced mode(s) can be activated by the nonlinearly coupled mode(s) which is directly forced, termed as *resonant interaction*. For example, Cammarano et al. [6] considered an in-linear lumped-mass nonlinear oscillator of two degrees of freedom whose two linear natural frequencies are close. This system is forced in the anti-phase mode (two masses moving in opposite directions), while its in-phase mode (two masses moving in an identical direction) responds due to the one-to-one internal resonance when the excitation is beyond a specific amplitude. This phenomenon was also observed in continuous structures: in [35], a taut cable under a purely vertical, in-plane support excitation at a frequency close to its second linear in-plane natural frequency exhibits a whirling behaviour, which was demonstrated to be because an out-of-plane mode of the cable is activated due to the one-to-one *out-of-unison* resonant interaction.

Except for the one-to-one resonant interaction, there exists *auto-parametric* resonance between modes. In [49], a 2-DoF system, consisting of a grounded nonlinear oscillator under harmonic excitation coupled to a light linear attachment, experiences a three-to-one resonant modal interaction. This resonance results in a localisation phenomenon that the primary and three-times harmonic components of the system response are localised to the nonlinear oscillator and the linear attachment respectively. This auto-parametric interaction can even cause more complex dynamic behaviours. In [87], a cantilever beam with a nonlinear spring at the tip experiencing a three-to-one modal interaction was observed to exhibit isolated resonant response (detached resonance) and quasi-periodic response.

The resonant modal interaction is not limited to happening within two nonlinear modes. Nayfeh et al. [68] investigated the three-mode interaction by considering the response of a 3-DoF system with quadratic nonlinearities under the internal resonant condition that $\omega_1 : \omega_2 : \omega_3 \approx 1 : 2 : 4$ to a harmonic excitation. It was found that this system undergoes periodic, quasi-periodic and chaotic motion as the amplitude of the excitation increases.

2.1.2 Effects of the nonlinearity in mechanical systems

The occurrence of nonlinearities may cause undesirable effects on engineering systems, which correspondingly brings some challenges to structural engineers. One of the chal-

allenges lies in the control design for nonlinear vibrations, e.g. nonlinear active feedback control. For the control of single-DoF systems, due to harmonic responses caused by the nonlinear terms, the control signal must include harmonic components, and, for that of multi-DoF systems, because of the modal interaction due to cross-coupling terms, all the associated modes instead of the one of interest must be considered together. Obviously, these significantly enhance the difficulty of control system designs for nonlinear structures.

The nonlinear feature of isolated resonant responses is also demonstrated to be problematic, e.g. causing large-amplitude responses [87]. This feature may significantly affect the performance of mechanical applications, e.g. this nonlinear large-amplitude response phenomenon caused by the detached resonance was observed in a nonlinear TMD studied by Alexander and Schilder [1], which consequently raises the question about the efficacy of nonlinear TMDs.

On the contrary, the presence of nonlinearity can be also beneficial in cases where it is properly exploited. For nonlinear TMDs, one of its advantages of efficient vibration suppression over a broad bandwidth is thanks to the resonance distortion. Another example of nonlinear applications may be the high-static-low-dynamic-stiffness (HSLDS) vibration isolator [25, 79]. The linear vibration isolator only works in the bandwidth far way from its natural frequency, [37], As $\omega_n = \sqrt{k/m}$, a smaller stiffness results in a wider frequency range of isolation, while its side-effect is a larger static displacement. To address this trade-off issue, softening nonlinear springs are used to induce an isolation of a high static stiffness, thus a small static displacement, but a low dynamic stiffness, and therefore a reduced natural frequency.

As with other nonlinear dynamic characteristics, the modal interactions in the dynamics of nonlinear systems also have many practical implications. For example, the motion confinement feature can be exploited in novel designs of the vibration isolator, where a disturbance caused by external forces is first spatially confined to a pre-designed part of the structure, and then, passively or actively dissipated [27, 29, 41, 43, 44, 50, 93, 95]. Additionally, the mode localisation can also be implemented in the micro-electro-mechanical system (MEMS) designs, e.g. micro-cantilever arrays and micro-resonator arrays [19]. It was suggested that the type of localisation due to the auto-parametric resonance found in [49] could be used to design new type of atomic force microscope (AFM) probe.

2.2 Methods for analysing nonlinear dynamics

For either avoiding or exploiting nonlinearities, understanding the behaviour of nonlinearity in structural dynamics seems to be essential. While the approaches recently used for exploring nonlinear dynamics are broad, they can be simply classified into three types: numerical, analytical and experimental methods. Due to the specific theme of this thesis, we only focus on the mathematical-model-based approaches, i.e. numerical and analytical methods, in this section. For the discussion of experimental methods for studying nonlinear dynamics, see [65]. Additionally, the approaches of modal analysis for nonlinear systems are briefly discussed.

2.2.1 Numerical methods

Given a dynamic mathematical model of a deterministic nonlinear system, the numerical techniques may be a straight-forward way to be employed for finding its solutions. As the mathematical models for physical systems could be depicted in various forms, an overview of only the methods for solving nonlinear ordinary differential equations (ODEs) will be provided because this is the primary method used in this thesis.

One of the numerical approaches for finding dynamic solutions is the direct time-integration of equations of motion (EoMs). The main advantage of this method is its simplicity and accessibility, e.g. the inbuilt ODE solvers in MATLAB[®] [58] are a good option. This technique is also not restricted to the forms of mathematical models, i.e. neither smooth nor non-smooth systems. Moreover, because it is a time-domain approach, the time-integration method is inherently employable for simulating system transient dynamic responses, which may be further processed to find solutions like the steady-state response or frequency response functions (FRFs). For example, in [71], Neild and Wagg found the steady-state of a single-DoF Duffing oscillator using this approach to validate their approximation results of resonance curves. However, the drawbacks of this method are also obvious. For example, it is significantly time-consuming and inefficient to implement this on problems of large-scale systems. Additionally, finding the steady state, or near steady state of a system using such techniques may take a long time, especially for systems with light damping. Besides, due to transient or numerical effects, it may be impossible to integrate the unstable steady-state solutions or even stable solutions but with weak attractions.

The other numerical approach, which is more specific to smooth nonlinear dynamic systems, is *numerical continuation*. The theoretical concept of numerical continuation, also known as parameter continuation, is based on a simple observation that the solutions to pa-

parameterised mathematical equations are a curve or a manifold of points. This suggests that the solution to a small, continuous change to a parameter of the EoMs of the underdetermined system will result in a small, continuous change in the solution. Therefore, given an initial solution point in the parameter space, the solution corresponding to a small change in a considered parameter can be traced in its immediate neighbourhood, this new found solution may then be used to find the next solution with another small parameter change and the procedure repeats. Compared with direct time-integration techniques, the numerical continuation is more efficient in finding the steady-state solutions. Also, the unstable solutions may also be traced using this technique.

The theory of numerical continuation has been implemented in a variety of software packages. Some well-known examples in the dynamic community are *AUTO-07p*, firstly proposed by Doedel in [21] and accessible from [22], *MatCont*, developed by Dhooge et al. [16] and available from [18] with new features added [17], *COCO*, introduced in [14] and available from [84] and *NNMcont*, discussed in [73] by Peeters et al. and available from [72]. Many of the continuation packages were initially developed for the mathematics community to use, e.g. *AUTO-07p*, *MatCont* and *COCO*. Due to their versatility and extensibility, they have been employed to help understand complex mechanical dynamic behaviours. For example, *AUTO-07p* was used, in [85], to conduct the bifurcation analysis of an aircraft, which was reported to be of importance during the aircraft design process. The other example of the combined use of numerical continuation and other techniques for experimental tests is given in [77], in which *COCO* in a controlled manner was adapted to track the locus of the resonant response of an experimental nonlinear oscillator set-up.

Unlike others, *NNMcont* is specifically designed for computing the response of nonlinear mechanical structures. More specifically, instead of computing the forced and damped, i.e. non-conservative, response of the nonlinear mechanical systems, this algorithm allows for finding the periodic solution of equivalent conservative structures based on the *nonlinear normal modes* (NNMs) theory [45]. There are numerous mechanical applications of *NNMcont*. For example, in the aerospace field, Kerschen et al. [46] adopted it to compute the NNMs of the airframe of the aircraft and Renson et al. [78] used it to find the NNMs of a satellite structure.

Comparing the example numerical continuation algorithms, *AUTO-07p* is written in Fortran while the other three are implemented in MATLAB[®]; therefore, *AUTO-07p* may be less familiar with structural dynamicists and less compatible with many existing software packages. Besides, *MatCont* and *NNMcont* both use the graphical user interface, which makes them easily implementable but correspondingly limits their flexibility in the aspect of re-

search. Therefore, *COCO* has been employed to conduct the works for this thesis.

2.2.2 Approximate analytical methods

Although numerical approaches are very powerful for solving the nonlinear EoMs of dynamic systems, there still exist limitations. Firstly, the numerical results could not implicitly present the relationships between physical properties of the mechanical systems and nonlinear dynamic behaviours they exhibit without additional tools to aid interpretation. The other limitation is that the numerical solution can be incomplete, especially when solving nonlinear dynamic equations with multiple solutions, which means that some solutions may not be found using numerical approaches. This was presented, for example, in [1] when exploring the dynamic behaviour of nonlinear TMDs that a family of isolated resonant response was missed in the numerical simulation in [29]. These drawbacks of the numerical approaches may restrict the insight gained into the mechanisms governing the dynamic behaviour, and, sometimes even worse, lead to a potential failure scenario.

Considering the analytical methods, the drawbacks of the numerical approach may be naturally circumvented. It is noteworthy that compared with numerical techniques, the analytical approach also has its limitations, one of which is that the upper bound of the application of analytical methods is not known a priori, i.e. the accuracy of the analytically approximated results for a specific system is unknown before compared with the real solutions. Therefore, the joint use of the numerical and analytical methods will be applied in this thesis. In the existing literature, the most commonly used approximation methods are *harmonic balance*, *averaging*, *multiple scales* and *normal form* [66, 98].

The harmonic balance method is a frequency domain method for calculating the steady state, which was originally implemented by Baily [3] and Lindenlaub [53]. The idea of this method is based on the substitution of a pre-assumed solution with a finite number of sinusoidal components into the differential EoM and balancing the terms at each frequency after expanding the expressions and ignoring the higher-order unbalanced terms. This method has been widely used to study mechanical structures, e.g. bladed discs [74] and MEMS [47]

The main advantage of the harmonic balance method is its simplicity as no specific assumption is needed, which correspondingly leads to one of its disadvantages that there are no strict rules for the assumption of the solution for the nonlinear governing ODEs. Thus the accuracy of this method strictly depends on the choice of the number of harmonics in the assumed solution [48]. For example, if specific harmonics are of interest, then they may be included in the assumed solution, which asks for the adopter to have prior knowledge

of the response of the system under consideration. The other disadvantage of the harmonic balance method is that its complexity grows exponentially with the number of the sinusoidal components in the assumed solution, which limits its application in large and complex systems, e.g. the one with many degrees of freedom. While the automated computation of the harmonic balance method [15, 97] with the help of the numerical treatment may circumvent this issue, this is based on the sacrifice of the advantages of the analytical method.

The averaging method is based on the averaging principle that the exact differential EoM is replaced by its averaged version, i.e. the average response over one period of motion is considered. Thus, the slow dynamic component of the response, i.e. the fundamental response, is retained for solving the response while the fast dynamics, i.e. the harmonics, have been removed. Similar to the harmonic balance method, the assumed solution needs to be substituted into the EoM. More details about the averaging method applied in nonlinear dynamic systems can be found in the textbook [83]. The significant advantage of this method is that not only can it be used to find the steady-state response of a system but also to determine its transient behaviour [96], with which feature the averaging method can be extensively employed to assess the stability of the steady-state solutions. For example, the method of averaging was adopted to determine the stability of the modal response solution of an inclined cable system in [28].

The averaging method also has several disadvantages, one of which is that because of the averaging process the harmonic terms cannot be considered directly, which limits the insight given by the solution only into the fundamental components of the response. Additionally, due to the assumption of small nonlinear terms, the application of the method of averaging is limited to weakly-nonlinear systems, where the nonlinear terms is much smaller than the linear ones [98]. While most of the nonlinear analytical approximation methods adopt the weakly-nonlinear assumption, thus this is not considered as a significant issue in the thesis. It is noteworthy that the harmonic balance method can approximately solve strongly nonlinear dynamic problems.

The multiple scales technique, as with the averaging method, employs the concept of multiple time scales so that the components of the response can be separated into fast and slow dynamics. However, the difference is that instead of removing the fast components via averaging, any terms are considered to be of equivalent order by applying different time scales. Similar to other analytical methods, the application becomes complex when systems become large.

About the normal form method, the French genius Henri Poincaré has to be mentioned. He pointed out it is possible to derive the most important information about the behaviour

of a family of solutions without having to solve the equation. The original context was that of conservative systems written in Hamiltonian form. The details about Hamiltonian normal form (or Birkhoff normal form) was introduced in [61]. This Hamiltonian normal form theory does not allow for the presence of damping, and it is not straightforward to include forcing. To eliminate the weakness, the other normal form technique about the transformation of first-order ODEs was developed, named as the *first-order normal form* technique [2]. It was first implemented in nonlinear dynamic systems in [40]. Compared with the Hamiltonian normal form, the damping and force can be treated in the first-order normal form.

However, there is still an obvious limitation of the first-order normal form technique, i.e. the coordinates used are non-physical and need to be transformed back to the physical domain. Consequently, a variant of the normal forms was firstly introduced by Neild and Wagg in [71] that can be directly applied to second-order differential equations; thus this method is called the *direct normal form* technique (or the *second-order normal form* technique originally). Because most of the mechanical vibration problems are naturally described in the second-order form, the direct normal form technique has its innate advantage. Additionally, the direct normal form technique is demonstrated to be able to provide more accurate approximation solutions than the first order equivalent does [71]. Compared with other techniques discussed so far, the primary advantage of the normal form technique is that it can inherently compute the harmonics without pre-assuming any specific harmonic components included in the trial solution. This means that no priori knowledge about the harmonic components in the response of the system is required and no additional complexity is needed when considering the harmonics. Besides, the process of normal forms can be formulated in a matrix based manner, which makes its application more appropriate for the computer automation.

There are a number of research works about nonlinear dynamics of mechanical systems based on the direct normal form technique. Xin et al. [102] used the direct normal form technique to consider the single-DoF nonlinear oscillators of polynomial-type nonlinearities involving velocities and displacements. They illustrated the contributions of the different polynomial nonlinearities in different forms to the system response by the resonance response functions (RRFs) results. In [86], the performance of the nonlinear vibration isolator was investigated using the direct normal form technique. The system was modelled as a single-DoF oscillator with cubic and quintic nonlinear terms. Shaw et al. [86] estimated a group of *backbone curves* of the nonlinear vibration isolator with considering its equivalent conservative system, which, with the aid of *limit curves*, can be used to predict the optimum

restriction of the nonlinear vibration isolator. Cammarano et al. [7] analytically and numerically investigated the optimal load for the nonlinear energy harvester in the case of purely resistive loads. They found the analytical results approximated using the direct normal form technique were very close to the numerical results within the frequency range of interest.

The direct normal form technique was also applied to study the nonlinear dynamic behaviours of multi-DoF systems. Cammarano et al. [6] studied the bifurcations of the backbone curves caused by the modal interaction by considering a 2-DoF oscillator with cubic nonlinearities and Hill et al. [35] considered the same system to introduce the out-of-unison resonance behaviour which was also observed in practical systems, such as the taut cable. In [32], Hill et al. discussed how backbone curves estimated using the normal form method can be used to guide the design and optimisation of weakly nonlinear systems of multiple degrees of freedom. The direct normal form technique has been chosen as the main analysis tool to estimate the dynamic response of the nonlinear systems considered in this thesis. Its applications and advantages will be demonstrated in detail in the following chapters.

2.2.3 Modal analysis

Modal analysis is based on the concept of *modes* of vibration which can be used to represent the system response. Linear modal analysis has been developed over the past half-century, during which it has been successfully implemented in many fields, e.g. sub-structuring techniques [11] and structural health monitoring [20]. For linear systems, these vibration modes are decoupled (mutually independent) and the system response can be expressed as the summation of the response from each mode. The vibration modes are only determined by the material properties, e.g. mass, damping and stiffness, and structural properties, e.g. boundary conditions, of the system. The number of modes is equal to the degrees of freedom of the system. Each mode is related to a natural frequency, modal damping and mode shape.

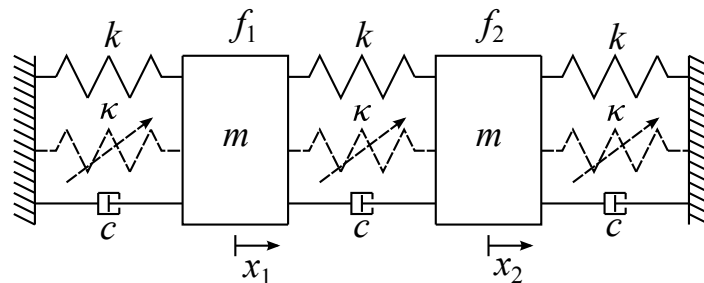


Fig. 2.1 A schematic diagram of an in-line, 2-DoF oscillator with masses, m , linear stiffness k , linear damping c and nonlinear stiffness κ .

For example, considering a linear 2-DoF system depicted in Fig. 2.1 whose motion is governed by the equations,

$$\begin{aligned} m\ddot{x}_1 + c(2\dot{x}_1 - \dot{x}_2) + k(2x_1 - x_2) &= f_1, \\ m\ddot{x}_2 + c(2\dot{x}_2 - \dot{x}_1) + k(2x_2 - x_1) &= f_2, \end{aligned} \quad (2.1)$$

there are two vibration modes: the two lumped masses oscillating in-phase and out-of-phase, i.e.

$$\phi_1^\top = [1 \quad 1] \quad \text{and} \quad \phi_2^\top = [1 \quad -1], \quad (2.2)$$

where ϕ_i is the i^{th} linear mode shape and the superscript \top denotes the transpose. The equations governing modal motions are

$$\begin{aligned} \ddot{q}_1 + 2\zeta_1\omega_{n1}\dot{q}_1 + \omega_{n1}^2q_1 &= f_{q1}, \\ \ddot{q}_2 + 2\zeta_2\omega_{n2}\dot{q}_2 + \omega_{n2}^2q_2 &= f_{q2}, \end{aligned} \quad (2.3)$$

where

$$\begin{aligned} \omega_{n1}^2 &= \frac{k}{m}, & \zeta_1 &= \frac{c}{2\sqrt{mk}}, & f_{q1} &= \frac{f_1 + f_2}{2m}, \\ \omega_{n2}^2 &= \frac{3k}{m}, & \zeta_2 &= \frac{\sqrt{3}c}{2\sqrt{mk}}, & f_{q2} &= \frac{f_1 - f_2}{2m}, \end{aligned} \quad (2.4)$$

are the natural frequencies, modal damping ratios and modal forces respectively. Eqs. (2.3) are fully decoupled which means the two modes can be considered separately and the physical response of the two lumped masses can then be computed using the superposition principle, i.e.

$$x_1 = q_1 + q_2 \quad \text{and} \quad x_2 = q_1 - q_2. \quad (2.5)$$

For modal analysis of nonlinear structures, one approach is to use the theory of NNMs. The NNMs concept was first introduced by Rosenberg [82] and, then, Rand [76] and Manevich and Mikhlin [55] used it to investigate nonlinear dynamic phenomena. Vakakis [94] systematically studied NNMs defined based on conservative systems. Shaw and Pierre [88] extended the concept of NNMs to deal with non-conservative systems and the most recent definition of NNMs was given in [45] by Kerschen et al..

There exist a number of definitions of NNMs in the literature. Rosenberg defined an NNM as a vibration in unison of the system, i.e. all system points reach their extreme values and pass through zero simultaneously. Therefore, it allows us to use the displacement of a

specific point as the reference and then the displacements of the remaining points can be described by the chosen reference. For example, considering the nonlinear 2-DoF system shown in Fig. 2.1, its EoMs (without damping or forcing in this case) are written as

$$\begin{aligned} m\ddot{x}_1 + k(2x_1 - x_2) + \kappa x_1^3 + \kappa(x_1 - x_2)^3 &= 0, \\ m\ddot{x}_2 + k(2x_2 - x_1) + \kappa x_2^3 + \kappa(x_2 - x_1)^3 &= 0. \end{aligned} \quad (2.6)$$

Using the displacement x_1 as the reference coordinate, x_2 can be expressed as

$$x_2 = \hat{x}_2(x_1), \quad (2.7)$$

where \hat{x}_2 is the expression of the modal curve. Then the second time derivative of x_2 is

$$\ddot{x}_2 = \hat{x}_2'' \dot{x}_1^2 + \hat{x}_2' \ddot{x}_1, \quad (2.8)$$

where prime denotes differentiation with respect to x_1 . Substituting Eqs. (2.7) and (2.8) into Eqs. (2.6) and then eliminating time dependence, i.e. \ddot{x}_1 and \dot{x}_1 , \hat{x}_2 may be found. The detailed introduction to techniques for computing NNMs can be found in [45]. The most significant advantage of the approach using NNMs is that it is not limited to weakly nonlinear systems.

The modal decomposition approach can also be incorporated for modal analysis of nonlinear systems. Employing the linear mode shapes derived from the underlying linear structure of nonlinear systems, the nonlinear EoMs are decomposed into a set of linearly uncoupled but potentially, nonlinearly coupled modes. For the example system described in Eq. (2.6), using the linear mode shapes, Eq. (2.2), the nonlinear modal EoMs are

$$\begin{aligned} \ddot{q}_1 + \omega_{n1}^2 q_1 + \frac{\kappa}{m}(q_1^3 + 3q_1 q_2^2) &= 0, \\ \ddot{q}_2 + \omega_{n2}^2 q_2 + \frac{\kappa}{m}(3q_1^2 q_2 + 9q_2^3) &= 0. \end{aligned} \quad (2.9)$$

Compared with Eqs. (2.3), Eqs. (2.9) has additional coupled nonlinear terms which means that the modes may interact and are not independent with each other anymore. This is the reason that the principle of superposition does not hold for nonlinear systems. The approximated solutions of Eqs. (2.9) can be computed using the normal form technique discussed in §2.2.2 through a series of transformations and the detailed derivation will be presented in §3.2. Compared with that using NNMs, the approach using normal form techniques based on the modal decomposition has two main advantages, especially for weakly nonlinear sys-

tems: modal interaction can be easily dealt with, and modal superposition can be tackled to some extent.

2.3 Nonlinear system identification

To apply either numerical or analytical technique to compute the system response for understanding nonlinearity in dynamic structures, a mathematical model of the system considered is required. The derivation of a mathematical model of some simple structures, e.g. a beam or a plate of simple structural and material properties and well-known and deterministic nonlinearities, may be straightforward. However, for more complex systems or structures of unknown/unclear nonlinearity, this could be less evident, in which case, a system identification technique may be adopted. In this section, the literature for nonlinear system identification is discussed. It is noteworthy that the discussion here is not a comprehensive review about the existing approaches for the identification of nonlinear dynamical structures as this subject is extremely broad, and an extensive literature exists.

One popular technique for nonlinear system identification is the *equivalent linearisation* method, which was inspired by the powerful linear system identification based on the modal analysis. The basic idea of the equivalent linearisation method is to describe the nonlinear system under identification using a linear system whose dynamic features of interest, e.g. FRFs and time-series response, are close to those of the nonlinear system. The advantages of this approach are obvious in that all the well-established linear dynamic techniques may be straightforwardly applied during its procedures and, also, the resulting linear systems are easy to solve for any further analysis.

However, there are limitations for the equivalent linearisation method. Due to the nonlinear dynamic response feature of the input-dependent output, the representative linear system may only be valid for a given excitation type at a specific excitation level. This means that different linearisation may be required for different excitation situations. Additionally, when FRFs are the considered criteria, this approach may work better for a system under a random excitation than under other types of forcing, e.g. harmonic excitation, as only the random excitation can generate the linear-system-FRFs-liked (nonlinear systems) FRFs. Besides, since the nonlinear systems are finally linearly described, the modal interaction may not be directly studied using the results of the equivalent linearisation method.

Another approach to nonlinear system identification is the *restoring force surface* (RFS) method. This method was firstly introduced by Masri and Caughey in [57] and a popular variation, known as *force-state mapping*, was developed independently by Crawley and

Aubert [12] and Crawley and O'Donnell [13]. This method involves formulating a surface describing the relationship between the internal restoring force, displacement and velocity of one degree of freedom associated with a nonlinearity and this surface is then used to estimate the parameters based on a proper model of internal forcing chosen based on the shape of the nonlinearity (surface).

There exist a number of example applications of RFS method to experiment systems. For example, Kerschen et al. [42] considered an impacting cantilever beam using RFS, where the system was excited using a band-limited white noise centred on the natural frequency of the mode of interest and a piecewise linear model was employed for parameters estimation. One significant advantage of this method is that no a priori knowledge of the system nonlinearity is required for obtaining the restoring force surface. Besides, the RFS method is not restricted to the types of system nonlinearity, e.g. smooth/non-smooth and strong/weak and the types of forcing, e.g. random excitation and harmonic excitation. However, its limitation is that this technique may be more appropriate to single-DoF systems or systems where nonlinear behaviour is located in one degree of freedom.

The NARMAX (*Nonlinear Auto-Regressive Moving-Average with eXogenous inputs*) modelling technique, which was firstly introduced by Leontaritis and Billings [51, 52], is the extension of ARX modelling technique to nonlinear systems and enables the addition of noise models to be included. This approach involves modelling nonlinear dynamic systems in a discrete-time manner, thus allowing it to inherently work for the physical experiment test. The NARMAX modelling technique is demonstrated to be very versatile in the sense that it is not limited to systems with polynomial nonlinearity and with low complexity [4]. The only issue of this approach is that the resulting models do not directly give insight into the physics of the system being modelled.

The final approach to nonlinear system identification considered is the *nonlinear resonant decay* (RD) method, which was firstly introduced by Naylor et al. [69] for the identification of non-proportionally damped linear systems. The basic idea of this approach is that the parameters of a system mode of interest can be determined from the free decay response of such a mode activated with an appropriated force pattern. Because this approach models the nonlinear systems in the modal space, the number of parameters to be identified may be enormous. To address this problem, during the initial procedure of RD techniques application, the system under identification is usually divided into a sequence of low-dimensional sub-systems which involves the modes of interaction. Although the RD method has not been used to identify large-scale continuous structures, there are still several remarkable applications to discrete systems. For example, Wright et al. [101] applied this method to a

5-DoF lumped-mass system with nonlinear springs of the cubic stiffness whose second and fourth modes are nonlinearly coupled.

2.4 Summary

In §2.1, the literature about the characteristics of nonlinearity in mechanical systems and their effects on system responses were discussed. Among the nonlinear dynamic features, modal interaction seems to be of prime importance as it results in the failure of the principle of superposition for nonlinear systems. The occurrence of modal interaction may be problematic, e.g. increasing the difficulty of nonlinear system designs and causing undesirable large-amplitude responses. However, the modal interaction can also bring benefits if it is properly utilised, e.g. the localisation phenomenon can be used for novel vibration isolator designs.

Based on the observations in §2.1, the following points are concluded:

- Modal interaction plays a significant role in distinguishing linear and nonlinear dynamic systems of multiple degrees of freedom, thus to better understand nonlinearity in mechanical systems this specific nonlinear feature will be mainly investigated in this thesis.
- Most previous work on modal interaction, especially those using analytical approaches, considered systems only having two degrees of freedom, hence this thesis will further explore the modal interaction of nonlinear systems of relatively higher degrees of freedom.
- The modal interaction phenomenon investigated in most literature occurs within systems under a single-frequency harmonic excitation. Hence the effect of modal interaction for the multi-frequency forcing situation will be considered here.

To understand nonlinearity in mechanical systems, the response solutions of nonlinear systems need to be found. Therefore, in §2.2, two main approaches for solving the solutions of mathematical models of nonlinear systems were discussed, i.e. numerical and analytical methods. The main advantage of the numerical approach is that they are not limited to the complexity of nonlinear systems; while one of its drawbacks is that the numerical results alone can provide limited insight into the explicit relationships between the physical properties and dynamic behaviour of systems. This numerical drawback can be inherently

addressed by analytical techniques. However, the upper bound of the application of analytical techniques is not known a priori, which, in turn, may be circumvented by validating the analytical results using numerical ones. Within the several widely-used analytical methods outlined, the direct normal form technique has been chosen to be employed to investigate nonlinear behaviour in this thesis due to its advantages for studying modal interaction which will be presented in detail throughout this thesis. Additionally, the modal analysis for nonlinear systems is discussed. Two approaches using NNMs and modal decomposition based on normal form technique are compared. The advantages of the normal form analysis approach are that it can better deal with modal interaction and partially tackle nonlinear modal superposition.

Based on the observations in §2.2, the following points are summarised:

- Considering the advantages and disadvantages of numerical and analytical techniques, they will be jointly implemented for the research in this thesis.
- Normal form analysis using the direct normal form technique will be the main approach for analysing the nonlinear systems in this thesis.

As a mathematical model is the basis of studying nonlinearity in mechanical systems, lastly, in §2.3, the literature about a number of powerful methods for nonlinear system identification were reviewed, and the limitations of these methods were discussed. For example, some of them are difficult to be extensively applied to large-scale systems (systems of multiple degrees of freedom), and some of them are incapable of producing a model providing physical insights.

Based on the discussion in §2.3, the following points are concluded:

- The nonlinear system identification approach introduced in this thesis will focus on the complex systems with modal interaction, suggesting that it may be potentially applicable to large-scale systems.
- The model generated by the introduced system identification approach must provide physical insight.

Chapter 3

Analysis tools for nonlinear systems

In this chapter we:

- Derive the direct normal form technique for the general forced and damped nonlinear system of multiple degrees of freedom.
- Introduce the assumptions made in the direct normal form technique and discuss the corresponding limitations.
- Derive a method, based on the direct normal form technique, for stability determination of the steady-state solutions.
- Introduce the backbone curve calculation of the equivalent conservative system of the general forced and damped nonlinear system using the direct normal form method.
- Demonstrate the capability of the direct normal form technique for estimating the steady-state forced response via its application to a 1-DoF Duffing oscillator.
- Apply the stability assessment method to analyse the stability of the normal form solutions of the 1-DoF Duffing oscillator.
- Calculate the backbone curve of the 1-DoF Duffing oscillator and demonstrate its relation with the forced responses.

3.1 Introduction

Given a mathematical description of a nonlinear system, there are mainly two approaches to tackle it: numerical and approximate analytical. The numerical approach seems to be

versatile and able to efficiently provide an approximate solution for problems in any form (e.g. ordinary differential equation or partial differential equation) with almost any type of nonlinearity (e.g. smooth or non-smooth nonlinear). However, using the numerical results to gain insight into the underlying physics of nonlinear systems remains challenging.

On the contrary, the analytical approach may often end up with explicit expressions describing the relationship between the nonlinear dynamic behaviour of systems (e.g. forced response), and their properties (e.g. physical parameters) and external excitations, such as the frequency response function (FRF). However, the significant shortcoming is that there is no exact analytical solution for the majority of nonlinear problems which means that the solutions often have to be approximated. In spite of this, as long as a sufficiently accurate solution is able to be provided, analytical techniques can still give a valuable insight to understanding the nonlinear behaviour of systems of interest. Besides, analytical techniques are generally limited to systems of low degrees of freedom, while it is sufficient for the works in this thesis.

There exist a number of analytical techniques that may be applicable for the nonlinear systems considered in this thesis, amongst which the most popular and widely used ones are *harmonic balance* and *multiple scales* [66, 98]. A key issue of these techniques is the complexity when they are applied to systems of multiple degrees of freedom. For example in the case of harmonic balance, it is incredibly challenging for the adaptor to decide which of the harmonic components should be included in the pre-assumed solution and in the case of multiple scales, finding the solutions of the resulting nested equations are often not straightforward. The other analytical method is the *normal form* technique which was firstly introduced in the version applied to first-order differential equations, termed as *first-order normal form* technique [2]. One of the advantages of the normal form technique is its inherent ability for considering the modal interaction, suggesting it is well suitable for systems with multiple degrees of freedom. However, the shortcoming of the first-order normal form technique is that, as described, it requires the problem to be formulated in a first-order or state-space form for its application, while, most of the vibration problems are naturally formulated with second-order differential EoMs. To circumvent this, a variant normal form, named as *direct normal form* and originally known as *second-order normal form* [71], was introduced. This technique can be directly applied to second-order differential equations of nonlinear oscillators. Compared with the first-order method, the second-order variant is demonstrated to be able to provide more accurate approximated solutions, see [71]. The direct normal form technique will be used throughout this thesis.

This chapter is composed of four themed sections. Section §3.2 presents the derivation

of the direct normal form technique applied to a general forced and damped nonlinear system of multiple degrees of freedom to estimate its steady-state response. It provides a basis introduction of the application of this technique, alongside with its assumptions and limitations. Then in the following section, §3.3, an analytical method used to assess the stability of the steady-state solutions is introduced. This method was introduced in [102] and has been applied to nonlinear forced systems in [98]. As this method is affiliated with the direct normal form technique, it can be directly applied to the normal form solutions. Section §3.4 derives the direct normal form technique for estimating backbone curves of the general nonlinear system. As the conservative EoM, in the unforced and undamped form, of the nonlinear system is under consideration when computing backbone curves, the derivation is presented in a way that distinguishes it from that in §3.2. In order to gain a more practical understanding, all the techniques outlined are applied to a 1-DoF, forced Duffing oscillator in the final themed section, §3.5. These techniques outlined will provide a foundation for the work presented in later chapters of this thesis.

3.2 Direct normal form method

Similar to some other nonlinear analytical techniques like *averaging* and *multiple scales*, the basic idea of the direct normal form method is: through transforming the original nonlinear EoM to one in terms of the coordinates composed of just the primary response (e.g. without harmonic components), the resulting approximated EoM may be then analytically solved directly. Based on the invertibility of the transforms, the approximated solutions, in terms of the original coordinates, can be finally reconstructed.

To better demonstrate the derivation of the direct normal form technique, an N -DoF nonlinear system forced at a single-frequency sine wave is considered. The EoM of this system may be described as,

$$\mathbf{M}\ddot{\mathbf{x}} + \varepsilon\mathbf{C}\dot{\mathbf{x}} + \mathbf{K}\mathbf{x} + \varepsilon\mathbf{\Gamma}_x(\mathbf{x}, \dot{\mathbf{x}}, \mathbf{r}) = \mathbf{P}_x\mathbf{r}, \quad (3.1)$$

where \mathbf{x} is an $\{N \times 1\}$ vector of physical displacements, and \mathbf{M} , \mathbf{C} and \mathbf{K} are $\{N \times N\}$ matrices of mass, linear damping and linear stiffness respectively. The external force is expressed as the product of an $\{N \times 2\}$ matrix \mathbf{P}_x and the $\{2 \times 1\}$ vector \mathbf{r} , written as

$$\mathbf{P}_x = \begin{bmatrix} \bar{\mathbf{P}}_x & \bar{\mathbf{P}}_x \\ 2 & 2 \end{bmatrix} \quad \text{and} \quad \mathbf{r}^T = (r_p \quad r_m) = \begin{pmatrix} e^{+i\Omega t} & e^{-i\Omega t} \end{pmatrix}, \quad (3.2)$$

where $\bar{\mathbf{P}}_x$ is an $\{N \times 1\}$ vector whose i^{th} element is the amplitude of the sinusoidal excitation applied to the i^{th} degree-of-freedom, Ω is the frequency of the external excitation, \mathbf{i} is the imaginary unit, and t is time. $\mathbf{\Gamma}_x(\mathbf{x}, \dot{\mathbf{x}}, \mathbf{r})$ is an $\{N \times 1\}$ vector containing stiffness, damping and forcing related nonlinear terms which are assumed to be able to be expressed in a polynomial form in terms of \mathbf{x} , $\dot{\mathbf{x}}$ and \mathbf{r} . In Eq. (3.1), a bookkeeping parameter, ε , is used to denote the *smallness* of the linear damping and nonlinear terms which are assumed to be small relative to the linear stiffness and inertia terms, i.e. weak nonlinearity. For the application of the direct normal form technique, it is conventional to cluster all the *small* terms, i.e. the one of order ε , thus Eq. (3.1) may become,

$$\mathbf{M}\ddot{\mathbf{x}} + \mathbf{K}\mathbf{x} + \varepsilon\mathbf{N}_x(\mathbf{x}, \dot{\mathbf{x}}, \mathbf{r}) = \mathbf{P}_x\mathbf{r}, \quad (3.3)$$

where $\varepsilon\mathbf{N}_x(\mathbf{x}, \dot{\mathbf{x}}, \mathbf{r}) = \varepsilon\mathbf{\Gamma}_x(\mathbf{x}, \dot{\mathbf{x}}, \mathbf{r}) + \varepsilon\mathbf{C}\dot{\mathbf{x}}$ such that \mathbf{N}_x is an $\{N \times 1\}$ vector containing the nonlinear and damping terms.

Now the direct normal form technique is ready to be applied and the whole process consists of three sequential transformations, i.e.

Linear modal transform	$\mathbf{x} \rightarrow \mathbf{q}$	This exact transform is to convert the EoM in terms of from the physical coordinates, \mathbf{x} , to the linear modal coordinates, \mathbf{q} , to decouple the linear terms.
Forcing transform	$\mathbf{q} \rightarrow \mathbf{v}$	This approximate transform is to describe the motion in new coordinates, \mathbf{v} , via removing the non-resonant forcing from the linear modal EoM in terms of \mathbf{q} .
Nonlinear near-identity transform	$\mathbf{v} \rightarrow \mathbf{u}$	This approximate transform is to describe the motion in resonant coordinates, \mathbf{u} , via removing the non-resonant, i.e. sub- and super-harmonic, terms from the transformed EoM in \mathbf{v} .

The details of each of these transforms will be introduced in the following subsections.

3.2.1 Linear modal transform

The first step of the direct normal form technique is the linear modal transform ($\mathbf{x} \rightarrow \mathbf{q}$), in which the linear terms in Eq. (3.3) are decoupled. Note that due to its aim, this transform

may be omitted for the case where EoMs are already described in the modal coordinates or in a linearly decoupled form. This linear modal transform is written as,

$$\mathbf{x} = \mathbf{\Phi}\mathbf{q}, \quad (3.4)$$

where \mathbf{q} is an $\{N \times 1\}$ vector of linear modal displacements and $\mathbf{\Phi}$ is an $\{N \times N\}$ linear modeshape matrix whose i^{th} column is the modeshape of the i^{th} linear mode. Here the modeshape matrix may be found from the eigenvalue problem described as

$$\mathbf{\Phi}\mathbf{\Lambda} = \mathbf{\Lambda}\mathbf{\Phi} = \mathbf{M}^{-1}\mathbf{K}\mathbf{\Phi}, \quad (3.5)$$

where $\mathbf{\Lambda}$ is an $\{N \times N\}$ diagonal matrix whose i^{th} leading diagonal term is the square of the natural frequency of the i^{th} linear mode, i.e.

$$\mathbf{\Lambda} = \begin{bmatrix} \omega_{n1}^2 & 0 & \cdots & 0 \\ 0 & \omega_{n2}^2 & \cdots & 0 \\ \vdots & \vdots & \ddots & \vdots \\ 0 & 0 & \cdots & \omega_{nN}^2 \end{bmatrix}. \quad (3.6)$$

Substituting Eq. (3.3) with the linear modal transform expression, Eq. (3.4), and then pre-multiplying by $\mathbf{\Phi}^T$ leads to

$$(\mathbf{\Phi}^T\mathbf{M}\mathbf{\Phi})\ddot{\mathbf{q}} + (\mathbf{\Phi}^T\mathbf{K}\mathbf{\Phi})\mathbf{q} + \varepsilon\mathbf{\Phi}^T\mathbf{N}_x(\mathbf{\Phi}\mathbf{q}, \mathbf{\Phi}\dot{\mathbf{q}}, \mathbf{r}) = \mathbf{\Phi}^T\mathbf{P}_x\mathbf{r}. \quad (3.7)$$

This is further premultiplied by $(\mathbf{\Phi}^T\mathbf{M}\mathbf{\Phi})^{-1}$ gives the EoM described in the linear modal coordinates,

$$\ddot{\mathbf{q}} + \mathbf{\Lambda}\mathbf{q} + \varepsilon\mathbf{N}_q(\mathbf{q}, \dot{\mathbf{q}}, \mathbf{r}) = \mathbf{P}_q\mathbf{r}. \quad (3.8)$$

The matrix of nonlinear and damping terms and force amplitude vector in modal coordinates \mathbf{q} are

$$\varepsilon\mathbf{N}_q(\mathbf{q}, \dot{\mathbf{q}}, \mathbf{r}) = \varepsilon\mathbf{\Phi}^{-1}\mathbf{M}^{-1}\mathbf{N}_x(\mathbf{\Phi}\mathbf{q}, \mathbf{\Phi}\dot{\mathbf{q}}, \mathbf{r}), \quad (3.9)$$

$$\mathbf{P}_q = \mathbf{\Phi}^{-1}\mathbf{M}^{-1}\mathbf{P}_x. \quad (3.10)$$

3.2.2 Forcing transform

The second step of the direct normal form technique is the forcing transform ($\mathbf{q} \rightarrow \mathbf{v}$), in which any non-resonant forcing terms are removed. Note that due to its aim, this transform

may be performed by simply applying $\mathbf{v} = \mathbf{q}$ for the case when systems are unforced (this case is illustrated in §3.4 related to backbone curves). This forcing transform is written as,

$$\mathbf{q} = \mathbf{v} + \mathbf{e}\mathbf{r}, \quad (3.11)$$

where \mathbf{e} is an $\{N \times 2\}$ transform matrix. Substituting Eq. (3.11) into Eq. (3.8) gives

$$\ddot{\mathbf{v}} + \mathbf{e}\mathbf{W}\mathbf{W}\mathbf{r} + \mathbf{\Lambda}\mathbf{v} + \mathbf{\Lambda}\mathbf{e}\mathbf{r} + \varepsilon\mathbf{N}_q(\mathbf{v} + \mathbf{e}\mathbf{r}, \dot{\mathbf{v}} + \mathbf{e}\mathbf{W}\mathbf{r}, \mathbf{r}) = \mathbf{P}_q\mathbf{r}, \quad (3.12)$$

where \mathbf{W} is a $\{2 \times 2\}$ diagonal matrix with diagonal elements $+i\Omega$ and $-i\Omega$, i.e.

$$\mathbf{W} = \begin{bmatrix} +i\Omega & 0 \\ 0 & -i\Omega \end{bmatrix}. \quad (3.13)$$

Once the non-resonant forcing terms have been removed, the transformed equation, Eq. (3.12), is expected to be of the form as

$$\ddot{\mathbf{v}} + \mathbf{\Lambda}\mathbf{v} + \varepsilon\mathbf{N}_v(\mathbf{v}, \dot{\mathbf{v}}, \mathbf{r}) = \mathbf{P}_v\mathbf{r}, \quad (3.14)$$

where \mathbf{N}_v is an $\{N \times 1\}$ vector of nonlinear and damping terms in \mathbf{v} and \mathbf{P}_v is an $\{N \times 2\}$ matrix of near-resonant forcing amplitudes in which the near-resonant one may be retained and non-resonant removed.

It is proposed in [98] that the forcing applied to the i^{th} linear mode is near-resonant when its frequency, Ω , is close to the linear natural frequency of that mode, ω_{ni} . Therefore the i^{th} row of \mathbf{P}_v may set to be

$$\mathbf{P}_{v,i} = \begin{cases} \mathbf{P}_{q,i} & \text{if: } \Omega \approx \omega_{ni}, \\ [0 \ 0] & \text{if: } \Omega \not\approx \omega_{ni}, \end{cases} \quad (3.15)$$

where the second subscript, i , of $\mathbf{P}_{v,i}$ and $\mathbf{P}_{q,i}$ denotes the i^{th} row of \mathbf{P}_v and \mathbf{P}_q .

Now, to determine the transform matrix \mathbf{e} , comparing Eq. (3.12) with Eq. (3.14) leads to

$$\varepsilon\mathbf{N}_v(\mathbf{v}, \dot{\mathbf{v}}, \mathbf{r}) = \varepsilon\mathbf{N}_q(\mathbf{v} + \mathbf{e}\mathbf{r}, \dot{\mathbf{v}} + \mathbf{e}\mathbf{W}\mathbf{r}, \mathbf{r}), \quad (3.16)$$

$$\mathbf{P}_v = \mathbf{P}_q - \mathbf{e}\mathbf{W}\mathbf{W} - \mathbf{\Lambda}\mathbf{e}. \quad (3.17)$$

Rearranging Eq. (3.17) with using Eq. (3.13) gives

$$\mathbf{P}_q = \mathbf{P}_v + (\mathbf{\Lambda} - \Omega^2\mathbf{I}_N)\mathbf{e}, \quad (3.18)$$

where \mathbf{I}_N is an $\{N \times N\}$ identity matrix. Then, the matrix \mathbf{e} can be calculated using

$$\mathbf{e} = (\mathbf{\Lambda} - \Omega^2 \mathbf{I}_N)^{-1} (\mathbf{P}_q - \mathbf{P}_v), \quad (3.19)$$

but using a unique arithmetic rule that $0/0 = 0$ in the case $\Omega = \omega_{ni}$. A more rigorous way of solving \mathbf{e} is to consider it row by row, i.e. taking the i^{th} row of Eq. (3.18) with Eq. (3.6) gives

$$\mathbf{P}_{q,i} = \mathbf{P}_{v,i} + (\omega_{ni}^2 - \Omega^2) \mathbf{e}_i; \quad (3.20)$$

where \mathbf{e}_i is the i^{th} row of \mathbf{e} . Considering Eqs. (3.15) and (3.20), \mathbf{e}_i may be defined as,

$$\mathbf{e}_i = \begin{cases} [0 \ 0] & \text{if: } \Omega \approx \omega_{ni}, \\ \frac{\mathbf{P}_{q,i}}{\omega_{ni}^2 - \Omega^2} & \text{if: } \Omega \not\approx \omega_{ni}. \end{cases} \quad (3.21)$$

After the force transform matrix \mathbf{e} is obtained, it can be used for computing the transformed vector \mathbf{N}_v , see Eq. (3.16).

3.2.3 Nonlinear near-identity transform

The last step of the direct normal form technique is the nonlinear near-identity transform ($\mathbf{v} \rightarrow \mathbf{u}$), in which the harmonic response components are removed from Eq. (3.14) resulting in a resonant EoM. This transform is written as,

$$\mathbf{v} = \mathbf{u} + \varepsilon \mathbf{H}(\mathbf{u}, \dot{\mathbf{u}}, \mathbf{r}), \quad (3.22)$$

where \mathbf{u} and \mathbf{H} are the fundamental and harmonic components of \mathbf{v} respectively. In the nonlinear near-identity transform, the harmonics are assumed to be small relative to the fundamental components due to the weak nonlinearity assumption, hence $\mathbf{H}(\mathbf{u}, \dot{\mathbf{u}}, \mathbf{r})$ is noted to be of order ε . Since the harmonic components are removed, it is reasonable for us to assume the solution of the i^{th} element of \mathbf{u} , which is the fundamental response of the i^{th} linear mode, to be

$$u_i = U_i \cos(\omega_{ri} t - \phi_i), \quad (3.23)$$

where U_i , ω_{ri} and ϕ_i are the response amplitude, frequency and phase of u_i respectively. Here, an $\{N \times N\}$ diagonal matrix $\mathbf{\Upsilon}$ of the resonant response frequencies is introduced and

its i^{th} leading diagonal terms is ω_{ri}^2 , thus

$$\mathbf{\Upsilon} = \begin{bmatrix} \omega_{r1}^2 & 0 & \cdots & 0 \\ 0 & \omega_{r2}^2 & \cdots & 0 \\ \vdots & \vdots & \ddots & \vdots \\ 0 & 0 & \cdots & \omega_{rN}^2 \end{bmatrix}. \quad (3.24)$$

Therefore, the second-order derivative of the resonant response vector, \mathbf{u} , may be expressed as

$$\ddot{\mathbf{u}} = -\mathbf{\Upsilon}\mathbf{u}. \quad (3.25)$$

After the nonlinear near-identity transform, the resulting transformed resonant EoM may be written in the form of

$$\ddot{\mathbf{u}} + \mathbf{\Lambda}\mathbf{u} + \varepsilon\mathbf{N}_u(\mathbf{u}, \dot{\mathbf{u}}, \mathbf{r}) = \mathbf{P}_u\mathbf{r}, \quad (3.26)$$

where \mathbf{N}_u is an $\{N \times 1\}$ vector of resonant nonlinear and damping terms, and \mathbf{P}_u is an $\{N \times 2\}$ matrix of resonant forcing amplitude terms. In Eq. (3.26), all terms in its i^{th} row respond sinusoidally at the resonant response frequency of the i^{th} linear mode, ω_{ri} . Using Eq. (3.25), the resonant EoM, Eq. (3.26), may be written as,

$$(\mathbf{\Lambda} - \mathbf{\Upsilon})\mathbf{u} + \varepsilon\mathbf{N}_u(\mathbf{u}, \dot{\mathbf{u}}, \mathbf{r}) = \mathbf{P}_u\mathbf{r}. \quad (3.27)$$

This equation is finally used to formulate a set of time-invariant expressions related to U_i , ω_{ri} and ϕ_i , which can be solved to find the solution in terms of \mathbf{u} .

Now to determinate the resonant terms retained in Eq. (3.14), the first step in the nonlinear near-identity transform is to substitute Eq. (3.22) into Eq. (3.14), giving

$$\ddot{\mathbf{u}} + \varepsilon\ddot{\mathbf{H}} + \mathbf{\Lambda}\mathbf{u} + \varepsilon\mathbf{\Lambda}\mathbf{H} + \varepsilon\mathbf{N}_v(\mathbf{u} + \varepsilon\mathbf{H}, \dot{\mathbf{u}} + \varepsilon\dot{\mathbf{H}}, \mathbf{r}) = \mathbf{P}_v\mathbf{r}. \quad (3.28)$$

Comparing Eq. (3.28) with Eq. (3.26) leads to

$$\varepsilon\ddot{\mathbf{H}} + \varepsilon\mathbf{\Lambda}\mathbf{H} + \varepsilon\mathbf{N}_v(\mathbf{u} + \varepsilon\mathbf{H}, \dot{\mathbf{u}} + \varepsilon\dot{\mathbf{H}}, \mathbf{r}) - \mathbf{P}_v\mathbf{r} = \varepsilon\mathbf{N}_u(\mathbf{u}, \dot{\mathbf{u}}, \mathbf{r}) - \mathbf{P}_u\mathbf{r}. \quad (3.29)$$

The vectors \mathbf{N}_u and \mathbf{H} are expressed in a series form as

$$\varepsilon\mathbf{N}_u(\mathbf{u}, \dot{\mathbf{u}}, \mathbf{r}) = \sum_{j=1}^{\infty} \varepsilon^j \mathbf{n}_{u(j)}(\mathbf{u}, \dot{\mathbf{u}}, \mathbf{r}) = \varepsilon\mathbf{n}_{u(1)}(\mathbf{u}, \dot{\mathbf{u}}, \mathbf{r}) + \varepsilon^2\mathbf{n}_{u(2)}(\mathbf{u}, \dot{\mathbf{u}}, \mathbf{r}) + \cdots, \quad (3.30)$$

$$\varepsilon \mathbf{H}(\mathbf{u}, \dot{\mathbf{u}}, \mathbf{r}) = \sum_{j=1}^{\infty} \varepsilon^j \mathbf{h}_{(j)}(\mathbf{u}, \dot{\mathbf{u}}, \mathbf{r}) = \varepsilon \mathbf{h}_{(1)}(\mathbf{u}, \dot{\mathbf{u}}, \mathbf{r}) + \varepsilon^2 \mathbf{h}_{(2)}(\mathbf{u}, \dot{\mathbf{u}}, \mathbf{r}) + \dots, \quad (3.31)$$

where $\mathbf{n}_{u(j)}$ and $\mathbf{h}_{(j)}$ are the $\{N \times 1\}$ vectors in the identical form of \mathbf{N}_u and \mathbf{H} respectively. Note that Eqs. (3.30) and (3.31) are not Taylor series expansions but decompositions into a series of terms of reducing significance. Also note that $\mathbf{n}_{u(j)}$ and $\mathbf{h}_{(j)}$ are different from $N_{u,i}$ and H_i which are the i^{th} elements of \mathbf{N}_u and \mathbf{H} respectively. Then, \mathbf{N}_v is expanded in a Taylor series about the equilibrium $[\mathbf{u}, \dot{\mathbf{u}}]$, written

$$\begin{aligned} & \mathbf{N}_v(\mathbf{u} + \varepsilon \mathbf{H}, \dot{\mathbf{u}} + \varepsilon \dot{\mathbf{H}}, \mathbf{r}) \\ &= \sum_{\ell_1=0}^{\infty} \sum_{\ell_2=0}^{\infty} \left[\frac{1}{\ell_1! \ell_2!} \nabla_{\dot{\mathbf{u}}}^{\ell_2} \left[\nabla_{\bar{\mathbf{u}}}^{\ell_1} \mathbf{N}_v(\bar{\mathbf{u}}, \dot{\bar{\mathbf{u}}}, \mathbf{r}) \{ \varepsilon \mathbf{H}(\mathbf{u}, \dot{\mathbf{u}}, \mathbf{r}) \}^{\ell_1} \right]_{\bar{\mathbf{u}}=\mathbf{u}} \{ \varepsilon \dot{\mathbf{H}}(\mathbf{u}, \dot{\mathbf{u}}, \mathbf{r}) \}^{\ell_2} \right]_{\dot{\bar{\mathbf{u}}}=\dot{\mathbf{u}}} \quad (3.32) \\ &= \mathbf{N}_v(\mathbf{u}, \dot{\mathbf{u}}, \mathbf{r}) + \varepsilon \left([\nabla_{\bar{\mathbf{u}}} \mathbf{N}_v(\bar{\mathbf{u}}, \dot{\bar{\mathbf{u}}}, \mathbf{r})]_{\bar{\mathbf{u}}=\mathbf{u}} \mathbf{H} + [\nabla_{\dot{\bar{\mathbf{u}}} \mathbf{N}_v(\bar{\mathbf{u}}, \dot{\bar{\mathbf{u}}}, \mathbf{r})}]_{\dot{\bar{\mathbf{u}}}=\dot{\mathbf{u}}} \dot{\mathbf{H}} \right) + \mathcal{O}(\varepsilon^2), \end{aligned}$$

where $\ell_i!$ denotes the factorial of ℓ_i , $\mathcal{O}(\varepsilon^2)$ includes the terms of second- and higher-order ε , and $\nabla_{\bar{\mathbf{u}}}$ and $\nabla_{\dot{\bar{\mathbf{u}}}}$ are the Jacobian operator in terms of $\bar{\mathbf{u}}$ and $\dot{\bar{\mathbf{u}}}$ respectively, written

$$\nabla_{\bar{\mathbf{u}}} = \frac{\partial}{\partial \bar{\mathbf{u}}} = \begin{bmatrix} \frac{\partial}{\partial \bar{u}_1} & \frac{\partial}{\partial \bar{u}_2} & \cdots & \frac{\partial}{\partial \bar{u}_N} \end{bmatrix}, \quad (3.33a)$$

$$\nabla_{\dot{\bar{\mathbf{u}}}} = \frac{\partial}{\partial \dot{\bar{\mathbf{u}}}} = \begin{bmatrix} \frac{\partial}{\partial \dot{\bar{u}}_1} & \frac{\partial}{\partial \dot{\bar{u}}_2} & \cdots & \frac{\partial}{\partial \dot{\bar{u}}_N} \end{bmatrix}. \quad (3.33b)$$

Besides, a frequency detuning process is introduced using the *detuning* expression, written as

$$\mathbf{\Lambda} = \mathbf{\Upsilon} + \varepsilon (\mathbf{\Lambda} - \mathbf{\Upsilon}), \quad (3.34)$$

which is based on the observation that the response frequencies of nonlinear systems are often distinct from linear natural frequencies, i.e. typically $\mathbf{\Lambda} \neq \mathbf{\Upsilon}$. In this process, it allows the approximation $\mathbf{\Lambda} = \mathbf{\Upsilon}$ to be made in the order ε^0 and the difference between $\mathbf{\Lambda}$ and $\mathbf{\Upsilon}$ is of order ε^1 . More detailed discussion about accuracy effects of the detuning step can be found in [70].

Now, substituting Eqs. (3.30-3.32) and Eq. (3.34) into Eq. (3.29) leads to

$$\begin{aligned} & \varepsilon \ddot{\mathbf{h}}_{(1)} + \varepsilon^2 \ddot{\mathbf{h}}_{(2)} + \varepsilon \mathbf{\Upsilon} \mathbf{h}_{(1)} + \varepsilon^2 (\mathbf{\Lambda} - \mathbf{\Upsilon}) \mathbf{h}_{(1)} + \varepsilon^2 \mathbf{\Lambda} \mathbf{h}_{(2)} + \varepsilon \mathbf{N}_v \\ & + \varepsilon^2 \left(\frac{\partial \mathbf{N}_v}{\partial \mathbf{u}} \mathbf{h}_{(1)} + \frac{\partial \mathbf{N}_v}{\partial \dot{\mathbf{u}}} \dot{\mathbf{h}}_{(1)} \right) - \mathbf{P}_v \mathbf{r} - \varepsilon \mathbf{n}_{u(1)} - \varepsilon^2 \mathbf{n}_{u(2)} - \mathbf{P}_u \mathbf{r} + \mathcal{O}(\varepsilon^3) = 0. \quad (3.35) \end{aligned}$$

ing to the terms in $\mathbf{u}_{(j)}^*$. For the case of polynomial nonlinear terms under consideration, the ℓ^{th} element of $\mathbf{u}_{(j)}^*$ may be written as

$$u_{(j)\ell}^* = r_p^{m_{pj,\ell}} r_m^{m_{mj,\ell}} \prod_{i=1}^N u_{ip}^{s_{pj,\ell,i}} u_{im}^{s_{mj,\ell,i}}, \quad (3.41)$$

where $m_{pj,\ell}$, $m_{mj,\ell}$, $s_{pj,\ell,i}$ and $s_{mj,\ell,i}$ are exponents of r_p , r_m , u_{ip} and u_{im} in the ℓ^{th} element of $\mathbf{u}_{(j)}^*$ respectively. By considering Eqs. (3.2) and (3.39), the ℓ^{th} element of $\mathbf{u}_{(j)}^*$ may also be written in the exponential form as

$$u_{(j)\ell}^* = U_{(j)\ell}^* \exp \left(\mathbf{i} \left[\boldsymbol{\omega}_{(j)\ell}^* t - \phi_{(j)\ell}^* \right] \right), \quad (3.42)$$

where

$$U_{(j)\ell}^* = \prod_{i=1}^N \left(\frac{U_i}{2} \right)^{s_{pj,\ell,i} + s_{mj,\ell,i}}, \quad (3.43a)$$

$$\phi_{(j)\ell}^* = \sum_{i=1}^N (s_{mj,\ell,i} - s_{pj,\ell,i}) \phi_i, \quad (3.43b)$$

$$\boldsymbol{\omega}_{(j)\ell}^* = (m_{pj,\ell} - m_{mj,\ell}) \boldsymbol{\Omega} + \sum_{i=1}^N (s_{pj,\ell,i} - s_{mj,\ell,i}) \boldsymbol{\omega}_{ri}. \quad (3.43c)$$

Then we may observe a significant feature of the elements of $\mathbf{u}_{(j)}^*$ that its second-order derivative is the product of a time-invariant coefficient and itself, i.e.

$$\ddot{u}_{(j)\ell}^* = -[\boldsymbol{\omega}_{(j)\ell}^*]^2 u_{(j)\ell}^*. \quad (3.44)$$

Therefore, $\ddot{\mathbf{u}}_{(j)}^*$ may be expressed as

$$\ddot{\mathbf{u}}_{(j)}^* = -[\mathcal{C}_{(j)}]^\top \circ \mathbf{u}_{(j)}^*. \quad (3.45)$$

where $[\mathcal{C}_{(j)}]$ is a $\{1 \times L_j\}$ row vector with the ℓ^{th} element given by,

$$[\mathcal{C}_{(j)}]_\ell = [\boldsymbol{\omega}_{(j)\ell}^*]^2, \quad (3.46)$$

and \circ denotes the *Hadamard* product operator with the definition: for two matrices, \mathbf{A} and \mathbf{B} , with the identical dimension, $\{M \times N\}$, their Hadamard product, $\mathbf{A} \circ \mathbf{B}$, is a matrix of the

same dimension, whose elements are

$$[\mathbf{A} \circ \mathbf{B}]_{i,j} = \mathbf{A}_{i,j} \mathbf{B}_{i,j}, \quad (3.47)$$

where $1 \leq i \leq M$ and $1 \leq j \leq N$. Now substituting Eqs. (3.40) and (3.45), the expression of the homological equation for ε^j (where $j > 0$) from Eq. (3.36) may become

$$[n_{u(j)}] \mathbf{u}_{(j)}^* = -[h_{(j)}] \left[[\mathcal{C}_{(j)}]^\top \circ \mathbf{u}_{(j)}^* \right] + \Upsilon [h_{(j)}] \mathbf{u}_{(j)}^* + [n_{v(j)}] \mathbf{u}_{(j)}^*, \quad (3.48a)$$

$$= -[\mathcal{C}_{(j)}]_{[N]} \circ [h_{(j)}] \mathbf{u}_{(j)}^* + [\Upsilon_{(j)}] \circ [h_{(j)}] \mathbf{u}_{(j)}^* + [n_{v(j)}] \mathbf{u}_{(j)}^*, \quad (3.48b)$$

where $[\mathcal{C}_{(j)}]_{[N]}$ is an $\{N \times L_j\}$ matrix whose n^{th} row is $[\mathcal{C}_{(j)}]$ and $[\Upsilon_{(j)}]$ is an $\{N \times L_j\}$ matrix whose n^{th} row is all of ω_{ri}^2 , i.e.

$$[\Upsilon_{(j)}] = \begin{bmatrix} \omega_{r1}^2 & \omega_{r1}^2 & \cdots & \omega_{r1}^2 \\ \omega_{r2}^2 & \omega_{r2}^2 & \cdots & \omega_{r2}^2 \\ \vdots & \vdots & \ddots & \vdots \\ \omega_{rn}^2 & \omega_{rn}^2 & \cdots & \omega_{rn}^2 \end{bmatrix}. \quad (3.49)$$

It can be seen that Eq. (3.48b) can be satisfied by simply setting

$$[n_{u(j)}] = [n_{v(j)}] - [\mathcal{C}_{(j)}]_{[N]} \circ [h_{(j)}] + [\Upsilon_{(j)}] \circ [h_{(j)}], \quad (3.50a)$$

$$= [n_{v(j)}] - \boldsymbol{\beta}_{(j)} \circ [h_{(j)}], \quad (3.50b)$$

where the $\boldsymbol{\beta}_{(j)} = [\mathcal{C}_{(j)}]_{[N]} - [\Upsilon_{(j)}]$ is an $\{N \times L_j\}$ matrix whose $\{i, \ell\}^{\text{th}}$ element is

$$\beta_{(j)i,\ell} = \omega_{j,\ell}^{*2} - \omega_{ri}^2. \quad (3.51)$$

Eq. (3.50b) cannot be solved uniquely yet due to the multiple unknowns, $[n_{u(j)}]$ and $[h_{(j)}]$, inherited from $\mathbf{n}_{u(j)}$ and $\mathbf{h}_{(j)}$ respectively. To address this, the definition of the nonlinear near-identity transform is reconsidered, which is the i^{th} element of $\mathbf{n}_{u(j)}$ is resonant which must respond at the frequency ω_{ri} and, while, that in $\mathbf{h}_{(j)}$ is non-resonant hence must respond at frequencies other than ω_{ri} . From Eq. (3.42), it is known that the frequency at which $u_{(j)\ell}^*$ oscillates is denoted by $\omega_{(j)\ell}^*$, hence if $\omega_{(j)\ell}^* = \pm \omega_{ri}$ it may be stated that the term $u_{(j)\ell}^*$ is resonant with the i^{th} mode. Therefore its corresponding element in the resonant coefficient matrix, $[n_{u(j)}]_{i,\ell}$, is expected to be equal to the nonlinear coefficients, $[n_{v(j)}]_{i,\ell}$, and the corresponding elements in the matrix of harmonic coefficients, is zero, i.e. $[h_{(j)}]_{i,\ell} = 0$. In

contrast, if $\omega_{(j)\ell}^* \neq \pm\omega_{ri}$, $u_{(j)\ell}^*$ is non-resonant with the i^{th} mode then the corresponding resonant coefficient should be zero, i.e. $[n_{u(j)}]_{i,\ell} = 0$, and harmonic coefficient must be non-zero, i.e. $[h_{(j)}]_{i,\ell} \neq 0$.

Considering Eq. (3.51), when $\omega_{(j)\ell}^* = \pm\omega_{ri}$, $\beta_{(j)i,\ell} = 0$ and when $\omega_{(j)\ell}^* \neq \pm\omega_{ri}$, then $\beta_{(j)i,\ell} \neq 0$. Hence the matrix $\boldsymbol{\beta}_{(j)}$ may be used as an index for the selection of resonant terms from $[n_{v(j)}]$, which correspondingly determines the values of elements in $[n_{u(j)}]$. Therefore, by using Eq. (3.50b) the criteria of the near-identity transform selection based on matrix $\boldsymbol{\beta}_{(j)}$ may be described as

$$[n_{u(j)}]_{i,\ell} = [n_{v(j)}]_{i,\ell} \quad \text{and} \quad [h_{(j)}]_{i,\ell} = 0, \quad \text{if: } \beta_{(j)i,\ell} = 0, \quad (3.52a)$$

$$[n_{u(j)}]_{i,\ell} = 0 \quad \text{and} \quad [h_{(j)}]_{i,\ell} = \frac{[n_{u(j)}]_{i,\ell}}{\beta_{(j)i,\ell}}, \quad \text{if: } \beta_{(j)i,\ell} \neq 0. \quad (3.52b)$$

This selection criteria can also be mathematically expressed as

$$[n_{u(j)}] = \delta(\boldsymbol{\beta}_{(j)}) \circ [n_{v(j)}], \quad (3.53a)$$

$$[h_{(j)}] = \left[[n_{v(j)}] - [n_{u(j)}] \right] \circ \boldsymbol{\beta}_{(j)}, \quad (3.53b)$$

where $\delta(\boldsymbol{\beta}_{(j)})$ is an $\{N \times L_j\}$ Dirac delta matrix with the element value to be 0 or 1 determined by the corresponding term value of $\boldsymbol{\beta}_{(j)}$ and \circ is the *Hadamard* division operator whose definition is that $\mathbf{C} = \mathbf{A} \circ \mathbf{B} : C_{ij} = A_{ij}/B_{ij}$. Note that $0/0 = 0$ is defined as with Eq. (3.19). This expression, Eqs. (3.53), can be directly applied in a computer program.

Once $[n_{u(j)}]$ and $[h_{(j)}]$ are determined to the required accuracy level, ε^j , Eqs. (3.40b) and (3.30) are used to compute \mathbf{N}_u . Based on the transform assumption that the i^{th} element of \mathbf{N}_u is resonating at the frequency ω_{ri} , it may be written as

$$N_{u,i} = N_{ui}^+ e^{+i\omega_{ri}t} + N_{ui}^- e^{-i\omega_{ri}t}, \quad (3.54)$$

where N_{ui}^+ and N_{ui}^- are a complex conjugate pair and time-invariant. Substituting Eq. (3.54) into Eq. (3.27) and using Eqs. (3.2) and (3.39), the i^{th} row of the resonant EoM may be written as

$$\left[(\omega_{ni}^2 - \omega_{ri}^2) \frac{U_i}{2} e^{-i\phi_i} + N_{ui}^+ - P_{u,i} \right] e^{+i\omega_{ri}t} + \left[(\omega_{ni}^2 - \omega_{ri}^2) \frac{U_i}{2} e^{+i\phi_i} + N_{ui}^- - P_{u,i} \right] e^{-i\omega_{ri}t} = 0, \quad (3.55)$$

where $P_{u,i}$ is the $\{i, 1\}^{\text{th}}$ element of \mathbf{P}_u . It can be seen that the content of the square brackets in Eq. (3.55) are a complex conjugate pair, so in order to satisfy the equation, both of them

must be zero, i.e.

$$(\omega_{ni}^2 - \omega_{ri}^2) \frac{U_i}{2} e^{\mp i\phi_i} + N_{ui}^{\pm} = P_{u,i}. \quad (3.56)$$

This equation can be solved to find the solutions of U_i and ϕ_i and then the vector of fundamental response, \mathbf{u} , can be formed.

Additionally based on Eqs. (3.40c) and (3.31), the vector of harmonic response is calculated via the expression

$$\mathbf{H}(\mathbf{u}, \dot{\mathbf{u}}, \mathbf{r}) = \sum_{j=1}^J [h_{(j)}] \mathbf{u}_j^*(\mathbf{u}_p, \mathbf{u}_m, r_p, r_m), \quad (3.57)$$

where J is the level of accuracy adopted.

After finding \mathbf{u} and \mathbf{H} , a series of inverting transforms are applied to find the solution \mathbf{x} : firstly, the nonlinear transform expression, Eq. (3.22), is applied to find the solution of \mathbf{v} . Then the response in the modal coordinates, \mathbf{q} , may be found using the forcing transform expression, Eq. (3.11) and lastly the physical response, \mathbf{x} , found using the linear modal transform Eq. (3.4). Finally, the solution of physical displacement response may be written as

$$\mathbf{x} = \Phi [\mathbf{u} + \mathbf{H}(\mathbf{u}, \dot{\mathbf{u}}, \mathbf{r}) + \mathbf{er}]. \quad (3.58)$$

The whole process of the application of the direct normal form technique on the N-DoF nonlinear system with polynomial nonlinearities is given in Algorithm 1.

3.2.4 Discussion of limitations

While the direct normal form technique outlined is powerful, there is still a number of limitations that we may see from its application process. The most obvious one may be that this technique is only applicable to systems with nonlinearities expressed in the polynomial form. But fortunately, many of the smooth nonlinearities of interest may be expressed or approximated to be in the polynomial form, e.g. using the Taylor series expansion, which will be seen in Chapter 6. Then another limitation should be caused by its smallness assumption of the nonlinear and damping terms, see Eq. (3.3), and the difference from the response frequency to the corresponding linear natural frequency, Eq. (3.34). The further limitation is that this technique can only be used to determine steady-state, periodic response due to the assumed sinusoidal solution, see Eq. (3.23). Therefore, the non-periodic solutions, e.g. transient, quasi-periodic and chaotic responses, may not be able to be approximated using this technique without some modification. Additionally, although the direct normal form

Algorithm 1 Direct normal form technique

Input: Mass matrix, \mathbf{M} , linear stiffness matrix \mathbf{K} , nonlinear and linear damping terms vector \mathbf{N}_x , forcing amplitudes matrix \mathbf{P}_x and forcing frequency Ω .

Output: Displacement response \mathbf{x} .

Linear modal transform:

- 1: Calculate linear natural frequencies, Λ , and modeshapes, Φ , using Eq. (3.5).
- 2: Calculate nonlinear and linear damping terms, \mathbf{N}_q , and forcing amplitudes, \mathbf{P}_q , in modal space using Eqs. (3.9) and (3.10) respectively.

Forcing transform:

- 3: Determine resonant forcing amplitudes, \mathbf{P}_v , using Eq. (3.15).
- 4: Calculate the forcing transform matrix, \mathbf{e} , using Eq. (3.19).
- 5: Calculate nonlinear and linear damping terms after the forcing transform, \mathbf{N}_v , using Eq. (3.16).

Nonlinear near-identity transform:

- 6: **for** $j = 1, \dots, J$ **do**
- 7: Calculate the nonlinear and linear damping terms in the j^{th} homological equation, $\mathbf{n}_{v(j)}$, using Eq. (3.37).
- 8: Determine the nonlinear and linear damping coefficients, $[n_{v(j)}]$, and unique combination of variables, $\mathbf{u}_{(j)}^*$, in the j^{th} homological equation, using Eq. (3.40a).
- 9: Calculate the indexes for determining resonant terms in the j^{th} homological equation, $\beta_{(j)}$, using Eq. (3.51).
- 10: Calculate the coefficients of resonant terms, $[n_{u(j)}]$, and of harmonic terms, $[h_{(j)}]$, in the j^{th} homological equation, using Eqs. (3.53).
- 11: **end for**
- 12: Calculate the resonant nonlinear and linear damping terms, \mathbf{N}_u , using Eqs. (3.40b) and (3.30).
- 13: Find N_{ui}^+ and N_{ui}^- of the i^{th} mode, using Eq. (3.54).
- 14: Solve the response amplitudes, U_i , and phases, ϕ_i , of the i^{th} mode using Eq. (3.56).
- 15: Form the fundamental modal response, \mathbf{u} , using Eq. (3.23).
- 16: Calculate the harmonic modal response, \mathbf{H} , using Eq. (3.57).

Inverse transforms:

- 17: Find the physical displacement response, \mathbf{x} , using Eq. (3.58).
-

technique is suitable for nonlinear systems of multiple degrees of freedom, it is still limited to low dimensional systems as the computing complexity will exponentially increase with the system degrees of freedom.

3.3 Stability analysis of the steady-state solution

Now a method for analysing the stability of the estimated solution obtained via the direct normal form technique application is introduced. This method is firstly used in [102] and re-derived in [31]. The idea of this method is based on considering a perturbation from the steady-state solution and then the stability of the solution is determined by examining the stability of the perturbation.

A solution of the i^{th} mode that deviates from its steady-state is first considered. The amplitude, U_i , and phase, ϕ_i , of the solution are allowed to be slowly varying with time, such that it can be written as

$$u_i = U_{pi}(\varepsilon t)e^{i\omega_{ri}t} + U_{mi}(\varepsilon t)e^{-i\omega_{ri}t}, \quad (3.59)$$

where t is time and $U_{pi}(\varepsilon t)$ and $U_{mi}(\varepsilon t)$ are a complex conjugate pair such that

$$U_{pi} = \frac{1}{2}U_i(\varepsilon t)e^{-i\phi_i(\varepsilon t)} \quad \text{and} \quad U_{mi} = \frac{1}{2}U_i(\varepsilon t)e^{+i\phi_i(\varepsilon t)}. \quad (3.60)$$

Here ε denotes smallness as with the normal form analysis, and the amplitude and phase of the solution are functions of time, i.e. $U_i = U_i(\varepsilon t)$ and $\phi_i = \phi_i(\varepsilon t)$, which represent the slowly time-varying assumptions. Then, the first and second time-derivatives of u_i , from Eq. (3.59), may be written as

$$\dot{u}_i = i\omega_{ri} \left(U_{pi}e^{+i\omega_{ri}t} - U_{mi}e^{-i\omega_{ri}t} \right) + \mathcal{O}(\varepsilon^1), \quad (3.61a)$$

$$\ddot{u}_i = -\omega_{ri}^2 u_i + \varepsilon i 2\omega_{ri} \left(U'_{pi}e^{+i\omega_{ri}t} - U'_{mi}e^{-i\omega_{ri}t} \right) + \mathcal{O}(\varepsilon^2), \quad (3.61b)$$

where the prime denotes the derivative with respect to (εt) , i.e.

$$U'_{pi} = \frac{dU_{pi}}{d(\varepsilon t)} \quad \text{and} \quad U'_{mi} = \frac{dU_{mi}}{d(\varepsilon t)}. \quad (3.62)$$

In Eq. (3.61), the \dot{u}_i is truncated at order ε^1 because the velocity related terms are assumed to only appear in nonlinear and damping terms which are considered to be of order ε^1 already,

while the acceleration related terms are considered to be of order ε^0 , hence \ddot{u}_i is truncated at order ε^2 . Therefore, the complete expression with their substitutions is truncated at order ε^2 . Substituting Eqs. (3.59) and (3.61) into the i^{th} resonant equation, Eq. (3.26), gives

$$\begin{aligned} & \left[+\mathbf{i}2\omega_{ri}U'_{pi} + (\omega_{ni}^2 - \omega_{ri}^2)U_{pi} + N_{ui}^+ - P_{ui} \right] e^{+\mathbf{i}\omega_{ri}t} \\ & + \left[-\mathbf{i}2\omega_{ri}U'_{mi} + (\omega_{ni}^2 - \omega_{ri}^2)U_{mi} + N_{ui}^- - P_{ui} \right] e^{-\mathbf{i}\omega_{ri}t} = 0, \end{aligned} \quad (3.63)$$

where the complex conjugate N_{ui}^+ and N_{ui}^- are those obtained from N_{ui} in the same manner as those from Eq. (3.54). To satisfy Eq. (3.63), the contents of the square brackets must be equated to zero, such that

$$U'_{pi} = +\frac{\mathbf{i}}{2\omega_{ri}} [(\omega_{ni}^2 - \omega_{ri}^2)U_{pi} + N_{ui}^+ - P_{ui}], \quad (3.64a)$$

$$U'_{mi} = -\frac{\mathbf{i}}{2\omega_{ri}} [(\omega_{ni}^2 - \omega_{ri}^2)U_{mi} + N_{ui}^- - P_{ui}]. \quad (3.64b)$$

Now introducing a vector of amplitude and phase components, written as \mathbf{U} , such that

$$\mathbf{U} = (U_{p1} \ U_{m1} \ \cdots \ U_{pi} \ U_{mi} \ \cdots \ U_{pN} \ U_{mN})^{\text{T}}, \quad (3.65)$$

Eqs. (3.64) may be expressed in a functional form, i.e.

$$\mathbf{U}' = (U'_{p1} \ U'_{m1} \ \cdots \ U'_{pi} \ U'_{mi} \ \cdots \ U'_{pN} \ U'_{mN})^{\text{T}} = \mathbf{f}(\mathbf{U}). \quad (3.66)$$

Considering that the initial definition of the solution, which is the one with a small derivation from its steady state, it can also be written as a sum of a steady-state solution, written as \mathbf{U}_{ss} , and a small perturbation, $\varepsilon\mathbf{U}_{pb}$, such that

$$\mathbf{U} = \mathbf{U}_{ss} + \varepsilon\mathbf{U}_{pb}. \quad (3.67)$$

Eq. (3.67) is substituted into the expression of \mathbf{U}' , Eq. (3.66), and then a Taylor series expansion to order ε^1 is applied, giving

$$\mathbf{U}'_{ss} + \varepsilon\mathbf{U}'_{pb} = \mathbf{f}(\mathbf{U}_{ss} + \varepsilon\mathbf{U}_{pb}) \quad (3.68a)$$

$$= \mathbf{f}(\mathbf{U}_{ss}) + \varepsilon\mathbf{f}'_{\mathbf{U}}(\mathbf{U}_{ss})\mathbf{U}_{bp} + \mathcal{O}(\varepsilon^2), \quad (3.68b)$$

where \mathbf{f}_U is the Jacobian matrix of \mathbf{f} with respect to \mathbf{U} , such that

$$\mathbf{f}_U = \begin{bmatrix} \frac{\partial f_1}{\partial U_{p1}} & \frac{\partial f_1}{\partial U_{m1}} & \cdots & \frac{\partial f_1}{\partial U_{pi}} & \frac{\partial f_1}{\partial U_{mi}} & \cdots & \frac{\partial f_1}{\partial U_{pN}} & \frac{\partial f_1}{\partial U_{mN}} \\ \frac{\partial f_2}{\partial U_{p1}} & \frac{\partial f_2}{\partial U_{m1}} & \cdots & \frac{\partial f_2}{\partial U_{pi}} & \frac{\partial f_2}{\partial U_{mi}} & \cdots & \frac{\partial f_2}{\partial U_{pN}} & \frac{\partial f_2}{\partial U_{mN}} \\ \vdots & \vdots & \ddots & \vdots & \vdots & \ddots & \vdots & \vdots \\ \frac{\partial f_{2N-1}}{\partial U_{p1}} & \frac{\partial f_{2N-1}}{\partial U_{m1}} & \cdots & \frac{\partial f_{2N-1}}{\partial U_{pi}} & \frac{\partial f_{2N-1}}{\partial U_{mi}} & \cdots & \frac{\partial f_{2N-1}}{\partial U_{pN}} & \frac{\partial f_{2N-1}}{\partial U_{mN}} \\ \frac{\partial f_{2N}}{\partial U_{p1}} & \frac{\partial f_{2N}}{\partial U_{m1}} & \cdots & \frac{\partial f_{2N}}{\partial U_{pi}} & \frac{\partial f_{2N}}{\partial U_{mi}} & \cdots & \frac{\partial f_{2N}}{\partial U_{pN}} & \frac{\partial f_{2N}}{\partial U_{mN}} \end{bmatrix}. \quad (3.69)$$

Using $\mathbf{U}'_{ss} = \mathbf{f}(\mathbf{U}_{ss})$ as with Eq. (3.66), Eq. (3.68b) is deduced to be

$$\mathbf{U}'_{pb} = \mathbf{f}_U(\mathbf{U}_{ss})\mathbf{U}_{pb}. \quad (3.70)$$

From Eq. (3.67), we know that the steady-state solution is stable if the solution of perturbation is stable around zero. Hence, the stability analysis may become an eigenvalue problem and the stability of the steady-state solution can be assessed from the eigenvalues of \mathbf{f}_U . From the theorem of stability, the solution becomes unstable when any one of the eigenvalues crosses the imaginary axis from left to right in the complex plane. Therefore, the criteria of stability determination may be concluded as:

- i. when all the eigenvalues have negative real components, the steady-state solution is stable.
- ii. when any eigenvalue has a zero real component and the others have negative real components, the steady-state solution is neutrally stable.
- iii. when any eigenvalue has a positive real component, the steady-state solution is unstable.

3.4 Backbone curves

Now a general process for calculating backbone curves of nonlinear systems using the direct normal form method is introduced. A backbone curve is a locus of the maximum responses of the nonlinear system, which describes the response of the unforced and undamped (equivalent conservative) systems. Compared with the forced responses of nonlinear systems which may vary with forced and damping configuration, conservative responses are invariant; hence it describes the global dynamic property of the system. Besides, forced

responses of nonlinear systems are often complicated, e.g. those when the modal interaction occurs, so that they would be highly difficult to be interpreted. But even so, in the case of lightly damped systems, important information about the forced, damped response can be obtained from the unforced, undamped response which is characterised by backbone curves. The significance of the backbone curves for nonlinear systems analysis will be further demonstrated and discussed in the later chapters.

To derive the backbone curves approximation process, the N -DoF nonlinear system is considered again. Here, its EoM, Eq. (3.3) with no forcing or damping term, is analysed, written as

$$\mathbf{M}\ddot{\mathbf{x}} + \mathbf{K}\mathbf{x} + \varepsilon\mathbf{N}_x(\mathbf{x}) = 0. \quad (3.71)$$

For backbone curves, as the response of conservative systems is considered, in contrast to Eq. (3.3), \mathbf{N}_x here is not a function of the velocity, $\dot{\mathbf{x}}$, or the force, \mathbf{r} , but simply contains the stiffness nonlinearities related to the displacement, \mathbf{x} .

As Eq. (3.71) is still a smooth second-order differential equation, the steps of calculating backbone curves are similar to those described in §3.2. Hence, in this section, it mainly focuses on their distinctions during each transforming step.

Linear modal transform

Identical to that in §3.2, the first step is the linear modal transform, $\mathbf{x} = \Phi\mathbf{q}$. As the mode-shape matrix is only related to the linear terms, i.e. the mass matrix \mathbf{M} and linear stiffness matrix \mathbf{K} , instead of the damping or forcing terms, see Eq. (3.5), the eigenvalue problem is solved to find natural frequencies matrix Λ and the resulting EoM is written in linear modal normal form, i.e.

$$\ddot{\mathbf{q}} + \Lambda\mathbf{q} + \varepsilon\mathbf{N}_q(\mathbf{q}) = 0, \quad (3.72)$$

where the nonlinear vector is found using Eq. (3.9) as before; however as with \mathbf{N}_x , \mathbf{N}_q is not a function of $\dot{\mathbf{q}}$ or \mathbf{r} for the conservative case.

Forcing transform

The second step of the direct normal form technique described in §3.2 is the forcing transform. However, as the equivalent conservative system, i.e. no forcing, is considered for backbone curves, this transform is a unity transform by simply using $\mathbf{v} = \mathbf{q}$.

Nonlinear near-identity transform

The following step is the nonlinear near-identity transform, $\mathbf{v} = \mathbf{u} + \mathbf{H}(\mathbf{u})$, which ends up with the resonant EoM in terms of \mathbf{u} , written

$$\ddot{\mathbf{u}} + \Lambda \mathbf{u} + \varepsilon \mathbf{N}_u(\mathbf{u}) = 0. \quad (3.73)$$

Similarly, here the harmonic response vector \mathbf{H} used in the transform and nonlinear terms vector \mathbf{N}_u do not include the $\dot{\mathbf{u}}$ and \mathbf{r} related terms. Therefore, all the associated vectors $\mathbf{n}_{v(j)}(\mathbf{u})$, $\mathbf{n}_{u(j)}(\mathbf{u})$ and $\mathbf{h}_{(j)}(\mathbf{u})$ are a function of the displacement \mathbf{u} only. The derivation process of the nonlinear near-identity transform is almost identical to its application on the forced and damped system. The only difference is about the vector of nonlinear polynomial terms, $\mathbf{u}_{(j)}^*$, which is not a function of the forcing anymore. Therefore, the expression of its elements, Eq. (3.41), may be rewritten as

$$u_{(j)\ell}^* = \prod_{i=1}^N u_{ip}^{s_{pj,\ell,i}} u_{im}^{s_{mj,\ell,i}}. \quad (3.74)$$

Hence the value of its corresponding element in $\beta_{(j)}$ is also redefined, using Eqs. (3.43c) and (3.51), to be

$$\beta_{(j)i,\ell} = \left[\sum_{n=1}^N (s_{pj,\ell,n} - s_{mj,\ell,n}) \omega_{rn} \right]^2 - \omega_{ri}^2. \quad (3.75)$$

The selection criteria for determining the value of elements in the resonant coefficient matrix $[n_{u(j)}]$, Eq. (3.52) or Eq. (3.53), is still valid for the backbone curves case. Substituting selected resonant nonlinear terms to the EoM, Eq. (3.73), its i^{th} row may become

$$\left[(\omega_{ni}^2 - \omega_{ri}^2) \frac{U_i}{2} e^{-i\phi_i} + N_{ui}^+ \right] e^{+i\omega_{ri}t} + \left[(\omega_{ni}^2 - \omega_{ri}^2) \frac{U_i}{2} e^{+i\phi_i} + N_{ui}^- \right] e^{-i\omega_{ri}t} = 0, \quad (3.76)$$

where no force term, P_{ui} , exists compared with Eq. (3.63). Equating the content of the square brackets to be zero gives the time-invariant equation of the i^{th} mode for the backbone curve case, i.e.

$$(\omega_{ni}^2 - \omega_{ri}^2) \frac{U_i}{2} e^{\mp i\phi_i} + N_{ui}^{\pm} = 0. \quad (3.77)$$

Eq. (3.77) is then solved to find the solutions of U_i and ω_{ri} which may be used to construct backbone curves in the modal coordinate \mathbf{u} . To solve Eq. (3.77) some assumptions are required to be made based on the structure of time-invariant equations and its solutions may also be affected by the modal phase difference, i.e. $|\phi_i - \phi_j|$. More details about the solutions

of backbone curves of specific nonlinear systems will be presented in the later chapters.

As with §3.2, the physical displacement response of backbone curves may be found via the related inverting transforms, written,

$$\mathbf{x} = \Phi[\mathbf{u} + \mathbf{H}(u)]. \quad (3.78)$$

Basically, the procedure of backbone curves computation using the direct normal form technique is a simplified version of its application on the forced and damped systems. Therefore for the case when the time-invariant equations describing the relation of the steady-state response and forcing, Eq. (3.56), have already been approximated for some purposes, the ones for backbone curves can be easily obtained via simply removing the terms associated with the forcing and damping, see the example in Chapter 4.

3.5 Application to an example system

In this section, the application of the previously outlined techniques to a 1-DoF Duffing oscillator is considered. The similar examples have been considered in [31, 71, 98] as well.

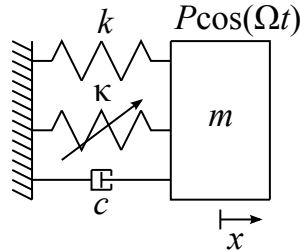


Fig. 3.1 A schematic diagram of a 1-DoF Duffing oscillator with mass m , linear stiffness k , linear damping c and nonlinear stiffness κ . This system responds at the displacement x to the external forcing with amplitude P at frequency Ω .

Fig. 3.1 shows the schematic of the forced Duffing oscillator and its EoM, in the physical displacement coordinate, x , is written

$$m\ddot{x} + c\dot{x} + kx + \kappa x^3 = P \cos(\Omega t). \quad (3.79)$$

3.5.1 Forced response approximation

Writing the EoM of the system, Eq. (3.79), in the conventional form, Eq. (3.3), the corresponding matrices and vectors are

$$\mathbf{x} = x_1, \quad \mathbf{M} = m, \quad \mathbf{K} = k, \quad \mathbf{N}_x = c\dot{x}_1 + \kappa x_1^3, \quad \mathbf{P}_x = \left(\frac{P_1}{2}, \frac{P_1}{2} \right), \quad (3.80)$$

where $x_1 = x$ and $P_1 = P$. Since this is a 1-DoF system, the linear transform may be a trivial step, which gives an expression in the form of Eq. (3.8) where

$$\mathbf{\Lambda} = \omega_{n1}^2 = \frac{k}{m}, \quad \mathbf{N}_q = \frac{c}{m}\dot{q}_1 + \frac{\kappa}{m}q_1^3, \quad \mathbf{P}_q = \left(\frac{P_1}{2m}, \frac{P_1}{2m} \right). \quad (3.81)$$

Here the resonant response of the system is considered so that the forcing frequency is assumed to be close to the linear natural frequency, i.e. $\Omega \approx \omega_{n1}$. Therefore, referring to Eq. (3.21), the force transform matrix $\mathbf{e} = [0, 0]$, thus the identity forcing transform that $\mathbf{q} = \mathbf{v}$ is used. This results the equation in \mathbf{v} written in the form of Eq. (3.14), where

$$\mathbf{N}_v = \frac{c}{m}\dot{v}_1 + \frac{\kappa}{m}v_1^3, \quad \mathbf{P}_v = \mathbf{P}_q = \left(\frac{P_1}{2m}, \frac{P_1}{2m} \right). \quad (3.82)$$

Then the nonlinear near-identity transform is considered. Here this transform is applied to the first level of accuracy, ε^1 , which will be presented to be sufficient later via comparison with numerical data. The application of the transform to a higher level of accuracy, e.g. ε^2 , can be referred to literature [31, 98].

For the first level of accuracy under consideration, the coefficient matrix $[n_{v(1)}]$ and the corresponding nonlinear terms vector, $\mathbf{u}_{(1)}^*(\mathbf{u}_p, \mathbf{u}_m, \mathbf{r})$, can easily found, using Eqs. (3.40a) and (3.37a), from

$$\mathbf{N}_v(\mathbf{u}, \dot{\mathbf{u}}, \mathbf{r}) = \mathbf{n}_{u(1)}(\mathbf{u}, \dot{\mathbf{u}}, \mathbf{r}) = [n_{v(1)}] \mathbf{u}_{(1)}^*(\mathbf{u}_p, \mathbf{u}_m, \mathbf{r}). \quad (3.83)$$

So simply substituting $\mathbf{v} = \mathbf{u}$ into the expression of $\mathbf{N}_v(\mathbf{v}, \dot{\mathbf{v}}, \mathbf{r})$, Eq. (3.82), with using Eq. (3.39), gives

$$\mathbf{N}_v(\mathbf{u}, \dot{\mathbf{u}}, \mathbf{r}) = \mathbf{i}\omega_{r1} \frac{c}{m} (u_{1p} - u_{1m}) + \frac{\kappa}{m} (u_{1p}^3 + u_{1m}^3 + 3u_{1p}^2 u_{1m} + 3u_{1p} u_{1m}^2). \quad (3.84)$$

Combining Eqs. (3.83) and (3.84), we may obtain

$$[n_{v(1)}]^\top = \frac{1}{m} \begin{pmatrix} \kappa \\ \kappa \\ 3\kappa \\ 3\kappa \\ \mathbf{i}\omega_{r1}c \\ -\mathbf{i}\omega_{r1}c \end{pmatrix}, \quad \mathbf{u}_{(1)}^* = \begin{pmatrix} u_{1p}^3 \\ u_{1m}^3 \\ u_{1p}^2 u_{1m} \\ u_{1p} u_{1m}^2 \\ u_{1p} \\ u_{1m} \end{pmatrix}, \quad \boldsymbol{\beta}_{(1)}^\top = \omega_{r1}^2 \begin{pmatrix} 8 \\ 8 \\ 0 \\ 0 \\ 0 \\ 0 \end{pmatrix}, \quad (3.85)$$

where the selection index matrix $\boldsymbol{\beta}_{(1)}$ is computed using Eqs. (3.43c) and (3.51). Now, using Eq. (3.52) or Eq. (3.53), $[n_{u(1)}]$ and $[h_{(j)}]$ may be found to be

$$[n_{u(1)}] = \frac{1}{m} \begin{pmatrix} 0 & 0 & 3\kappa & 3\kappa & \mathbf{i}\omega_{r1}c & -\mathbf{i}\omega_{r1}c \end{pmatrix}, \quad (3.86a)$$

$$[h_{(1)}] = \frac{1}{8\omega_{r1}^2} \begin{pmatrix} \kappa & \kappa & 0 & 0 & 0 & 0 \end{pmatrix} \quad (3.86b)$$

Then $\mathbf{n}_{u(1)}$ and $\mathbf{h}_{(1)}$ are found using Eq. (3.40b) and Eq. (3.40c) respectively to be

$$\mathbf{n}_{u(1)} = \mathbf{i} \frac{\omega_{r1}c}{m} (u_{1p} - u_{1m}) + \frac{3\kappa}{m} (u_{1p}^2 u_{1m} + u_{1p} u_{1m}^2), \quad (3.87a)$$

$$\mathbf{h}_{(1)} = \frac{\kappa}{8m\omega_{r1}^2} (u_{1p}^3 + u_{1m}^3). \quad (3.87b)$$

For the case with the first level of accuracy, ε^1 , Eqs. (3.40a) and (3.40c) simply become

$$\mathbf{N}_u = \mathbf{n}_{u(1)}, \quad \text{and} \quad \mathbf{H} = \mathbf{h}_{(1)}. \quad (3.88)$$

Separating \mathbf{N}_u into the form of Eq. (3.54) with using Eq. (3.39) gives,

$$\begin{aligned} N_{u,1} &= N_{u1}^+ e^{+\mathbf{i}\omega_{r1}t} + N_{u1}^- e^{-\mathbf{i}\omega_{r1}t}, \\ &= \left[\left(\frac{3\kappa}{8m} U_1^3 + \mathbf{i} \frac{\omega_{r1}c}{2m} \right) e^{-\mathbf{i}\phi_1} \right] e^{+\mathbf{i}\omega_{r1}t} + \left[\left(\frac{3\kappa}{8m} U_1^3 - \mathbf{i} \frac{\omega_{r1}c}{2m} \right) e^{+\mathbf{i}\phi_1} \right] e^{-\mathbf{i}\omega_{r1}t}, \end{aligned} \quad (3.89)$$

which ends up with a time-invariant equation as Eq. (3.55), written as

$$(\omega_{n1}^2 - \Omega^2) \frac{U_1}{2} e^{-\mathbf{i}\phi_1} + \left(\frac{3\kappa}{8m} U_1^3 + \mathbf{i} \frac{\Omega c}{2m} \right) e^{-\mathbf{i}\phi_1} = \frac{P_1}{2m}. \quad (3.90)$$

where the assumption that the response frequency is equal to the forcing frequency, i.e.

$\omega_{r1} = \Omega$, has been made and used. Multiplying through by $e^{i\phi_1} = \cos(\phi_1) + i\sin(\phi_1)$ and balancing the real and imaginary parts of Eq. (3.90) gives

$$\text{Re :} \quad P_1 \cos(\phi_1) = (\omega_{n1}^2 - \Omega^2)mU_1 + \frac{3}{4}\kappa U_1^3, \quad (3.91a)$$

$$\text{Im :} \quad P_1 \sin(\phi_1) = \Omega c U_1. \quad (3.91b)$$

Eliminating the phase ϕ_1 by squaring and then summing the equations of Re and Im leads to

$$\left[(\omega_{n1}^2 - \Omega^2)mU_1 + \frac{3}{4}\kappa U_1^3 \right]^2 + [\Omega c U_1]^2 = P_1^2. \quad (3.92)$$

This equation is solved to find the fundamental displacement response amplitude, U_1 , and the phase, ϕ_1 , is then calculated, using Eq. (3.91b), from

$$\phi_1 = \arcsin\left(\frac{\Omega c U_1}{P_1}\right). \quad (3.93)$$

With the solution of amplitude and phase, the harmonics are found using Eqs. (3.87b) and (3.88) as

$$\mathbf{H} = \frac{\kappa U_1^3}{32m\Omega^2} \cos(3[\Omega t - \phi_1]). \quad (3.94)$$

Here it can be seen that to the first-level accuracy, ε^1 , only one harmonic component which responds at the 3 times of forcing frequency is estimated. Higher-order harmonics can also be approximated by considering the application with a higher level of accuracy of normal forms and the examples are in [31, 98].

Finally, the inverse transforms are applied, using Eq. (3.58), to find the displacement response in the physical coordinate, \mathbf{x} , as

$$x_1 = \mathbf{x} = \mathbf{q} = \mathbf{v} = \mathbf{u} + \mathbf{H} = U_1 \cos(\Omega t - \phi_1) + H_U \cos(3\Omega t - \phi_H) \quad (3.95)$$

where H_U and ϕ_H are the amplitude and phase of the approximated harmonic component respectively, written

$$H_U = \frac{\kappa U_1^3}{32m\Omega^2}, \quad \text{and} \quad \phi_H = 3\phi_1. \quad (3.96)$$

Now, we consider the response results of a Duffing oscillator, described by Eq. (3.79), with the specific parameters: $m = 1$, $c = 0.05$, $k = 1$ and $\kappa = 1$. The system is forced at three different levels of amplitude $P_1 = 0.01$, 0.03 and 0.05 and the result is shown in Fig. 3.2 which is presented in the projection of the forcing frequency, Ω , against the displacement

response amplitude, $|x_1| = U_1 + H_U$. In order to validate the results approximated by the normal form technique, the response computed using the numerical continuation toolbox based on Matlab named COCO [14] is compared. From the result, it can be seen that the normal form predictions and numerical results are generally in good agreement. The approximated and numerical results for the cases of $P_1 = 0.01$ and 0.03 are almost on top with each other, with the maximum relative differences 0.78% and 0.97% respectively, while their difference for $P_1 = 0.05$ is relatively obvious near the maximum response amplitude region, i.e. the maximum differences is 2.5% . However, considering the ε^1 accuracy, this level of distinction is acceptable and the more accurate solution may be achieved when the normal form technique with a higher level of accuracy is applied but additional complexity of the computation is needed correspondingly.

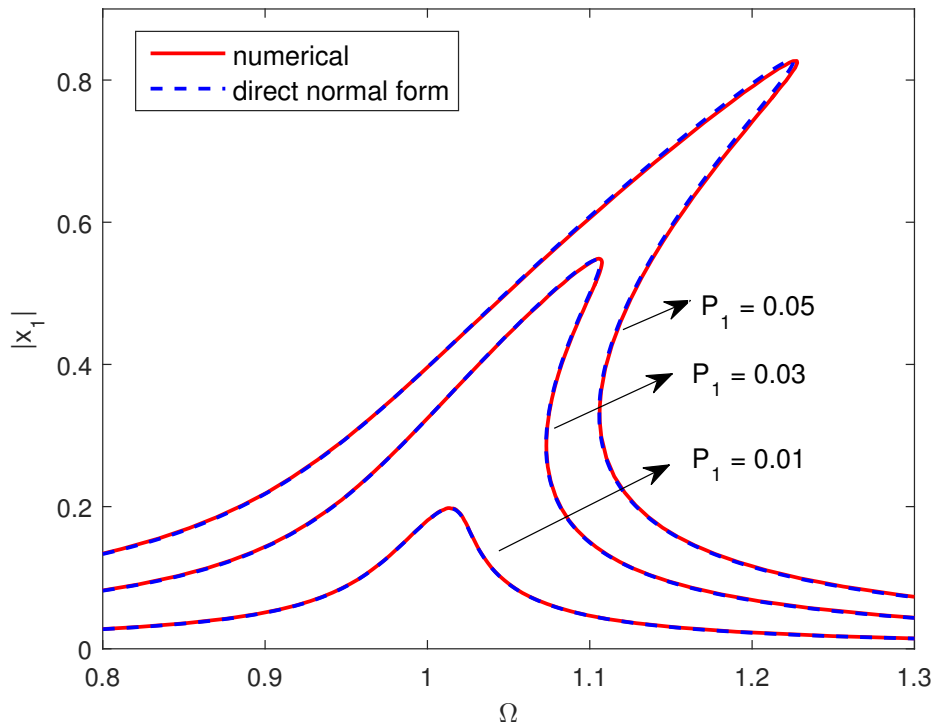


Fig. 3.2 The responses of a 1-DoF Duffing oscillator excited at three force amplitudes. The plot is in the projection of forcing frequency, Ω , against the displacement response amplitude, $|x_1|$. The dashed-blue lines represent the results calculated using the direct normal form technique to ε^1 accuracy and the solid-red lines denote the numerical solution found using the COCO toolbox based on Matlab.

3.5.2 Stability analysis

Now we consider the stability of the response results of the 1-DoF Duffing oscillator approximated by the direct normal form technique using the approach introduced in §3.3.

Firstly, using Eqs. (3.87a) and (3.59), the nonlinear terms $N_{u,1}$ are separated in the manner of Eq. (3.54), which results in

$$N_{u1}^+ = +\mathbf{i}\frac{\omega_{r1}c}{m}U_{p1} + \frac{3\kappa}{m}U_{p1}^2U_{m1}, \quad (3.97a)$$

$$N_{u1}^- = -\mathbf{i}\frac{\omega_{r1}c}{m}U_{m1} + \frac{3\kappa}{m}U_{p1}U_{m1}^2. \quad (3.97b)$$

Substituting Eq. (3.97) and $P_{u1} = P_1/2m$ into Eq. (3.64), the function vector of $\mathbf{U} = [U_{p1}, U_{m1}]$, in the form of Eq. (3.66), is constructed, written as

$$\mathbf{f}(\mathbf{U}) = \frac{\mathbf{i}}{2\Omega} \begin{pmatrix} +(\omega_{n1}^2 - \Omega^2)U_{p1} + \mathbf{i}\frac{\Omega c}{m}U_{p1} + \frac{3\kappa}{m}U_{p1}^2U_{m1} - \frac{P_1}{2m} \\ -(\omega_{n1}^2 - \Omega^2)U_{m1} + \mathbf{i}\frac{\Omega c}{m}U_{m1} - \frac{3\kappa}{m}U_{p1}U_{m1}^2 + \frac{P_1}{2m} \end{pmatrix}, \quad (3.98)$$

where as with Eq. (3.90), the assumption $\omega_{r1} = \Omega$ is used. Then using Eq. (3.69), the Jacobian matrix of \mathbf{f} with respect to \mathbf{U} may be calculated, as

$$\mathbf{f}_{\mathbf{U}} = \frac{\mathbf{i}}{2\Omega} \begin{bmatrix} \omega_{n1}^2 - \Omega^2 + \mathbf{i}\frac{\Omega c}{m} + \frac{6\kappa}{m}U_{p1}U_{m1} & \frac{3\kappa}{m}U_{p1}^2 \\ -\frac{3\kappa}{m}U_{m1}^2 & \Omega^2 - \omega_{n1}^2 + \mathbf{i}\frac{\Omega c}{m} - \frac{6\kappa}{m}U_{p1}U_{m1} \end{bmatrix}. \quad (3.99)$$

Then the eigenvalues, λ , of $\mathbf{f}_{\mathbf{U}}$ are found from the equation,

$$\lambda^2 + \frac{c}{m}\lambda + \frac{1}{4\Omega^2} \left[\left(\omega_{n1}^2 - \Omega^2 + \frac{3\kappa}{2m}U_1^2 \right)^2 + \left(\frac{3\kappa}{4m}U_1^2 \right)^2 + \left(\frac{\Omega c}{m} \right)^2 \right] = 0, \quad (3.100)$$

where $U_{p1}U_{m1} = U_1^2/4$ is used. The solutions of Eq. (3.100) is written in the form of

$$\lambda = \frac{-B \pm \sqrt{B^2 - 4C}}{2}, \quad (3.101)$$

where

$$B = \frac{c}{m}, \quad (3.102a)$$

$$C = \frac{1}{4\Omega^2} \left[\left(\omega_{n1}^2 - \Omega^2 + \frac{3\kappa}{2m} U_1^2 \right)^2 - \left(\frac{3\kappa}{4m} U_1^2 \right)^2 + \left(\frac{\Omega c}{m} \right)^2 \right]. \quad (3.102b)$$

Here, the neutrally stable condition, which is the boundary of the stable and unstable solutions, is considered. From the stability criteria listed in §3.3 that the solution is of neutral stability when one of the eigenvalues has a zero real component, the bifurcation points are found, from Eq. (3.101), by setting

$$\operatorname{Re} \left\{ \frac{-B \pm \sqrt{B^2 - 4C}}{2} \right\} = 0. \quad (3.103)$$

As B must be real, Eq. (3.103) may be written as

$$\operatorname{Re} \left\{ \frac{-B \pm \sqrt{B^2 - 4C}}{2} \right\} = -\frac{B}{2} \pm \operatorname{Re} \left\{ \frac{\sqrt{B^2 - 4C}}{2} \right\} = 0, \quad (3.104)$$

in which $(\sqrt{B^2 - 4C})/2$ can only be either a non-negative real number when $B^2 \geq 4C$ or a purely imaginary number when $B^2 < 4C$. Therefore, it can be seen that a valid solution of Eq. (3.103) may be found, by assuming $B^2 \geq 4C$, from

$$\frac{-B \pm \sqrt{B^2 - 4C}}{2} = 0, \quad (3.105)$$

which is rearranged to give $C = 0$ and then using Eq. (3.102b) gives

$$\left[3 \left(\frac{3\kappa}{4m} \right)^2 \right] U_1^4 + \left[(\omega_{n1}^2 - \Omega^2) \frac{3\kappa}{m} \right] U_1^2 + \left[(\omega_{n1}^2 - \Omega^2)^2 + \left(\frac{\Omega c}{m} \right)^2 \right] = 0. \quad (3.106)$$

This equation describing the relationship between response amplitude and forcing frequency is solved to find the stability boundary at which a bifurcation may occur. Besides, it can be seen from Eq. (3.106) that this amplitude-frequency relationship is independent of forcing amplitude, which means that the region where solutions are unstable is not affected by the forcing amplitude.

Fig. 3.3 shows the stability result of the 1-DoF Duffing oscillator depicted in the previous section. The forced response curves in Fig. 3.2 are shown again but with the stability distinction pattern. The stability of the numerical solutions is determined based on the Floquet eigenvalues automatically computed during the continuation and that of the normal form solutions is found using the eigenvalues, Eq. (3.101), based on the stability criteria.

The stability boundary (dashed-blue line) presenting a family of bifurcation points is also computed using Eq. (3.106), which is compared with the numerically calculated results of the locus of saddle-node bifurcations (solid-red line). From Fig. 3.3, it can be seen that bifurcation positions predicted by the normal form method and numerical approach are in good agreement and the solutions within the stability boundary are unstable.

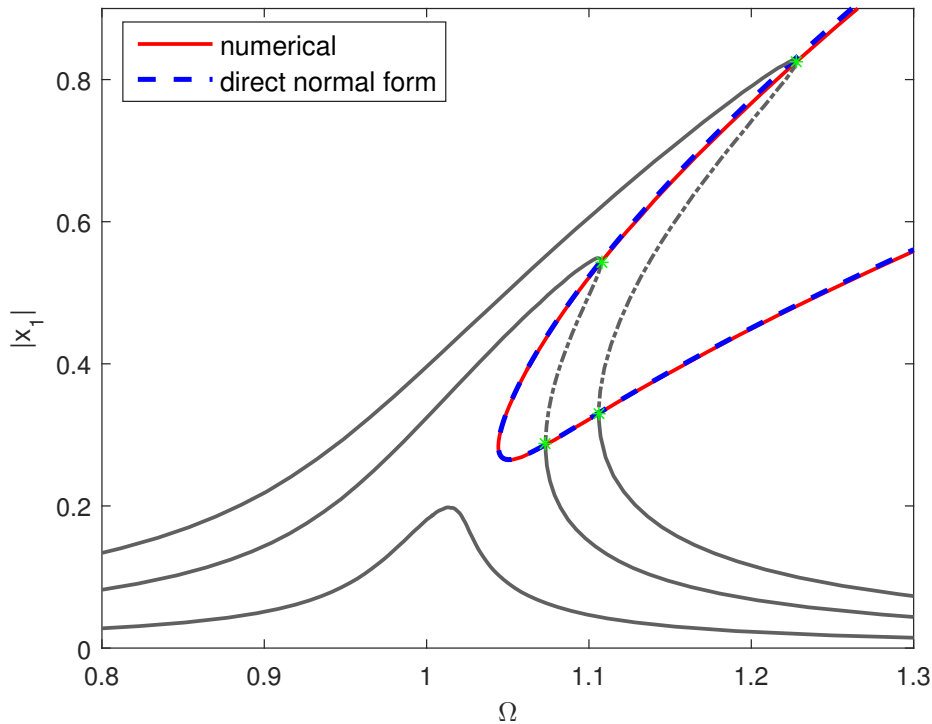


Fig. 3.3 The response stability of a 1-DoF Duffing oscillator excited at three forced amplitudes. The plot is in the projection of forcing frequency, Ω , against the response amplitude, $|x_1|$. The black and grey lines represent the results calculated by the direct normal form method and the numerical continuation toolbox COCO respectively. For both sets of solutions, solid parts denote the stable solutions and dashed-dotted parts denote the unstable solutions. The dashed-blue and solid-red lines represent the stability boundary solutions predicted analytically and numerically, respectively. The green asterisks denote the numerically-computed fold points.

3.5.3 Backbone curve calculation

Now we consider the backbone curve of the 1-DoF Duffing oscillator. In §3.5.1, the forced response of the system has already been approximated to the first-level of accuracy via the direct normal form technique. Hence, instead of applying the normal form method to the

conservative EoM of this system, the expression of backbone curves can be obtained from the results of forced response via removing the forcing and damping terms.

From Eq. (3.90), the corresponding time-invariant equation for the backbone curve case may be written as

$$\left[(\omega_{n1}^2 - \Omega^2) \frac{U_1}{2} + \frac{3\kappa}{8m} U_1^3 \right] e^{-i\phi_1} = 0. \quad (3.107)$$

The phase can be directly eliminated via multiplying through $e^{+i\phi_1}$, which, via rearranging, leads to the equation describing the backbone curve in \mathbf{u} , as

$$\Omega^2 = \omega_{n1}^2 + \frac{3k}{4m} U_1^2. \quad (3.108)$$

For the phase, ϕ_1 , due to its definition of the phase difference between the force and response signal, it is physically meaningless for the 1-DoF system for the unforced situation, hence there is no result of ϕ_1 for this case. The harmonic response is computed identically as with the forced response case using Eq. (3.94) and then the physical displacement response in \mathbf{x} is calculated using Eq. (3.95).

Fig. 3.4 shows the backbone curve of the Duffing oscillator for the system depicted in Fig. 3.2. The backbone curve solution calculated by the normal form technique is compared to that found using COCO. Besides, to demonstrate the feature of backbone curves that is the locus of points of the maximum response amplitude, the forced response curves shown in Fig. 3.2 is plotted as the reference. It can be seen, from Fig. 3.4, that there is a good agreement between the solution calculated by the numerical continuation and by the analytical technique outlined. It can also be seen that all the maximum response points for three excitation cases are close to the backbone curve.

3.6 Summary

In this chapter, an analytical method – the direct normal form technique – for solving the nonlinear systems has been derived via its application on a non-conservative N -DoF nonlinear system for computing the steady-state response. We have seen that this improved normal form technique is able to be directly applied to the second-order differential equations of motion, unlike previous normal form methods. Besides, the ability of this technique to naturally estimate the harmonic components of a response has been demonstrated. Although there exist several limitations about the direct normal form technique, i.e. applicable to systems of polynomial nonlinear terms only, the smallness assumption of nonlinear and

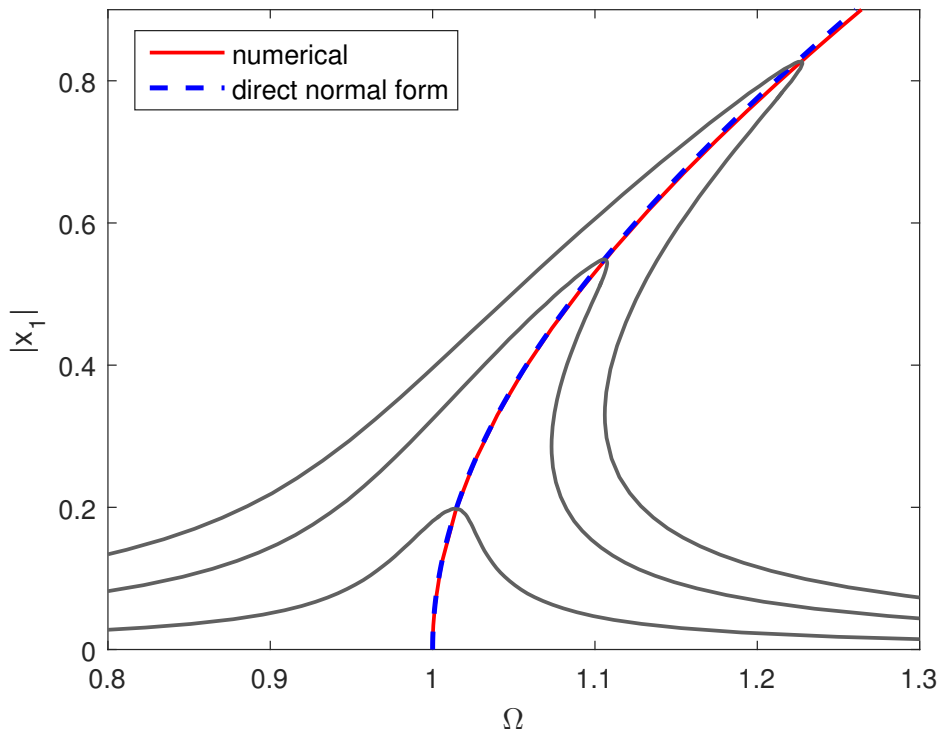


Fig. 3.4 The backbone curve of a 1-DoF Duffing oscillator. The plot is represented in the projection of forcing frequency, Ω , against the response amplitude, $|x_1|$. The dash-blue and solid-red lines represent the backbone curve solution predicted using the direct normal form technique and the toolbox COCO respectively. The black and grey lines denote the analytical and numerical solution of force responses shown in Fig. 3.2, respectively.

damping terms and frequency detuning and restricted determination of steady-state solutions, as discussed, this technique is declared to be powerful enough for studying the nonlinear systems in this thesis.

Then a method used for accessing the stability of the steady-state response has been presented. The most attractive aspect of this stability determination technique is that it is readily applicable to the normal form solution as it is introduced based on the direct normal form technique. This method can help us to deeply explore the mechanisms of the stable and unstable behaviours for the nonlinear systems, e.g. nonlinear modal interactions and bifurcations.

The idea of backbone curves, which are the locus of the free response of the equivalent conservative system of the fundamental nonlinear structures, has been briefly introduced. Its computational process using the direct normal form has been presented in a way that distinguishes the differences from forced response estimation for the non-conservative nonlinear

systems. The backbone curve is a very powerful tool for interpreting the complex response of nonlinear systems, the discussions of which are presented in Chapter 4, 5 and 6.

It is known that one main thing makes the response of nonlinear system far more complex, which also makes it distinct from that of the linear system, is the nonlinear modal interaction. It is a nonlinear behaviour of energy transferring between (or amongst) linearly decoupled but nonlinearly coupled modes. So in the next two chapters, we will explore the effects of nonlinear modal interaction and the relationship of its occurrence with the system structures, system parameters, and external excitations. This is achieved using the nonlinear analysis techniques outlined in this chapter.

Chapter 4

$N - i$ modal interaction of nonlinear multi-degree-of-freedom systems

In this chapter we:

- Compute the backbone curves of a 3-DoF nonlinear oscillator with one to one nonlinear modal interaction due to the bilaterally symmetric nature of its linear structure.
- Consider the stability of the backbone curves using the method outlined in §3.4 and the bifurcations of mixed-mode backbone curves from single-mode backbone curves.
- Find the relationship between the backbone curves and forced-response curves and illustrate the ability of backbone curves to interpret the complicated forced response.
- Investigate the relationship between the occurrence of the modal interaction and the external force amplitude via considering the bifurcations on the primary single-mode forced-response curves.

4.1 Introduction

One of the factors distinguishing linear and nonlinear dynamic systems is the modal interaction. In linear systems, the fundamental vibration modes are independent of each other such that they can be considered separately. However, this is not the case for multi-DoF nonlinear systems where modes have the possibility of interacting with each other, which is also why many of the existing linear analysis tools or techniques are no longer worthy

for understanding the mechanical structures behaving in nonlinear regions. Therefore, understanding the effects of modal interaction is an essential step in being able to predict the subsequent nonlinear dynamic responses.

For a nonlinear system with N (where $N \geq 2$) modes, it is possible for response solutions to exist in which a subset of, i.e. $N - i$ (where $N - i \geq 2$), or all, i.e. N , of its underlying modes interact. In this chapter, we consider the case where $N - i$ modal interaction can occur. More specifically, the case where $N = 3$ is analysed, such that only two, i.e. $N - 1$, modes can interact. To do this, we choose a specific configuration of an in-line 3-DoF lumped mass weakly nonlinear oscillator with small forcing and light damping. Due to its structural symmetry, one of the modes of this system is linear, and the other two are nonlinear. So even though all the natural frequencies are close, the linear mode behaves independently. Hence the study about the example 3-DoF system is focused on the modal interaction of the two coupled modes.

In this chapter, we first apply the direct normal form technique to the example system under damping and forcing to derive the time-invariant equations describing the relationship between modal responses and external forcing. These equations are found to be complicated to solve due to the existence of the nonlinear coupled terms. Hence in §4.3.1, we try to find the solutions after removing damping and forcing related terms, i.e. computing the backbone curves instead. For this example 3-DoF system, we find three primary backbone curves, one linear and two nonlinear, each including the response of a single mode only. The two nonlinear primary backbone curves tend to respond as the underlying linear system does when their amplitudes are close to zero. Additionally, for the case where the nonlinear constant of coupling springs is negative, there are bifurcations on the nonlinear primary backbone curves where extra backbone curves involving $N - 1$ modal interaction emanate. In §4.3.2, the stability of the primary backbone curves, i.e. bifurcation points, are studied using the technique outlined in §3.4.

In §4.4, we consider the relationship between the backbone curves and the forced responses. The ability of backbone curves to interpret the modal interaction of the forced responses is first demonstrated in §4.4.1. Then, in §4.4.2, the relationship between the occurrence of bifurcations on the single-mode forced-response curves and the forcing amplitude is investigated. It is found that with knowing the bifurcations on primary forced-response curves, backbone curves may be able to predict the occurrence of nonlinear modal interaction for the non-conservative situation.

4.2 Nonlinear 3-DoF system with bilateral symmetry

Throughout this chapter, we consider the 3-DoF oscillator depicted in Fig. 4.1. This system has a bilaterally symmetric structure which consists of three identical lumped masses, m . The three masses are grounded via the same linear springs of the stiffness, k , and viscous dampers, c . Additionally, the mass in the middle is connected to the other two at the sides via viscous dampers \bar{c} and cubic nonlinear springs of linear and nonlinear constants \bar{k} and κ respectively. The elastic force characteristics of these nonlinear springs is $F = \bar{k}(\Delta x) + \kappa(\Delta x)^3$ where Δx is the spring deflection. Furthermore, each mass is sinusoidally excited at an identical frequency Ω , with amplitude P_i , and has displacement response x_i , where $i = 1, 2$, and 3.

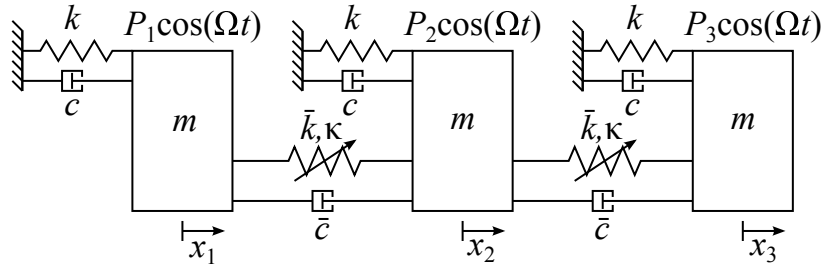


Fig. 4.1 A schematic diagram of an in-line, 3-DoF system with a bilaterally symmetric structure and cubic nonlinear springs.

The EoM of this system, in the coordinates of physical displacement response $\mathbf{x} = [x_1 \ x_2 \ x_3]^T$, may be written in the conventional form as Eq. (3.3) for the application of the direct normal form technique, where the linear stiffness matrix, external force amplitude vector and small (nonlinear and linear damping) terms vector are respectively given by

$$\mathbf{K} = \begin{bmatrix} k + \bar{k} & -\bar{k} & 0 \\ -\bar{k} & k + 2\bar{k} & -\bar{k} \\ 0 & -\bar{k} & k + \bar{k} \end{bmatrix}, \quad \mathbf{P}_x = \frac{1}{2} \begin{bmatrix} P_1 & P_1 \\ P_2 & P_2 \\ P_3 & P_3 \end{bmatrix}. \quad (4.1a)$$

$$\mathbf{N}_x = \begin{bmatrix} c + \bar{c} & -\bar{c} & 0 \\ -\bar{c} & c + 2\bar{c} & -\bar{c} \\ 0 & -\bar{c} & c + \bar{c} \end{bmatrix} \dot{\mathbf{x}} + \kappa \begin{pmatrix} (x_1 - x_2)^3 \\ (x_2 - x_1)^3 + (x_2 - x_3)^3 \\ (x_3 - x_2)^3 \end{pmatrix}, \quad (4.1b)$$

Now the first step of the direct normal form technique, i.e. the linear modal transform, may be applied to decouple the linear stiffness terms. This results in the EoM in the modal displacement responses \mathbf{q} , of the form Eq. (3.8). The matrices of modal natural frequencies,

$\mathbf{\Lambda}$, and linear modeshape, $\mathbf{\Phi}$, of this system are found by solving the eigenvalue problem, Eq. (3.5), written as

$$\mathbf{\Lambda} = \begin{bmatrix} \omega_{n1}^2 & 0 & 0 \\ 0 & \omega_{n2}^2 & 0 \\ 0 & 0 & \omega_{n3}^2 \end{bmatrix} = \frac{1}{m} \begin{bmatrix} k & 0 & 0 \\ 0 & k + \bar{k} & 0 \\ 0 & 0 & k + 3\bar{k} \end{bmatrix}, \quad (4.2a)$$

$$\mathbf{\Phi} = \begin{bmatrix} 1 & 1 & 1 \\ 1 & 0 & -2 \\ 1 & -1 & 1 \end{bmatrix}. \quad (4.2b)$$

Then, the vector of nonlinear stiffness and damping terms in modal coordinates is found, using Eq. (3.16), to be

$$\mathbf{N}_q = \mu \begin{pmatrix} \eta_1 \dot{q}_1 \\ \eta_2 \dot{q}_2 + q_2^3 + 27q_2q_3^2 \\ \eta_3 \dot{q}_3 + 9q_2^2q_3 + 27q_3^3 \end{pmatrix}. \quad (4.3)$$

where $\eta_i = c_{mi}/\mu$, $\mu = \kappa/m$, $c_{m1} = c$, $c_{m2} = c + \bar{c}$ and $c_{m3} = c + 3\bar{c}$. Using Eq. (3.17), the transformed vector of force amplitudes is given by

$$\mathbf{P}_q = \frac{1}{2} \begin{bmatrix} P_{m1} & P_{m1} \\ P_{m2} & P_{m2} \\ P_{m3} & P_{m3} \end{bmatrix} = \frac{1}{12m} \begin{bmatrix} 2P_1 + 2P_2 + 2P_3 & 2P_1 + 2P_2 + 2P_3 \\ 3P_1 - 3P_3 & 3P_1 - 3P_3 \\ P_1 - 2P_2 + P_3 & P_1 - 2P_2 + P_3 \end{bmatrix} \quad (4.4)$$

Then the forcing transform, the second step of the direct normal form technique, is applied. Here, the forcing frequency is assumed to be close to the system linear natural frequencies, i.e. $\Omega \approx \omega_{n1} \approx \omega_{n2} \approx \omega_{n3}$. This assumption may be reasonable when the linear constant of the coupling springs is small compared to that of the grounding springs, i.e. $\bar{k} \ll k$. Therefore, $\mathbf{v} = \mathbf{q}$ is used for this transform as the forcing transform matrix $\mathbf{e} = [\mathbf{0}]_{\{3 \times 2\}}$. Using Eqs. (3.21) and (3.11), the vector of small terms and matrix of force amplitudes in the EoM in \mathbf{v} , as Eq. (3.14), are

$$\mathbf{N}_v(\mathbf{v}, \dot{\mathbf{v}}) = \mathbf{N}_q(\mathbf{v}, \dot{\mathbf{v}}) \quad (4.5a)$$

$$\mathbf{P}_v = \mathbf{P}_q. \quad (4.5b)$$

The final step is the nonlinear near-identity transform which leads to the resonant EoM in \mathbf{u} , as Eq. (3.26). From the results of the Duffing oscillator in §3.5, we have seen a good

agreement between the normal form results of the first-level accuracy and numerical results. Hence, for this 3-DoF system, the nonlinear transform is again applied to the accuracy level ε^1 and this level of accuracy will be approved later via comparison with numerical results, see §4.4.

Substituting the first equality of Eq. (3.39) into Eq. (4.5a), we may find the polynomial terms vector, $\mathbf{u}_{(1)}^*$, and the corresponding coefficient matrix, $[n_{v(1)}]$, from Eqs. (3.37a) and (3.40a) and, then, using Eqs. (3.43c) and (3.51), the matrix $\boldsymbol{\beta}_{(1)}$ may be computed, i.e.

$$\mathbf{u}_{(1)}^* = \begin{pmatrix} u_{2p}^3 \\ u_{2m}^3 \\ u_{2p}^2 u_{2m} \\ u_{2p} u_{2m}^2 \\ u_{2p} u_{3p}^2 \\ u_{2m} u_{3m}^2 \\ u_{2p} u_{3p} u_{3m} \\ u_{2m} u_{3p} u_{3m} \\ u_{2p} u_{3m}^2 \\ u_{2m} u_{3p}^2 \\ u_{2p}^2 u_{3p} \\ u_{2m}^2 u_{3m} \\ u_{2p} u_{2m} u_{3p} \\ u_{2p} u_{2m} u_{3m} \\ u_{2m}^2 u_{3p} \\ u_{2p}^2 u_{3m} \\ u_{3p}^3 \\ u_{3m}^3 \\ u_{3p}^2 u_{3m} \\ u_{3p} u_{3m}^2 \\ u_{1p} \\ u_{1m} \\ u_{2p} \\ u_{2m} \\ u_{3p} \\ u_{3m} \end{pmatrix}, [n_{v(1)}]^\top = \boldsymbol{\mu} \begin{bmatrix} 0 & 1 & 0 \\ 0 & 1 & 0 \\ 0 & 3 & 0 \\ 0 & 3 & 0 \\ 0 & 27 & 0 \\ 0 & 27 & 0 \\ 0 & 54 & 0 \\ 0 & 54 & 0 \\ 0 & 27 & 0 \\ 0 & 27 & 0 \\ 0 & 0 & 9 \\ 0 & 0 & 9 \\ 0 & 0 & 18 \\ 0 & 0 & 18 \\ 0 & 0 & 9 \\ 0 & 0 & 9 \\ 0 & 0 & 27 \\ 0 & 0 & 27 \\ 0 & 0 & 81 \\ 0 & 0 & 81 \\ i\tilde{\eta}_1 & 0 & 0 \\ -i\tilde{\eta}_1 & 0 & 0 \\ 0 & i\tilde{\eta}_2 & 0 \\ 0 & -i\tilde{\eta}_2 & 0 \\ 0 & 0 & i\tilde{\eta}_3 \\ 0 & 0 & -i\tilde{\eta}_3 \end{bmatrix}, \boldsymbol{\beta}_{(1)}^\top = \omega_{r2}^2 \begin{bmatrix} - & 8 & - \\ - & 8 & - \\ - & 0 & - \\ - & 0 & - \\ - & 8 & - \\ - & 8 & - \\ - & 0 & - \\ - & 0 & - \\ - & 0 & - \\ - & 0 & - \\ - & - & 8 \\ - & - & 8 \\ - & - & 0 \\ - & - & 0 \\ - & - & 0 \\ - & - & 0 \\ - & - & 8 \\ - & - & 8 \\ - & - & 0 \\ - & - & 0 \\ 0 & - & - \\ 0 & - & - \\ - & 0 & - \\ - & 0 & - \\ - & - & 0 \\ - & - & 0 \end{bmatrix}, \quad (4.6)$$

where $\tilde{\eta}_i = \omega_{r_i} \eta_i$ and a dash in $\boldsymbol{\beta}_{(1)}$ represents that its value is insignificant as the corresponding coefficient in $[n_{v(1)}]$ is zero. When calculating $\boldsymbol{\beta}_{(1)}$, it has been assumed that $\Omega = \omega_{r_2} = \omega_{r_3}$ for the situation that $\Omega \approx \omega_{n_2} \approx \omega_{n_3}$. Once matrix $\boldsymbol{\beta}_{(1)}$ has been determined, Eq. (3.52) is used to find $[n_{u(1)}]$ and Eq. (4.10) is then used to compute the vector of nonlinear and damping terms in the resonant EoM, written as

$$\mathbf{N}_u = \mu \begin{pmatrix} \mathbf{i}\eta_1 \omega_{r_1} (u_{1p} - u_{1m}) \\ \mathbf{i}\eta_2 \omega_{r_2} (u_{2p} - u_{2m}) + [3u_{2p}u_{2m} + 54u_{3p}u_{3m}]u_2 + 27[u_{2m}u_{3p}^2 + u_{2p}u_{3m}^2] \\ \mathbf{i}\eta_3 \omega_{r_3} (u_{3p} - u_{3m}) + [18u_{2p}u_{2m} + 81u_{3p}u_{3m}]u_3 + 9[u_{2p}^2u_{3m} + u_{2m}^2u_{3p}] \end{pmatrix}. \quad (4.7)$$

Then using Eq. (3.54), the time-invariant complex coefficient corresponding to $e^{+i\omega_{r_i}t}$ in the i^{th} row of Eq. (4.7) may be found, as

$$N_{u1}^+ = \mathbf{i}\mu\eta_1\omega_{r_1}e^{-i\phi_1}, \quad (4.8a)$$

$$N_{u2}^+ = \mathbf{i}\mu\eta_2\omega_{r_2}e^{-i\phi_2} + \frac{3}{8}\mu e^{-i\phi_2}U_2 \left[U_2^2 + 18U_3^2 + 9e^{+i2(\phi_2-\phi_3)}U_3^2 \right], \quad (4.8b)$$

$$N_{u3}^+ = \mathbf{i}\mu\eta_3\omega_{r_3}e^{-i\phi_3} + \frac{9}{8}\mu e^{-i\phi_3}U_3 \left[2U_2^2 + 9U_3^2 + e^{-i2(\phi_2-\phi_3)}U_2^2 \right], \quad (4.8c)$$

where $\omega_{r_2} = \omega_{r_3}$ is provided and $\phi_2 - \phi_3$ represents the phase difference between the second and third modes. Substituting Eqs. (4.8) into Eq. (3.56) and then eliminating the terms of ϕ_i in the equation of the i^{th} mode, the time-invariant equations for the example system depicted in Fig. 4.1 may be written as

$$\left\{ [\omega_{n_1}^2 - \omega_{r_1}^2]^2 + (c_{m1}\omega_{r_1})^2 \right\} U_1^2 = P_{m1}^2, \quad (4.9a)$$

$$\left\{ \left[\omega_{n_2}^2 - \omega_{r_2}^2 + \frac{3}{4}\mu \left\{ U_2^2 + (18 + 9e^{i2(\phi_2-\phi_3)})U_3^2 \right\} \right]^2 + (c_{m2}\omega_{r_2})^2 \right\} U_2^2 = P_{m2}^2, \quad (4.9b)$$

$$\left\{ \left[\omega_{n_3}^2 - \omega_{r_3}^2 + \frac{3}{4}\mu \left\{ 27U_3^2 + (6 + 3e^{-i2(\phi_2-\phi_3)})U_2^2 \right\} \right]^2 + (c_{m3}\omega_{r_3})^2 \right\} U_3^2 = P_{m3}^2, \quad (4.9c)$$

where $c_{mi} = \mu\eta_i$ is used. Looking at Eqs. (4.9), we can see that due to the existence of nonlinear coupled terms in Eqs. (4.9b) and (4.9c), the solutions may not be easy to find. Therefore, in later sections, instead of solving Eqs. (4.9) to find the nonlinear steady-state forced response, we choose to consider the backbone curves of this example system to simplify this problem.

4.3 Backbone curves

4.3.1 Calculation of backbone curves

To calculate the backbone curves of the example system, we simply set the damping and external force to be zero, i.e. $c_{mi} = 0$ and $P_{mi} = 0$, in Eqs. (4.9). This gives the time-invariant equations governing the modal response amplitudes and frequencies for the corresponding conservative system, written as

$$[\omega_{n1}^2 - \omega_{r1}^2] U_1 = 0, \quad (4.10a)$$

$$\left[\omega_{n2}^2 - \omega_{r2}^2 + \frac{3}{4}\mu \left\{ U_2^2 + (18 + 9e^{i2(\phi_2 - \phi_3)})U_3^2 \right\} \right] U_2 = 0, \quad (4.10b)$$

$$\left[\omega_{n3}^2 - \omega_{r3}^2 + \frac{3}{4}\mu \left\{ 27U_3^2 + (6 + 3e^{-i2(\phi_2 - \phi_3)})U_2^2 \right\} \right] U_3 = 0. \quad (4.10c)$$

One trivial solution of Eqs. (4.10) is $U_1 = U_2 = U_3 = 0$ which represents no motion. Three more straightforward sets of solutions can also be found in the situations where each mode is assumed to behave independently. On these backbone curves, the response only includes the contribution of one mode; thus they are termed as *single-mode* backbone curve. Successively setting $U_2 = U_3 = 0$, $U_1 = U_3 = 0$ and $U_1 = U_2 = 0$ in Eqs. (4.10) leads to the expressions describing the frequency-amplitude relationships of the three single-mode backbone curves labelled $S1$, $S2$ and $S3$:

$$S1: \quad U_1 \neq 0, U_2 = U_3 = 0, \quad \omega_{r1}^2 = \omega_{n1}^2, \quad (4.11a)$$

$$S2: \quad U_2 \neq 0, U_1 = U_3 = 0, \quad \omega_{r2}^2 = \omega_{n2}^2 + \frac{3}{4}\mu U_2^2, \quad (4.11b)$$

$$S3: \quad U_3 \neq 0, U_1 = U_2 = 0, \quad \omega_{r3}^2 = \omega_{n3}^2 + \frac{81}{4}\mu U_3^2, \quad (4.11c)$$

where the letter S in the backbone curve label stands for single-mode and the following number represents the activated mode.

Furthermore, additional solutions, in which two related modes are simultaneously present, may also exist. For the problem under consideration, the only solution may be $U_1 = 0$ and $U_2 \neq 0$, $U_3 \neq 0$ as the first mode must behave independently. So substituting $U_1 = 0$ into Eqs. (4.10) gives

$$-\omega_{r2}^2 + \omega_{n2}^2 + \frac{3}{4}\mu \left\{ U_2^2 + (18 + 9e^{i2(\phi_2 - \phi_3)})U_3^2 \right\} = 0, \quad (4.12a)$$

$$-\omega_{r3}^2 + \omega_{n3}^2 + \frac{3}{4}\mu \left\{ 27U_3^2 + (6 + 3e^{-i2(\phi_2 - \phi_3)})U_2^2 \right\} = 0, \quad (4.12b)$$

which may contain complex components from the phase related terms as

$$e^{\pm i2(\phi_2 - \phi_3)} = \cos(2[\phi_2 - \phi_3]) \pm i \sin(2[\phi_2 - \phi_3]). \quad (4.13)$$

Balancing the imaginary components in Eq. (4.12) gives

$$\sin(2[\phi_2 - \phi_3]) = 0, \quad (4.14)$$

which may be satisfied by $|\phi_2 - \phi_3| = 0, \frac{\pi}{2}, \pi, \dots$. Therefore, a phase-related variable is defined as

$$p = e^{i2(|\phi_2 - \phi_3|)} = \begin{cases} +1 & \text{when: } |\phi_2 - \phi_3| = 0, \pi, \dots, \\ -1 & \text{when: } |\phi_2 - \phi_3| = \frac{\pi}{2}, \frac{3\pi}{2}, \dots \end{cases} \quad (4.15)$$

Now Eqs. (4.12) may be written as

$$\omega_{r2}^2 = \omega_{n2}^2 + \frac{3}{4}\mu \left\{ U_2^2 + (18 + 9p)U_3^2 \right\}, \quad (4.16a)$$

$$\omega_{r3}^2 = \omega_{n3}^2 + \frac{3}{4}\mu \left\{ 27U_3^2 + (6 + 3p)U_2^2 \right\}. \quad (4.16b)$$

For the case where $p = +1$, Eqs. (4.16) may be combined to give

$$\omega_r^2 = \omega_{n2}^2 + \frac{3}{4}\mu \left\{ U_2^2 + 27U_3^2 \right\} = \omega_{n3}^2 + \frac{3}{4}\mu \left\{ 27U_3^2 + 9U_2^2 \right\}, \quad (4.17)$$

where $\omega_{r2} = \omega_{r3} = \omega_r$ is used. Eq. (4.17) may be further arranged to be

$$D23_{[i]} : \begin{cases} U_2^2 = \frac{\omega_{n2}^2 - \omega_{n3}^2}{6\mu}, \\ \omega_r^2 = \frac{9\omega_{n2}^2 - \omega_{n3}^2}{8} + \frac{81}{4}\mu U_3^2, \end{cases} \quad (4.18)$$

which describes the amplitude-frequency relationships of a further set of *double-mode* backbone curves. For the solutions of Eq. (4.18), the second and third modes can behave either in-phase, i.e. $|\phi_2 - \phi_3| = 0$, or anti-phase, $|\phi_2 - \phi_3| = \pi$, see from Eq. (4.15). Therefore Eq. (4.18) describes two backbone branches labelled $D23_{[i]}^+$ and $D23_{[i]}^-$ which respectively

have the phase relationships

$$D23_{[i]}^+ : \phi_2 - \phi_3 = 0 \quad \text{and} \quad D23_{[i]}^- : \phi_2 - \phi_3 = \pi. \quad (4.19)$$

The in-phase and anti-phase backbone curves are both termed as *in-unison* because on the locus of these curves the two involved modes reach their maximum values and pass through zero simultaneously. For example, in the time domain, the responses of the second and third modes on $D23_{[i]}^\pm$, using Eq. (3.23), may be written as

$$\begin{aligned} D23_{[i]}^+ : u_2 &= U_2 \cos(\omega_r t) \quad \text{and} \quad u_3 = +U_3 \cos(\omega_r t), \\ D23_{[i]}^- : u_2 &= U_2 \cos(\omega_r t) \quad \text{and} \quad u_3 = -U_3 \cos(\omega_r t). \end{aligned} \quad (4.20)$$

Hence in the label of double-mode backbone curves, e.g. $D23_{[i]}^+$, letter D denotes the double-mode, numbers present the modes involved as with single-mode solutions, subscript $[i]$ indicates in-unison and the superscript denotes the modal phase difference.

For the case where $p = -1$, Eqs. (4.16) may also be written as

$$\omega_r^2 = \omega_{n2}^2 + \frac{3}{4}\mu \{U_2^2 + 9U_3^2\} = \omega_{n3}^2 + \frac{3}{4}\mu \{27U_3^2 + 3U_2^2\}. \quad (4.21)$$

This is then arranged to give the expression describing an extra pair of double-mode backbone curves, i.e.

$$D23_{[o]} : \begin{cases} U_2^2 = \frac{2(\omega_{n2}^2 - \omega_{n3}^2)}{3\mu} - 9U_3^2, \\ \omega_r^2 = \frac{3\omega_{n2}^2 - \omega_{n3}^2}{2}, \end{cases} \quad (4.22)$$

which again represents two phase-difference cases:

$$D23_{[o]}^+ : \phi_2 - \phi_3 = +\frac{\pi}{2} \quad \text{and} \quad D23_{[o]}^- : \phi_2 - \phi_3 = -\frac{\pi}{2}. \quad (4.23)$$

Hence, the modal responses on these backbone curves may be

$$\begin{aligned} D23_{[o]}^+ : u_2 &= U_2 \cos(\Omega t) \quad \text{and} \quad u_3 = +U_3 \sin(\Omega t), \\ D23_{[o]}^- : u_2 &= U_2 \cos(\Omega t) \quad \text{and} \quad u_3 = -U_3 \sin(\Omega t). \end{aligned} \quad (4.24)$$

Eqs. (4.24) indicate that when one of the modes reaches its maximum amplitude the other one has zero response and this behaviour is termed to be *out-of-unison* which is denoted in the backbone curve label using subscript $[o]$.

In Fig. 4.2, the modal responses for each backbone curve outlined above is illustrated in a 3-D plot in the projections of u_1 against u_2 against u_3 .

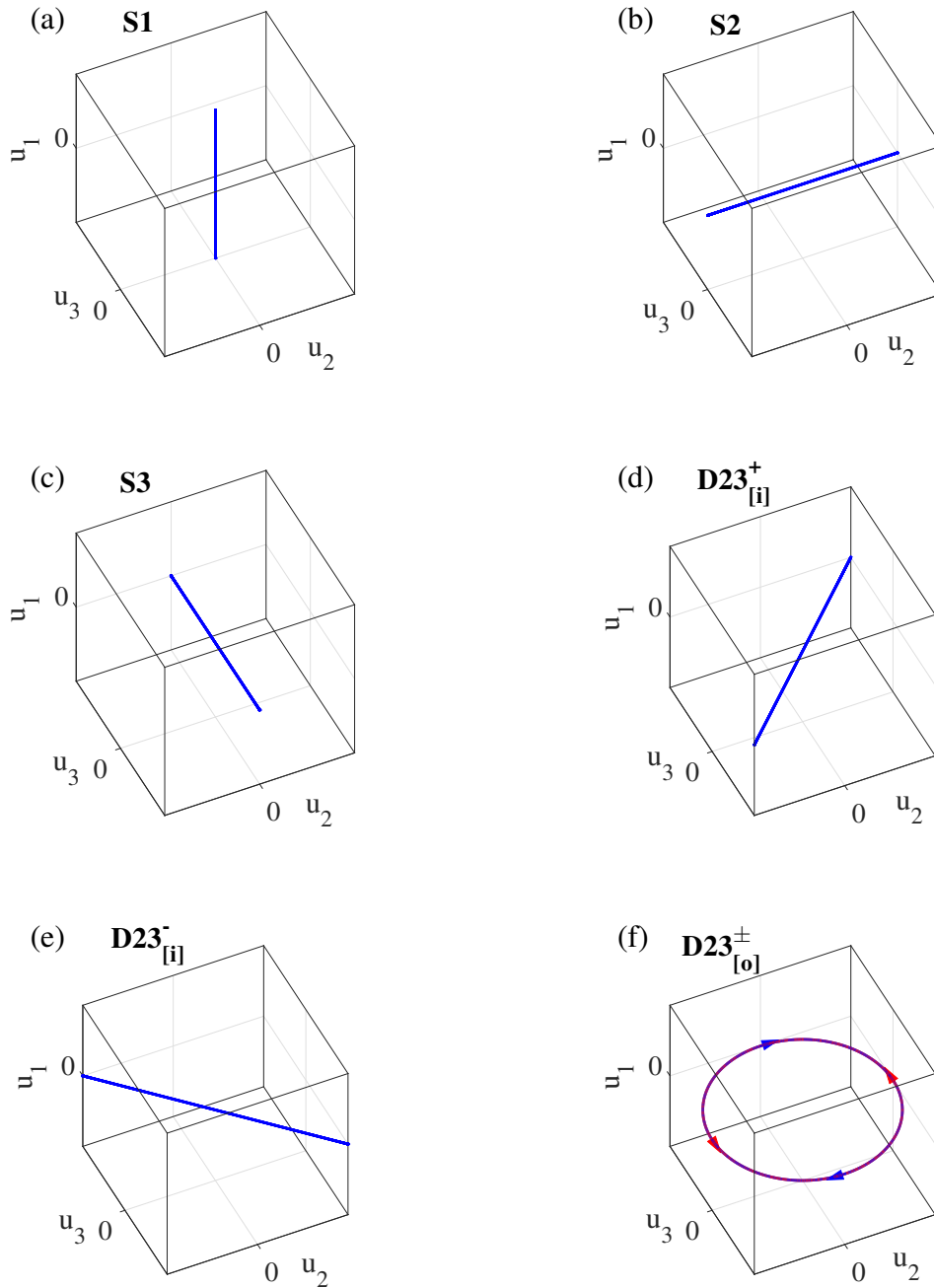


Fig. 4.2 The projection diagrams of u_1 against u_2 against u_3 of the response on the backbone curve branches: (a) $S1$, (b) $S2$, (c) $S3$, (d) $D23^+_{[i]}$, (e) $D23^-_{[i]}$ and (f) $D23^\pm_{[o]}$. The blue and red arrows in (f) denote the motion direction of $D23^+_{[o]}$ and $D23^-_{[o]}$ respectively.

When computing the physical responses, the harmonics are assumed to be negligible, such that in the near-identity nonlinear transform $\mathbf{H} = 0$. This assumption will be justified to be sufficiently accurate via the comparison of the normal form results with numerical results, see §4.4. Therefore, the physical response is found simply using $\mathbf{x} = \Phi \mathbf{u}$, see Eq. (3.78), with Eq. (4.2b), i.e.

$$\begin{pmatrix} x_1 \\ x_2 \\ x_3 \end{pmatrix} = \begin{pmatrix} u_1 + u_2 + u_3 \\ u_1 - 2u_3 \\ u_1 - u_2 + u_3 \end{pmatrix}. \quad (4.25)$$

For the backbone curves outlined, as all the activated mode(s) is(are) assumed to respond at an identical frequency ω_r , the physical displacements must be sinusoidal at this frequency. This may allow us to write

$$\begin{pmatrix} x_1 \\ x_2 \\ x_3 \end{pmatrix} = \begin{pmatrix} X_1 \cos(\omega_r t - \phi_{x1}) \\ X_2 \cos(\omega_r t - \phi_{x2}) \\ X_3 \cos(\omega_r t - \phi_{x3}) \end{pmatrix}, \quad (4.26)$$

where X_i and ϕ_{xi} are the amplitude and phase of x_i respectively. For the single-mode backbone curves, these amplitudes may be written

$$S1: \begin{pmatrix} X_1 \\ X_2 \\ X_3 \end{pmatrix} = \begin{pmatrix} U_1 \\ U_1 \\ U_1 \end{pmatrix}, \quad S2: \begin{pmatrix} X_1 \\ X_2 \\ X_3 \end{pmatrix} = \begin{pmatrix} U_2 \\ 0 \\ U_2 \end{pmatrix}, \quad S3: \begin{pmatrix} X_1 \\ X_2 \\ X_3 \end{pmatrix} = \begin{pmatrix} U_3 \\ 2U_3 \\ U_3 \end{pmatrix}. \quad (4.27)$$

For the cases where u_2 and u_3 are in-unison, i.e. in-phase and anti-phase, the amplitude relationship may be written

$$D23_{[i]}^+ : \begin{pmatrix} X_1 \\ X_2 \\ X_3 \end{pmatrix} = \begin{pmatrix} U_2 + U_3 \\ 2U_3 \\ U_2 - U_3 \end{pmatrix}, \quad D23_{[i]}^- : \begin{pmatrix} X_1 \\ X_2 \\ X_3 \end{pmatrix} = \begin{pmatrix} U_2 - U_3 \\ 2U_3 \\ U_2 + U_3 \end{pmatrix}, \quad (4.28)$$

and for the cases where u_2 and u_3 are out-of-unison, the amplitude relationship may be

$$D23_{[o]}^\pm : \begin{pmatrix} X_1 \\ X_2 \\ X_3 \end{pmatrix} = \begin{pmatrix} \sqrt{U_2^2 + U_3^2} \\ 2U_3 \\ \sqrt{U_2^2 + U_3^2} \end{pmatrix}. \quad (4.29)$$

From a further inspection of Eqs. (4.18) and (4.22), it can be seen that μ must be negative

to ensure that these equations have real solutions, corresponding to the backbone branches of physically meaning as $\omega_{n3} > \omega_{n2}$, see Eq. (4.2a) with the assumption $\bar{k} > 0$. Referring $\mu \propto \kappa$, the sign of μ is determined by the type of the system nonlinearity. Hence the hardening and softening nonlinear cases are considered separately in the following subsections to discuss the occurrence of double-mode backbone curves (resonant modal interactions) and also the relationship between each type of backbone curves.

Hardening nonlinearity

When the nonlinear springs are assumed hardening, i.e. $\mu > 0$, all amplitude solutions of Eqs. (4.18) and (4.22) must be complex, which means that double-mode backbone branches do not exist. While as Eqs. (4.22) may always have physical solutions, single-mode backbone curves $S1$, $S2$ and $S3$ unconditionally exist. The inexistence of double-mode backbone curves suggests that there is no modal interaction between the three underlying modes.

The backbone curves of the example system of hardening nonlinear springs are shown in Fig. 4.3, where $\omega_{n1} = 1$, $\omega_{n2} = 1.005$, $\omega_{n3} = 1.0015$ and the system parameters used are: $m = 1$, $k = 1$, $\bar{k} = 0.01$, and $\kappa = 0.05$. All panels show the backbone curves plotted in the projection of the response frequency against the displacement response amplitude. The panels in the first column show the amplitude of the fundamental components of the modal response, i.e. U_i , and the second column shows the that of the physical displacement response of individual masses, X_i . The $S1$, $S2$ and $S3$ branches are the single-mode backbone curves. The backbone curve $S1$ is linear as expected and $S2$ and $S3$ show the characteristic shape of a hardening response which is similar to that of the single-DoF Duffing oscillator shown in §3.5.3.

In the first column of Fig. 4.3, one interesting feature about single-mode backbone curves is that all these branches emerge from the frequency axis, more specifically from the points at the linear natural frequencies with zero response amplitude, i.e. $\omega_{ri} = \omega_{ni}$ and $U_i = 0$. Considering the expression of branch $S2$, Eq. (4.11b), when $U_2 = 0$, the response frequency is equal to the second natural frequency, i.e. $\omega_{r2} = \omega_{n2}$. Similarly, for Eqs. (4.11a) and (4.11c) of $S1$ and $S3$, when $U_1 = 0$ and $U_3 = 0$, then $\omega_{r1} = \omega_{n1}$ and $\omega_{r3} = \omega_{n3}$ respectively. These starting points of each single-mode backbone curves, which are also the zero-amplitude solutions, may be regarded as Hamiltonian Hopf bifurcation points, suggesting that the single-mode backbone curves bifurcate from the no-motion trivial solution. This phenomenon is in keeping with the assumption of normal form techniques that there is an underlying linear system, i.e. the nonlinear system tends to behave as its equivalent linear system does as the amplitude tends to zero.

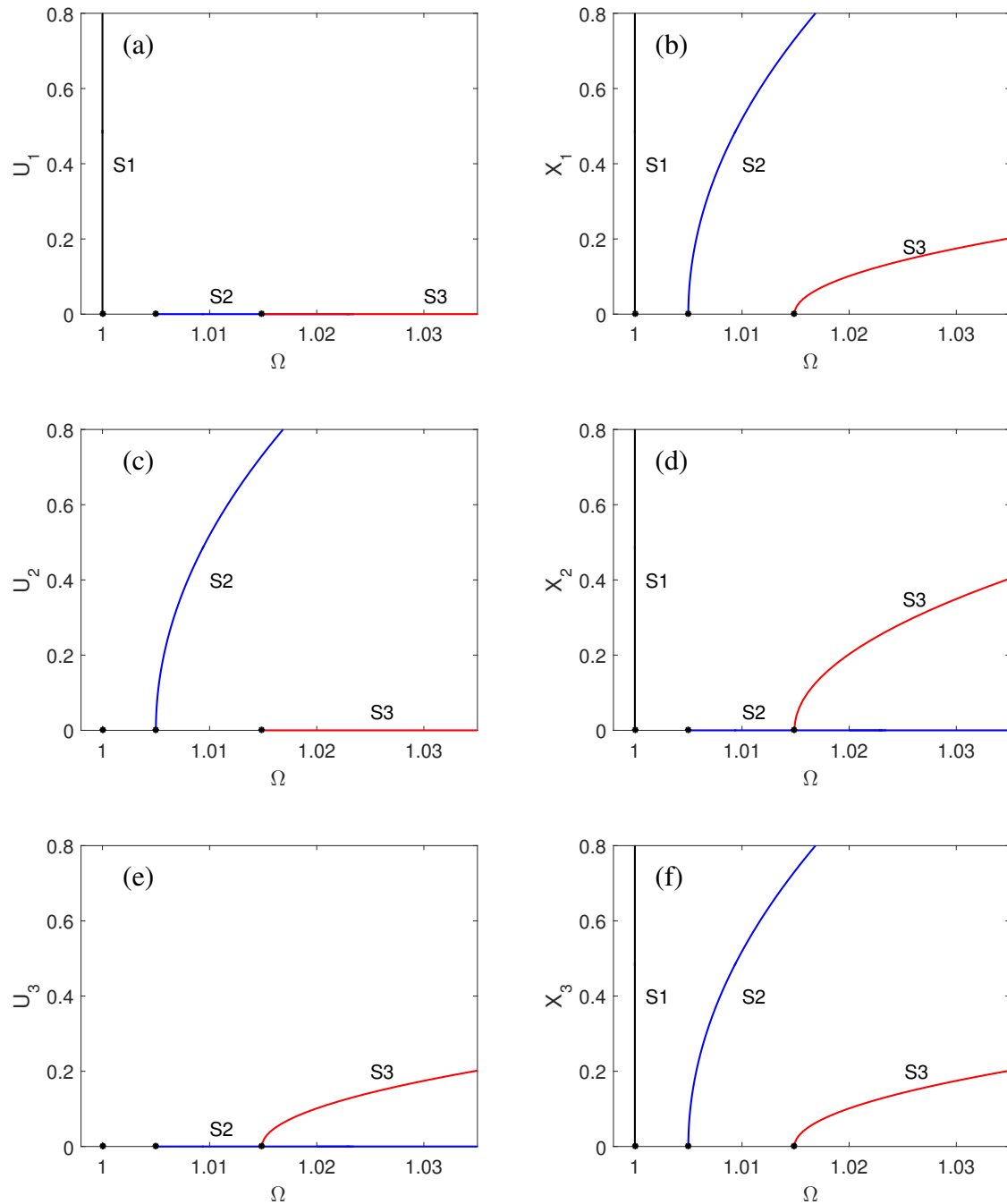


Fig. 4.3 The backbone curves of the 3-DoF oscillator depicted in Fig. 4.1 with the physical parameters $m = 1$, $k = 1$, $\bar{k} = 0.01$ and $\kappa = 0.05$. The panels in the first and second column show the results of the underlying vibrations modes and the physical masses respectively. Specific backbone curves are labelled respectively, and bifurcation points are denoted by dots. The black dots mark the system linear natural frequencies.

From the panels in the second column of Fig. 4.3, it can be seen that, due to the structural symmetry of the example, the backbone curve results of the masses on both sides for the hardening case are the same.

Softening nonlinearity

Considering the case where the nonlinear springs are softening, i.e. $\mu < 0$, Eqs. (4.18) and (4.22) may have real solutions. Therefore, the in-unison, $D23_{[i]}^{\pm}$, and out-of-unison, $D23_{[o]}^{\pm}$, backbone curves may be physically realistic. In Fig. 4.4, the backbone curves of the system with softening nonlinear springs are shown. As with the hardening case, $S1$, $S2$ and $S3$ of the first and third masses are the same, where branch $S1$ is vertically straight, and $S2$ and $S3$ are curved, but bending oppositely compared with those in Fig. 4.3. However, backbone curves $D23_{[i]}^{\pm}$ for these two symmetric masses come with the position swapped. Although the phase differences between the second and third modes are different for the out-of-unison backbone curves, $D23_{[o]}^+$ and $D23_{[o]}^-$, their amplitude projections are the same. Therefore, $D23_{[o]}^+$ and $D23_{[o]}^-$ overlay each other in the results.

Here, the double-mode backbone curves $D23_{[i]}^{\pm}$ and $D23_{[o]}^{\pm}$, where both the second and third modes are activated, are of primary interest. In Fig. 4.4, it can be seen that $D23_{[i]}^{\pm}$ emanate from branch $S2$ and $D23_{[o]}^{\pm}$ appear between $S2$ and $S3$. Considering the starting point of $D23_{[i]}^{\pm}$ by substituting $U_3 = 0$ into Eq. (4.18) gives

$$U_2^2 = \frac{\omega_{n2}^2 - \omega_{n3}^2}{6\mu} \quad \text{and} \quad \Omega^2 = \frac{9\omega_{n2}^2 - \omega_{n3}^2}{8}. \quad (4.30)$$

It can be seen, from Eq. (4.11b), that Eq. (4.30) describes a point on $S2$. Additionally, when $\Omega = 0$ in Eq. (4.18), then

$$U_3^2 = \frac{\omega_{n3}^2 - 9\omega_{n2}^2}{162\mu}. \quad (4.31)$$

which corresponds to a point on the response-amplitude axis. Therefore, it can be deduced that in-unison backbone curves $D23_{[i]}^{\pm}$ bifurcate from the single-mode backbone curves $S2$ and ends at zero-frequency axis, which matches the observation of Fig. 4.4.

Similarly, substituting $U_3 = 0$ into the expressions of $D23_{[o]}^{\pm}$, i.e. Eq. (4.22), gives

$$U_2^2 = \frac{2(\omega_{n2}^2 - \omega_{n3}^2)}{3\mu} \quad \text{and} \quad \Omega^2 = \frac{3\omega_{n2}^2 - \omega_{n3}^2}{2}, \quad (4.32)$$

which can be seen from Eq. (4.11b) that it describes another point on $S2$. When substituting

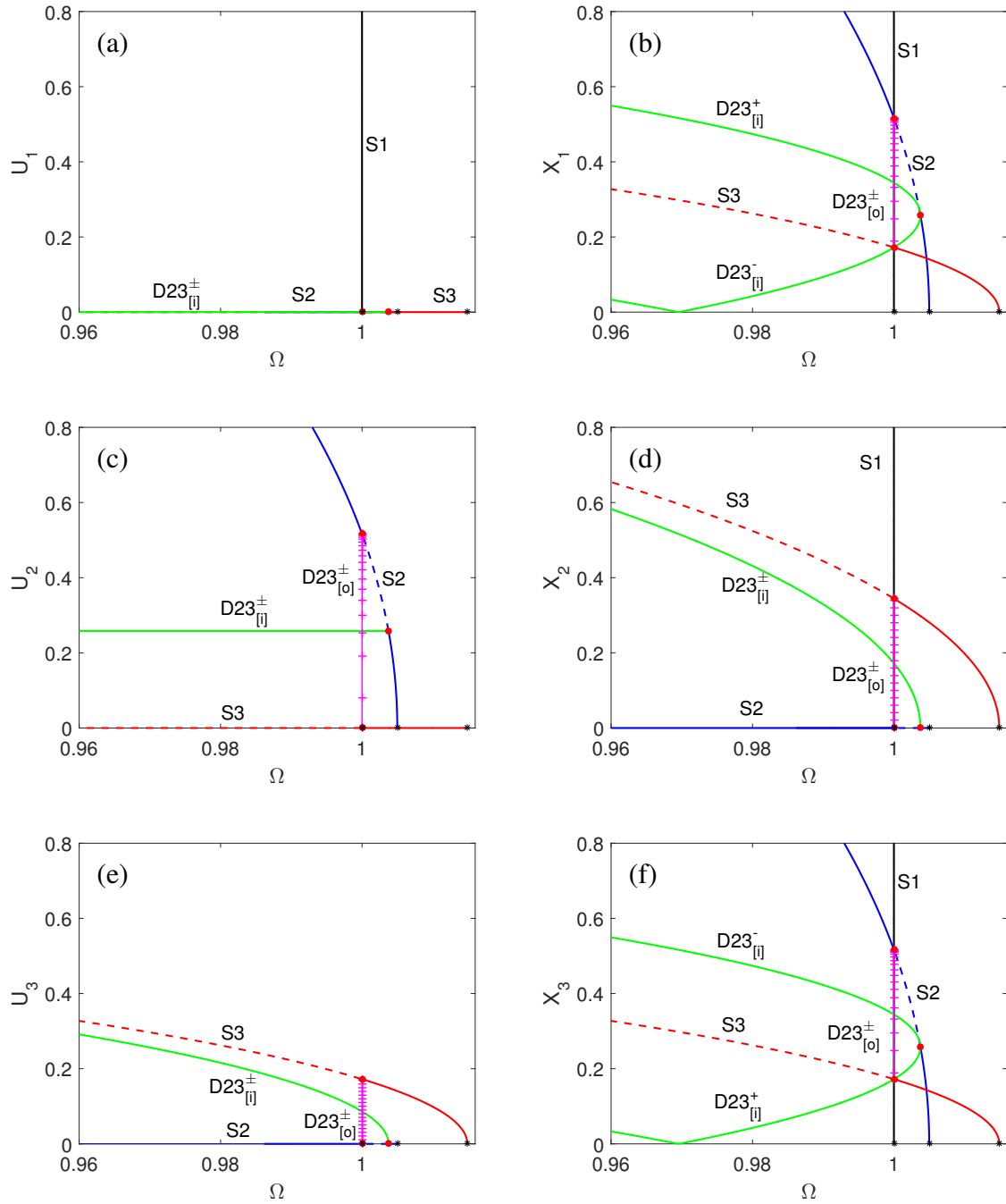


Fig. 4.4 The backbone curves of the 3-DoF oscillator depicted in Fig. 4.1 with the physical parameters $m = 1$, $k = 1$, $\bar{k} = 0.01$ and $\kappa = -0.05$. Specific backbone curves respectively are labelled. Solid and dashed lines denote the stable and unstable solutions respectively. Bifurcation points are denoted by dots. Note that as $D23_{[o]}^{\pm}$ overlay the $S1$, the backbone curves $D23_{[i]}^{\pm}$ are indicated by short cross lines for distinction.

$U_2 = 0$ into Eq. (4.22), it gives

$$U_3^2 = \frac{2(\omega_{n2}^2 - \omega_{n3}^2)}{18\mu} \quad \text{and} \quad \Omega^2 = \frac{3\omega_{n2}^2 - \omega_{n3}^2}{2}, \quad (4.33)$$

which describes a point on $S3$, see Eq. (4.11c). This agrees with the observation from Fig. 4.4 that the out-of-unison double-mode backbone curves emerge from single-mode backbone curves $S2$ and end at $S3$ (or described the other way around). These bifurcation phenomena of backbone curves have also been observed in other 2-DoF systems, see for example [6, 35]. A significant difference from the previous systems in the literature is that backbone curves $D23_{[i]}^\pm$ here is vertically straight with a limited length, which suggests that the out-of-unison resonance only happens within a specific amplitude (power) range for this system.

4.3.2 Stability of the backbone curves

In §4.3.1, we have seen the nonlinear behaviour of double-mode backbone curves bifurcating from the single-mode backbone curves. As the existence of a bifurcation may be associated with changes in stability, the stability of backbone curves is considered using the technique outlined in §3.3.

It is known, from Fig. 4.4, that there are two bifurcations on backbone curve $S2$ where $D23_{[i]}^\pm$ and $D23_{[o]}^\pm$ emerge from respectively; hence the stability of $S2$ is chosen to be considered in detail. On branch $S2$, the response only contains that of the second mode; thus $u_3 = 0$. So the stability of $S2$ may be determined by considering the dynamics of u_3 about its zero-solution. It is noteworthy that u_1 is not considered here due to its independence from u_2 and u_3 . This may allow us to simplify the problem via considering the resonant EoM of the third mode only instead of that of the whole system. Using Eq. (4.7), resonant nonlinear terms in the EoM of the third mode are

$$N_{u,3} = 9\mu [2u_{2p}u_{2m}u_3 + (u_{2p}^2u_{3m} + u_{2m}^2u_{3p})], \quad (4.34)$$

where, as u_3 is considered around its zero-solution, the term $u_{3p}u_{3m}u_3$ is so small that it has been neglected. Using Eq. (3.54), the complex coefficients, $N_{u,3}^+$ and $N_{u,3}^-$, are found to be

$$N_{u,3}^+ = \frac{9\mu}{4} (2U_{p2}U_{m2}U_{p3} + U_{p2}^2U_{m3}), \quad (4.35a)$$

$$N_{u,3}^- = \frac{9\mu}{4} (2U_{p2}U_{m2}U_{m3} + U_{m2}^2U_{p3}). \quad (4.35b)$$

Based on Eq. (3.64), the vector \mathbf{f} of this problem, defined using $\mathbf{U}'_3 = \mathbf{f}(\mathbf{U}_3)$, see Eq. (3.66), for the backbone curve case may be constructed, i.e.

$$\mathbf{f} = \begin{pmatrix} U'_{p3} \\ U'_{m3} \end{pmatrix} = \frac{\mathbf{i}}{2\omega_{r3}} \begin{pmatrix} +(\omega_{n3}^2 - \omega_{r3}^2)U_{p3} + N_{u3}^+ \\ -(\omega_{n3}^2 - \omega_{r3}^2)U_{m3} - N_{u3}^- \end{pmatrix}. \quad (4.36)$$

So, substituting Eqs. (4.35) into Eq. (4.36) gives

$$\mathbf{f} = \frac{\mathbf{i}}{2\omega_{r3}} \begin{pmatrix} +(\omega_{n3}^2 - \omega_{r3}^2)U_{p3} + \frac{9\mu}{4}(2U_{p2}U_{m2}U_{p3} + U_{p2}^2U_{m3}) \\ -(\omega_{n3}^2 - \omega_{r3}^2)U_{m3} - \frac{9\mu}{4}(2U_{2p}U_{m2}U_{m3} + U_{m2}^2U_{p3}) \end{pmatrix}, \quad (4.37)$$

whose Jacobian may be computed as

$$\mathbf{f}_{\mathbf{U}_3} = \frac{\mathbf{i}}{2\omega_{r3}} \begin{bmatrix} (\omega_{n3}^2 - \omega_{r3}^2) + \frac{9\mu}{2}U_{p2}U_{m2} & \frac{9\mu}{4}U_{p2}^2 \\ -\frac{9\mu}{4}U_{m2}^2 & -(\omega_{n3}^2 - \omega_{r3}^2) - \frac{9\mu}{2}U_{p2}U_{m2} \end{bmatrix}. \quad (4.38)$$

Now, the eigenvalues, λ , of $\mathbf{f}_{\mathbf{U}}$ may be found from

$$\lambda^2 + \frac{1}{4\omega_{r3}^2} \left[\left(\omega_{n3}^2 - \omega_{r3}^2 + \frac{9\mu}{2}U_2^2 \right)^2 - \left(\frac{9\mu}{4}U_2^2 \right)^2 \right] = 0, \quad (4.39)$$

where $U_2^2 = U_{p2}U_{m2}$ is used. From Eq. (4.39), it can be seen that the eigenvalues are either real pair of opposite sign, i.e. $\lambda = \pm R$ where $R \in \mathbb{R}$, or purely imaginary conjugates, i.e. $\lambda = \pm I$ where $I \in \mathbb{I}$. Therefore, the backbone curve $S2$ may only be unstable when the eigenvalues are non-zero real, or neutrally stable when eigenvalues are on the imaginary axis. This is different from the forced case which will be shown in §4.4 where the eigenvalues may be complex conjugate pairs, i.e. $\lambda = R \pm I$, corresponding to three stability situations listed in §3.3.

From Eq. (4.39), the unstable region is given by

$$\text{Re} \left\{ \sqrt{\left(\omega_{n3}^2 - \omega_{r3}^2 + \frac{9\mu}{2}U_2^2 \right)^2 - \left(\frac{9\mu}{4}U_2^2 \right)^2} \right\} > 0, \quad (4.40)$$

which may be simplified to

$$\left| \omega_{n3}^2 - \omega_{r3}^2 + \frac{9\mu}{2} U_2^2 \right| > \left| \frac{9\mu}{4} U_2^2 \right|. \quad (4.41)$$

This implies that the changes in stability occur when both sides of inequality given by Eq. (4.41) are equal, where $\lambda = 0$. Hence substituting the solution expression of $S2$, given by Eq. (4.11b), into Eq. (4.41), gives

$$\left| \omega_{n3}^2 - \omega_{n2}^2 + \frac{15\mu}{4} U_2^2 \right| = \left| \frac{9\mu}{8} U_2^2 \right|, \quad (4.42)$$

which may be solved to find the positions of bifurcations on $S2$.

When $\mu > 0$, the content within the absolute value sign at both sides of Eq. (4.42) are unconditionally positive; hence Eq. (4.42) may be rearranged to give

$$-\frac{21}{8} U_2^2 = \omega_{n3}^2 - \omega_{n2}^2, \quad (4.43)$$

which is unphysical, recalling $\omega_{n3} > \omega_{n2} > 0$. This suggests that there is no bifurcation on $S2$ for the hardening case.

When $\mu < 0$, Eq. (4.42) has two valid solutions, which describe the positions of bifurcations, given by

$$BP_{S2}^{D23[i]} : \begin{cases} \Omega^2 = \frac{9\omega_{n2}^2 - \omega_{n3}^2}{8}, \\ U_2^2 = \frac{\omega_{n2}^2 - \omega_{n3}^2}{6\mu}, \end{cases} \quad (4.44)$$

and

$$BP_{S2}^{D23[o]} : \begin{cases} \Omega^2 = \frac{3\omega_{n2}^2 - \omega_{n3}^2}{2}, \\ U_2^2 = \frac{2(\omega_{n2}^2 - \omega_{n3}^2)}{3\mu}. \end{cases} \quad (4.45)$$

Those are the identical points where $D23_{[i]}^{\pm}$ and $D23_{[o]}^{\pm}$ emerge from $S2$, given in Eq. (4.30) and Eq. (4.32) respectively. So in the notation of the bifurcation points, the subscript denotes which backbone curve they are on, and the superscript indicates which backbone curves emerge. It can also be easily found that the parts of $S2$ below bifurcation point $BP_{S2}^{D23[i]}$ and above $BP_{S2}^{D23[o]}$ are stable and that between them is unstable.

The same analysis could be applied to the solution of $S3$ to find where the bifurcation happens. As with branch $S2$, there is no valid solution for the hardening case. The bifurcat-

ing position on $S3$ for the softening case is predicted to be

$$BP_{S3}^{D23[\sigma]} : \begin{cases} \Omega^2 = \frac{3\omega_{n2}^2 - \omega_{n3}^2}{2}, \\ U_3^2 = \frac{2(\omega_{n2}^2 - \omega_{n3}^2)}{27\mu}, \end{cases} \quad (4.46)$$

which is the intersection point of $S3$ and $D23_{[\sigma]}^{\pm}$, given by Eq. (4.33). The stability condition of branch $S3$ is that the section below $BP_{S3}^{D23[\sigma]}$ is stable and above is unstable. In addition, using the bifurcation theory for Hamiltonian systems, all these bifurcation points detected are the (Hamiltonian) pitchfork bifurcation. Note that as the first mode is linear, the whole trajectory of $S1$ is neutrally stable and no bifurcation occurs on it.

In Fig. 4.4, the information regarding the stability of the single-mode backbone curves $S2$ and $S3$ is also indicated: the stable and unstable responses are represented by solid and dashed lines respectively.

4.4 Forced response

4.4.1 Relation between forced response and backbone curves

In this section, the relationship between forced responses and backbone curves is explored, especially the ability of backbone curves to interpret the modal interaction occurring for the forced situation is demonstrated. As the occurrence of modal interaction may be affected by the sign of the nonlinear stiffness value for the example system, as discussed in §4.3, the forced response for the hardening and softening cases are investigated separately.

Hardening case

Fig. 4.5 shows the forced-response curves of the example system with hardening springs. The damping coefficients used are $c = 2 \times 10^{-3}$ and $\bar{c} = 2 \times 10^{-5}$, such that the modal damping ratios are $\zeta_i \approx 0.1\%$. The amplitude of the external force applied is $(P_1, P_2, P_3) = (3, -1, 1) \times 10^{-3}$. This forcing scenario ensures that all three modes are excited at the same level, i.e. $(P_{m1}, P_{m2}, P_{m3}) = (1, 1, 1) \times 10^{-3}$, see Eqs. (4.2b) and (3.10). The purpose of choosing this forcing scenario is for presenting the modal independence of the hardening system under excitation. The forced response was numerically computed using the Matlab continuation toolbox, COCO.

For the forced responses, it is assumed that the fundamental response frequency, ω_{ri} , is equal to the forcing frequency, Ω . Hence, Fig. 4.5 is plotted in the projection of the forcing frequency, Ω , against the displacement response amplitude of the three masses, X_1 , X_2 and X_3 . From the result, it can be seen that the response curves may be able to be divided into three regions by two minima for separate observation (from left to right):

- For the first resonance, the response curves of three masses are similar to that of the linear oscillator and are centred around the backbone curve $S1$.
- For the second resonance, the familiar shape of the response of a typical Duffing oscillator is following $S2$, and the jump phenomenon can be observed on the right part of the curve for the first and third masses. Due to the speciality of the modeshape of the second mode, i.e. $\Phi_2 = (1, 0, -1)^T$, there is no resonant response for the second mass in Fig. 4.5(b) within this bandwidth.
- For the third resonance, in Fig. 4.5(a), the curve around $S3$ contains a loop where the upper trajectory is unstable, which occurs from the addition and subtraction of the modal contributions. In Fig. 4.5(b) and Fig. 4.5(c), the response of the typical Duffing oscillator can be observed enveloping $S3$.

For the first part of the response, the resonant peak points are exactly on the linear backbone curve $S1$, and for the other parts of the forced-response curves, they cross the backbone curves $S2$ and $S3$ almost at the fold points. This observation is in line with the results found for systems with a lower number of degrees of freedom. In Fig. 4.5, no modal interaction phenomenon is observed which demonstrates the modal independence of the hardening nonlinear system. This result matches the prediction of the backbone curves.

Softening case

Now the forced response of the system with softening nonlinear springs is considered. From the backbone curve results shown in Fig. 4.4, it is known that for this case the modal interactions may occur between the second and third modes. Therefore, the single-mode forcing configuration is chosen. More specifically, considering both types of double-mode backbone curves emerging from $S2$, the external forcing is chosen to be applied to the second mode only, i.e. $P_{m2} \neq 0$ and $P_{m1} = P_{m3} = 0$. The physical parameters used are: $c = 2 \times 10^{-3}$, $\bar{c} = 2 \times 10^{-5}$ and $(P_1, P_2, P_3) = 0.4, 0.9, 1.5 \times (1, 0, -1) \times 10^{-3}$, which corresponds to $\zeta_i \approx 0.1\%$ and $P_{m2} = 0.4, 0.9, 1.5 (\times 10^{-3})$.

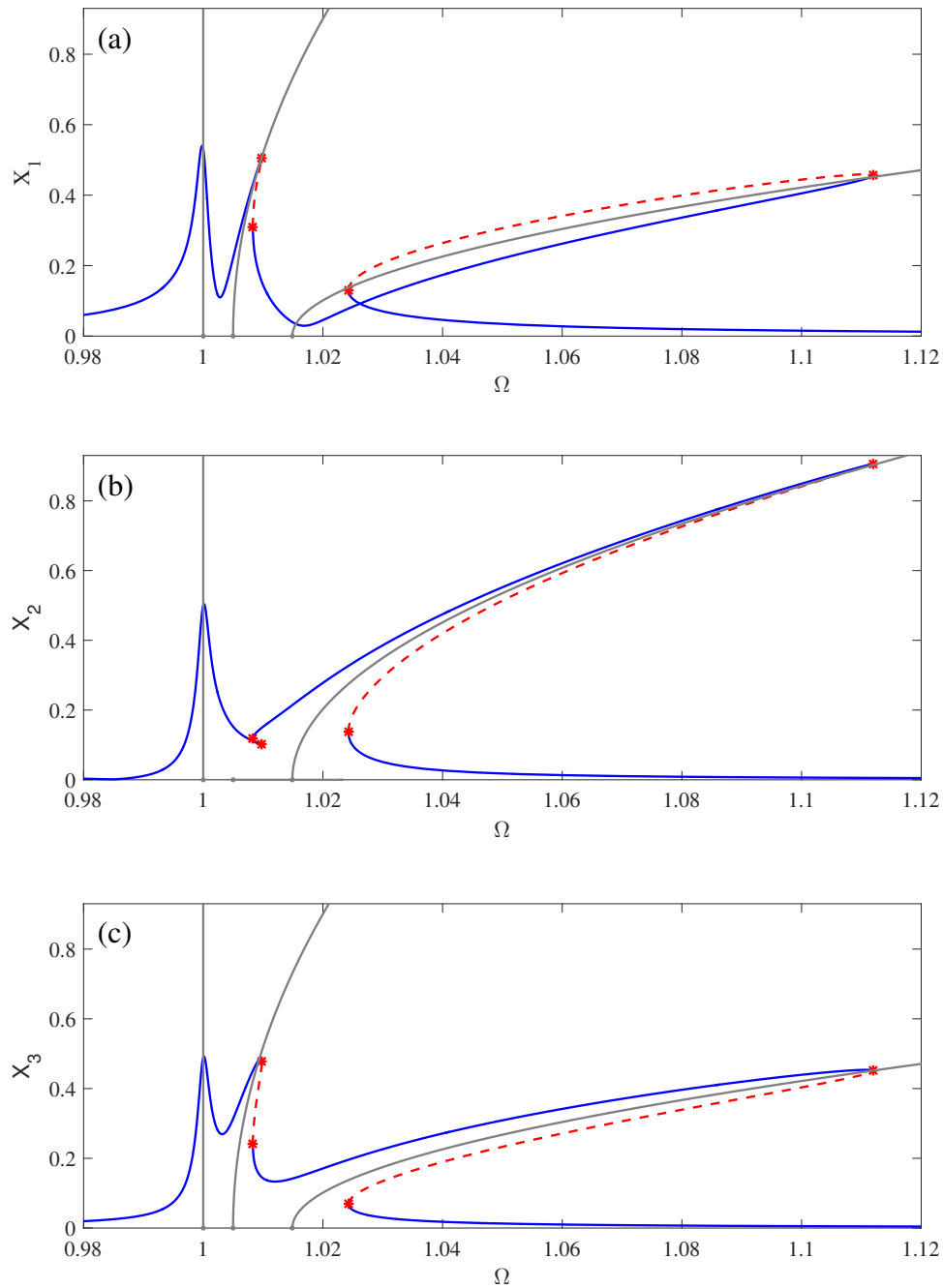


Fig. 4.5 The displacement response curves of the 3-DoF system depicted in Fig. 4.1 when it is externally forced at amplitude $(P_1, P_2, P_3) = (3, -1, 1) \times 10^{-3}$ with physical parameters $m = 1, k = 1, \bar{k} = 0.01, \kappa = 0.05, c = 2 \times 10^{-3}$ and $\bar{c} = 2 \times 10^{-5}$. The solid-blue and dashed-red lines represent the stable and unstable response respectively. The grey lines represent the backbone curves and the red asterisks represent the fold points. (a) Mass 1, X_1 , (b) Mass 2, X_2 , and (c) Mass 3, X_3 .

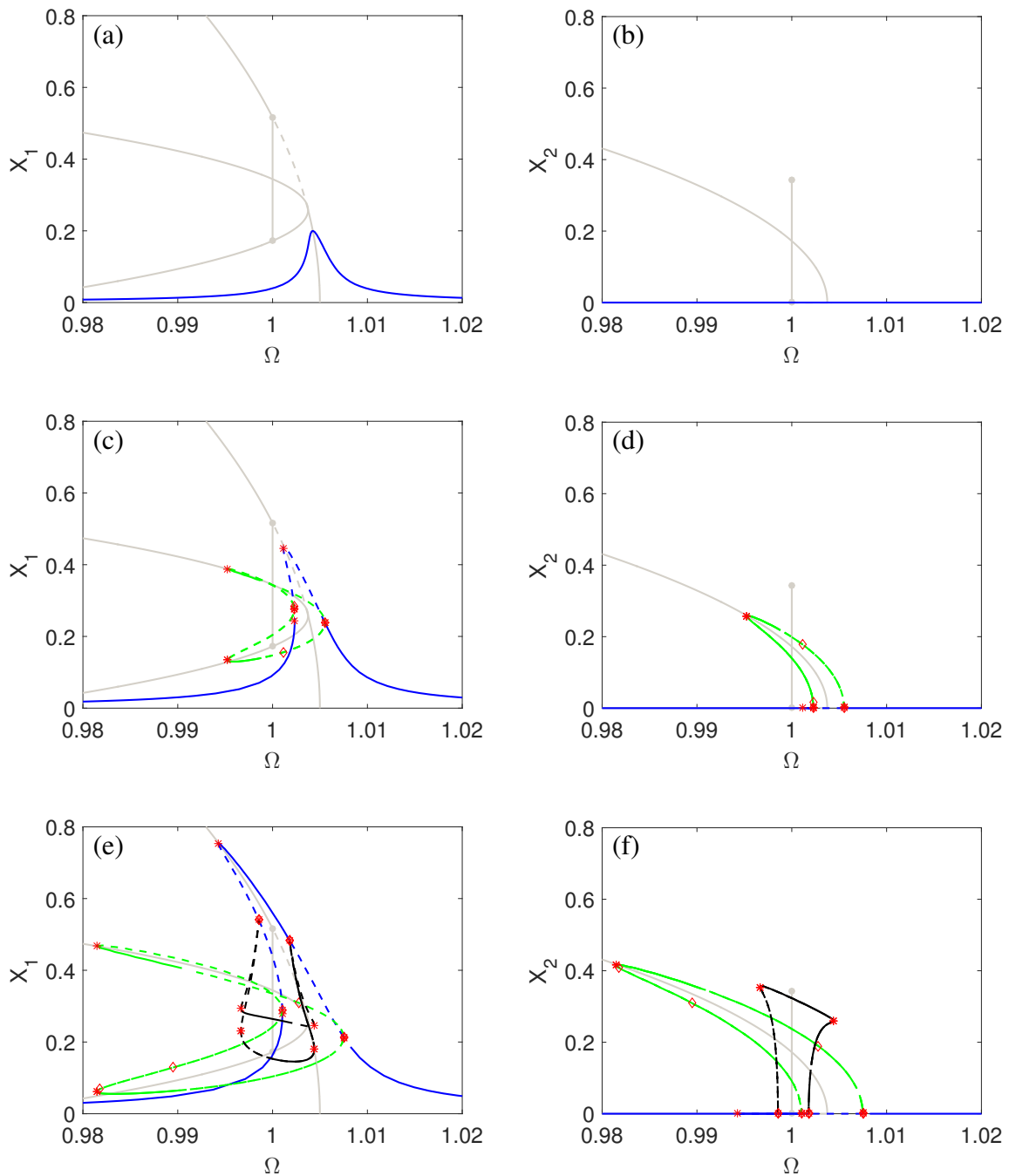


Fig. 4.6 The response curves of the 3-DoF system depicted in Fig. 4.1 excited in the second mode only at three different amplitudes. The system parameters used are the same as those in Fig. 4.4 and the damping values are $c = 2 \times 10^{-3}$ and $\bar{c} = 2 \times 10^{-5}$. The solid and dashed lines represent the stable and unstable responses respectively. The diamonds and asterisks indicate secondary bifurcation and fold points. The grey lines represent the backbone curves. Note that due to the specific forcing configuration, the backbone curves S1 and S3 have been omitted.

Fig. 4.6 shows the forced response results superimposed on the backbone curves for the first and second masses in panels of the first and second columns respectively. Due to the bilateral symmetry of the system structure and the forcing configuration, the response curves of the first and third mass look the same. Thus the results of the third mass are omitted. It can be observed, from Fig. 4.6, that:

- for the small force amplitude situation, Fig. 4.6(a) and Fig. 4.6(b), there is only one response branch centred around $S2$. The curve for the first mass is like that of a softening Duffing oscillator and only composed of the response of the second mode, u_2 , such that no motion of the second mass is observed. For this case, the force is insufficient to trigger the modal interaction or jump.
- for the medium force amplitude situation, Fig. 4.6(c) and Fig. 4.6(d), there are three response branches, i.e. one blue and two green. The two green curves following $D23_{[i]}^{\pm}$ (with their fold points almost on $D23_{[i]}^{\pm}$) bifurcate from the primary (single-mode) response curve (the blue one) at two secondary bifurcation points respectively, and they are composed of the responses of both the second and third modes, i.e. u_2 and u_3 . The instability of the upper-right part of the trajectory of the primary response curve (the section above the second bifurcation) is in keeping with that of $S2$.
- for the large force amplitude situation, Fig. 4.6(e) and Fig. 4.6(f), there are two additional response curves, i.e. the black ones, which corresponds to $D23_{[o]}^{\pm}$, which again bifurcate from the primary response curve of the second mode. On these two curves, both the second and third modes are present. However, unlike other double-mode response curves, no fold point of these two new response curves is close to the out-of-unison backbone curves $D23_{[o]}^{\pm}$. The occurrence of the bifurcation of the response corresponding to $D23_{[o]}^{\pm}$ from the primary response is after that to $D23_{[i]}^{\pm}$. This bifurcation sequence is in line with the positions of the bifurcation points $BP_{S2}^{D23_{[i]}}$ and $BP_{S2}^{D23_{[o]}}$ on backbone curve $S2$. Besides, for the right trajectory of the primary response curve, it turns back stable after the second secondary bifurcation which matches the characteristics of the backbone curves.

From the results in Fig. 4.6, it can be noticed that for the situation where a single nonlinear mode is externally excited, the other nonlinear coupled modes may be activated due to the modal interaction. Also, the occurrence of this modal interaction is affected by the force amplitude. More specifically, some critical values of the force amplitude must be reached to trigger the modal interaction. Besides, the nonlinear dynamic phenomena of the forced

responses are in good agreement with those of the backbone curves: the stability characteristics of the primary single-mode responses, the position of the local maximum amplitude for both single- and multi-mode forced response and the occurrence of bifurcations due to modal interaction (both the types and occurring sequence).

Fig. 4.6 shows that all the double-mode response curves emanate from the primary response curves at secondary bifurcation points, and the forced responses and their bifurcations can be associated with the corresponding backbone curves. It is inferred that for the single-mode excited situation if the bifurcations of primary response curves are known, the occurrence of the multi-mode forced response may be predicted without calculating the full response curves. In §4.4.2, we will consider the stability of the single-mode response curves to find the relation between the occurrence of the modal interaction and the force amplitude.

4.4.2 Relation between modal interactions and force amplitudes

As it is known that there is a change in the stability of the single-mode response curve across the points where the mixed-mode responses emanate from, it allows us to apply the stability analysis technique mentioned in §3.4 to find the bifurcation positions.

Here, we consider the situation where only the second mode is forced again. The primary response curve contains the second mode only, and the third mode is known to be not activated. Therefore, the stability of the primary response curve of the second mode may be found by considering the stability of the zero-solution of the third mode. When the zero solution for the response of the unforced mode is stable/unstable, the single-mode response curve of the forced mode is also stable/unstable. As a result, the point of neutral stability is the (secondary) bifurcation point.

Before the stability analysis, we must find the steady-state response when only the second mode of the system is assumed to be activated. Hence the resonant EoM of the second mode is considered, in which the nonlinear and damping terms, using Eq. (4.7), are given by

$$N_{u,2} = \mathbf{i}c_{m2}\Omega(u_{2p} - u_{2m}) + 3\mu u_{2p}u_{2m}u_2, \quad (4.47)$$

where the u_3 related terms have been removed as the third mode is assumed inactive on the primary response curve of the second mode, i.e. $u_3 = 0$. Based on Eqs. (3.54) and (3.56), the time-invariant equation is found to be

$$(\omega_{n2}^2 - \Omega^2) \frac{U_2}{2} + 3\mu \frac{U_2^3}{8} + \mathbf{i}c_{m2}\Omega \frac{U_2}{2} = \frac{P_{m2}}{2} e^{\mathbf{i}\phi_2}. \quad (4.48)$$

Eliminating the phase terms in Eq. (4.48) gives the equation describing the relation between the response and force amplitude, i.e.

$$9\mu^2 U_2^6 + 24\mu(\omega_{n2}^2 - \Omega^2)U_2^4 + 16[(\omega_{n2}^2 - \Omega^2)^2 + (c_{m2}\Omega)^2]U_2^2 = 16P_{m2}^2. \quad (4.49)$$

Then the zero-solution of the third mode is considered. The nonlinear and damping terms in the resonant EoM of the third mode are

$$N_{u,3} = \mathbf{i}c_{m3}\Omega(u_{3p} - u_{3m}) + 18u_{2p}u_{2m}u_3 + 9(u_{2p}^2 u_{3m} + u_{2m}^2 u_{3p}), \quad (4.50)$$

where, as with Eq. (4.34), the $u_{3p}u_{3m}u_3$ term has been ignored due to its smallness. From Eq. (4.50), the conjugate coefficients $N_{u,3}^\pm$ are found using Eq. (3.53), and, then the function of $\mathbf{U}_3 = [U_{p3} \ U_{m3}]^\top$, i.e. $\mathbf{F}(\mathbf{U}_3)$, is formulated, using Eq. (3.63), given

$$\mathbf{F} = \frac{\mathbf{i}}{2\omega_{r3}} \begin{pmatrix} +(\omega_{n3}^2 - \Omega^2)U_{p3} + \frac{9\mu}{4}(2U_{p2}U_{m2}U_{p3} + U_{p2}^2 U_{m3}) + \mathbf{i}c_{m3}\Omega U_{p3} \\ -(\omega_{n3}^2 - \Omega^2)U_{m3} - \frac{9\mu}{4}(2U_{2p}U_{m2}U_{m3} + U_{m2}^2 U_{p3}) + \mathbf{i}c_{m3}\Omega U_{m3} \end{pmatrix}, \quad (4.51)$$

Note that the notation \mathbf{F} is used here to be distinct from \mathbf{f} in §4.3.2 for the backbone curve case. Therefore, the Jacobian of \mathbf{F} is found to be

$$\mathbf{F}_{\mathbf{U}_3} = \frac{\mathbf{i}}{2\Omega} \begin{bmatrix} \omega_{n3}^2 - \Omega^2 + \frac{9\mu}{2}U_{2p}U_{2m} + \mathbf{i}c_{m3}\Omega & \frac{9\mu}{4}U_{2p}^2 \\ -\frac{9\mu}{4}U_{2m}^2 & -\left(\omega_{n3}^2 - \Omega^2 + \frac{9\mu}{2}U_{2p}U_{2m}\right) + \mathbf{i}c_{m3}\Omega \end{bmatrix}. \quad (4.52)$$

Then the eigenvalues, λ , for $\mathbf{F}_{\mathbf{U}_3}$ may be found from

$$\lambda^2 + B\lambda + C = 0, \quad (4.53)$$

where,

$$B = c_{m3}, \quad (4.54a)$$

$$C = \frac{(\Omega^2 - \omega_{n3}^2)^2 - 9\mu U_2^2(\Omega^2 - \omega_{n3}^2) + \frac{243}{16}U_2^4 + (c_{m3}\Omega)^2}{4\Omega^2}. \quad (4.54b)$$

The solutions of Eq. (4.53) may be written as,

$$\lambda = \frac{-B \pm \sqrt{B^2 - 4C}}{2}. \quad (4.55)$$

Similar to the discussion for the Duffing oscillator in §3.5.2, the bifurcation happens when the eigenvalues are on the imaginary axis, which finally leads to $C = 0$. Hence, equating Eq. (4.54b) to zero and rearranging it gives

$$243\mu^2 U_2^4 + 144\mu(\omega_{n3}^2 - \Omega^2)U_2^2 + 16[(\omega_{n3}^2 - \Omega^2)^2 + (c_{m3}\Omega)^2] = 0, \quad (4.56)$$

which describes the locus of points where the modal interaction may occur. Combining Eqs. (4.50) and (4.56), it may allow us to find the number and positions of their intersection points. To ensure the solutions are physically reasonable, only the intersection points at $U_i > 0$ and $\Omega > 0$ are considered. Those points are secondary bifurcation points that can be used to predict the onset of the modal interaction. There are three possible cases:

- (i) if zero or one (for the special case) intersection point, there will be no modal interaction, e.g. Fig. 4.7(a).
- (ii) if two or three (for the special case) intersection points, the double-mode response caused by the modal interaction following the in-unison backbone curves will exist, e.g. Fig. 4.7(b).
- (iii) if four intersection points, both the double-mode response corresponding to the in-unison and out-of-unison backbone curves will occur, e.g. Fig. 4.7(c).

Fig. 4.7 shows the curves of Eq. (4.49) (green line) and Eq. (4.56) (red line) with the same parameter values of the softening nonlinear system depicted in Fig. 4.6 and their intersection points are marked by red dots. For comparison, the numerically calculated response curves (black) in Fig. 4.5 are also shown here. From Fig. 4.6, it can be seen that the single-mode response curve results approximated using the normal form technique and those numerically calculated are in good agreement. Besides, the intersections of Eqs. (4.49) and (4.56) are very close to the numerically predicted secondary bifurcation points for every case. The observation implies that the normal form technique is capable to detect the occurrence of modal interaction and identify the position of bifurcation points.

Furthermore, for the situation where only the third mode is externally forced, the same analysis can be applied to find the bifurcation points at the single-mode response curve

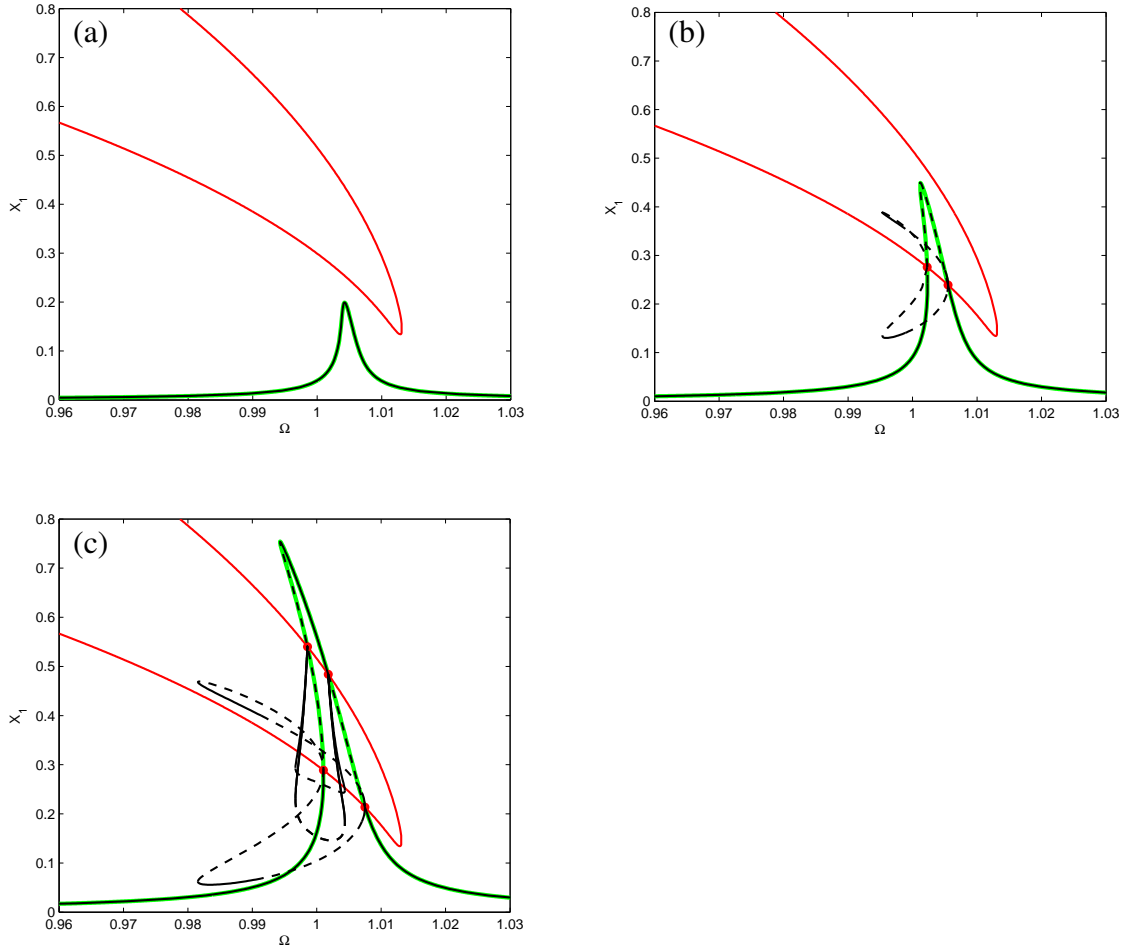


Fig. 4.7 The intersections between the forced response curve of the first mass, Eq. (4.56) and the stability boundary, Eq. (4.49), of the 3-DoF system depicted in Fig. 4.1 when only its second mode is forced at three different amplitudes. The parameters used are the same as those in Fig. 4.6. The green and red lines represent the forced response curve and stability boundary respectively. The red dots mark the intersection points. The solid- and dashed-black lines represent the stable and unstable forced response results numerically computed.

composed of only u_3 . This leads to two equations, i.e.

$$2187\mu^2 U_3^4 - 432\mu(\Omega^2 - \omega_{n2}^2)U_3^2 + 16[(\Omega^2 - \omega_{n2}^2)^2 + (c_{m2}\Omega)^2] = 0, \quad (4.57)$$

and

$$6561\mu^2 U_3^6 + 648\mu(\omega_{n3}^2 - \Omega^2)U_3^4 + 16[(\omega_{n3}^2 - \Omega^2)^2 + (c_{m3}\Omega)^2] U_3^2 = 16P_{m3}^2, \quad (4.58)$$

which describe the trajectory of secondary bifurcation points and the relationship between force and response amplitudes respectively. Similarly, combining Eqs. (4.57) and (4.58) to find the position and number of their intersection points, we can predict the occurrence of modal interaction for the third-mode-forced-only situation. Fig. 4.8 shows the position relationship between these two curves of the example system of softening nonlinear springs. Two force amplitudes are considered: $P_{m3} = 0.5 \times 10^{-3}$ and $P_{m3} = 1.0 \times 10^{-3}$. The intersection points are marked by red dots. The corresponding backbone curves $S3$ and $D23_{[o]}^{\pm}$ in Fig. 4.4 and response curves computed using COCO are also shown to make the comparison.

For these two forced situations, there is no intersection point in Fig. 4.8(a), and two intersection points in Fig. 4.8(b) between curves of Eqs. (4.57) and (4.58) respectively. As expected, there is no double-mode response in Fig. 4.8(a). In Fig. 4.8(b), it can be seen that the double-mode response curves following $D23_{[o]}^{\pm}$ emanate from the single-mode response curve from the intersection points. Here, the maximum number of the intersection points between the primary response curve of the third mode, Eq. (4.58), and the curve of Eq. (4.57) is two within the frequency range of interest. This means that only one kind of double-mode response, which is the one following $D23_{[o]}^{\pm}$ shown in the results, may occur when the third mode of the system is externally forced. This is also in agreement with the observation of the backbone curve results that only a pair of out-of-unison resonant backbone curves $D23_{[o]}^{\pm}$ emanate from $S3$.

4.5 Summary

In this chapter, we considered a specific 3-DoF system with cubic stiffness nonlinearity to investigate the modal interaction involving a subset of modes of nonlinear systems of multiple degrees of freedom. Due to the bilateral symmetry of the example system structure, one of its vibration modes is linearly independent, which makes the modal interaction only happen between the other two modes. It is noteworthy that a more common reason why the resonant modal interaction is limited to a subset of vibration modes of the nonlinear multi-DoF system is that no corresponding resonant cross-coupling term exists given the specific commensurable natural frequencies, and an example of this case is shown in Appendix B.

In §4.2, through the application of the direct normal form technique to example system under forcing and damping, the time-invariant equations describing the relationship between the external forcing and fundamental modal response were derived. These equations were found to be difficult to solve due to the existence of pairwise interacting terms. There-

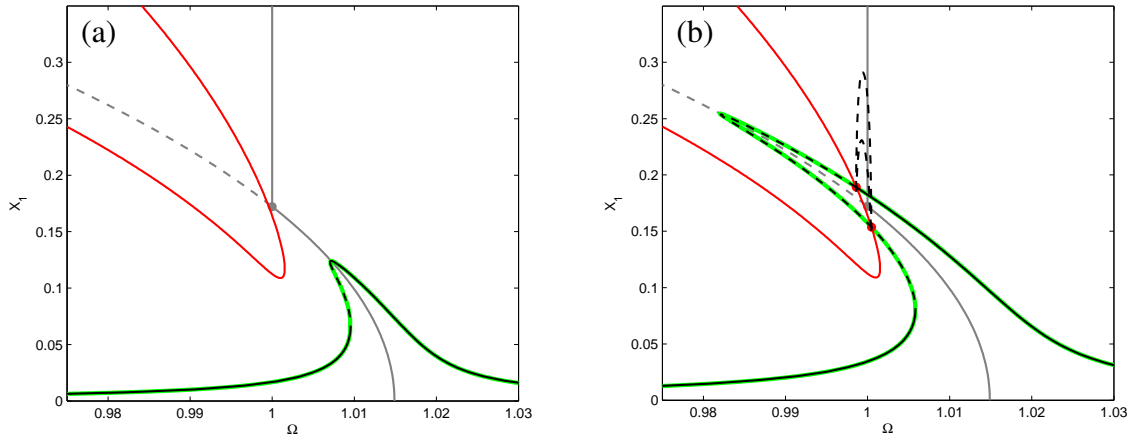


Fig. 4.8 The intersections between the forced response curve of the first mass, Eq. (4.57) and the stability boundary, Eq. (4.58), of the 3-DoF system depicted in Fig. 4.1 when only its third mode is forced at two different amplitudes. The system parameters used are the same as those in Fig. 4.4 and the force amplitudes are (a) $P_{m3} = 0.5 \times 10^{-3}$ and (b) $P_{m3} = 1.0 \times 10^{-3}$. The green and red lines represent the forced response curve and stability boundary respectively. The red dots mark the intersection points. The solid- and dashed-black lines represent the stable and unstable forced response results numerically computed. The grey lines represent the backbone curves.

fore, the terms relating to forcing and damping were removed for considering the backbone curves of the underlying conservative system instead.

It has been shown, in §4.3.1, that the nonlinear stiffness would affect the occurrence of the modal interaction. For the system considered in this chapter, only if its nonlinear stiffness constant of the coupling springs is negative, bifurcations would occur on the single-mode backbone curves which lead to additional double-mode backbone curves. Based on the phase differences between the two involved modes, the double-mode backbone curves may be classified into two types, i.e. in-unison backbone curves where both modes reach their maximum and zero simultaneously, and out-of-unison backbone curves where one mode reaches its peak while the other one is zero. The occurrence of these modal interaction has made the number of backbone curves much more than that of the system degrees of freedom, which also illustrates the complexity of the systems with nonlinearly coupled modes. In §4.3.2, the stability of the single-mode backbone curves has been considered, and the results have shown that the bifurcations points are precisely where the stability of these backbone curves changes.

The forced-response curves are compared with the backbone curves in §4.4.1 and it has

been shown that both the structure and stability of the backbone curves are analogous to the forced responses. For the hardening case where no bifurcation on the single-mode backbone curves occur, the forcing scenario where all three modes of the system are simultaneously forced has been used. The results have shown that as with backbone curves no modal interaction occurs and three ‘witch-hat’ shaped response curves respectively surround the three primary backbone curves in the vicinity of their corresponding linear natural frequencies.

When the nonlinear springs were assumed softening, it has been shown that the backbone curves can precisely capture the behaviour of the forced responses for the single-mode-forced situation. More specifically, the modal interaction type and their occurring sequence from the single-mode response curves are in agreement with those of the backbone curves. Based on the observation, it has enabled us to locate the bifurcations on the single-mode forced-response curves, combined with the knowledge of backbone curves, to predict the modal interaction for a nonlinear system under a specific excitation.

Throughout this chapter, we have seen that due to the feature of the underlying linear structure, e.g. bilaterally symmetric, only $N - i$ modes may resonantly interact with each other in a N -DoF nonlinear system so that sub-modal-structures may be separately studied instead of the whole system to reduce the problem complexity. While for some other situations where all of the nonlinear system vibration modes may be involved in the resonant interaction, N nonlinear modes have to be considered together and this case will be studied in the next chapter.

Chapter 5

N modal interaction of nonlinear multi-degree-of-freedom systems

In this chapter we:

- Develop analytical models of the backbone curves of the general 3-DoF oscillator with cubic nonlinear springs.
- Compute the backbone curves of an example nonlinear oscillator of 1 : 1 : 1 resonant modal interaction.
- Find the relationship between the backbone curves and forced-response curves when the 1 : 1 : 1 resonant interaction may occur.
- Investigate the bifurcation feature of the triple-mode response caused by the nonlinear resonant interaction.
- Study the auto-parametric resonant interaction among multiple modes using backbone curves by considering an example system of the approximated 1 : 2 : 3 linear natural frequency ratio.

5.1 Introduction

As discussed in Chapter 4, because of the characteristic of the underlying linear structure, $N - i$ modes of N -DoF nonlinear systems may be involved in a resonant interaction. This feature may allow us to analyse the system using subsystems composing of the interacted $N - i$ modes for some specific excitation scenarios, e.g. single mode forced. While, for some

engineering systems, e.g. periodically symmetric structures like the blade disc component of gas turbines, all considered modes formulating the analytical model of the nonlinear system may resonantly interact with each other. Therefore, it may make us have to consider all the N modes of the nonlinear system together.

In this chapter, we investigate the dynamic behaviour of nonlinear systems whose N modes may be involved in the resonant interaction. As presented in the last chapter, the backbone curves of the underlying unforced, undamped system enable us to largely simplify the computation, accurately predict the resonant modal interaction and precisely explain the system forced response features. Therefore, the backbone curve is used as the primary tool throughout this chapter.

Firstly in §5.2, the direct normal form technique is applied to a generic conservative 3-DoF lumped mass system with cubic springs for the development of a backbone curve model. In this model, the conditionally resonant terms decided by the fundamental response frequencies are examined because of their effect on the resonant interaction which is presented in later sections.

In §5.3, an example nonlinear 3-DoF system with a geometrically symmetric structure is specifically designed to have three nonlinear coupled modes of similar natural frequencies, which is to investigate the $1 : 1 : 1$ resonant interaction. The developed generic backbone curve model is used to find the time-invariant equations describing the response amplitude and frequencies for this specific system. The existence of backbone solutions including the contributions of single, double and triple nonlinear mode(s) are theoretically analysed alongside a discussion about the effect of the phase differences. Then specific parameters values of the system are chosen to calculate the backbone curve results for hardening and softening cases respectively to demonstrate the occurrence and effects of the resonant interaction. The numerical forced response results are then used to validate the backbone curves once again.

In §5.4, the generic 3-DoF system is specifically designed to have three coupled nonlinear modes with commensurable natural frequencies, i.e. $1 : 2 : 3$ relations, for studying the auto-parametric resonant interaction among multiple modes. The backbone curve expressions for this auto-parametric resonant case are found and the results presented show that due to the multi-mode interaction, the preconceived non-resonant modes may also interact.

5.2 Backbone curve model of the generic 3-DoF system with cubic nonlinear springs

To better explore the resonant interaction among N ($N \geq 3$) modes, a generic nonlinear 3-DoF oscillator with cubic springs is considered to develop a backbone curve model. The schematic of the generic nonlinear 3-DoF system is shown in Fig. 5.1. This system consists of three lumped masses, m_i , where $i = 1, 2, 3$, and each individual is grounded via a viscous damper, of damping constant c_i , and a nonlinear spring, of linear stiffness, k_i , and cubic nonlinear stiffness, κ_i . Additionally, three nonlinear springs connect individual pair of the three masses, whose linear and nonlinear constant are $k_{i,i+1}$ and $\kappa_{i,i+1}$. Note that $k_{31} = k_{34} = k_{13}$ and $\kappa_{31} = \kappa_{34} = \kappa_{13}$. The elastic force characteristics of these nonlinear springs are $F = k(\Delta x) + \kappa(\Delta x)^3$ where Δx is the deflection of the spring, and k and κ denote the linear and nonlinear constants respectively. Besides, the damper between each of the masses is linear of constant $c_{i,i+1}$. The three masses of the oscillator are forced sinusoidally at the same frequency Ω with amplitudes P_i and have displacement responses x_i .

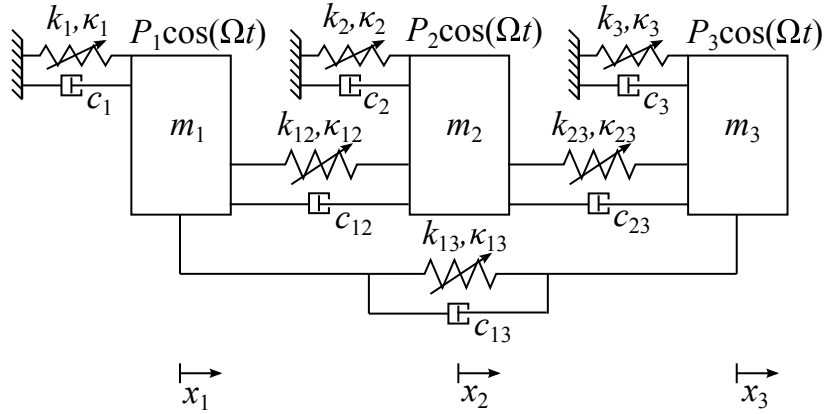


Fig. 5.1 A schematic diagram of the generic, in-line, lumped-mass 3-DoF system with cubic nonlinear springs.

The EoM of this nonlinear 3-DoF system, in the physical displacement coordinate x_i , is written as

$$m_i \ddot{x}_i + c_i \dot{x}_i + k_i x_i + k_{i-1,i} (x_i - x_{i-1}) + k_{i,i+1} (x_i - x_{i+1}) + \kappa_i x_i^3 + \kappa_{i-1,i} (x_i - x_{i-1})^3 + \kappa_{i,i+1} (x_i - x_{i+1})^3 = P_i \cos(\Omega t), \quad (5.1)$$

where $i = 1, 2, 3$, $k_{01} = k_{34} = k_{13}$ and $\kappa_{01} = \kappa_{34} = \kappa_{13}$. To compute the backbone curves of this system, the EoM of the equivalent conservative system must be considered. Hence, Eq. (5.1) is written in an unforced and undamped form, as Eq. (3.71), which is shown again

here

$$\mathbf{M}\ddot{\mathbf{x}} + \mathbf{K}\mathbf{x} + \varepsilon\mathbf{N}_x(\mathbf{x}) = 0, \quad (5.2)$$

where the linear stiffness matrix and nonlinear terms vector for this nonlinear system are

$$\mathbf{K} = \begin{bmatrix} k_1 + k_{12} + k_{13} & -k_{12} & -k_{13} \\ -k_{12} & k_2 + k_{12} + k_{23} & -k_{23} \\ -k_{13} & -k_{23} & k_3 + k_{13} + k_{23} \end{bmatrix}, \quad (5.3a)$$

$$\mathbf{N}_x(\mathbf{x}) = \begin{pmatrix} \kappa_1 x_1^3 + \kappa_{13}(x_1 - x_3)^3 + \kappa_{12}(x_1 - x_2)^3 \\ \kappa_2 x_2^3 + \kappa_{12}(x_2 - x_1)^3 + \kappa_{23}(x_2 - x_3)^3 \\ \kappa_3 x_3^3 + \kappa_{23}(x_3 - x_2)^3 + \kappa_{13}(x_3 - x_1)^3 \end{pmatrix}. \quad (5.3b)$$

Following the application steps of the direct normal form technique, the linear modal transform is firstly applied to Eq. (5.2) to find the EoM in linear modal displacements, \mathbf{q} , in the form of Eq. (3.72), as

$$\ddot{\mathbf{q}} + \mathbf{\Lambda}\mathbf{q} + \varepsilon\mathbf{N}_q(\mathbf{q}) = 0. \quad (5.4)$$

The linear natural frequencies matrix, $\mathbf{\Lambda}$, and modeshape matrix, $\mathbf{\Phi}$, used in the linear modal transform is found via solving the eigenvalue problem, given in Eq. (3.5). The nonlinear terms vector, \mathbf{N}_q , is then found using Eq. (3.9). As multiple unspecific coefficient parameters are involved, i.e. m , k and κ , the expressions of elements in \mathbf{N}_q is highly complex so that may not be written explicitly. While considering the specific nonlinearity type of the 3-DoF oscillator, i.e. cubic, and the linear transform not changing the order of the polynomial terms in the EoM, the vector of nonlinear terms, \mathbf{N}_q , may be written in the form as

$$\mathbf{N}_q = [n_q] \mathbf{q}^*, \quad (5.5)$$

where \mathbf{q}^* is a $\{10 \times 1\}$ vector of all unique third-power polynomial combinations of q_i and

$[n_q]$ is a $\{3 \times 10\}$ matrix of the corresponding coefficients, which may be written

$$\mathbf{q}^* = \begin{pmatrix} q_1^3 \\ q_1 q_2^2 \\ q_1 q_3^2 \\ q_1^2 q_2 \\ q_2^3 \\ q_2 q_3^2 \\ q_1^2 q_3 \\ q_2^2 q_3 \\ q_3^3 \\ q_1 q_2 q_3 \end{pmatrix}, \quad [n_q]^\top = \begin{bmatrix} \alpha_1^{[1]} & \alpha_1^{[2]} & \alpha_1^{[3]} \\ \alpha_2^{[1]} & \alpha_2^{[2]} & \alpha_2^{[3]} \\ \alpha_3^{[1]} & \alpha_3^{[2]} & \alpha_3^{[3]} \\ \alpha_4^{[1]} & \alpha_4^{[2]} & \alpha_4^{[3]} \\ \alpha_5^{[1]} & \alpha_5^{[2]} & \alpha_5^{[3]} \\ \alpha_6^{[1]} & \alpha_6^{[2]} & \alpha_6^{[3]} \\ \alpha_7^{[1]} & \alpha_7^{[2]} & \alpha_7^{[3]} \\ \alpha_8^{[1]} & \alpha_8^{[2]} & \alpha_8^{[3]} \\ \alpha_9^{[1]} & \alpha_9^{[2]} & \alpha_9^{[3]} \\ \alpha_0^{[1]} & \alpha_0^{[2]} & \alpha_0^{[3]} \end{bmatrix}, \quad (5.6)$$

where the superscript, $[i]$, of the elements in matrix $[n_q]$ denotes the related mode.

As no force is applied to the conservative system, the following forcing transform step of the direct normal form technique is omitted for the backbone curve case. Considering the force transform in §4.2 where the linear natural frequencies were discussed to obtain the force transform matrix, this simplification is also one of the significant advantages of considering backbone curves to investigate systems of multiple degrees of freedom.

The final step is the nonlinear near-identity transform which leads to the resonant EoM, written as

$$\ddot{\mathbf{u}} + \Lambda \mathbf{u} + \varepsilon \mathbf{N}_u(\mathbf{u}) = 0. \quad (5.7)$$

For the level of accuracy ε^1 considered here, it is known that we have the relationship

$$[n_{q(1)}] \mathbf{u}_{(1)}^*(\mathbf{u}_p, \mathbf{u}_m) = \mathbf{n}_{q(1)}(\mathbf{u}) = \mathbf{N}_q(\mathbf{u}). \quad (5.8)$$

Substituting $\mathbf{q} = \mathbf{u}$ into Eq. (5.6) and using

$$\begin{aligned} u_i^3 &= (u_{ip} + u_{im})^3 \\ &= (u_{ip}^3 + u_{im}^3) + 3(u_{ip}^2 u_{im} + 3u_{ip} u_{im}^2), \end{aligned} \quad (5.9a)$$

$$\begin{aligned} u_i^2 u_j &= (u_{ip} + u_{im})^2 (u_{jp} + u_{jm}) \\ &= (u_{ip}^2 u_{jp} + u_{im}^2 u_{jm}) + 2(u_{ip} u_{im} u_{jp} + u_{ip} u_{im} u_{jm}) + (u_{ip}^2 u_{jm} + u_{im}^2 u_{jp}), \end{aligned} \quad (5.9b)$$

$$\begin{aligned}
u_i u_j u_k &= (u_{ip} + u_{im}) (u_{jp} + u_{jm}) (u_{kp} + u_{km}) \\
&= (u_{ip} u_{jp} u_{kp} + u_{im} u_{jm} u_{km}) + (u_{ip} u_{jp} u_{km} + u_{im} u_{jm} u_{kp}) \\
&\quad + (u_{ip} u_{jm} u_{kp} + u_{im} u_{jp} u_{km}) + (u_{im} u_{jp} u_{kp} + u_{ip} u_{jm} u_{km}),
\end{aligned} \tag{5.9c}$$

the polynomial terms vector $\mathbf{u}_{(1)}^*$ may be obtained. Then using Eq. (3.75) and Eq. (3.52), the coefficient matrix $[n_{q(1)}]$ and resonant term index matrix $\boldsymbol{\beta}_{(1)}$ may be computed. Here notations describing the relationship of the modal response frequencies are defined, written as

$$r = \frac{\omega_{r2}}{\omega_{r1}} \quad \text{and} \quad \bar{r} = \frac{\omega_{r3}}{\omega_{r1}}. \tag{5.10}$$

The elements of $\mathbf{u}_{(1)}^*$, $[n_{q(1)}]$ and $\boldsymbol{\beta}_{(1)}$ of the generic nonlinear 3-DoF oscillator depicted in Fig. 5.1 are defined in Eq. (5.16). It can be seen that elements in the i^{th} row of $\boldsymbol{\beta}_{(1)}$ corresponding to some polynomial terms in $\mathbf{u}_{(1)}^*$, i.e. $u_{ip} u_{jp} u_{jm}$ and $u_{im} u_{jp} u_{jm}$, must be zero. This means that these terms must be retained in the resonant EoM without being affected by the relationship of modal response frequencies, i.e. r and \bar{r} , so that they are denoted to be *unconditionally resonant*. Besides, there are also other nonlinear terms that are conditionally resonant based on the response relationship. For example, e.g. $u_{1p} u_{2m}^2$ and $u_{1m} u_{2p}^2$ may be a pair of resonant terms for the first mode when $r = 1$. Therefore, it may allow us to write the vector of resonant nonlinear terms as

$$\mathbf{N}_u = \mathbf{N}_{[uc]} + \mathbf{N}_{[cd]}, \tag{5.11}$$

where $\mathbf{N}_{[uc]}$ and $\mathbf{N}_{[cd]}$ are the vectors of unconditionally and conditionally resonant nonlinear terms respectively. Writing $N_{[uc],i}$ and $N_{[cd],i}$ in the form of Eq. (3.54) to find the complex conjugate coefficients and then substituting into Eq. (3.56) gives

$$(\omega_{ni}^2 - \omega_{ri}^2) \frac{U_i}{2} e^{\mp i\phi_i} + N_{[uc],i}^{\pm} + N_{[cd],i}^{\pm} = 0. \tag{5.12}$$

Using Eq. (5.16), it can be concluded that the unconditional resonant terms for the i^{th} mode of a 3-DoF system of cubic stiffness nonlinearity may be written as

$$N_{[uc],i} = (u_{ip} + u_{im}) \left[2\alpha_{3i-2}^{[i]} u_{1p} u_{1m} + 2\alpha_{3i-1}^{[i]} u_{2p} u_{2m} + 2\alpha_{3i}^{[i]} u_{3p} u_{3m} + \alpha_{4i-3}^{[i]} u_{ip} u_{im} \right], \tag{5.13}$$

which may be used to find

$$N_{[uc],i}^{\pm} = \frac{1}{8} \left(2\alpha_{3i-2}^{[i]} U_1^2 + 2\alpha_{3i-1}^{[i]} U_2^2 + 2\alpha_{3i}^{[i]} U_3^2 + \alpha_{4i-3}^{[i]} U_i^2 \right) U_i e^{\mp i\phi_i}. \quad (5.14)$$

Then the time-invariant equations of the system are obtained via substituting Eq. (5.14) into Eq. (5.12), i.e.

$$(\omega_{ni}^2 - \omega_{ri}^2) U_i + \frac{1}{4} U_i \left(2\alpha_{3i-2}^{[i]} U_1^2 + 2\alpha_{3i-1}^{[i]} U_2^2 + 2\alpha_{3i}^{[i]} U_3^2 + \alpha_{4i-3}^{[i]} U_i^2 \right) + 2N_{[cd],i}^{\pm} e^{\pm i\phi_i} = 0. \quad (5.15)$$

From the discussions in §4.2, we know that the modal response frequencies are related to their corresponding linear natural frequencies – also see the frequency detuning expression, Eq. (3.34). Hence, the system parameters, especially the linear ones like k and m , are required to be specified to find the conditionally resonant terms retained in N_{cd} then to be used for substitution of Eq. (5.15). In later sections, different specific linear parameters will be chosen to investigate the nonlinear dynamic behaviour caused by different nonlinear modal interactions.

5.3 1 : 1 : 1 modal interaction

Fig. 5.2 shows the specific 3-DoF nonlinear oscillating system considered in this section.

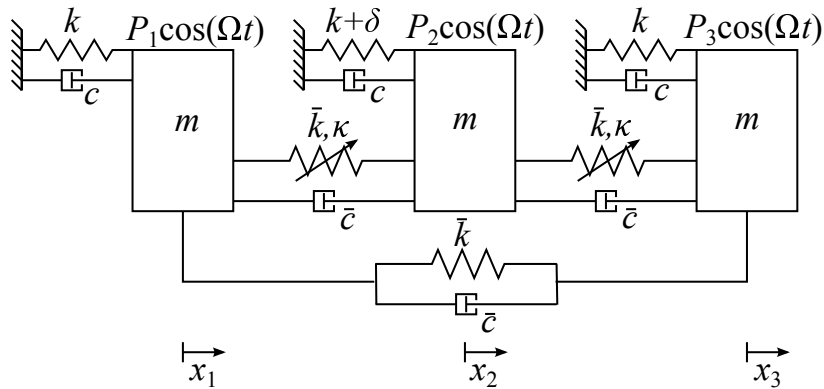


Fig. 5.2 A schematic diagram of an in-line, 3-DoF system with a mistuned periodically symmetric structure and cubic nonlinear springs. The three underlying modes of this system have similar linear natural frequencies and are nonlinearly coupled with each other such that the 1 : 1 : 1 modal interaction may occur.

The system is developed based on an ideal periodically symmetric version of the generic oscillator depicted in Fig. 5.1 that the linear grounding and nonlinear coupling springs and

$$\mathbf{u}_{(1)}^* = \begin{bmatrix} u_{1p}^3 \\ u_{1m}^3 \\ u_{1p}^2 u_{1m} \\ u_{1p} u_{1m}^2 \\ u_{1p} u_{2p}^2 \\ u_{1m} u_{2m}^2 \\ u_{1p} u_{2p} u_{2m} \\ u_{1m} u_{2p} u_{2m} \\ u_{1p} u_{2m}^2 \\ u_{1m} u_{2p}^2 \\ u_{1p} u_{3p}^2 \\ u_{1m} u_{3m}^2 \\ u_{1p} u_{3p} u_{3m} \\ u_{1m} u_{3p} u_{3m} \\ u_{1p} u_{3m}^2 \\ u_{1m} u_{3p}^2 \\ u_{1p}^2 u_{2p} \\ u_{1m}^2 u_{2m} \\ u_{1p} u_{1m} u_{2p} \\ u_{1p} u_{1m} u_{2m} \\ u_{1m}^2 u_{2p} \\ \vdots \end{bmatrix}, \quad [\mathbf{n}_{q(1)}]^\top = \begin{bmatrix} \alpha_1^{[1]} & \alpha_1^{[2]} & \alpha_1^{[3]} \\ \alpha_1^{[1]} & \alpha_1^{[2]} & \alpha_1^{[3]} \\ 3\alpha_1^{[1]} & 3\alpha_1^{[2]} & 3\alpha_1^{[3]} \\ 3\alpha_1^{[1]} & 3\alpha_1^{[2]} & 3\alpha_1^{[3]} \\ \alpha_2^{[1]} & \alpha_2^{[2]} & \alpha_2^{[3]} \\ \alpha_2^{[1]} & \alpha_2^{[2]} & \alpha_2^{[3]} \\ 2\alpha_2^{[1]} & 2\alpha_2^{[2]} & 2\alpha_2^{[3]} \\ 2\alpha_2^{[1]} & 2\alpha_2^{[2]} & 2\alpha_2^{[3]} \\ \alpha_2^{[1]} & \alpha_2^{[2]} & \alpha_2^{[3]} \\ \alpha_2^{[1]} & \alpha_2^{[2]} & \alpha_2^{[3]} \\ \alpha_3^{[1]} & \alpha_3^{[2]} & \alpha_3^{[3]} \\ \alpha_3^{[1]} & \alpha_3^{[2]} & \alpha_3^{[3]} \\ 2\alpha_3^{[1]} & 2\alpha_3^{[2]} & 2\alpha_3^{[3]} \\ 2\alpha_3^{[1]} & 2\alpha_3^{[2]} & 2\alpha_3^{[3]} \\ \alpha_3^{[1]} & \alpha_3^{[2]} & \alpha_3^{[3]} \\ \alpha_3^{[1]} & \alpha_3^{[2]} & \alpha_3^{[3]} \\ \alpha_4^{[1]} & \alpha_4^{[2]} & \alpha_4^{[3]} \\ \alpha_4^{[1]} & \alpha_4^{[2]} & \alpha_4^{[3]} \\ 2\alpha_4^{[1]} & 2\alpha_4^{[2]} & 2\alpha_4^{[3]} \\ 2\alpha_4^{[1]} & 2\alpha_4^{[2]} & 2\alpha_4^{[3]} \\ \alpha_4^{[1]} & \alpha_4^{[2]} & \alpha_4^{[3]} \\ \vdots & \vdots & \vdots \end{bmatrix}, \quad \boldsymbol{\beta}_{(1)}^\top = \omega_{r1}^2 \begin{bmatrix} 8 & 9-r^2 & 9-\bar{r}^2 \\ 8 & 9-r^2 & 9-\bar{r}^2 \\ 0 & 1-r^2 & 1-\bar{r}^2 \\ 0 & 1-r^2 & 1-\bar{r}^2 \\ (1+2r)^2-1 & (1+2r)^2-r^2 & (1+2r)^2-\bar{r}^2 \\ (1+2r)^2-1 & (1+2r)^2-r^2 & (1+2r)^2-\bar{r}^2 \\ 0 & 1-r^2 & 1-\bar{r}^2 \\ 0 & 1-r^2 & 1-\bar{r}^2 \\ (1-2r)^2-1 & (1-2r)^2-r^2 & (1-2r)^2-\bar{r}^2 \\ (1-2r)^2-1 & (1-2r)^2-r^2 & (1-2r)^2-\bar{r}^2 \\ (1+2\bar{r})^2-1 & (1+2\bar{r})^2-r^2 & (1+2\bar{r})^2-\bar{r}^2 \\ (1+2\bar{r})^2-1 & (1+2\bar{r})^2-r^2 & (1+2\bar{r})^2-\bar{r}^2 \\ 0 & 1-r^2 & 1-\bar{r}^2 \\ 0 & 1-r^2 & 1-\bar{r}^2 \\ (1-2\bar{r})^2-1 & (1-2\bar{r})^2-r^2 & (1-2\bar{r})^2-\bar{r}^2 \\ (1-2\bar{r})^2-1 & (1-2\bar{r})^2-r^2 & (1-2\bar{r})^2-\bar{r}^2 \\ (2+r)^2-1 & (2+r)^2-r^2 & (2+r)^2-\bar{r}^2 \\ (2+r)^2-1 & (2+r)^2-r^2 & (2+r)^2-\bar{r}^2 \\ r^2-1 & 0 & r^2-\bar{r}^2 \\ r^2-1 & 0 & r^2-\bar{r}^2 \\ (2-r)^2-1 & (2-r)^2-r^2 & (2-r)^2-\bar{r}^2 \\ \vdots & \vdots & \vdots \end{bmatrix}. \quad (5.16)$$

$$\mathbf{u}_{(1)}^* = \begin{pmatrix} \vdots \\ u_{1p}^2 u_{2m} \\ u_{2p}^3 \\ u_{2m}^3 \\ u_{2p}^2 u_{2m} \\ u_{2p} u_{2m}^2 \\ u_{2p} u_{3p}^2 \\ u_{2m} u_{3m}^2 \\ u_{2p} u_{3p} u_{3m} \\ u_{2m} u_{3p} u_{3m} \\ u_{2p} u_{3m}^2 \\ u_{2m} u_{3p}^2 \\ u_{1p}^2 u_{3p} \\ u_{1m}^2 u_{3m} \\ u_{1p} u_{1m} u_{3p} \\ u_{1p} u_{1m} u_{3m} \\ u_{1m}^2 u_{3p} \\ u_{1p}^2 u_{3m} \\ u_{2p}^2 u_{3p} \\ u_{2m}^2 u_{3m} \\ u_{2p} u_{2m} u_{3p} \\ u_{2p} u_{2m} u_{3m} \\ u_{2m}^2 u_{3p} \\ u_{2p}^2 u_{3m} \\ \vdots \end{pmatrix}, \quad [\mathbf{n}_{q(1)}]^\top = \begin{pmatrix} \vdots \\ \alpha_4^{[1]} & \alpha_4^{[2]} & \alpha_4^{[3]} \\ \alpha_5^{[1]} & \alpha_5^{[2]} & \alpha_5^{[3]} \\ \alpha_5^{[1]} & \alpha_5^{[2]} & \alpha_5^{[3]} \\ 3\alpha_5^{[1]} & 3\alpha_5^{[2]} & 3\alpha_5^{[3]} \\ 3\alpha_5^{[1]} & 3\alpha_5^{[2]} & 3\alpha_5^{[3]} \\ \alpha_6^{[1]} & \alpha_6^{[2]} & \alpha_6^{[3]} \\ \alpha_6^{[1]} & \alpha_6^{[2]} & \alpha_6^{[3]} \\ 2\alpha_6^{[1]} & 2\alpha_6^{[2]} & 2\alpha_6^{[3]} \\ 2\alpha_6^{[1]} & 2\alpha_6^{[2]} & 2\alpha_6^{[3]} \\ \alpha_6^{[1]} & \alpha_6^{[2]} & \alpha_6^{[3]} \\ \alpha_6^{[1]} & \alpha_6^{[2]} & \alpha_6^{[3]} \\ \alpha_7^{[1]} & \alpha_7^{[2]} & \alpha_7^{[3]} \\ \alpha_7^{[1]} & \alpha_7^{[2]} & \alpha_7^{[3]} \\ 2\alpha_7^{[1]} & 2\alpha_7^{[2]} & 2\alpha_7^{[3]} \\ 2\alpha_7^{[1]} & 2\alpha_7^{[2]} & 2\alpha_7^{[3]} \\ \alpha_7^{[1]} & \alpha_7^{[2]} & \alpha_7^{[3]} \\ \alpha_7^{[1]} & \alpha_7^{[2]} & \alpha_7^{[3]} \\ \alpha_8^{[1]} & \alpha_8^{[2]} & \alpha_8^{[3]} \\ \alpha_8^{[1]} & \alpha_8^{[2]} & \alpha_8^{[3]} \\ 2\alpha_8^{[1]} & 2\alpha_8^{[2]} & 2\alpha_8^{[3]} \\ 2\alpha_8^{[1]} & 2\alpha_8^{[2]} & 2\alpha_8^{[3]} \\ \alpha_8^{[1]} & \alpha_8^{[2]} & \alpha_8^{[3]} \\ \alpha_8^{[1]} & \alpha_8^{[2]} & \alpha_8^{[3]} \\ \vdots & \vdots & \vdots \end{pmatrix}, \quad \boldsymbol{\beta}_{(1)}^\top = \omega_{r1}^2 \begin{pmatrix} \vdots \\ (2-r)^2 - 1 & (2-r)^2 - r^2 & (2-r)^2 - \bar{r}^2 \\ 9r^2 - 1 & 8r^2 & 9r^2 - \bar{r}^2 \\ 9r^2 - 1 & 8r^2 & 9r^2 - \bar{r}^2 \\ r^2 & 0 & r^2 - \bar{r}^2 \\ r^2 & 0 & r^2 - \bar{r}^2 \\ (r+2\bar{r})^2 - 1 & (r+2\bar{r})^2 - r^2 & (r+2\bar{r})^2 - \bar{r}^2 \\ (r+2\bar{r})^2 - 1 & (r+2\bar{r})^2 - r^2 & (r+2\bar{r})^2 - \bar{r}^2 \\ r^2 - 1 & 0 & r^2 - \bar{r}^2 \\ r^2 - 1 & 0 & r^2 - \bar{r}^2 \\ (r-2\bar{r})^2 - 1 & (r-2\bar{r})^2 - r^2 & (r-2\bar{r})^2 - \bar{r}^2 \\ (r-2\bar{r})^2 - 1 & (r-2\bar{r})^2 - r^2 & (r-2\bar{r})^2 - \bar{r}^2 \\ (2+\bar{r})^2 - 1 & (2+\bar{r})^2 - r^2 & (2+\bar{r})^2 - \bar{r}^2 \\ (2+\bar{r})^2 - 1 & (2+\bar{r})^2 - r^2 & (2+\bar{r})^2 - \bar{r}^2 \\ \bar{r}^2 - 1 & \bar{r}^2 - r^2 & 0 \\ \bar{r}^2 - 1 & \bar{r}^2 - r^2 & 0 \\ (2-\bar{r})^2 - 1 & (2-\bar{r})^2 - r^2 & (2-\bar{r})^2 - \bar{r}^2 \\ (2-\bar{r})^2 - 1 & (2-\bar{r})^2 - r^2 & (2-\bar{r})^2 - \bar{r}^2 \\ (2r+\bar{r})^2 - 1 & (2r+\bar{r})^2 - r^2 & (2r+\bar{r})^2 - \bar{r}^2 \\ (2r+\bar{r})^2 - 1 & (2r+\bar{r})^2 - r^2 & (2r+\bar{r})^2 - \bar{r}^2 \\ \bar{r}^2 - 1 & \bar{r}^2 - r^2 & 0 \\ \bar{r}^2 - 1 & \bar{r}^2 - r^2 & 0 \\ (2r-\bar{r})^2 - 1 & (2r-\bar{r})^2 - r^2 & (2r-\bar{r})^2 - \bar{r}^2 \\ (2r-\bar{r})^2 - 1 & (2r-\bar{r})^2 - r^2 & (2r-\bar{r})^2 - \bar{r}^2 \\ \vdots & \vdots & \vdots \end{pmatrix}. \quad (5.16)$$

$$\mathbf{u}_{(1)}^* = \begin{bmatrix} \vdots \\ u_{3p}^3 \\ u_{3m}^3 \\ u_{3p}^2 u_{3m} \\ u_{3p} u_{3m}^2 \\ u_{1p} u_{2p} u_{3p} \\ u_{1m} u_{2m} u_{3m} \\ u_{1p} u_{2p} u_{3m} \\ u_{1m} u_{2m} u_{3p} \\ u_{1p} u_{2m} u_{3p} \\ u_{1m} u_{2p} u_{3m} \\ u_{1m} u_{2p} u_{3p} \\ u_{1p} u_{2m} u_{3m} \end{bmatrix}, \quad [\mathbf{n}_{q(1)}]^\top = \begin{bmatrix} \vdots & \vdots & \vdots \\ \alpha_9^{[1]} & \alpha_9^{[2]} & \alpha_9^{[3]} \\ \alpha_9^{[1]} & \alpha_9^{[2]} & \alpha_9^{[3]} \\ 3\alpha_9^{[1]} & 3\alpha_9^{[2]} & 3\alpha_9^{[3]} \\ 3\alpha_9^{[1]} & 3\alpha_9^{[2]} & 3\alpha_9^{[3]} \\ \alpha_0^{[1]} & \alpha_0^{[2]} & \alpha_0^{[3]} \end{bmatrix}, \quad \boldsymbol{\beta}_{(1)}^\top = \omega_{r1}^2 \begin{bmatrix} \vdots & \vdots & \vdots \\ 9\bar{r}^2 - 1 & 9\bar{r}^2 - r^2 & 8\bar{r}^2 \\ 9\bar{r}^2 - 1 & 9\bar{r}^2 - r^2 & 8\bar{r}^2 \\ \bar{r}^2 - 1 & \bar{r}^2 - r^2 & 0 \\ \bar{r}^2 - 1 & \bar{r}^2 - r^2 & 0 \\ (1+r+\bar{r})^2 - 1 & (1+r+\bar{r})^2 - r^2 & (1+r+\bar{r})^2 - \bar{r}^2 \\ (1+r+\bar{r})^2 - 1 & (1+r+\bar{r})^2 - r^2 & (1+r+\bar{r})^2 - \bar{r}^2 \\ (1+r-\bar{r})^2 - 1 & (1+r-\bar{r})^2 - r^2 & (1+r-\bar{r})^2 - \bar{r}^2 \\ (1+r-\bar{r})^2 - 1 & (1+r-\bar{r})^2 - r^2 & (1+r-\bar{r})^2 - \bar{r}^2 \\ (1-r+\bar{r})^2 - 1 & (1-r+\bar{r})^2 - r^2 & (1-r+\bar{r})^2 - \bar{r}^2 \\ (1-r+\bar{r})^2 - 1 & (1-r+\bar{r})^2 - r^2 & (1-r+\bar{r})^2 - \bar{r}^2 \\ (1-r-\bar{r})^2 - 1 & (1-r-\bar{r})^2 - r^2 & (1-r-\bar{r})^2 - \bar{r}^2 \\ (1-r-\bar{r})^2 - 1 & (1-r-\bar{r})^2 - r^2 & (1-r-\bar{r})^2 - \bar{r}^2 \end{bmatrix}. \quad (5.16)$$

grounding and coupling dampers are all identical. As with the system in Fig. 4.1, the linear stiffness of grounding springs is much larger than that of the coupling ones, and the nonlinear constant of the nonlinear spring is small. To slightly break the symmetry of the system structure, a small mistuning term δ is added to the stiffness of the grounding spring related to the second mass, and the nonlinear constant of coupling springs connecting the first and third masses is set to zero. Therefore,

$$\begin{aligned} k_1 = k, \quad k_2 = k + \delta, \quad k_3 = k, \quad k_{12} = \bar{k}, \quad k_{23} = \bar{k}, \quad k_{13} = \bar{k}, \\ \kappa_1 = 0, \quad \kappa_2 = 0, \quad \kappa_3 = 0, \quad \kappa_{12} = \kappa, \quad \kappa_{23} = \kappa, \quad \kappa_{13} = 0, \end{aligned} \quad (5.17)$$

where $\bar{k} \ll k$, $\kappa \ll k$ and $\delta \ll k$. Through substituting Eqs. (5.17) into Eqs. (5.3), the linear stiffness matrix and nonlinear term vectors for this system are written as

$$\mathbf{K} = \begin{bmatrix} k + 2\bar{k} & -\bar{k} & -\bar{k} \\ -\bar{k} & k + 2\bar{k} + \delta & -\bar{k} \\ -\bar{k} & -\bar{k} & k + 2\bar{k} \end{bmatrix}, \quad (5.18a)$$

$$\mathbf{N}_x(\mathbf{x}) = \kappa \begin{pmatrix} (x_1 - x_2)^3 \\ (x_2 - x_1)^3 + (x_2 - x_3)^3 \\ (x_3 - x_2)^3 \end{pmatrix}. \quad (5.18b)$$

Hence the matrix of linear modeshape is found to be

$$\Phi = \begin{bmatrix} 1 & 1 & 1 \\ a & 0 & b \\ 1 & -1 & 1 \end{bmatrix}, \quad (5.19)$$

where

$$a = -\frac{\delta + \bar{k} + \Delta}{2\bar{k}}, \quad b = -\frac{\delta + \bar{k} - \Delta}{2\bar{k}}, \quad \Delta^2 = (\delta + \bar{k})^2 + 8\bar{k}^2. \quad (5.20)$$

The modal natural frequencies are

$$\Lambda = \begin{bmatrix} 1 + \frac{1}{2}(\delta + 3\bar{k} - \Delta) & 0 & 0 \\ 0 & 1 + 3\bar{k} & 0 \\ 0 & 0 & 1 + \frac{1}{2}(\delta + 3\bar{k} + \Delta) \end{bmatrix} \quad (5.21)$$

and the coefficient matrix of modal nonlinear terms, $[n_q]$, is

$$[n_q]^T = \frac{\kappa}{b-a} \begin{bmatrix} (a-1)^3(b+2) & 0 & (1-a)^3(a+2) \\ 3(a-1)(b+2) & 0 & 3(1-a)(a+2) \\ 3(a-1)(b-1)^2(b+2) & 0 & 3(1-a)(1-b)^2(a+2) \\ 0 & 3(a-1)^2(a-b) & 0 \\ 0 & a-b & 0 \\ 0 & 3(b-1)^2(a-b) & 0 \\ 3(a-1)^2(b-1)(b+2) & 0 & 3(1-a)^2(1-b)(a+2) \\ 3(b-1)(b+2) & 0 & 3(1-b)(a+2) \\ (b-1)^3(b+2) & 0 & (1-b)^3(a+2) \\ 0 & 6(a-1)(b-1)(a-b) & 0 \end{bmatrix}. \quad (5.22)$$

Note that to simplify the symbol manipulation, $k = 1$ and $m = 1$ are used without the sacrifice of the problem generality.

As the assumption that $\bar{k} \ll k$ and $\delta \ll k$ has been made, the linear natural frequencies of this system are close, i.e. $\omega_{n1} : \omega_{n2} : \omega_{n3} \approx 1 : 1 : 1$, see Eq. (5.21); hence it is reasonable to assume that $\omega_{r1} = \omega_{r2} = \omega_{r3}$ when computing $\beta_{(1)}$. Therefore, the vector of the conditionally resonant nonlinear terms with non-zero coefficient under the condition that $r = \bar{r} = 1$ is found to be

$$\mathbf{N}_{[cd]} = \begin{pmatrix} \alpha_2^{[1]}(u_{1m}u_{2p}^2 + u_{1p}u_{2m}^2) + \alpha_3^{[1]}(u_{1m}u_{3p}^2 + u_{1p}u_{3m}^2) + 3\alpha_9^{[1]}u_{3p}u_{3m}u_3 \\ \alpha_4^{[2]}(u_{1p}^2u_{2m} + u_{1m}^2u_{2p}) + \alpha_6^{[2]}(u_{2m}u_{3p}^2 + u_{2p}u_{3m}^2) \\ \alpha_7^{[3]}(u_{1p}^2u_{3m} + u_{1m}^2u_{3p}) + \alpha_8^{[3]}(u_{2p}^2u_{3m} + u_{3m}^2u_{3p}) + 3\alpha_1^{[3]}u_1u_{1p}u_{1m} \\ + \alpha_7^{[1]}(u_{1p}^2u_{3m} + u_{1m}^2u_{3p} + 2u_{1p}u_{1m}u_3) + \alpha_8^{[1]}(u_{2p}^2u_{3m} + u_{2m}^2u_{3p} + 2u_{2p}u_{2m}u_3) \\ + \alpha_0^{[2]}(u_1u_{2p}u_{3m} + u_{1m}u_2u_{3p} + u_{1p}u_{2m}u_3) \\ + \alpha_2^{[3]}(u_{1p}u_{2m}^2 + u_{1m}u_{2p}^2 + 2u_1u_{2p}u_{2m}) + \alpha_3^{[3]}(u_{1p}u_{3m}^2 + u_{1m}u_{3p}^2 + 2u_1u_{3p}u_{3m}) \end{pmatrix}. \quad (5.23)$$

It can be seen that the number of the resonant cross-coupling terms retained is much more than that of the oscillator in Chapter 4. This suggests that the behaviour of the system considered in this chapter may be more complex. Then the time-invariant components of

Eq. (5.23) that corresponding to $e^{+i\omega_{rj}t}$ is obtained to be

$$N_{[cd],1}^+ = \frac{1}{8} e^{-i\phi_1} \left\{ \alpha_2^{[1]} U_1 U_2^2 e^{+i2\phi_{12}^d} + \alpha_3^{[1]} U_1 U_3^2 e^{-i2\phi_{31}^d} + 3\alpha_9^{[1]} U_3^3 e^{-i\phi_{31}^d} \right. \\ \left. + \alpha_7^{[1]} U_1^2 U_3 [e^{+i\phi_{31}^d} + 2e^{-i\phi_{31}^d}] + \alpha_8^{[1]} U_2^2 U_3 [e^{+i(\phi_{12}^d - \phi_{23}^d)} + 2e^{-i\phi_{31}^d}] \right\}, \quad (5.24a)$$

$$N_{[cd],2}^+ = \frac{1}{8} e^{-i\phi_2} \left\{ \alpha_4^{[2]} U_1^2 U_2 e^{-i2\phi_{12}^d} + \alpha_6^{[2]} U_2 U_3^2 e^{+i2\phi_{23}^d} \right. \\ \left. + \alpha_0^{[2]} U_1 U_2 U_3 [e^{+i\phi_{31}^d} + e^{-i(\phi_{12}^d - \phi_{23}^d)} + e^{-i\phi_{31}^d}] \right\}, \quad (5.24b)$$

$$N_{[cd],3}^+ = \frac{1}{8} e^{-i\phi_3} \left\{ \alpha_7^{[3]} U_1^2 U_3 e^{+i2\phi_{31}^d} + \alpha_8^{[3]} U_2^2 U_3 e^{-i2\phi_{23}^d} + 3\alpha_1^{[3]} U_1^3 e^{+i\phi_{31}^d} \right. \\ \left. + \alpha_2^{[3]} U_1 U_2^2 [e^{+i(\phi_{12}^d - \phi_{23}^d)} + 2e^{+i\phi_{31}^d}] + \alpha_3^{[3]} U_1 U_3^2 [e^{-i\phi_{31}^d} + 2e^{+i\phi_{31}^d}] \right\}, \quad (5.24c)$$

where $\phi_{12}^d = \phi_1 - \phi_2$, $\phi_{23}^d = \phi_2 - \phi_3$ and $\phi_{31}^d = \phi_3 - \phi_1$. Now using Eq. (5.15), the time-invariant resonant EoM for this specific nonlinear system may be written

$$(\omega_{n1}^2 - \omega_{r1}^2) U_1 + \frac{1}{4} \left[3\alpha_1^{[1]} U_1^2 + 2\alpha_2^{[1]} U_2^2 + 2\alpha_3^{[1]} U_3^2 \right] U_1 \\ + \frac{1}{4} \left[e^{+i2\phi_{12}^d} \alpha_2^{[1]} U_2^2 + e^{-i2\phi_{31}^d} \alpha_3^{[1]} U_3^2 + (e^{+i\phi_{31}^d} + 2e^{-i\phi_{31}^d}) \alpha_7^{[1]} U_1 U_3 \right] U_1 \\ + \frac{1}{4} \left[(e^{+i(\phi_{12}^d - \phi_{23}^d)} + 2e^{-i\phi_{31}^d}) \alpha_8^{[1]} U_2^2 U_3 + 3e^{-i\phi_{31}^d} \alpha_9^{[1]} U_3^3 \right] = 0, \quad (5.25a)$$

$$(\omega_{n2}^2 - \omega_{r2}^2) U_2 + \frac{1}{4} \left[2\alpha_4^{[2]} U_1^2 + 3\alpha_5^{[2]} U_2^2 + 2\alpha_6^{[2]} U_3^2 \right] U_2 \\ + \frac{1}{4} \left[e^{-i2\phi_{12}^d} \alpha_4^{[2]} U_1^2 + e^{+i2\phi_{23}^d} \alpha_6^{[2]} U_3^2 + \alpha_0^{[2]} (e^{+i\phi_{31}^d} + e^{-i(\phi_{12}^d - \phi_{23}^d)} + e^{-i\phi_{31}^d}) U_1 U_3 \right] U_2 = 0, \quad (5.25b)$$

$$(\omega_{n3}^2 - \omega_{r3}^2) U_3 + \frac{1}{4} \left[2\alpha_7^{[3]} U_1^2 + 2\alpha_8^{[3]} U_2^2 + 3\alpha_9^{[3]} U_3^2 \right] U_3 \\ + \frac{1}{4} \left[e^{+i2\phi_{31}^d} \alpha_7^{[3]} U_1^2 + e^{-i2\phi_{23}^d} \alpha_8^{[3]} U_3^2 + (e^{-i\phi_{31}^d} + 2e^{+i\phi_{31}^d}) \alpha_3^{[3]} U_1 U_3 \right] U_3 \\ + \frac{1}{4} \left[3e^{+i\phi_{31}^d} \alpha_1^{[3]} U_1^3 + (e^{+i(\phi_{12}^d - \phi_{23}^d)} + 2e^{+i\phi_{31}^d}) \alpha_2^{[3]} U_1 U_2^2 \right] = 0. \quad (5.25c)$$

From Eq. (5.25), it can be seen that the three modes of this system are nonlinearly coupled with each other as designed which may cause the nonlinear resonant interactions between (among) any three underlying modes. Furthermore, we may also observe that all the conditionally resonant terms result in the components related to the phase difference in the time-invariant equations. Based on the findings in Chapter 4, it may allow us to guess that

different types of backbone branches involving the same nonlinear modes may exist. Besides, the appearance of these phase-related terms is an essential condition of the occurrence of the resonant modal interaction, which will be discussed in Chapter 6. In the later subsections, we will calculate the backbone curve solutions for this system to investigate the effect of the three-mode modal interaction.

5.3.1 Calculation of backbone curves

From Eqs. (5.25), we know that the three underlying nonlinear modes of the 3-DoF system considered here may interact with each other due to the close linear natural frequencies and the coupled terms. Thus, the investigation of the backbone curve solutions of Eqs. (5.25) may be classified into three types based on the number of involved modes: single-, double- and triple-mode backbone curves. Note that the trivial solution of Eq. (5.25) corresponding to no motion, i.e. $U_1 = U_2 = U_3 = 0$, also exists for this system.

Firstly, we consider the single-mode backbone solution where the response of only one underlying mode is present. Similar to the analysis in Chapter 4, successfully equating the fundamental response amplitude of each nonlinear mode to non-zero and those of the other two to zero, the expressions of the single-mode backbone curves may be obtained.

To find backbone S1, $U_2 = U_3 = 0$ is substituted into Eq. (5.25), leading to

$$\omega_{r1}^2 = \omega_{n1}^2 + \frac{3}{4}\alpha_1^{[1]}U_1^2, \quad (5.26a)$$

$$\frac{3}{4}e^{+i\phi_{31}^d}\alpha_1^{[3]}U_1^3 = 0. \quad (5.26b)$$

These equations can be satisfied only if $U_1 = 0$ as $\alpha_1^{[3]} \neq 0$, see Eqs. (5.22) and (5.20). The similar result may be obtained when seeking backbone S3, i.e. Eqs. (5.25), with the substitution $U_1 = U_3 = 0$, turns out to be

$$\omega_{r3}^2 = \omega_{n3}^2 + \frac{3}{4}\alpha_3^{[3]}U_3^2 \quad (5.27a)$$

$$\frac{3}{4}e^{-i\phi_{31}^d}\alpha_3^{[3]}U_3^3 = 0, \quad (5.27b)$$

which can only be true if $U_3 = 0$. These findings suggest that the single-mode backbone solutions S1 and S3 do not physically exist for the system under consideration. When only the second mode is assumed active, substituting $U_1 = U_3 = 0$ into Eqs. (5.25) gives the

expression of backbone solution $S2$, written as

$$S2 : \quad U_2 \neq 0, U_1 = U_3 = 0, \quad \omega_{r2}^2 = \omega_{n2}^2 + \frac{3}{4}\alpha_5^{[2]}U_2^2. \quad (5.28)$$

Then, the solutions of double-mode backbone curves are explored. Based on the specific two activated modes without considering their phase differences, there may potentially exist three clusters of backbone branches labelled $D12$, $D23$ and $D13$. For backbone curves $D12$ where the first and second modes contribute to the response, substituting $U_3 = 0$ into Eqs. (5.25) gives

$$\omega_r^2 = \omega_{n1}^2 + \frac{3}{4}\alpha_1^{[1]}U_1^2 + \frac{1}{4}(2 + e^{+i\phi_{12}^d})\alpha_2^{[1]}U_2^2, \quad (5.29a)$$

$$\omega_r^2 = \omega_{n2}^2 + \frac{3}{4}\alpha_5^{[2]}U_2^2 + \frac{1}{4}(2 + e^{-i\phi_{12}^d})\alpha_4^{[2]}U_1^2, \quad (5.29b)$$

$$\left(\alpha_1^{[3]}U_1^2 + \alpha_2^{[3]}U_2^2\right)U_1 = 0, \quad (5.29c)$$

where $\omega_{r1} = \omega_{r2} = \omega_r$ has been used. It can be easily predicted that unless the coefficients $\alpha_1^{[3]} = \alpha_2^{[3]} = 0$ the solution of Eqs. (5.29) must be $U_1 = C_1$ and $U_2 = C_2$ where C_1 and C_2 are non-negative constants if real solutions exist, which finally leads to a single point instead of a curve on the amplitude-frequency plane. Similarly, it is also the case for backbone curves $D23$. Therefore, double-mode backbone curves $D12$ and $D23$ are regarded to be inexistent here. When only the first and third modes are assumed to be present which corresponds to backbone curves $D13$, substituting $U_2 = 0$ into Eqs. (5.25) leads to

$$\begin{aligned} (\omega_{n1}^2 - \omega_r^2) + \frac{3}{4}e^{-i\phi_{31}^d}\alpha_9^{[1]}\frac{U_3^3}{U_1} \\ + \frac{1}{4}\left[3\alpha_1^{[1]}U_1^2 + (2 + e^{-i2\phi_{31}^d})\alpha_3^{[1]}U_3^2 + (e^{+i\phi_{31}^d} + 2e^{-i\phi_{31}^d})\alpha_7^{[1]}U_1U_3\right] = 0, \end{aligned} \quad (5.30a)$$

$$\begin{aligned} (\omega_{n3}^2 - \omega_r^2) + \frac{3}{4}e^{+i\phi_{31}^d}\alpha_1^{[3]}\frac{U_1^3}{U_3} \\ + \frac{1}{4}\left[(2 + e^{+i2\phi_{31}^d})\alpha_7^{[3]}U_1^2 + 3\alpha_9^{[3]}U_3^2 + (e^{-i\phi_{31}^d} + 2e^{+i\phi_{31}^d})\alpha_3^{[3]}U_1U_3\right] = 0. \end{aligned} \quad (5.30b)$$

It can be seen that Eqs. (5.30) contain complex terms, which the imaginary components of Eqs. (5.30) may lead to

$$\left[\alpha_7^{[1]}U_1^2 + 2\alpha_3^{[1]}U_1U_3 \cos(\phi_{31}^d) + 3\alpha_9^{[1]}U_3^2\right] \sin(\phi_{31}^d) = 0, \quad (5.31a)$$

$$\left[3\alpha_1^{[3]}U_1^2 + 2\alpha_7^{[3]}U_1U_3 \cos(\phi_{31}^d) + \alpha_3^{[3]}U_3^2\right] \sin(\phi_{31}^d) = 0. \quad (5.31b)$$

These equations may be satisfied by $\sin(\phi_{31}^d) = 0$ such that $\phi_3 - \phi_1 = 0, \pi, 2\pi, \dots$, which correspond to the in-unison response. This may allow us to define a variable \bar{p}_{31} using

$$\bar{p}_{31} = e^{i|\phi_{31}^d|} = \begin{cases} +1 & \text{when } \phi_3 - \phi_1 = 0, 2\pi, \dots, \\ -1 & \text{when } \phi_3 - \phi_1 = \pi, 3\pi, \dots. \end{cases} \quad (5.32)$$

Therefore, the variable $p_{31} = e^{2i|\phi_{31}^d|}$ related to the two times of the modal phase difference, discussed in Chapter 4, could only be equal to one, i.e.

$$p_{31} = \bar{p}_{31}^2 = 1. \quad (5.33)$$

It implies that because of the existence of $e^{i|\phi_{31}^d|}$ in Eqs. (5.30), the phase difference between the first and third modes cannot be $\pm\pi/2$, so that the out-of-unison backbone curves $D13_{[o]}$ do not exist for this system. Now using Eqs. (5.32) and (5.33), Eqs. (5.30) may be rearranged to give

$$\begin{aligned} \alpha_9^{[1]} U_3^4 + \bar{p}_{13}(\alpha_3^{[1]} - \alpha_9^{[3]}) U_1 U_3^3 + (\alpha_7^{[1]} - \alpha_3^{[3]}) U_1^2 U_3^2 \\ + \bar{p}_{13}[(\alpha_1^{[1]} - \alpha_7^{[3]}) U_1^3 + \frac{4}{3}(\omega_{n1}^2 - \omega_{n3}^2) U_1] U_3 - \alpha_1^{[3]} U_1^4 = 0, \end{aligned} \quad (5.34)$$

which describes the response frequency and amplitude relationship of the first or third modes. From Eq. (5.34), it can be seen that U_1 is an explicit function of U_3 or other way around, i.e.

$$U_1 = \mathcal{F}_U(U_3) \quad \text{or} \quad U_3 = \mathcal{F}_U(U_1). \quad (5.35)$$

Then through rearranging anyone of Eqs. (5.30) with the substitution of Eq. (5.35), the response frequency may also be expressed as the function of response amplitudes, i.e.

$$\omega_r = \mathcal{F}_\omega(U_3) \quad \text{or} \quad \omega_r = \mathcal{F}_\omega(U_1). \quad (5.36)$$

Hence the backbone curves $D13_{[i]}$ may be symbolically expressed as

$$D13_{[i]}^\pm : \begin{cases} U_1 = \mathcal{F}_U(U_3), \\ \omega_r = \mathcal{F}_\omega(U_3), \end{cases} \quad \text{or} \quad \begin{cases} U_3 = \mathcal{F}_U(U_1), \\ \omega_r = \mathcal{F}_\omega(U_1). \end{cases} \quad (5.37)$$

Considering Eqs. (4.18) and (4.22), the expressions of the double-mode backbone curves of the nonlinear system in Chapter 4 are special cases of Eq. (5.37). It is noteworthy that Eq. (5.37) cannot ensure the existence of the backbone curve $D13_{[i]}^\pm$ as its valid solutions are

further decided by the coefficient values of nonlinear terms, i.e. $\alpha_\ell^{[i]}$.

Lastly, we investigate the existence of triple-mode backbone curves where the resonant interaction occurs among three nonlinear modes. As the presence of the phase terms may lead to complex components, we consider the imaginary components of Eq. (5.25b), written as

$$\alpha_4^{[2]} \sin(2\phi_{12}^d) U_1^2 - \alpha_6^{[2]} \sin(2\phi_{23}^d) U_3^2 + \alpha_0^{[2]} \sin(\phi_{12}^d - \phi_{23}^d) = 0, \quad (5.38)$$

which may only be satisfied by

$$\begin{cases} \phi_{12}^d = 0, \pi, \dots & \text{and} & \phi_{23}^d = 0, \pi, \dots & \text{therefore} & \phi_{31}^d = 0, \pi, \dots, \\ \phi_{12}^d = \frac{\pi}{2}, \frac{3\pi}{2}, \dots & \text{and} & \phi_{23}^d = \frac{\pi}{2}, \frac{3\pi}{2}, \dots & \text{therefore} & \phi_{31}^d = 0, \pi, \dots. \end{cases} \quad (5.39)$$

Therefore, two extra phase-related variables are defined as

$$p_{12} = e^{i2|\phi_{12}^d|} \quad \text{and} \quad p_{23} = e^{i2|\phi_{23}^d|}, \quad (5.40)$$

which makes Eq. (5.39) also be expressed as

$$\begin{cases} p_{12} = p_{23} = 1 & \text{and} & \bar{p}_{31} = \pm 1, \\ p_{12} = p_{23} = -1 & \text{and} & \bar{p}_{31} = \pm 1. \end{cases} \quad (5.41)$$

For the case where $p_{12} = p_{23} = 1$, Eqs. (5.25) may be rearranged to be

$$\begin{aligned} & (\alpha_1^{[1]} - \alpha_4^{[2]}) U_1^3 + (\alpha_2^{[1]} - \alpha_5^{[2]}) U_1 U_2^2 + \bar{p}_{13} \alpha_8^{[1]} U_2^2 U_3 + \bar{p}_{13} \alpha_9^{[1]} U_3^3 \\ & + (\alpha_3^{[1]} - \alpha_6^{[2]}) U_1 U_3^2 + \bar{p}_{13} (\alpha_7^{[1]} - \alpha_0^{[2]}) U_1^2 U_3 + \frac{4}{3} (\omega_{n1}^2 - \omega_{n2}^2) U_1 = 0, \end{aligned} \quad (5.42a)$$

$$\begin{aligned} & \bar{p}_{13} \alpha_1^{[3]} U_1^3 + \bar{p}_{13} \alpha_2^{[3]} U_1 U_2^2 + (\alpha_8^{[3]} - \alpha_5^{[2]}) U_2^2 U_3 + (\alpha_9^{[3]} - \alpha_6^{[2]}) U_3^3 \\ & + \bar{p}_{13} (\alpha_3^{[3]} - \alpha_0^{[2]}) U_1 U_3^2 + (\alpha_7^{[3]} - \alpha_4^{[2]}) U_1^2 U_3 + \frac{4}{3} (\omega_{n3}^2 - \omega_{n2}^2) U_3 = 0. \end{aligned} \quad (5.42b)$$

With treating anyone of the modal response amplitude U_i as the reference variable, Eq. (5.42) may be solved to find the solutions of the other two. For example, regarding U_2 as the reference, Eqs. (5.42) become a cubic equation set in U_1 and U_3 . Once the response amplitudes relationship has been found, the response frequency may be computed by substituting the amplitude solutions into one of Eqs. (5.25), e.g.

$$\omega_r^2 = \omega_{n2}^2 + \frac{3}{4} \left[\alpha_4^{[2]} U_1^2 + \alpha_5^{[2]} U_2^2 + \alpha_6^{[2]} U_3^2 + \alpha_0^{[1]} U_1 U_3 \right], \quad (5.43)$$

derived from rearranging Eq. (5.25b). These solutions correspond to the triple-mode backbone curves labelled $T123_{[i,i]}^{\pm,\pm}$, in which T stands for triple-mode and the subscripts denote the type of resonance interaction regarding the first mode listed and superscripts denote their phase differences.

For the case where $p_{12} = p_{23} = -1$, Eqs. (5.25) may be re-written to give the equations describing the relationship of the modal response amplitude as

$$(3\alpha_1^{[1]} - \alpha_4^{[2]})U_1^3 + (\alpha_2^{[1]} - 3\alpha_5^{[2]})U_1U_2^2 + 3\bar{p}_{13}\alpha_8^{[1]}U_2^2U_3 + 3\bar{p}_{13}\alpha_9^{[1]}U_3^3 + (3\alpha_3^{[1]} - \alpha_6^{[2]})U_1U_3^2 + 3\bar{p}_{13}(\alpha_7^{[1]} - \alpha_0^{[2]})U_1^2U_3 + 4(\omega_{n1}^2 - \omega_{n2}^2)U_1 = 0, \quad (5.44a)$$

$$3\bar{p}_{13}\alpha_1^{[3]}U_1^3 + 3\bar{p}_{13}\alpha_2^{[3]}U_1U_2^2 + (\alpha_8^{[3]} - 3\alpha_5^{[2]})U_2^2U_3 + (3\alpha_9^{[3]} - \alpha_6^{[2]})U_3^3 + 3\bar{p}_{13}(\alpha_3^{[3]} - \alpha_0^{[2]})U_1U_3^2 + (3\alpha_7^{[3]} - \alpha_4^{[2]})U_1^2U_3 + 4(\omega_{n3}^2 - \omega_{n2}^2)U_3 = 0, \quad (5.44b)$$

and Eq. (5.25b) may be arranged to give the response frequency equation as

$$\omega_r^2 = \omega_{n2}^2 + \frac{1}{4} \left[\alpha_4^{[2]}U_1^2 + 3\alpha_5^{[2]}U_2^2 + \alpha_6^{[2]}U_3^2 + 3\alpha_0^{[2]}U_1U_3 \right]. \quad (5.45)$$

Seeing Eqs. (5.41) and (5.39), we know the solution sets of Eqs. (5.44) and (5.45) correspond to the triple-mode backbone curve $T123_{[o,i]}^{\pm,\pm}$. In fact, we may guess that, in general, other two groups of triple-mode backbone curves, $T123_{[i,o]}^{\pm,\pm}$ and $T123_{[o,o]}^{\pm,\pm}$, may exist for systems with three nonlinearly coupled modes. However, for this system, because of the requirement of specific phase difference led by some conditionally resonant terms, these backbone solutions do not exist. The modal responses on the triple-mode backbone curves outlined above are shown in Fig. 5.3.

All these backbone curves in modal coordinates can be converted to the results of physical responses via the inverse transformations mentioned in Chapter 3. Similarly, as with Chapter 4, the harmonics are assumed small and so neglected. Using Eq. (5.19), the physical response amplitudes on each backbone curves may be written as

$$S2 : \begin{pmatrix} X_1 \\ X_2 \\ X_3 \end{pmatrix} = \begin{pmatrix} U_2 \\ 0 \\ U_2 \end{pmatrix}, \quad (5.46a)$$

$$D13_{[i]}^{\pm} : \begin{pmatrix} X_1 \\ X_2 \\ X_3 \end{pmatrix} = \begin{pmatrix} U_1 + U_3 \\ aU_1 + bU_3 \\ U_1 + U_3 \end{pmatrix}, \quad (5.46b)$$

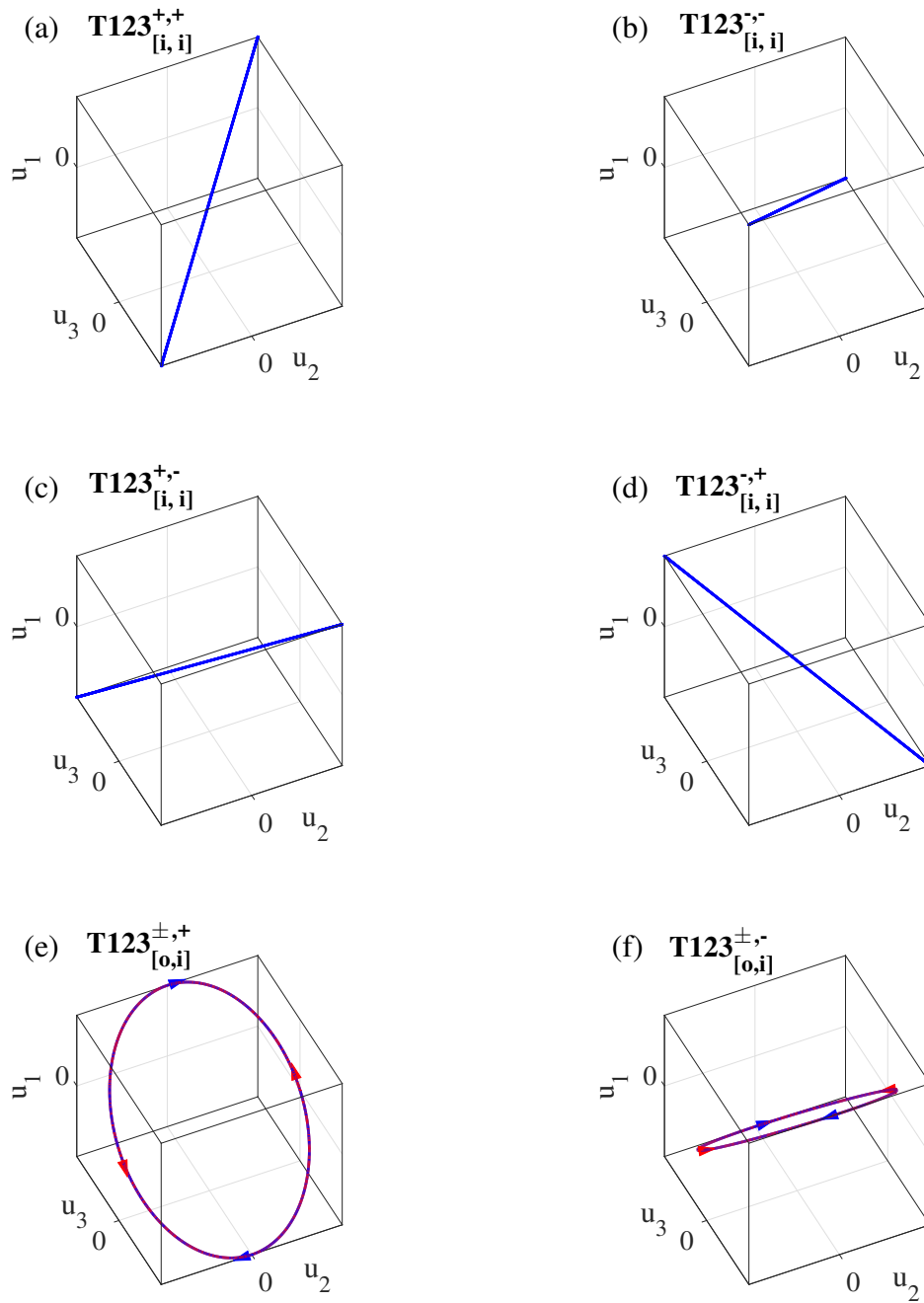


Fig. 5.3 The projection diagrams of u_1 against u_2 against u_3 of the response on the backbone curve branches: (a) $T123^{+,+}_{[i,i]}$, (b) $T123^{-,-}_{[i,i]}$, (c) $T123^{+,-}_{[i,i]}$, (d) $T123^{-,+}_{[i,i]}$, (e) $T123^{\pm,+}_{[o,i]}$ and (f) $T123^{\pm,-}_{[o,i]}$. The blue and red arrows in (e) and (f) denote the motion direction of $T123^{+,+}_{[o,i]}$ and $T123^{-,+}_{[o,i]}$, and $T123^{+,-}_{[o,i]}$ and $T123^{-,-}_{[o,i]}$ respectively.

$$T123_{[i,i]}^{\pm,\pm} : \begin{pmatrix} X_1 \\ X_2 \\ X_3 \end{pmatrix} = \begin{pmatrix} U_1 \pm_{(1)} U_2 \pm_{(2)} U_3 \\ aU_1 \pm_{(2)} bU_3 \\ U_1 \mp_{(1)} + U_2 \pm_{(2)} U_3 \end{pmatrix}, \quad (5.46c)$$

$$T123_{[o,i]}^{\pm,\pm} : \begin{pmatrix} X_1 \\ X_2 \\ X_3 \end{pmatrix} = \begin{pmatrix} \sqrt{(U_1 \pm_{(2)} U_3)^2 + U_2^2} \\ aU_1 \pm_{(2)} bU_3 \\ \sqrt{(U_1 \pm_{(2)} U_3)^2 + U_2^2} \end{pmatrix}, \quad (5.46d)$$

where the superscript of \pm denotes its corresponding sequential modal phase difference.

Now we choose specific values of the system parameters to compute the backbone curve results. Fig. 5.4 and Fig. 5.5 show the backbone curves for the hardening and softening cases respectively. All panels show the backbone curves plotted in the projection of response frequency against displacement amplitude. For both cases, the linear natural frequencies are $\omega_{n1} = 1.0025$, $\omega_{n2} = 1.0150$ and $\omega_{n3} = 1.0250$ where linear parameters are $k = 1$, $\bar{k} = 0.01$ and $\delta = 0.025$ and the cubic stiffness is $\kappa = \pm 0.025$ respectively. Also, the linear modeshapes are $\Phi_1 = [1, 0.5, 1]^T$, $\Phi_2 = [1, 0, 1]^T$ and $\Phi_3 = [1, -4, 1]^T$.

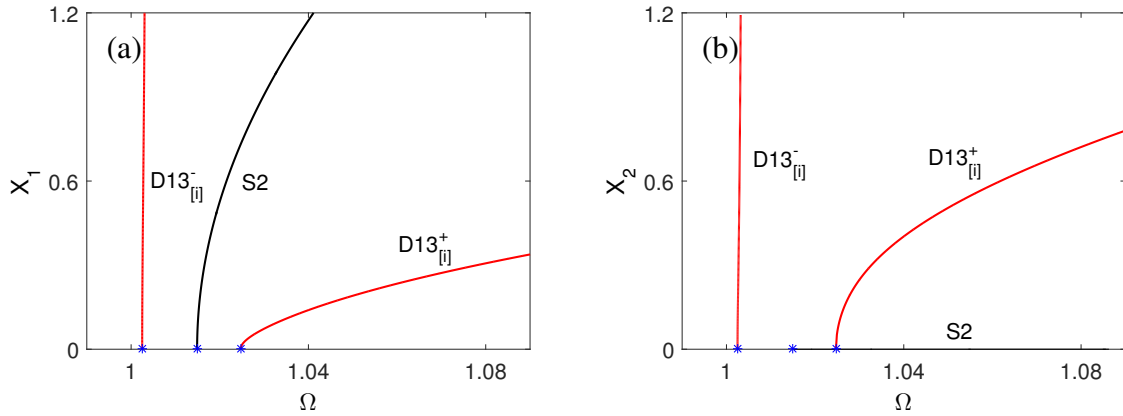


Fig. 5.4 The backbone curves of the 3-DoF system depicted in Fig. 5.2 with physical parameters $m = 1$, $k = 1$, $\bar{k} = 0.01$, $\delta = 0.025$ and $\kappa = 0.025$. Specific backbone curves are labelled respectively. The blue asterisks mark the system linear natural frequencies.

From Fig. 5.4, it can be seen that for the hardening situation there exist three backbone curves, i.e. one single-mode backbone curve, i.e. $S2$, and two double-mode backbone curves, $D13_{[i]}^{\pm}$. Note that due to the bilateral symmetry of the system structure, the backbone curves of the first and third masses are identical, also see Eqs. (5.46a) and (5.46b); thus the result of the third mass is omitted. In Fig. 5.4, all these backbone curves emerge from the response-frequency axis with the coordinates ω_{n1} , ω_{n2} and ω_{n3} respectively, which makes the double-

mode backbone curves seem to bifurcate from the trivial solution directly. This phenomenon is contrary to what has been observed in Chapter 4 where the double-mode backbone curves appear from the bifurcation points on the primary single-mode backbone curves. While considering the findings of Eqs. (5.26), we may also regard that the single-mode backbone curve $S1$ does exist but loses the stability at its starting point on the response-frequency axis, where $D13_{[i]}^-$ appears, due to the resonant modal interaction. Similarly, the behaviour of backbone curves $S3$ and $D13_{[i]}^+$ may also be explained in the same way. So the points where the double mode backbone curves of this example appear are co-dimension two bifurcations, i.e. one bifurcation on top of the other. Furthermore, this backbone curve behaviour also suggests that neither the first nor the third mode can be present alone under any circumstance as a resonant interaction between them must occur as long as anyone of them is activated. There is no triple-mode backbone curve for the system of hardening nonlinear springs since there is no valid solution for Eq. (5.34).

Fig. 5.5 shows the backbone curve results for the softening case. It can be seen that it is far more complicated than the results in Fig. 5.4. There are eight branches including all three types of backbone curves. Same as those of the hardening case, single- and double-mode backbone curves directly start from the points at the response frequency axis with the coordinates of linear natural frequencies. For the triple-mode backbone curves, they seem to appear from either a single-mode backbone curve, i.e. $T123_{[i,i]}^{\pm,-}$ from $S2$, or double-mode backbone curves, i.e. $T123_{[i,i]}^{\pm,+}$ from $D13_{[i]}^+$ and $T123_{[o,i]}^{\pm,-}$ from $D13_{[i]}^-$. The phenomenon that triple-mode backbone curves bifurcate from a single-mode backbone curve may also explain in the same manner that double-mode backbone curves appear from the trivial solution. For example, it may be regarded that double-mode backbone curves $D12_{[i]}$ and $D23_{[i]}$ lose their stability when they start from $S2$ and then they immediately bifurcate to $T123_{[i,i]}^{\pm,-}$. Therefore, the bifurcation points on $S2$ may also be co-dimension two bifurcations. Here backbone curves $T123_{[o,i]}^{\pm,+}$ do not exist due to the in-existence of valid solutions. Note that here the backbone curves of the first and third masses are no longer the same as the positions of branches $T123_{[i,i]}^{-,+}$ & $T123_{[i,i]}^{+,+}$ and $T123_{[i,i]}^{+,-}$ & $T123_{[i,i]}^{-,-}$ swap respectively.

In Fig. 5.5, it is interesting to see that the branches $T123_{[i,i]}^{\pm,-}$ start and end at the same backbone curve $S2$. This backbone curve behaviour suggests that when only the second mode is externally forced, the modal interaction may only occur within a specific frequency range. Another interesting observation is that the bifurcation point on $D13_{[i]}^-$ where the triple-mode backbone curves $T123_{[o,i]}^{\pm,-}$ emanate is on the frequency axis, which suggests that the triple-mode interaction can happen unconditionally, i.e. not restricted to the force amplitude, to cause all the three modes to be activated for specific forcing scenarios.

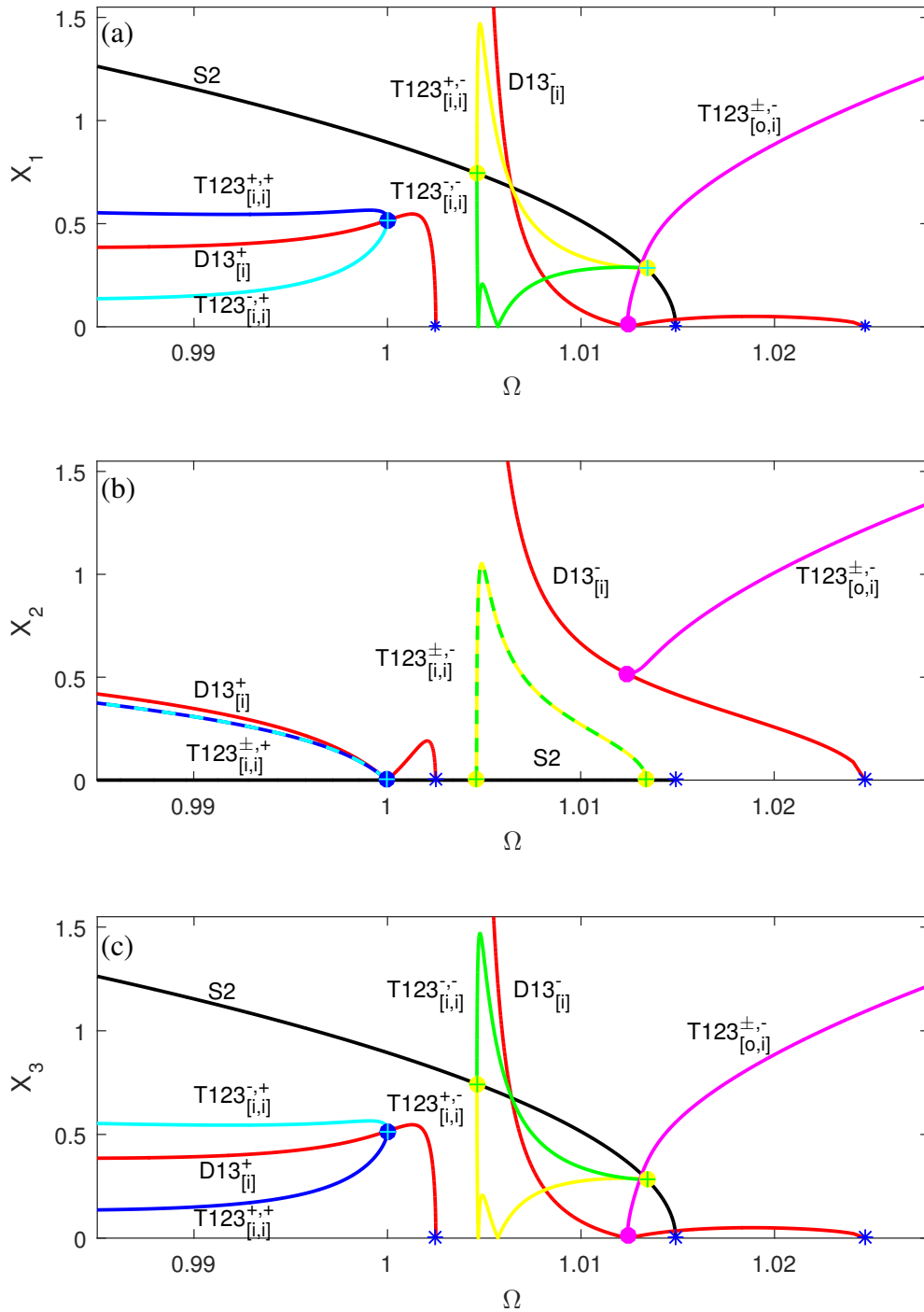


Fig. 5.5 The backbone curves of the 3-DoF system depicted in Fig. 5.2 with physical parameters $m = 1$, $k = 1$, $\bar{k} = 0.01$, $\delta = 0.025$ and $\kappa = -0.025$. Specific backbone curves are labelled respectively, bifurcation points are denoted by dots and blue asterisks mark the system linear natural frequencies.

5.3.2 Forced response

Now the numerical forced response results computed using COCO is compared with the backbone curves. As the result of the softening system includes all the types of backbone curves of hardening system, only the softening case is considered here. Fig. 5.6 shows the responses of the system with softening nonlinear springs when forced directly in the second mode, i.e. $P_1 = -P_3 = P_{m2}$ and $P_2 = 0$, at four incremental magnitudes, i.e. $P_{m2} = 5, 10, 15, 20 (\times 10^{-4})$. Because of this specific forcing shape, it is expected that the forced responses should only follow backbone curves related $S2$ and itself, i.e. $S2$ and $T123_{[i,i]}^{\pm,-}$; therefore the other unrelated backbone curves are omitted from the results. From Fig. 5.6, it can be seen that

- in Fig. 5.6(a), the simple result shows a typical Duffing-like softening response which envelops the backbone curve $S2$.
- in Fig. 5.6(b), a pair of extra forced-response curves, following backbone curve $T123_{[i,i]}^{+,\pm}$ respectively, appears from the primary response curve at the same bifurcation points, beyond which the stability of the primary response curve changes. The beginning parts of the new forced-response curves are unstable, and this occurs because of the occurrence of quasi-periodic response which is unable to be numerically computed.
- in Fig. 5.6(c), two more bifurcation points appearing on the primary response curve leads to a pair of further extra response curves which are close to the finishing (vertical) parts of backbone curve $T123_{[i,i]}^{\pm,-}$. Beyond the ‘new’ upper bifurcation point, the upper trajectory of the primary response curve becomes stable.
- in Fig. 5.6(d), the scope of each response curve increases, but the triple-mode response curves seem not to go beyond the specific frequency range, which verifies the prediction of backbone curves.

Furthermore, the responses when the system are excited at only the first mode or the third mode are investigated respectively, i.e. $P_1 = P_3 = P_{m1}$ & $P_2 = 0.5P_{m1}$ and $P_1 = P_3 = P_{m3}$ & $P_2 = -4P_{m3}$. Only the results when the system is excited strongly enough to result in the resonant modal interactions are illustrated in Fig. 5.7, i.e. the forced amplitudes used here are $P_{m1} = 20 \times 10^{-4}$ for Fig. 5.7(a) and $P_{m3} = 15 \times 10^{-4}$ for Fig. 5.7(b) respectively.

When the system is excited in the first-mode-forced-only scenario, Fig. 5.7(a), there is a primary forced-response curve including the contributions of the first and third modes enveloping the double-mode backbone curve $D13_{[i]}^+$. Here no single-mode response is observed as with the backbone curves. From this double-mode primary response curve, a pair

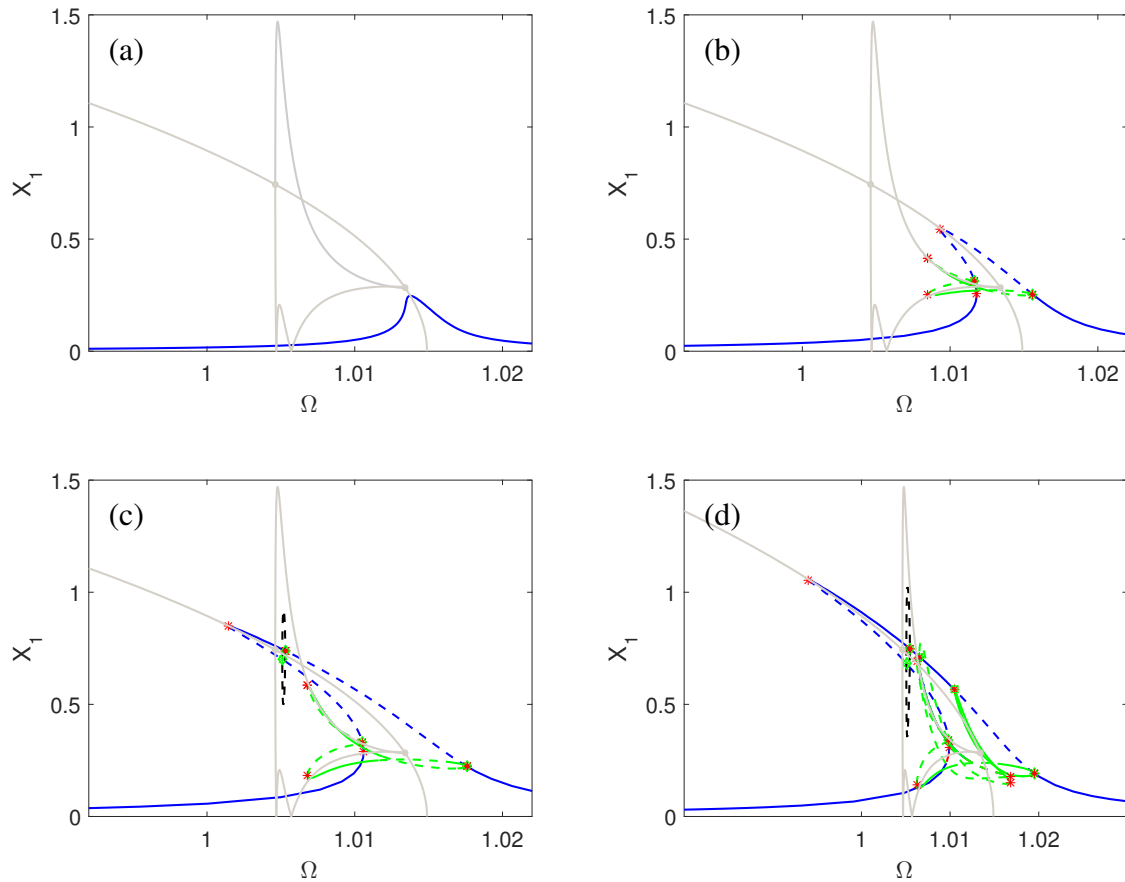


Fig. 5.6 The response curves of the 3-DoF system depicted in Fig. 5.2 excited in the second mode only at four different amplitude. The results are computed using the numerical continuation toolbox COCO. The system parameters used are the same as those in Fig. 5.5 and the force amplitudes are (a) $(P_1, P_2, P_3) = (5, 0, -5) \times 10^{-4}$, (b) $(P_1, P_2, P_3) = (10, 0, -10) \times 10^{-4}$, (c) $(P_1, P_2, P_3) = (15, 0, -15) \times 10^{-4}$ and (d) $(P_1, P_2, P_3) = (20, 0, -20) \times 10^{-4}$. The solid and dashed lines represent the stable and unstable responses respectively. The red asterisks denote the fold points on the forced-response curves, and the green diamonds mark the branch-point bifurcations where the triple-mode forced-response curves emerge from the single-mode forced-response curve. The grey lines denote the backbone curves.

of extra response curves appears on which all three underlying modes are present. These triple-mode response curves precisely follow $T123_{[i, i]}^{+, -}$ and $T123_{[i, i]}^{-, -}$ respectively with their folding points almost on the corresponding backbone curves.

When the system is forced in the third mode only, see Fig. 5.7(b), there is a primary double-mode response curve located around $D13_{[i]}^-$. Additionally, a pair of triple-mode response curves corresponding to $T123_{[o, i]}^{+, -}$ emanate from the bifurcation points on the primary response curve. It is interesting to see that one of the branch bifurcation points is close to

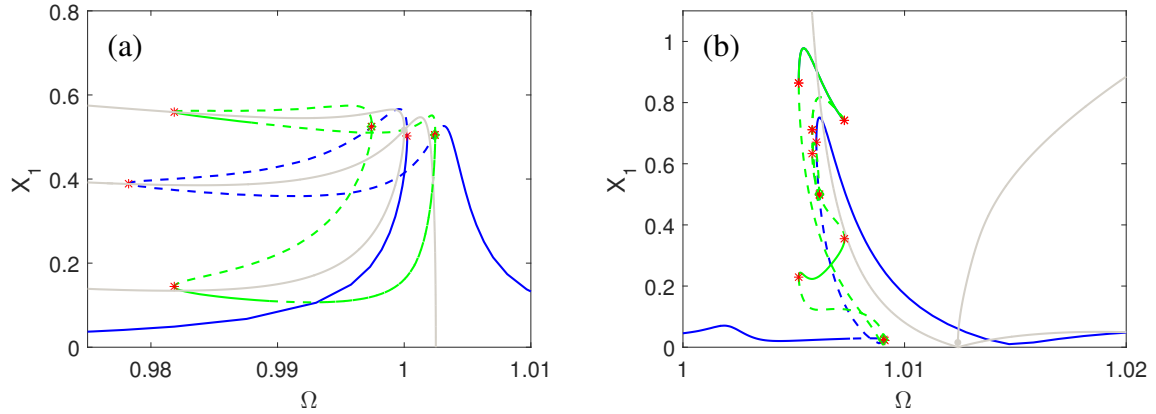


Fig. 5.7 The response curves of the 3-DoF system depicted in Fig. 5.2 excited in the first or third mode only. The force amplitudes are (a) $(P_1, P_2, P_3) = (20, 10, 20) \times 10^{-4}$ and (b) $(P_1, P_2, P_3) = (15, -60, 15) \times 10^{-4}$. The plot denotations are identical to those of Fig. 5.6 and the system parameters used are the same as those in Fig. 5.5.

the frequency axis, i.e. $X_1 \approx 0$. It is noteworthy that no matter how small the force applied at the third mode is, the triple-mode responses always exist for this situation. These bifurcation features of the forced response are in line with the prediction of the backbone curves $T_{123}^{\pm, -}_{[o, i]}$.

From the results of Fig. 5.6 and Fig. 5.7, we have seen the occurrence of the resonant interaction among three nonlinear coupled modes when the system is forced in a single mode. For these specific forcing situations, the unique phenomena of the extinction of the single-mode response and the triple-mode response bifurcating from either single-mode or double-mode response are investigated. Surprisingly, all these nonlinear behaviours can be interpreted and predicted by their corresponding backbone curves to some extent.

5.4 Auto-parametric modal interaction

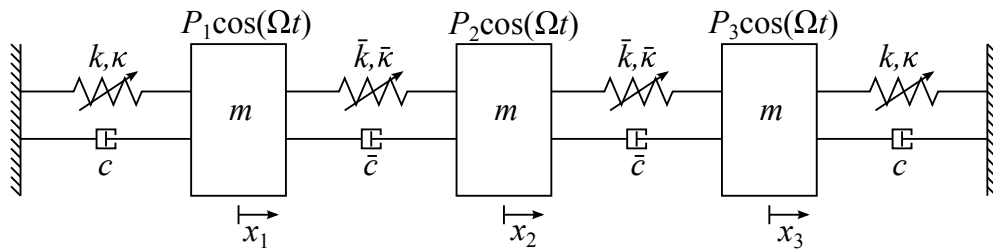


Fig. 5.8 A schematic diagram of an in-line, 3-DoF oscillator with cubic nonlinear springs.

In §5.3, the resonant interaction between/among nonlinear modes of similar natural frequencies and responding at same frequencies has been investigated. Now, we study the auto-parametric modal interaction that also involves multiple modes of nonlinear systems. The nonlinear oscillating system used for demonstration is shown in Fig. 5.8. The system consists of three identical lumped masses with a bilaterally symmetric structure. The two side masses are grounded via a cubic nonlinear spring, with linear constant, k , and nonlinear constant, κ , and a viscous damper, c , and the mass in the middle connects the two side masses with a nonlinear spring, i.e. \bar{k} and $\bar{\kappa}$. Using the annotations of the generic nonlinear 3-DoF system depicted in Fig. 5.1, the stiffness parameters may be written as

$$\begin{aligned} k_1 = k, \quad k_2 = 0, \quad k_3 = k, \quad k_{12} = \bar{k}, \quad k_{23} = \bar{k}, \quad k_{13} = 0, \\ \kappa_1 = \kappa, \quad \kappa_2 = 0, \quad \kappa_3 = \kappa, \quad \kappa_{12} = \bar{\kappa}, \quad \kappa_{23} = \bar{\kappa}, \quad \kappa_{13} = 0. \end{aligned} \quad (5.47)$$

Substituting Eqs. (5.47) into Eqs. (5.3) gives the linear stiffness matrix and nonlinear stiffness terms vector for this system, i.e.

$$\mathbf{K} = \begin{bmatrix} k + \bar{k} & -\bar{k} & 0 \\ -\bar{k} & 2\bar{k} & -\bar{k} \\ 0 & -\bar{k} & k + \bar{k} \end{bmatrix}, \quad (5.48a)$$

$$\mathbf{N}_x = \begin{pmatrix} \kappa x_1^3 + \bar{\kappa}(x_1 - x_2)^3 \\ \bar{\kappa}(x_2 - x_1)^3 + \bar{\kappa}(x_2 - x_3)^3 \\ \kappa x_3^3 + \bar{\kappa}(x_3 - x_2)^3 \end{pmatrix}. \quad (5.48b)$$

Then the eigenvalue problem, $\mathbf{M}^{-1}\mathbf{K}\Phi = \Phi\Lambda$, may be formulated to find linear modeshapes and corresponding natural frequencies, i.e.

$$\Phi = \begin{bmatrix} 1 & 1 & 1 \\ a & 0 & b \\ 1 & -1 & 1 \end{bmatrix}, \quad (5.49a)$$

$$\Lambda = \frac{1}{m} \begin{bmatrix} \frac{k + 3\bar{k} - \Delta}{2} & 0 & 0 \\ 0 & k + \bar{k} & 0 \\ 0 & 0 & \frac{k + 3\bar{k} + \Delta}{2} \end{bmatrix}, \quad (5.49b)$$

where

$$a = \frac{k - \bar{k} + \Delta}{2\bar{k}}, \quad b = \frac{k - \bar{k} - \Delta}{2\bar{k}}, \quad \Delta^2 = k^2 - 2k\bar{k} + 9\bar{k}^2. \quad (5.50)$$

Once the linear modeshapes have been found, the vector of nonlinear term in the modal coordinates, \mathbf{N}_q , may be calculated using Eq. (3.9). However, it may not be easy to write the elements of \mathbf{N}_q symbolically. From the previous studies, we have known that the underlying linear structure of the nonlinear system may decide the potential resonant modal interaction by affecting the linear natural frequencies. Therefore, here the specific values of the linear stiffness are designed before continuing the nonlinear transformation which may largely simplify the calculating process.

5.4.1 Design of the underlying linear structure

Firstly the mass is set to be unity, i.e. $m = 1$. Then the linear modal frequencies may be scaled. Using the simple expression of the natural frequency of the second mode, see Eq. (5.49b), as the scaled reference, i.e. $\omega_{n2}^2 = k + \bar{k} = 1$, it may allow us to write $k = 1 - \bar{k}$. Note that the usage of the specific parameter values here does not sacrifice the problem generality as it can also be obtained through the scaling process. $k = 1 - \bar{k}$ is then substituted into Eqs. (5.49b) and (5.50) which allows us to re-write the natural frequencies and the associated coefficients as

$$\begin{pmatrix} \omega_{n1}^2 \\ \omega_{n2}^2 \\ \omega_{n3}^2 \end{pmatrix} = \begin{pmatrix} 0.5 + \bar{k} - 0.5\Delta \\ 1 \\ 0.5 + \bar{k} + 0.5\Delta \end{pmatrix}, \quad (5.51)$$

and

$$a = \frac{1 - 2\bar{k} - \Delta}{2\bar{k}}, \quad b = \frac{1 - 2\bar{k} + \Delta}{2\bar{k}}, \quad \Delta^2 = 12\bar{k}^2 - 4\bar{k} + 1. \quad (5.52)$$

Now the linear modal frequencies are the functions of \bar{k} only and Fig. 5.9 shows the varying trend of ω_{ni} against \bar{k} . To ensure the linear stiffness of the ground springs be positive, i.e. $k \geq 0$, the considered range of \bar{k} is $[0, 1]$. In Fig. 5.9, an interesting case may be that when $\bar{k} = 0.65$ the natural frequency ratio is $\omega_{n1} : \omega_{n2} : \omega_{n3} \approx 1 : 2 : 3$, which is marked by the black dots in the plot.

Furthermore, to ensure each mode make a relative balanced contribution to the response of each linear modeshape, the values of the elements in the modeshape matrix, Φ , must be reasonable, i.e. the values of a and b should not be too large or too small. From the observation of the varying trend of a and b against \bar{k} , shown in Fig. 5.10, it may be regarded

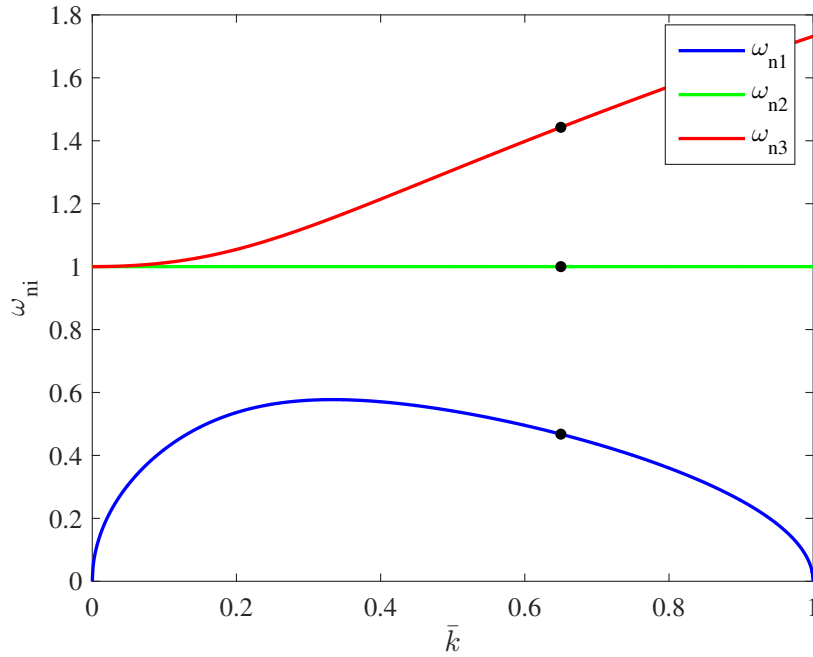


Fig. 5.9 The variation of the linear natural frequencies, ω_{ni} , with the value of the linear stiffness of coupling springs, \bar{k} .

that when $\bar{k} > 0.15$ the linear modeshape values are reasonable ($a = 6$ is regarded as the biggest acceptable ratio value here).

From the above discussion, $k = 0.35$ and $\bar{k} = 0.65$ are chosen for the study of auto-parametric resonant interaction.

5.4.2 Backbone curves

When the linear constants of springs are $k = 0.35$ and $\bar{k} = 0.65$, the system natural frequencies are $\omega_{n1} = 0.4676$, $\omega_{n2} = 1$ and $\omega_{n3} = 1.4427$, i.e. $\omega_{n1} : \omega_{n2} : \omega_{n3} \approx 1 : 2 : 3$. Therefore, the assumption of the response frequency ratio, $\omega_{r1} : \omega_{r2} : \omega_{r3} = 1 : 2 : 3$, may be reasonably made to be used in the nonlinear near-identity transform. Substituting the values of k and \bar{k} into Eq. (5.49a) leads to

$$\Phi = \begin{bmatrix} 1 & 1 & 1 \\ 1.2021 & 0 & -1.6637 \\ 1 & -1 & 1 \end{bmatrix}, \quad (5.53)$$

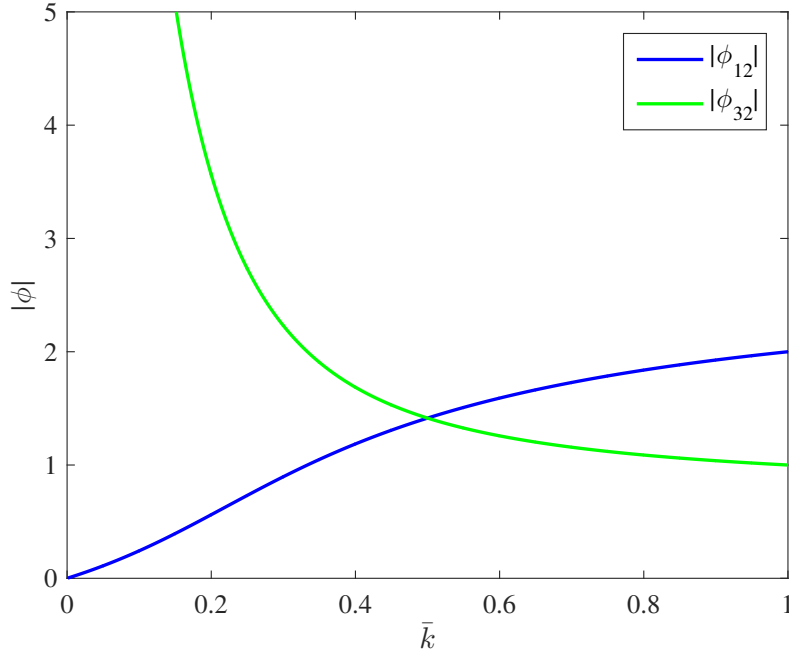


Fig. 5.10 The variation of the absolute values of the linear modeshapes, $|\phi_{12}|$ and $|\phi_{32}|$, with the value of the linear stiffness of coupling springs, \bar{k} .

and then the nonlinear modal coefficient matrix, $[n_q]$, is computed, as

$$[n_q]^T = \kappa \begin{bmatrix} 0.5806 + 0.0010\lambda & 0 & 0.5814 - 0.0101\lambda \\ 1.7418 + 0.0711\lambda & 0 & 1.7442 - 0.7756\lambda \\ 1.7418 + 0.5042\lambda & 0 & 1.7442 - 5.5030\lambda \\ 0 & 3 + 0.1225\lambda & 0 \\ 0 & 1 + \lambda & 0 \\ 0 & 3 + 21.2859\lambda & 0 \\ 1.7418 - 0.0383\lambda & 0 & 1.7442 + 0.4175\lambda \\ 1.7418 - 0.9366\lambda & 0 & 1.7442 + 10.2222\lambda \\ 0.5806 - 2.2151\lambda & 0 & 0.5814 + 24.1766\lambda \\ 0 & 6 - 3.23\lambda & 0 \end{bmatrix}, \quad (5.54)$$

where $\lambda = \bar{k}/\kappa$. Now $r = 2$ and $\bar{r} = 3$ are substituted into Eqs. (5.16) to distinguish the conditionally resonant terms and then the time-independent equations of the system here

are found using Eqs. (3.54) and (5.15), given by

$$(\omega_{n1}^2 - \omega_{r1}^2)U_1 + \frac{1}{4} \left[3\alpha_1^{[1]}U_1^2 + 2\alpha_2^{[1]}U_2^2 + 2\alpha_3^{[1]}U_3^2 \right] U_1 + \frac{1}{4} \left[e^{+i(3\phi_1 - \phi_3)} \alpha_7^{[1]}U_1^2U_3 + e^{+i(\phi_1 - 2\phi_2 + \phi_3)} \alpha_8^{[1]}U_2^2U_3 \right] = 0, \quad (5.55a)$$

$$(\omega_{n2}^2 - \omega_{r2}^2)U_2 + \frac{1}{4} \left[2\alpha_4^{[2]}U_1^2 + 3\alpha_5^{[2]}U_2^2 + 2\alpha_6^{[2]}U_3^2 \right] U_2 + \frac{1}{4} e^{-i(\phi_1 - 2\phi_2 + \phi_3)} \alpha_0^{[2]}U_1U_2U_3 = 0, \quad (5.55b)$$

$$(\omega_{n3}^2 - \omega_{r3}^2)U_3 + \frac{1}{4} \left[2\alpha_7^{[3]}U_1^2 + 2\alpha_8^{[3]}U_2^2 + 3\alpha_9^{[3]}U_3^2 \right] U_3 + \frac{1}{4} \left[e^{-i(3\phi_1 - \phi_3)} \alpha_1^{[3]}U_1^3 + e^{+i(\phi_1 - 2\phi_2 + \phi_3)} \alpha_2^{[3]}U_1U_2^2 \right] = 0. \quad (5.55c)$$

From Eqs. (5.55), it may be found that S2 and S3, the solutions of the single-mode backbone curves associated to the second and third modes respectively, for the system depicted in Fig. 5.8 are governed by the expressions as

$$S2 : \quad U_2 \neq 0, U_1 = U_3 = 0, \quad \omega_{r2}^2 = \omega_{n2}^2 + \frac{3}{4} \alpha_5^{[2]}U_2^2, \quad (5.56a)$$

$$S3 : \quad U_3 \neq 0, U_1 = U_2 = 0, \quad \omega_{r3}^2 = \omega_{n3}^2 + \frac{3}{4} \alpha_9^{[3]}U_3^2. \quad (5.56b)$$

However, the solution S1 may not always exist, as its existence depends on the value of $\alpha_1^{[3]}$ to satisfy Eq. (5.55c) with the substitution $U_1 \neq 0$ and $U_2 = U_3 = 0$: when $\alpha_1^{[3]} = 0$ then S1 exists or vice versa. So, only if $\alpha_1^{[3]} = 0$, such that the nonlinear stiffness ratio $\lambda \approx 55$, we have

$$S1 : \quad U_1 \neq 0, U_2 = U_3 = 0, \quad \omega_{r1}^2 = \omega_{n1}^2 + \frac{3}{4} \alpha_1^{[1]}U_1^2, \quad (5.57)$$

Furthermore, the solutions in which more than one mode is present may also exist. Considering the double-mode solutions, u_1 and u_3 are first assumed activated simultaneously. Substituting $U_2 = 0$ into Eqs. (5.55) leads to

$$(\omega_{n1}^2 - \omega_{r1}^2) + \frac{1}{4} \left[3\alpha_1^{[1]}U_1^2 + 2\alpha_3^{[1]}U_3^2 \right] + \frac{1}{4} e^{+i(3\phi_1 - \phi_3)} \alpha_7^{[1]}U_1U_3 = 0, \quad (5.58a)$$

$$(\omega_{n3}^2 - \omega_{r3}^2) + \frac{1}{4} \left[2\alpha_7^{[3]}U_1^2 + 3\alpha_9^{[3]}U_3^2 \right] + \frac{1}{4} e^{-i(3\phi_1 - \phi_3)} \alpha_1^{[3]}U_1^3/U_3 = 0. \quad (5.58b)$$

Due to the phase-caused complex components, Eqs. (5.58) can only be satisfied when $\sin(|3\phi_1 - \phi_3|) = 0$, such that $|3\phi_1 - \phi_3| = 0, \pi, 2\pi, \dots$. Therefore, a variable $\bar{p}_{31}^{\{1:3\}}$ is defined

that

$$\bar{p}_{31}^{\{1:3\}} = e^{i|3\phi_1 - \phi_3|} = \begin{cases} +1 & \text{when: } |3\phi_1 - \phi_3| = 0, 2\pi, \dots, \\ -1 & \text{when: } |3\phi_1 - \phi_3| = \pi, 3\pi, \dots. \end{cases} \quad (5.59)$$

Using $\bar{p}_{31}^{\{1:3\}}$, Eqs. (5.58) are combined (using $\omega_{r3} = 3\omega_{r1}$) to give the equation describing the relation between the modal response amplitudes, i.e.

$$(18\alpha_3^{[1]} - 3\alpha_9^{[3]})U_3^3 + 9\bar{p}_{31}^{\{1:3\}}\alpha_7^{[1]}U_1U_3^2 + \left[(27\alpha_1^{[1]} - 2\alpha_7^{[3]})U_1^2 + 4(9\omega_{n1}^2 - \omega_{n3}^2) \right] U_3 - \bar{p}_{31}^{\{1:3\}}\alpha_1^{[3]}U_1^3 = 0, \quad (5.60)$$

and rearranged to lead to the those of the response frequencies, i.e.

$$\omega_{r1}^2 = \omega_{n1}^2 + \frac{1}{4}(3\alpha_1^{[1]}U_1^2 + 2\alpha_3^{[1]}U_3^2 + \bar{p}_{31}^{\{1:3\}}\alpha_7^{[1]}U_1U_3), \quad (5.61a)$$

$$\omega_{r3}^2 = \omega_{n3}^2 + \frac{1}{4}(2\alpha_7^{[3]}U_1^2 + 3\alpha_9^{[3]}U_3^2 + \bar{p}_{31}^{\{1:3\}}\alpha_1^{[3]}U_1^3/U_3). \quad (5.61b)$$

Considering Eqs. (3.23) and (5.59), on the backbone curves governed by Eqs. (5.60) and (5.61), when the first mode reaches its peak and zero, the third mode also has the maximum and zero response respectively. However, the reverse description does not hold: when the third mode reaches its peak and zero, the first mode does not have to have the maximum or zero response respectively. Hence, this behaviour can be regarded as the in-unison resonance for the three-to-one auto-parametric interaction case. Therefore, these backbone curves are labelled as $D13_{[i]}^{\pm, \{1:3\}}$, where the superscript indicates the value of $\bar{p}_{31}^{\{1:3\}}$.

The double-mode solutions consisting of either the responses of only the first and second modes or the second and third modes do not exist because when substituting $U_3 = 0$ or $U_1 = 0$ into Eqs. (5.55), it leads to

$$e^{-i(3\phi_1 - \phi_3)}\alpha_1^{[3]}U_1^3 + e^{+i(\phi_1 - 2\phi_2 + \phi_3)}\alpha_2^{[3]}U_1U_2^2 = 0, \quad (5.62)$$

derived from Eq. (5.55c), and

$$e^{+i(\phi_1 - 2\phi_2 + \phi_3)}\alpha_8^{[1]}U_2^2U_3 = 0, \quad (5.63)$$

from Eq. (5.55a) respectively. These equations may only be satisfied by $\alpha_1^{[3]} = \alpha_2^{[3]} = 0$ and $\alpha_8^{[1]} = 0$ which is not the case with the arbitrary values of nonlinear constants.

When all three modes are assumed to be present, i.e. $U_1 \neq 0$, $U_2 \neq 0$ and $U_3 \neq 0$, to

balance the complex components in Eqs. (5.55), the phase differences must be

$$|\phi_1 - 2\phi_2 + \phi_3| = 0, \pi, 2\pi, \dots \quad \text{and} \quad |3\phi_1 - \phi_3| = 0, \pi, 2\pi, \dots \quad (5.64)$$

which leads to

$$\begin{cases} |2\phi_1 - \phi_2| = 0, \pi, 2\pi, \dots \\ |3\phi_1 - \phi_3| = 0, \pi, 2\pi, \dots \end{cases} \quad \text{and} \quad \begin{cases} |2\phi_1 - \phi_2| = \frac{\pi}{2}, \frac{3\pi}{2}, \frac{5\pi}{2}, \dots \\ |3\phi_1 - \phi_3| = 0, \pi, 2\pi, \dots \end{cases} \quad (5.65)$$

Therefore, we define another phase-related variable

$$p_{12}^{\{1:2\}} = e^{2i|2\phi_1 - \phi_2|} = \begin{cases} +1 & \text{when: } |2\phi_1 - \phi_2| = 0, \pi, \dots, \\ -1 & \text{when: } |3\phi_1 - \phi_2| = \frac{\pi}{2}, \frac{3\pi}{2}, \dots. \end{cases} \quad (5.66)$$

When $p_{12}^{\{1:2\}} = +1$, such that $|2\phi_1 - \phi_2| = 0$ or π , Eqs. (5.55) may be arranged, using $\omega_{r2} = 2\omega_{r1}$ and $\omega_{r3} = 3\omega_{r1}$, to be

$$\omega_{r1}^2 = \omega_{n1}^2 + \frac{1}{4}[3\alpha_1^{[1]}U_1^2 + 2\alpha_2^{[1]}U_2^2 + 2\alpha_3^{[1]}U_3^2 + \bar{p}_{31}^{\{1:3\}}\alpha_7^{[1]}U_1U_3 + \bar{p}_{31}^{\{1:3\}}\alpha_8^{[1]}\frac{U_2^2U_3}{U_1}], \quad (5.67a)$$

$$= \frac{1}{4}\omega_{n2}^2 + \frac{1}{16}[2\alpha_4^{[2]}U_1^2 + 3\alpha_5^{[2]}U_2^2 + 2\alpha_6^{[2]}U_3^2 + \bar{p}_{31}^{\{1:3\}}\alpha_0^{[2]}U_1U_3], \quad (5.67b)$$

$$= \frac{1}{9}\omega_{n3}^2 + \frac{1}{36}[2\alpha_7^{[3]}U_1^2 + 2\alpha_8^{[3]}U_2^2 + 3\alpha_9^{[3]}U_3^2 + \bar{p}_{31}^{\{1:3\}}\alpha_1^{[3]}\frac{U_1^3}{U_3} + \bar{p}_{31}^{\{1:3\}}\alpha_2^{[3]}\frac{U_1U_2^2}{U_3}]. \quad (5.67c)$$

For this case, when the first mode has the maximum response, the second mode also reaches its peak (while when the first mode has zero response, the second mode does not pass zero but also has the maximum response). Therefore, we regard this behaviour as the in-unison resonance for the two-to-one auto-parametric interaction case and label the backbone curve

solution described by Eqs. (5.67) as $T123_{[i,i]}^{\pm,\pm}$.

When $p_{12}^{\{1:2\}} = -1$, such that $|2\phi_1 - \phi_2| = \pi/2$, the modal responses are governed by

$$\omega_{r1}^2 = \omega_{n1}^2 + \frac{1}{4}[3\alpha_1^{[1]}U_1^2 + 2\alpha_2^{[1]}U_2^2 + 2\alpha_3^{[1]}U_3^2 + \bar{p}_{31}^{\{1:3\}}\alpha_7^{[1]}U_1U_3 - \bar{p}_{31}^{\{1:3\}}\alpha_8^{[1]}\frac{U_2^2U_3}{U_1}], \quad (5.68a)$$

$$= \frac{1}{4}\omega_{n2}^2 + \frac{1}{16}[2\alpha_4^{[2]}U_1^2 + 3\alpha_5^{[2]}U_2^2 + 2\alpha_6^{[2]}U_3^2 - \bar{p}_{31}^{\{1:3\}}\alpha_0^{[2]}U_1U_3], \quad (5.68b)$$

$$= \frac{1}{9}\omega_{n3}^2 + \frac{1}{36}[2\alpha_7^{[3]}U_1^2 + 2\alpha_8^{[3]}U_2^2 + 3\alpha_9^{[3]}U_3^2 + \bar{p}_{31}^{\{1:3\}}\alpha_1^{[3]}\frac{U_1^3}{U_3} - \bar{p}_{31}^{\{1:3\}}\alpha_2^{[3]}\frac{U_1U_2^2}{U_3}]. \quad (5.68c)$$

For this case, when the first mode has the maximum response, the second mode passes zero (while when the first mode has zero-amplitude response, the second mode also responses zero). Therefore, we regard this behaviour as the out-of-unison resonance for the two-to-one auto-parametric interaction case and label the backbone curve solution described by Eqs. (5.68) as $T123_{[o, i]}^{\pm, \pm}$.

The backbone curve results of the nonlinear system depicted in Fig. 5.8 are shown in Fig. 5.11. All panels show the backbone curves in the projection of the modal response frequency against displacement amplitude. The values of the system parameters used are: $m = 1$, $k = 0.35$, $\bar{k} = 0.65$, $\kappa = -1$, and $\bar{\kappa} = 1.01$.

In Fig. 5.11, three backbone curve emanate from the frequency axis with the coordinates of each modal natural frequency respectively, i.e. $D13_{[i]}^+$, S2 and S3, which is similar to that of the system of 1 : 1 : 1 resonant interaction, see Fig. 5.4 and Fig. 5.5. The triple-mode backbone curves $T123_{[o, i]}^{\pm, +}$ and $T123_{[i, i]}^{\pm, -}$ appear from the identical bifurcation point on S2 and all of them show a hardening nonlinear property, i.e. bending to the frequency-increase direction. Note that the backbone solutions $D13_{[i]}^-$, $T123_{[o, i]}^{\pm, -}$ and $T123_{[i, i]}^{\pm, +}$ do not exist as there is not valid solution for their corresponding governing equations.

In Fig. 5.11, the existence of backbone curves $T123_{[o, i]}^{\pm, +}$ and $T123_{[i, i]}^{\pm, -}$ demonstrates the occurrence of the resonant interaction between the second mode and other two modes. Considering the linear natural frequency relationship and nonlinearity type of the example system, this phenomenon is unique to the modal interaction involving multiple modes. More specifically, it is believed that in general, the two-to-one or three-to-two auto-parametric interaction may only occur between two modes of a system of corresponding stiffness nonlinearities, e.g. quadratic and quartic. Hence when considering the double-mode interaction, the second mode of the example system could never get internal resonance with any of the other two modes alone. This observation suggests that the unexpected lower-number-mode resonant interaction may occur in a nonlinear system of multiple degrees of freedom when additional mode(s) is(are) involved. Therefore, when a number of modes of a system are nonlinearly coupled, it may be necessary to consider the modal interaction involving as many modes as possible to prevent ignoring any multi-mode resonant interactions.

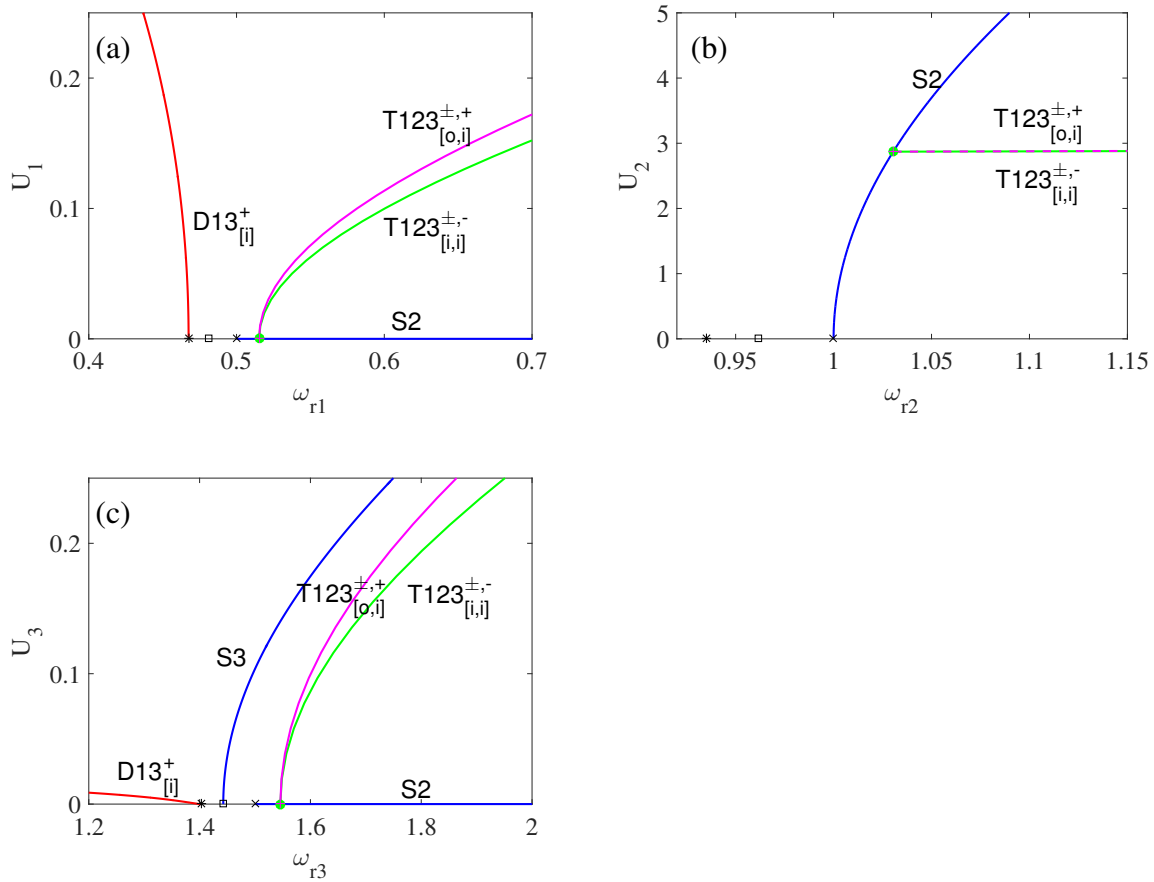


Fig. 5.11 The backbone curves of the 3-DoF system depicted in Fig. 5.8 with physical parameters $m = 1$, $k = 0.35$, $\bar{k} = 0.65$, $\kappa = -1$ and $\bar{\kappa} = 1.01$. Specific backbone curves are labelled respectively, and the bifurcation points are denoted by dots. The asterisk, cross and square denote the corresponding scaled linear natural frequencies.

5.5 Summary

In this chapter, we have investigated the interaction between/among all the underlying modes of some nonlinear oscillating systems of multiple degrees of freedom using backbone curves. The 3-DoF oscillator with cubic nonlinear springs has been considered throughout as the example system to explore different types of resonant multi-mode interactions that potentially occur.

In §5.2, the backbone curve model of a generic 3-DoF lumped-mass oscillator of cubic nonlinearity was first developed using the direct norm form technique. During the derivation, the vector of nonlinear terms in the modal coordinates was expressed as the product

of a polynomial-term vector and its corresponding symbolised-coefficient matrix. Hence, in the final time-invariant equations, the origin of the resonant terms transformed to be retained could be detected. In the backbone curve model, the resonant terms have been classified to be unconditionally and conditionally resonant based on their relationship with the response frequency ratios. The latter has been demonstrated to be always resulting in phase-related terms which may finally lead to several backbone curve branches involving identical system modes but of different phase differences.

The effect of one-to-one-to-one resonant modal interaction has specifically been investigated in §5.3. As the nonlinear system was designed to have three nature modes that are nonlinearly coupled and have close natural frequencies, the one-to-one-to-one triple-mode interaction may occur. It has been demonstrated that the existence of triple-mode backbone curves is still affected by the values of nonlinear stiffness parameters, e.g. the triple-mode backbone curves do not exist when the nonlinear constants of the system springs are positive, which is in keeping with the finding in Chapter 4.

When the nonlinear springs were assumed to be softening, the triple-mode backbone curves were shown to be able to bifurcate from either single- or double-mode backbone curves. The corresponding bifurcation points on single-mode backbone curve turn out to be co-dimension two bifurcation points where the associated double-mode backbone curves appear, loss stability and then lead to triple-mode branches. The similar phenomenon was also observed for the bifurcation of double-mode backbone curves from the no-motion trivial solution for the example system considered here. This backbone curve behaviour suggests that when a single mode is directly forced, (i) a single-mode forced response may not be observed but the double-mode one would directly appear instead, and (ii) three modes may be activated without experiencing the two-mode-activation process. These backbone curve predictions have been demonstrated by the numerical forced-response results for the single-mode-forced situation.

The auto-parametric interaction involving multiple modes has also been investigated in §5.4 via considering another 3-DoF system whose natural frequencies are $\omega_{n1} : \omega_{n2} : \omega_{n3} \approx 1 : 2 : 3$. As expected, it has been shown that the three-to-one auto-parametric modal interaction may occur between the first and third modes of this system of cubic nonlinearity. But here, a unique nonlinear behaviour of multi-DoF systems was found that the unexpected resonance mode, i.e. the second mode of the example system, would get resonance with the other two when the three modes are also present for the single-mode-forced situation. This finding demonstrated that for systems of several nonlinearly coupled modes, it is essential to examine their natural frequencies to prevent ignoring modal interactions occurring among

multiple modes.

Throughout Chapter 4 and Chapter 5, we have investigated nonlinear interactions involving different numbers of coupled modes with different response frequency relations and their corresponding effects in the forced responses. It has been demonstrated that these modal interactions can get resonance between involved modes: when one of the modes is externally forced, the other unforced modes would also be activated. All these kinds of modal interactions are based on a specific fixed response frequency ratio regarding a corresponding type of nonlinearity, e.g. one-to-one and three-to-one modal interaction for the cubic nonlinearity, and two-to-one for the quadratic nonlinearity. However, if the nonlinearly coupled modes of multi-DoF systems interact with each other but not in a resonant way, what kinds of nonlinear dynamic characteristics may then result in? In the next chapter, we will investigate the effect of the non-resonant modal interaction, and in the subsequent chapter, one of its application is introduced.

Chapter 6

Resonant frequency shift

In this chapter we:

- Show the resonant-frequency-shift phenomenon occurs in nonlinear systems under the multi-mode excitation due to membrane stress.
- Investigate the contribution of different nonlinear terms, single-mode and coupled-mode ones, during frequency shift.
- Use nonlinear reduced-order models to demonstrate the importance of the nonlinear coupled-mode terms on accurate response prediction.
- Introduce the concept of the non-resonant interaction between nonlinearly coupled modes and demonstrate its existence in continuous structures.
- Demonstrate the influence of the non-resonant interaction on the system response for the multi-mode-excited situation.

6.1 Introduction

In Chapter 5, different kinds of N modal interaction were discussed. It has been shown how the backbone curves provide a means for accurately predicting the forced responses and interpreting different resonant modal interactions. However, all the forcing conditions considered in the previous chapters tend to be single-frequency while the real working environment of practical machines may be much more complicated. For example, aircraft fuselage structures subjected to high aeroelastic or acoustic loading.

In this chapter, we investigate dynamic behaviours of nonlinear systems when multiple modes are externally forced under a relatively complex excitation, e.g. random excitation and hybrid excitation of random and harmonic-wave components. The chapter begins by introducing a thin rectangular plate with the edges simply supported. Its unique dynamic behaviour, i.e. resonant frequency shift, due to the membrane stresses under multi-mode excitation is the key point of interest.

The accurate prediction of the nonlinear response of plates and shells still presents challenges, especially for structures of low stiffness and strong flexibility under high environmental loads, resulting in significant nonlinear behaviours. The linear analysis techniques fail to capture this nonlinear behaviour, particularly at high levels of dynamic excitation when, for example, the resonant frequencies can vary with amplitude. For plate structures, it is accepted that in general when the transverse deflection approaches the thickness of the plate, the effect of the nonlinearity becomes significant. For a pinned plate, this is primarily because the in-plane stress starts to make the response amplitude dependent [10].

One approach to studying this problem is to perform full-order model simulations using a finite element software. The computation time is the limitation of this approach for practical applications. Another promising alternative strategy for addressing these drawbacks is using reduced order modelling (ROM), more specifically, nonlinear reduced order modelling (NROM) techniques [62]. NROMs consist of a low number of modes that include linear and nonlinear terms, typically in the form of a series of quadratic and cubic terms in the modal coordinates.

The underlying linear modes can be easily determined using the well-established linear modal techniques, e.g. the linear Galerkin decomposition method for systems described using a partial differential equation (PDE) model [66]. The main challenge in developing an accurate NROM lies in the determination of the nonlinear stiffness coefficients. The methods for computing the nonlinear stiffness coefficients can mainly be classified into direct and indirect approaches. The direct approach applies the modal transformation on the full-order nonlinear stiffness matrices [64, 89] or decompose the nonlinear PDEs [98]. The indirect approach uses the static nonlinear solution of a full finite element model to determine stiffness coefficients [36, 59, 60, 63]. Due to the simple structure of the plate under consideration, we can easily write the PDE of the nonlinear version; hence the direct approach, i.e. Galerkin decomposition, is employed to derive the NROM.

In §6.3, using linear modeshape functions, we decompose the nonlinear PDE of the example plate into a set of ordinary differential equations (ODEs) with nonlinear cubic terms in the modal coordinates. It is found that the resulting NROM is still not easy to solve

due to the existence of nonlinearly coupled terms. The majority of these coupled-mode terms are believed to be insignificant for single-frequency excitation situation, which leads us to consider whether they can also be ignored for complex excitation cases. Therefore, the forced response of two kinds of NROMs, with and without coupled-mode terms are simulated and qualitatively compared with the full model simulation results. It turns out that the NROM including the coupled-mode terms can more accurately represent the nonlinear behaviour (resonant frequency shift) for the excitation situations under consideration.

In §6.4, the backbone curve tool is used again to help explain the effect of the non-resonant coupled-terms, and then a non-resonant interaction is introduced. Due to simultaneous activation of multiple non-resonant coupled modes, their presence tends to make each other stiffen or soften (based on the sign of the associated stiffness values). The forced response curves under multi-mode excitations are again found to have a good match with the updated backbone curves where the non-resonant modal interaction is considered.

6.2 Frequency shift of an example pinned-pinned plate

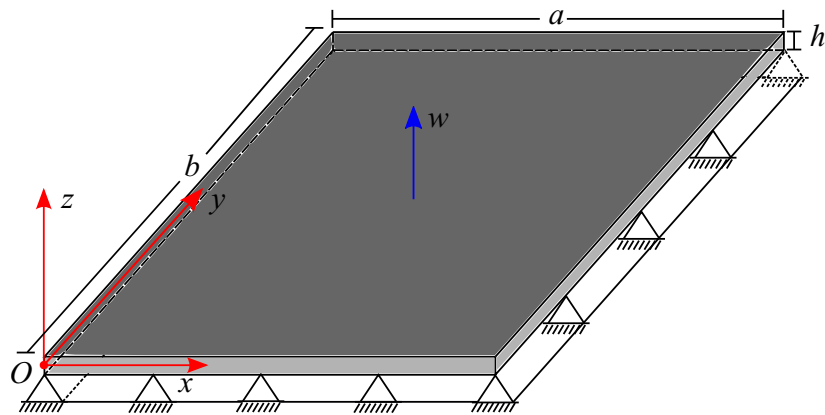


Fig. 6.1 A schematic diagram of a thin, rectangular plate with the edges simply supported and the coordinate system.

Throughout this chapter we consider the transverse deflection of a thin rectangular plate with all edges simply supported (i.e. pinned). The schematic of the example plate is shown in Fig. 6.1. An associated coordinate system $(O; x, y, z)$ is overlaid on the plate with its origin O at one corner. For an arbitrary point of coordinates (x, y) on the middle surface of the plate, its out-of-plane (i.e. z -direction) displacement is denoted by $w(x, y)$. The geometric and material properties of the example plate are listed in Table 6.1.

Length [mm]	Width [mm]	Thickness [mm]
$a = 500$	$b = 520$	$h = 5$
Density [kg/m ³]	Young's modulus [GPa]	Poisson's ratio
$\rho = 2700$	$E = 70$	$\nu = 0.31$

Table 6.1 Properties of the example plate.

Firstly, the full-order simulations are performed in Abaqus[®], a commercial finite element (FE) analysis software, to illustrate the resonant frequency-shift phenomenon. 1600 thick shell elements (S8R in Abaqus[®]) are used to discretise the plate. This specific element is adopted as it includes membrane stretching effects for large displacements. This FE model is used to simulate the transient response of the example plate under specific excitations, and then the response results are analysed in the frequency domain to examine the varying of the system resonant frequencies.

Before performing the transient dynamic response simulation, the linear modal analysis (the job model *LnDynModal* in Abaqus[®]) is conducted to understand the modeshape patterns of the underlying linear structure. Fig. 6.2 shows the configurations of the first four non-rigid-body modes denoted as Mode I, II, III and IV and their natural frequencies are $\omega_{n1} = 58.707$ rad/s, $\omega_{n2} = 143.33$ rad/s, $\omega_{n3} = 150.24$ rad/s and $\omega_{n4} = 234.83$ rad/s respectively. These four modes will be mainly considered in the following study.

For the transient simulation, the *Abaqus/Implicit*s integrator in *Abaqus/Standard* solver is adopted. To ensure a stable (physical) response, the value of the only parameter α_n specifying the integrator is chosen to $\alpha_n = -\frac{1}{6}$ to impose adequate numerical damping during integration. As for the forcing input, a group of random data with the sampling rate of 10kHz for a period $T = 50$ s was generated using Matlab[®] function *rand* initially and then substituted into Abaqus[®] as the random input amplitude. The model was integrated over the input period at a minimum sampling time of 10^{-8} s. The displacement response at the centre of the right-top quadrant of the plate (with coordinates $(x, y) = \frac{3}{4}(a, b)$) is used as a metric. This point is chosen to guarantee that the responses of all the first four bending modes are considered. The time-domain response is processed to obtain the spectrum result via the PSD (power spectral density) estimator based on the AR (auto-regression) model in Matlab[®]. One issue of using the AR-based PSD estimator is the determination of the AR model order for the specific signal considered. Here FPE (Final Prediction Error), AIC (Akaike Information Criterion), MDL (Rissanen's Minimum Description Length) and CAT

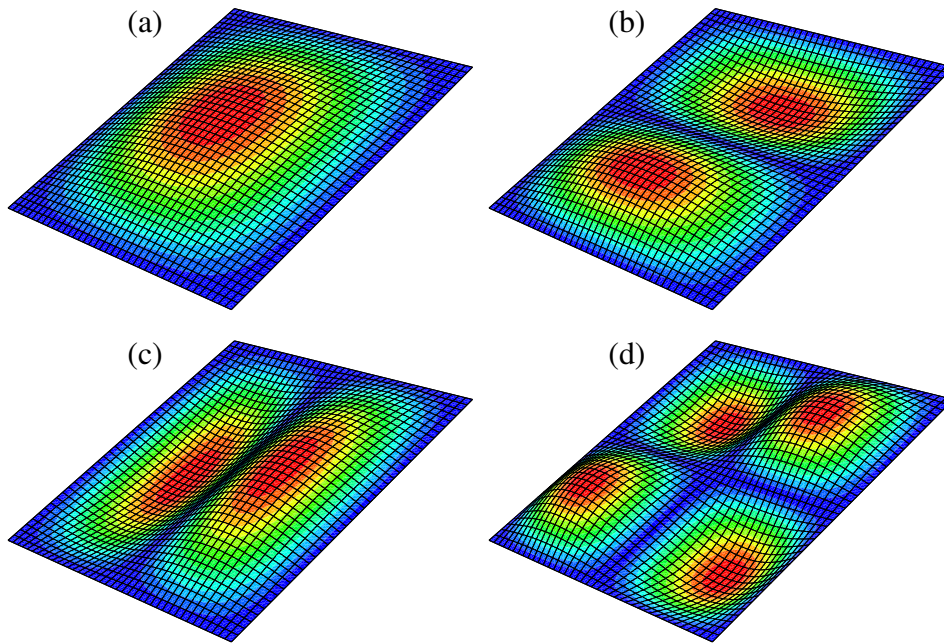


Fig. 6.2 The linear modeshape configurations of the first four bending modes of the plate depicted in Fig. 6.1 with the properties described in Table 6.1, computed using Abaqus[®] linear modal analysis. (a) Mode I, (b) Mode II, (c) Mode III and (d) Mode IV.

(Parzen's Criterion AR Transfer) order selection criterion are employed for the work in this thesis. In Appendix A, the details of the AR power spectral estimation and order selection criteria can be found. To demonstrate the effects of nonlinearity, each forcing situation is simulated with the two control settings, i.e. *Nlgeom* 'Off' and 'On', for exclusion and inclusion of the nonlinear effects of large displacements respectively in the model.

Fig. 6.3 shows the spectral responses of the plate when a random uniform pressure load is applied at the bottom-left quadrant area. This force scenario is chosen to ensure that the four modes of interest are directly excited. Besides, the pressure excitation can represent which modes are directly forced better, see Fig. 6.2. For this group of simulations, two force magnitudes, denoted as A , are used. For the result (i) in Fig. 6.3, the force magnitude used is low, i.e. $A = 10^{-2}$, and the maximum displacement response amplitude of the whole plate is less than 20% of the thickness of the plate, i.e. $w_{max} < 0.2h$. For the result (ii), the force magnitude is relatively high, i.e. $A = 1$, which results a maximum displacement response amplitude larger than the plate thickness, i.e. $w_{max} > h$.

From Fig. 6.3, it can be seen that for the low-level excitation situation the linear and nonlinear results are almost on top of each other and their resonant frequencies are close to the corresponding linear natural frequencies. This implies that the plate behaves linearly

for this case. When the excitation level increases, the difference between the linear and nonlinear results becomes obvious: the resonant frequencies of the linear results are still close to the linear natural frequencies, but those of the nonlinear results have all shifted to the right significantly.

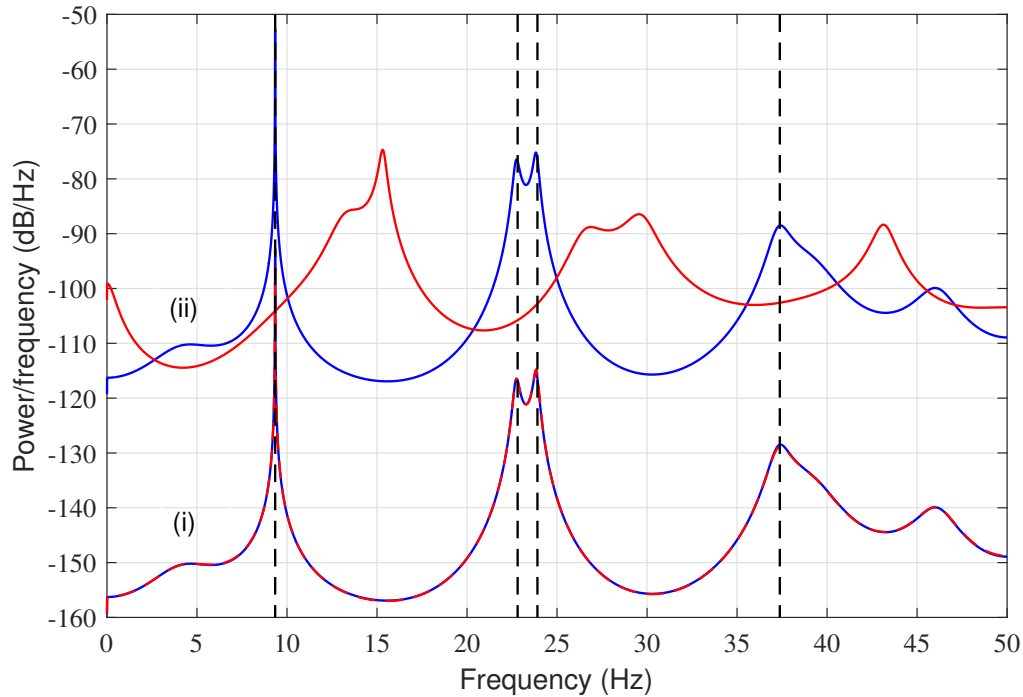


Fig. 6.3 The power spectral density of the response of the plate depicted in Fig. 6.1 to random excitations, computed using the FE simulation data. The plate is under a uniform pressure load random excitation on the left-bottom quarter area at two amplitude: (i) $A = 10^{-2}$ and (ii) $A = 1$, and the displacement response at the point with the coordinates $(x, y) = \frac{3}{4}(a, b)$ is considered. The blue and red lines represent the results excluding and including the large-amplitude nonlinear effects respectively, and the dash-black lines denote the linear natural frequencies.

Fig. 6.4 shows the simulation results when the plate is under a hybrid excitation of random and harmonic forces. The random component is identical to that used for the case (i) in Fig. 6.3, which aims to ensure all modes of interest be mildly active. The harmonic component is a point force applied at the centre of the plate. The specific loading point chosen is for forcing Mode I only (among the four modes under consideration) to increase its power (amplitude). Hence the forcing frequency is chosen to equate the first linear natural frequency, i.e. $\Omega = \omega_{n1}$.

We already know, from Fig. 6.3, that for the mildly random excitation situation, all four

modes behave linearly and no frequency shift is observed. In Fig. 6.4, the linear result (the blue line) shows no apparent difference in the resonant frequencies and the PSD levels of Mode II, III and IV to that in Fig. 6.3. However, due to the additive harmonic force, the PSD of Mode I significantly increases. For the nonlinear result (the red line), there are clear double peaks near the first modal frequency and, furthermore, the positions of resonant frequencies have shifted to the right for the rest of the modes.

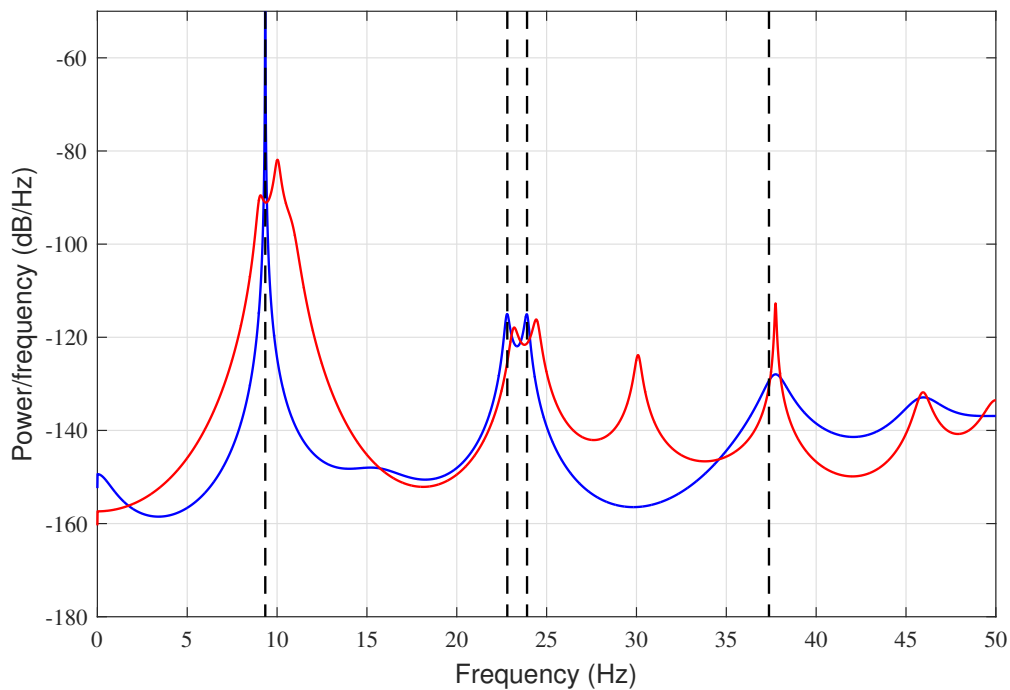


Fig. 6.4 The power spectral density of the response of the plate depicted in Fig. 6.1 to a hybrid excitation, computed using the FE simulation data. The plate is under the excitation comprising a random component identical to that used for the case (i) in Fig. 6.3 and a harmonic component applied at the plate centre with the amplitude $F_h = 5 \times 10^{-3}$ at frequency $\Omega = \omega_{n1}$. The displacement response at the point with the coordinates $(x, y) = \frac{3}{4}(a, b)$ is considered. The denotations are the same as those of Fig. 6.3.

The results shown in Fig. 6.3 and Fig. 6.4 demonstrate that:

- when the response amplitude becomes large, the nonlinearity due to the membrane stretching effect would cause the resonant frequencies of the structure to shift
- the source of this nonlinear effect on the frequency shift is not limited to individual modes, but maybe from the interaction between relevant modes.

In the following sections, we will analytically investigate this nonlinear phenomenon using dynamic tools such as nonlinear reduced-order models and backbone curves.

6.3 Nonlinear reduced-order model

To investigate the nonlinearity of the plate, a mathematical model that can not only accurately make the prediction of the forced response but also give some insight into the system physical parameters is needed. Therefore, the parametric physical model, NROM, is one of the candidates. Although there are numerous studies about how to create accurate NROMs, the techniques for geometrically nonlinear structures may be mainly classified as direct and indirect/non-intrusive. Details about the techniques for developing the reduced-order model for nonlinear mechanical systems can be found in [62]. In this section, considering the simple geometry of the plate under consideration, a direct method of decomposing the nonlinear PDE using functions of linear modeshapes is employed to develop the NROM. Then the effects of different nonlinear terms are analysed based on the NROM simulation results.

6.3.1 Development of a nonlinear reduced-order model

From [98], through the analysis of nonlinear strain-displacement relationships, the PDE of the plate behaving in the nonlinear region is written as

$$\rho h \frac{\partial^2 w}{\partial t^2} + D \nabla^2 \nabla^2 w - \left(\frac{\partial^2 \Phi}{\partial y^2} \frac{\partial^2 w}{\partial x^2} - 2 \frac{\partial^2 \Phi}{\partial x \partial y} \frac{\partial^2 w}{\partial x \partial y} + \frac{\partial^2 \Phi}{\partial x^2} \frac{\partial^2 w}{\partial y^2} \right) = P_f, \quad (6.1)$$

with a compatibility equation,

$$\frac{1}{Eh} \nabla^2 \nabla^2 \Phi + \frac{\partial^2 w}{\partial x^2} \frac{\partial^2 w}{\partial y^2} - \left(\frac{\partial^2 w}{\partial x \partial y} \right)^2 = 0, \quad (6.2)$$

where $w(x, y, t)$ is the transverse deflection, $D = \frac{Eh^3}{12[1-\nu^2]}$ is the flexural rigidity of the plate under the assumption of the homogeneous, isotropic, and elastic material, $\Phi(x, y, t)$ is the in-plane constraint force function due to the pre-stressing of the plate between its boundary supports for the large transverse deflection situation, also known as *Airy stress function*, $P_f(x, y, t)$ is the external in-plane force and ρ , h , E and ν represent the corresponding structural parameters in Table 6.1 and the operator $\nabla^2 = \frac{\partial^2}{\partial x^2} + \frac{\partial^2}{\partial y^2}$. Note that Eqs. (6.1) and (6.2) do not include the damping related terms and the artificial modal-type damping will be added later.

To decompose the spatial and temporal variables, a modal description is adopted, such that the deflection, w , is written,

$$w(x, y, t) = \sum_{m=1}^M \sum_{n=1}^N \phi_{x,m}(x) \phi_{y,n}(y) q_{mn}(t), \quad (6.3)$$

where $\phi_{x,m}(x)$ and $\phi_{y,n}(y)$ are the spatial coordinate, describing the 2-dimensional m^{th} and n^{th} linear modeshape in the x and y directions respectively and $q_{mn}(t)$ is the temporal coordinate, describing the displacement of the $\{m, n\}^{\text{th}}$ linear mode. The modeshapes only account for the linear contribution from the spring mechanism, but not the nonlinear component. The expressions of linear modeshapes of the simply supported plate can be explicitly written as [5]

$$\phi_{x,m}(x) = \sin\left(\frac{m\pi}{a}x\right) \quad \text{and} \quad \phi_{y,n}(y) = \sin\left(\frac{n\pi}{b}y\right). \quad (6.4)$$

Similarly, the Airy stress function is described in the same form, written as

$$\Phi(x, y, t) = \sum_{r=1}^R \sum_{s=1}^S \varphi_{x,r}(x) \varphi_{y,s}(y) \eta_{rs}(t), \quad (6.5)$$

where

$$\varphi_{x,r}(x) = \sin\left(\frac{r\pi}{a}x\right) \quad \text{and} \quad \varphi_{y,s}(y) = \sin\left(\frac{s\pi}{b}y\right). \quad (6.6)$$

Now, substituting Eqs. (6.3) and (6.5) into Eq. (6.1) gives

$$\begin{aligned} & \sum_{M,N} \left\{ D \left(\frac{d^4 \phi_{x,m}}{dx^4} \phi_{y,n} + 2 \frac{d^2 \phi_{x,m}}{dx^2} \frac{d^2 \phi_{y,n}}{dy^2} + \phi_{x,m} \frac{d^4 \phi_{y,n}}{dy^4} \right) q_{mn} + \rho h \phi_{x,m} \phi_{y,n} \ddot{q}_{mn} \right\} \\ & - \sum_{M,N,R,S} \left\{ \left(\varphi_{x,r} \frac{d^2 \varphi_{y,s}}{dy^2} \frac{d^2 \phi_{x,m}}{dx^2} \phi_{y,n} - 2 \frac{d\varphi_{x,r}}{dx} \frac{d\varphi_{y,s}}{dy} \frac{d\phi_{x,m}}{dx} \frac{d\phi_{y,n}}{dy} + \frac{d^2 \varphi_{x,r}}{dx^2} \varphi_{y,s} \phi_{x,m} \frac{d^2 \phi_{y,n}}{dy^2} \right) \eta_{rs} q_{mn} \right\} = P_f. \end{aligned} \quad (6.7)$$

Similarly, the associated compatibility equation with the substitution of w and Φ becomes,

$$\begin{aligned} & \sum_{R,S} \left\{ \frac{1}{Eh} \left(\frac{d^4 \varphi_{x,r}}{dx^4} \varphi_{y,s} + 2 \frac{d^2 \varphi_{x,r}}{dx^2} \frac{d^2 \varphi_{y,s}}{dy^2} + \varphi_{x,r} \frac{d^4 \varphi_{y,s}}{dy^4} \right) \eta_{rs} \right\} \\ & + \sum_{G,H,T,U} \left\{ \left(\frac{d^2 \phi_{x,g}}{dx^2} \phi_{y,h} \phi_{x,t} \frac{d^2 \phi_{y,u}}{dy^2} - \frac{d\phi_{x,g}}{dx} \frac{d\phi_{y,h}}{dy} \frac{d\phi_{x,t}}{dx} \frac{d\phi_{y,u}}{dy} \right) \right\} q_{gh} q_{tu} = 0. \end{aligned} \quad (6.8)$$

Then the Galerkin process is applied to above resulting equations: multiply Eq. (6.7) by arbitrary modeshape functions $\phi_{x,i}$ and $\phi_{y,j}$ on both sides and integrate across the whole area

of the plate. Furthermore, the orthogonality conditions of linear modeshapes, i.e.

$$\begin{aligned} \int_0^a \phi_{x,i} \phi_{x,j} dx &= \int_0^a \frac{d^2 \phi_{x,i}}{dx^2} \frac{d^2 \phi_{x,j}}{dx^2} dx \\ &= \int_0^a \frac{d^4 \phi_{x,i}}{dx^4} \frac{d^4 \phi_{x,j}}{dx^4} dx = 0, \end{aligned} \quad \text{when } i \neq j, \quad (6.9)$$

is used to modally decouple the EoM. This process leads to a set of ODEs in terms of linear modal coordinates, written as,

$$\ddot{q}_{ij} + \omega_{ij}^2 q_{ij} - \sum^{M,N,R,S} \Theta_{mnr sij} \eta_{rs} q_{mn} = f_{ij}, \quad (6.10)$$

where the linear modal frequencies,

$$\omega_{ij}^2 = \pi^2 \left(\frac{i^2}{a^2} + \frac{j^2}{b^2} \right) \sqrt{\frac{D}{\rho h}}, \quad (6.11)$$

the external force in modal coordinates,

$$f_{ij} = \int_0^a \int_0^b P_f \phi_{x,i} \phi_{y,j} dx dy, \quad (6.12)$$

that may be calculated with extra information about the force pattern, and

$$\begin{aligned} \Theta_{mnr sij} &= \frac{4}{\rho h a b} \int_0^a \int_0^b \left(\phi_{x,r} \frac{d^2 \phi_{y,s}}{dy^2} \frac{d^2 \phi_{x,m}}{dx^2} \phi_{y,n} \right. \\ &\quad \left. - 2 \frac{d\phi_{x,r}}{dx} \frac{d\phi_{y,s}}{dy} \frac{d\phi_{x,n}}{dx} \frac{d\phi_{y,m}}{dy} + \frac{d^2 \phi_{x,r}}{dx^2} \phi_{y,s} \phi_{x,m} \frac{d^2 \phi_{y,n}}{dy^2} \right) \phi_{x,i} \phi_{y,j} dy dx. \end{aligned} \quad (6.13)$$

Similarly, Eq. (6.8) becomes,

$$\Upsilon_{rs} \eta_{pq} + \sum^{G,H,T,U} \Gamma_{ghturs} q_{gh} q_{tu} = 0, \quad (6.14)$$

where,

$$\Gamma_{ghturs} = \int_0^a \int_0^b \left\{ \frac{d^2 \phi_{x,g}}{dx^2} \phi_{y,h} \phi_{x,t} \frac{d^2 \phi_{y,u}}{dy^2} - \left(\frac{d\phi_{x,g}}{dx} \frac{d\phi_{y,h}}{dy} \frac{d\phi_{x,t}}{dx} \frac{d\phi_{y,u}}{dy} \right) \right\} \phi_{x,r} \phi_{y,s} dy dx, \quad (6.15a)$$

$$\Upsilon_{rs} = \frac{ab}{4Eh} \pi^4 \left(\frac{r^2}{a^2} + \frac{s^2}{b^2} \right)^2. \quad (6.15b)$$

Combining Eqs. (6.10) and (6.14) to eliminate η_{rs} gives,

$$\ddot{q}_{ij} + \omega_{ij}^2 q_{ij} + \left\{ \sum^{M,N,G,H,T,U} \mu_{ij,ghtumn} q_{gh} q_{tu} q_{mn} \right\} = f_{ij}, \quad (6.16)$$

where

$$\mu_{ij,ghtumn} = \sum^{R,S} \frac{\Gamma_{ghturs} \Theta_{mnr sij}}{\Upsilon_{rs}}. \quad (6.17)$$

Eq. (6.16) describes the motion of the undamped $\{i, j\}^{\text{th}}$ modes of the plate. These EoMs can be sorted by the magnitude of the linear natural frequencies and written in our familiar matrix form, see Eq. (3.1), with the imposed modal damping terms, as

$$\ddot{\mathbf{q}} + \mathbf{C}\dot{\mathbf{q}} + \mathbf{\Lambda}\mathbf{q} + \mathbf{N}_q(\mathbf{q}) = \mathbf{F}_m, \quad (6.18)$$

where \mathbf{C} is a diagonal matrix of damping coefficients, $\mathbf{\Lambda}$ is a diagonal matrix of the squares of modal natural frequencies, \mathbf{N}_q is the column vector containing the nonlinear terms whose n^{th} element may be written

$$N_{q,n} = \sum_{r=1}^N \sum_{s=r}^N \sum_{t=s}^N \alpha_\ell^{[n]} q_r q_s q_t, \quad (6.19)$$

and \mathbf{F}_m is a vector of modal forcing terms.

Substituting Eqs. (6.4) and (6.6) with the example plate parameters values in Table 6.1 into Eqs. (6.11), (6.13), (6.15) and (6.19) may result in the values of linear natural frequencies and coefficients of nonlinear stiffness terms. Table 6.2 lists the values of the linear natural frequencies and the non-zero coefficients of nonlinear terms for the first four modes of the plate. The configurations of the linear modeshapes of the first four modes, plotted using Eqs. (6.4), are shown in Fig. 6.5. It can be seen that these results are almost identical to those of the FE simulation, see Fig. 6.2.

6.3.2 Simulation results

In the EoM of the n^{th} mode, the nonlinear terms can be mainly classified into two types, i.e. *single-mode* terms, q_n^3 , and *mixed-mode* terms, $q_i q_j q_k$ where $i \neq n$, $j \neq n$ or $k \neq n$, see Table 6.2. It is known that the single-mode terms can only affect the resonant frequency of its corresponding mode; while the mixed-mode ones may affect the response of other modes via the modal interaction for the situation of the single-mode-single-frequency excitation.

Mode No.	ω_n [rad/s]	Coefficients ($\times 10^9$)	NL term
Mode I	58.9	$\alpha_1^I = 5.45$	q_1^3
		$\alpha_2^I = 23.6$	$q_1 q_2^2$
		$\alpha_3^I = 22.7$	$q_1 q_3^2$
		$\alpha_4^I = 24.4$	$q_1 q_4^2$
		$\alpha_5^I = 74.3$	$q_2 q_3 q_4$
Mode II	143.9	$\alpha_1^{II} = 23.6$	$q_1^2 q_2$
		$\alpha_2^{II} = 31.4$	q_2^3
		$\alpha_3^{II} = 65.1$	$q_2 q_3^2$
		$\alpha_4^{II} = 124.3$	$q_2 q_4^2$
		$\alpha_5^{II} = 74.3$	$q_1 q_3 q_4$
Mode III	150.8	$\alpha_1^{III} = 22.7$	$q_1^2 q_3$
		$\alpha_2^{III} = 65.1$	$q_2^2 q_3$
		$\alpha_3^{III} = 31.4$	q_3^3
		$\alpha_4^{III} = 132.4$	$q_3 q_4^2$
		$\alpha_5^{III} = 74.3$	$q_1 q_2 q_4$
Mode IV	235.8	$\alpha_1^{IV} = 24.4$	$q_1^2 q_4$
		$\alpha_2^{IV} = 124.3$	$q_2^2 q_4$
		$\alpha_3^{IV} = 132.4$	$q_3^2 q_4$
		$\alpha_4^{IV} = 55.8$	q_4^3
		$\alpha_5^{IV} = 74.3$	$q_1 q_2 q_3$

Table 6.2 Linear natural frequencies and nonlinear parameters for the first four modes of the example plate.

The result in Fig. 6.4 has already demonstrated that there exists a modal interaction between Mode I and other three modes of the plate structure. Hence, to investigate the effects of the single- and mixed-mode nonlinear terms on the resonant frequency shift for the multi-mode forced situation, two kinds of nonlinear four-mode truncation models for the example plate are employed to qualitatively compare with the FE model, i.e. a coupled model including nonlinear mixed-mode terms and an uncoupled model excluding mixed-mode term. Their

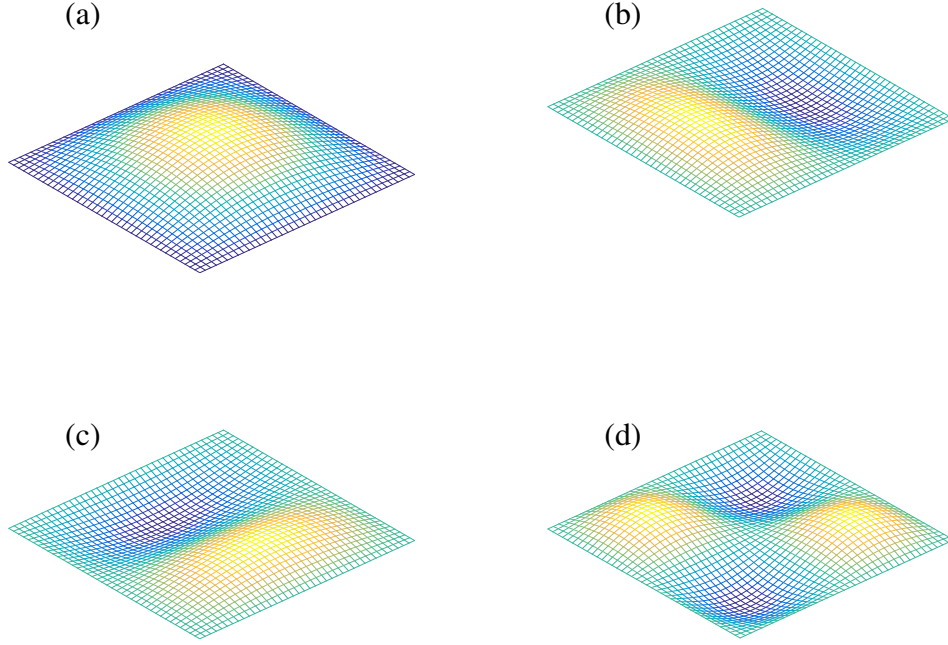


Fig. 6.5 The linear modeshape configurations of the first four modes of the plate depicted in Fig. 6.1 with the properties described in Table 6.1, used in the Galerkin decomposition. (a) Mode I, (b) Mode II, (c) Mode III and (d) Mode IV.

respective EoMs are stated as,

$$\text{Coupled NROM : } \quad \ddot{\mathbf{q}} + \mathbf{C}\dot{\mathbf{q}} + \Lambda\mathbf{q} + \mathbf{N}_q(\mathbf{q}) = \mathbf{F}_m(t), \quad (6.20a)$$

$$\text{Uncoupled NROM : } \quad \ddot{\tilde{\mathbf{q}}} + \mathbf{C}\dot{\tilde{\mathbf{q}}} + \Lambda\tilde{\mathbf{q}} + \tilde{\mathbf{N}}_{\tilde{q}}(\tilde{\mathbf{q}}) = \mathbf{F}_m(t), \quad (6.20b)$$

where the modal force vector $\mathbf{F}_m(t)$ may be written

$$\mathbf{F}_m = \mathbf{P}_r r(t) + \mathbf{P}_h \cos(\Omega t), \quad (6.21)$$

where $r(t)$ is the scaled random input signal (i.e. the random amplitude input in FE simulation), \mathbf{P}_r is the vector magnitude of the modal random force component and \mathbf{P}_h is the vector amplitude of the harmonic component. \mathbf{N}_q and $\tilde{\mathbf{N}}_{\tilde{q}}$ are the vectors of nonlinear terms,

written as

$$\mathbf{N}_q = \begin{pmatrix} \alpha_1^I q_1^3 + \alpha_2^I q_1 q_2^2 + \alpha_3^I q_1 q_3^2 + \alpha_4^I q_1 q_4^2 + \alpha_5^I q_2 q_3 q_4 \\ \alpha_1^{II} q_1^2 q_2 + \alpha_2^{II} q_2^3 + \alpha_3^{II} q_2 q_3^2 + \alpha_4^{II} q_2 q_3^2 + \alpha_5^{II} q_1 q_3 q_4 \\ \alpha_1^{III} q_1^2 q_3 + \alpha_2^{III} q_2^2 q_3 + \alpha_3^{III} q_3^3 + \alpha_4^{III} q_3 q_4^2 + \alpha_5^{III} q_1 q_2 q_4 \\ \alpha_1^{IV} q_1^2 q_4 + \alpha_2^{IV} q_2^2 q_4 + \alpha_3^{IV} q_3^2 q_4 + \alpha_4^{IV} q_4^3 + \alpha_5^{IV} q_1 q_2 q_3 \end{pmatrix}, \quad (6.22)$$

and,

$$\tilde{\mathbf{N}}_{\tilde{q}} = \begin{pmatrix} \alpha_1^I \tilde{q}_1^3 \\ \alpha_2^{II} \tilde{q}_2^3 \\ \alpha_3^{III} \tilde{q}_3^3 \\ \alpha_4^{IV} \tilde{q}_4^3 \end{pmatrix}. \quad (6.23)$$

It is noteworthy that due to unstable responses, another NROM candidate which only consists of the mixed-mode terms is unable to be employed for comparison.

In both NROMs, viscous damping is added, and the damping ratio is assumed to be $\zeta = 0.1\%$ for all modes. These two equations are integrated over the same force time history defined at discrete data points for each specific excitation case using the fourth-order Runge-Kutta integration operator. The random data is generated identically for that used in the previous FE simulation. The discrete-time period between consecutive time history points is 10^{-4} s and the integration was performed over a period of 50 s. The displacement response of the same point considered in the FE simulation is again used here, and similarly, the spectrum results are employed to demonstrate the frequency-shift phenomenon.

Firstly, the excitations considered in Fig. 6.3 are simulated using two NROMs, and the result is shown in Fig. 6.6. For this excitation case, the magnitudes of the random components are $\mathbf{P}_r = \frac{4}{\pi^2 \rho h} [1, 1, 1, 1]^T \times 10^{-2}$ and $\mathbf{P}_r = \frac{4}{\pi^2 \rho h} [1, 1, 1, 1]^T$ for the simulation (i) and (ii) respectively. The magnitudes of harmonic component for both cases are $\mathbf{P}_h = [\mathbf{0}]^T$. From the results of the simulation (i), it can be seen that the responses of the uncoupled and coupled models are nearly identical and their resonant frequencies are close to the linear natural frequencies. As expected, this observation confirms that the effect of the coupled-mode terms is insignificant for the low-response-amplitude situation. For the high-level excitation situation, the result (ii), the resonant frequencies for both models tend to shift to higher values. However, the shift level of the coupled model is more significant than that of the uncoupled model. Note that the frequency shift for the results of the uncoupled model is due to the backbone curve distortion. This result demonstrates that both single- and mixed-mode terms can cause frequency shifting in the nonlinear region. Based on the qualitative comparison between Fig. 6.3 and Fig. 6.6, it is unable to distinguish which NROM is more

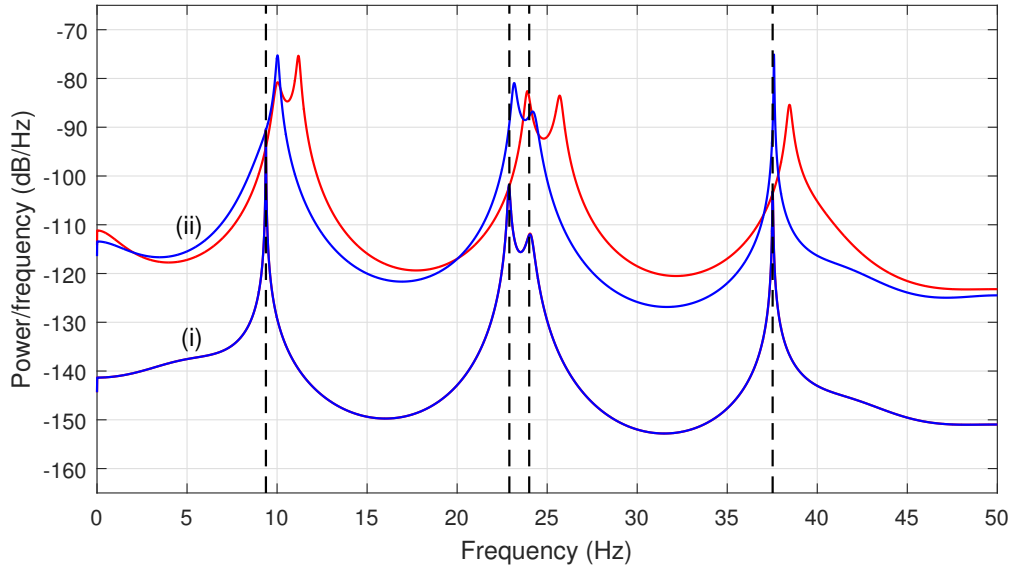


Fig. 6.6 The power spectral density of the response of the plate depicted in Fig. 6.1 to random excitations in the first four modes, computed using NROM simulation data. The two force amplitudes used are: (i) $\mathbf{P}_r = \frac{4 \times 10^{-2}}{\pi^2 \rho h} (1, 1, 1, 1)^\top$ and (ii) $\mathbf{P}_r = \frac{4}{\pi^2 \rho h} (1, 1, 1, 1)^\top$. The displacement response $x = \frac{1}{2}q_1 - \frac{\sqrt{2}}{2}q_2 - \frac{\sqrt{2}}{2}q_3 + q_4$ is considered, which is equivalent to that at the point with the coordinates $(x, y) = \frac{3}{4}(a, b)$. The blue and red lines represent the results of the uncoupled and coupled models respectively, and the dashed-black lines denote the linear natural frequencies.

accurate for describing the nonlinear behaviour of the example plate.

Then, the NROMs are used to simulate the plate under the hybrid excitation considered in Fig. 6.4. The corresponding force amplitudes used are $\mathbf{P}_r = \frac{4}{\pi^2 \rho h} (1, 1, 1, 1)^\top \times 10^{-2}$ and $\mathbf{P}_h = \frac{4}{\rho h a b} (5, 0, 0, 0)^\top \times 10^{-3}$. Fig. 6.7 shows the simulation results for this case. We can see that for Mode II, III and IV, compared with linear natural frequencies, their resonant frequencies of the coupled model result have increased, while those in the uncoupled model result have not changed. For this case, it is the coupled model that can more accurately represent the nonlinear behaviour of the full-order FE model, see from the comparison between Fig. 6.4 and Fig. 6.6.

The NROM simulation results in Fig. 6.6 and Fig. 6.7 have further demonstrated that the mixed-mode terms would cause modal interactions, especially for the multi-mode excitation situation. However, it is not clear whether this modal interaction is the resonant one investigated in Chapter 5. Note that the one-to-one modal interaction is excluded as it may only occur between Mode II and III. By examining the linear frequencies ratio and nonlinear terms, it can be predicted that the multi-mode auto-parametric interaction involving the

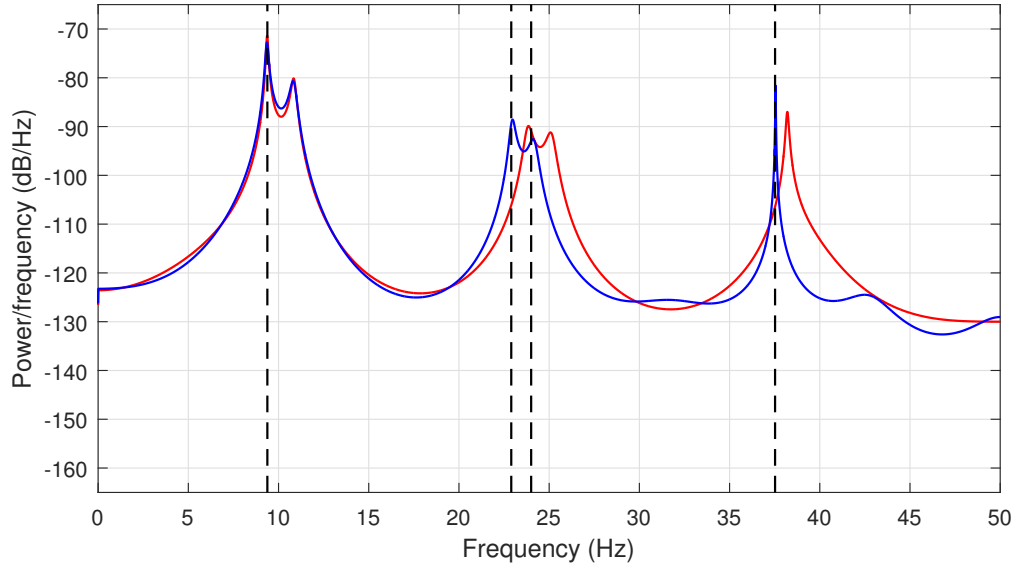


Fig. 6.7 The power spectral density of the response of the plate depicted in Fig. 6.1 to a hybrid excitation in the first four modes, computed using NROM simulation data. The hybrid excitation scenario is that all four modes are randomly excited and Mode I is sinusoidal forced simultaneously: $\mathbf{P}_r = \frac{4 \times 10^{-1}}{\pi^2 \rho h} (1, 1, 1, 1)^\top$, $\mathbf{P}_h = \frac{4 \times 10^{-3}}{\rho h a b} (5, 0, 0, 0)^\top$ and $\Omega = \omega_{n1}$. The displacement response $x = \frac{1}{2}q_1 - \frac{\sqrt{2}}{2}q_2 - \frac{\sqrt{2}}{2}q_3 + q_4$ is considered. The denotations are the same as those of Fig. 6.6.

four modes of interest may occur. For example, the nonlinear terms $q_2 q_3 q_4$ in the EoM of Mode I may give birth to a complex conjugate $u_{2p} u_{3p} u_{4m}$ and $u_{2m} u_{3m} u_{4p}$ during the nonlinear near-identity transform of the direct normal form technique application. These derived terms respond at the fundamental frequency of Mode I, thus causing a resonant modal interaction. Therefore, a group of extra NROM simulations is performed in which only Mode I and Mode III are directly excited:

- In Fig. 6.8(a), Mode I and III are randomly forced at two levels: (i) $\mathbf{P}_r = \frac{4}{\pi^2 \rho h} (1, 0, 1, 0)^\top \times 10^{-2}$ and $\mathbf{P}_h = (\mathbf{0})^\top$, and (ii) $\mathbf{P}_r = \frac{4}{\pi^2 \rho h} (1, 0, 1, 0)^\top$ and $\mathbf{P}_h = (\mathbf{0})^\top$.
- In Fig. 6.8(b), Mode I and III are randomly forced at a relatively low level and an extra sine-wave force is applied to Mode I: $\mathbf{P}_r = \frac{4}{\pi^2 \rho h} (1, 0, 1, 0)^\top \times 10^{-2}$, $\mathbf{P}_h = \frac{4}{\rho h a b} (5, 0, 0, 0)^\top \times 10^{-3}$ and $\Omega = \omega_{n1}$.
- In Fig. 6.8(c), Mode I and III are randomly forced at a relatively low level and an extra sine-wave force is applied to Mode III: $\mathbf{P}_r = \frac{4}{\pi^2 \rho h} (1, 0, 1, 0)^\top \times 10^{-2}$, $\mathbf{P}_h = \frac{4}{\rho h a b} (0, 0, 5, 0)^\top \times 10^{-3}$ and $\Omega = \omega_{n3}$.

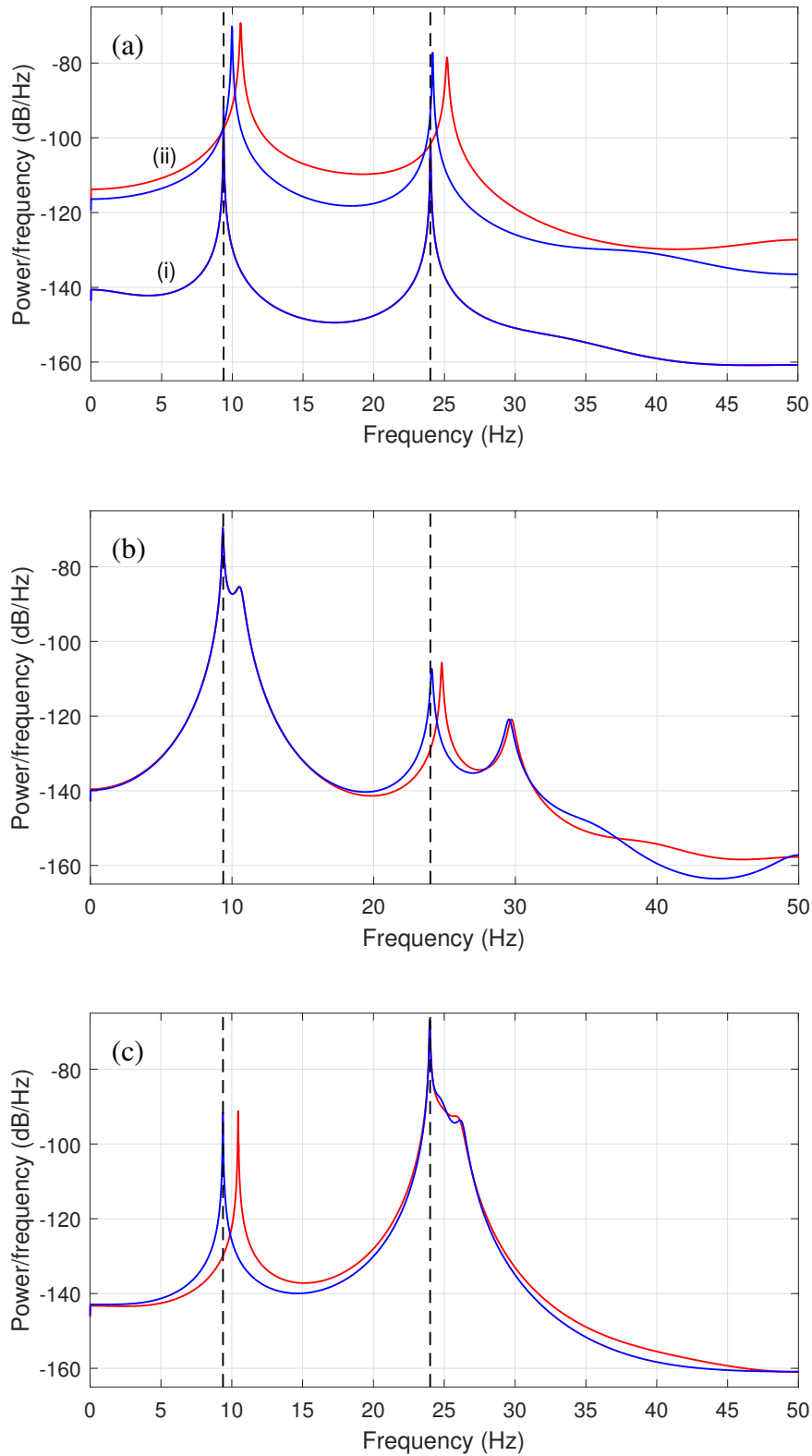


Fig. 6.8 The power spectral density of the response of the plate depicted in Fig. 6.1, computed using the NROM simulation data, when (a) Mode I and III are randomly forced, (b) only Mode I is additionally forced harmonically and (c) only Mode III is additionally forced harmonically.

As with Fig. 6.6, Fig. 6.8(a) shows a similar result that for the low-level forcing case, the results of coupled and uncoupled models are close and for the high-level case, they both present frequency-shift phenomena and the shift level of the coupled model results is higher. Also, the observation from Fig. 6.8(b) and Fig. 6.8(c) is similar to that of Fig. 6.7 that the power increment of one mode due to the harmonic forcing results in a resonant frequency increasing of the other mode. Note that in Fig. 6.8(b), the resonant peak at around 30Hz is due to the three-times harmonic response of Mode I. From the results illustrated in Fig. 6.8, we may conclude that:

- the frequency shift is not caused by the double-mode one-to-one or multi-mode auto-parametric modal interaction because Mode II and IV are always still for this case.
- the occurrence of the frequency shift is not affected by the number of modes involved but the power level of the nonlinear dynamic system.
- the effect of modal interactions in the example plate due to mixed-mode terms is bilateral, see from Fig. 6.8(b) and Fig. 6.8(c).

6.4 Effect of the nonlinear coupled-mode terms explanation

In this section, backbone curves, approximated by the direct normal form technique, are used to explain the effect of mixed-mode terms on the frequency shift when systems are under multi-frequency-multi-mode excitation. More specifically, we investigate how the inclusion of mixed-mode terms affects the configuration of the ‘original’ backbone curves of the modes without resonant modal interaction. During the approximation of backbone curves, the applicability of the single-fundamental-response-frequency assumption used in previous chapters is further discussed. Based on that, a non-resonant modal interaction related to the mixed-mode nonlinear terms is introduced which is helpful for understanding the frequency-shift phenomenon.

6.4.1 Non-resonant interaction

To exclude the potential occurrence of the multi-mode auto-parametric interaction since it was demonstrated to not occur in the previous simulations, a three-mode truncated NROM consisting of Mode I, II and III is considered instead for simplifying the problem. Using

Eq. (6.20a), the EoM of the equivalent conservative system is written as,

$$\ddot{\mathbf{q}} + \mathbf{\Lambda}\mathbf{q} + \mathbf{N}_q(\mathbf{q}) = \mathbf{0}, \quad (6.24)$$

where the vector of nonlinear terms is,

$$\mathbf{N}_q = \begin{pmatrix} \alpha_1^I q_1^3 + \alpha_2^I q_1 q_2^2 + \alpha_3^I q_1 q_3^2 + \alpha_4^I q_1 q_4^2 \\ \alpha_1^{II} q_1^2 q_2 + \alpha_2^{II} q_2^3 + \alpha_3^{II} q_2 q_3^2 + \alpha_4^{II} q_2 q_3^2 \\ \alpha_1^{III} q_1^2 q_3 + \alpha_2^{III} q_2^2 q_3 + \alpha_3^{III} q_3^3 + \alpha_4^{III} q_3 q_4^2 \end{pmatrix}. \quad (6.25)$$

Based on the linear natural frequencies values in Table 6.2, i.e. $\omega_{n1} : \omega_{n2} : \omega_{n3} \approx 1 : 2.5 : 2.5$, a reasonable modal response frequency relation may be assumed, i.e. $\omega_{r1} : \omega_{r2} : \omega_{r3} = 1 : 2.5 : 2.5$. Through the application of the direct normal form technique, the resulting time-invariant equations are,

$$\left[(\omega_{n1}^2 - \omega_{r1}^2) + \frac{1}{4} (3\alpha_1^I U_1^2 + 2\alpha_2^I U_2^2 + 2\alpha_3^I U_3^2) \right] U_1 = 0, \quad (6.26a)$$

$$\left[(\omega_{n2}^2 - \omega_{r2}^2) + \frac{1}{4} (2\alpha_1^{II} U_1^2 + 3\alpha_2^{II} U_2^2 + (2+p)\alpha_3^{II} U_3^2) \right] U_2 = 0, \quad (6.26b)$$

$$\left[(\omega_{n3}^2 - \omega_{r3}^2) + \frac{1}{4} (2\alpha_1^{III} U_1^2 + (2+p)\alpha_2^{III} U_2^2 + 3\alpha_3^{III} U_3^2) \right] U_3 = 0, \quad (6.26c)$$

where $\omega_{r2} = \omega_{r3}$ has been used, $p = e^{i2|\phi_2 - \phi_3|}$ and U_i , ω_{ri} and ϕ_i are the fundamental response amplitude, frequency and phase of the i^{th} mode respectively.

Following the ‘classic’ steps of backbone curve solution approximation, see Chapter 4 and Chapter 5, successively setting U_2 and U_3 , U_1 and U_3 , and U_1 and U_2 to zero in Eqs. (6.26) gives the expressions of three single-mode backbone curves, as

$$S1 : \quad \omega_{r1}^2 = \omega_{n1}^2 + \frac{3}{4} \alpha_1^I U_1^2, \quad (6.27a)$$

$$S2 : \quad \omega_{r2}^2 = \omega_{n2}^2 + \frac{3}{4} \alpha_2^{II} U_2^2, \quad (6.27b)$$

$$S3 : \quad \omega_{r3}^2 = \omega_{n3}^2 + \frac{3}{4} \alpha_3^{III} U_3^2. \quad (6.27c)$$

Furthermore, because of the specific natural frequencies relation and the phase-related terms associated with Mode II and III, there exist double-mode backbone curve solutions, i.e. $D23$, related to these two modes here. So if $U_1 = 0$, while $U_2 \neq 0$ and $U_3 \neq 0$ and Mode II and III are assumed to respond at the same frequency, Eqs. (6.26b) and (6.26c) can be rearranged

with submission of $\omega_r = \omega_{r2} = \omega_{r3}$. Therefore, the expressions of $D23$ may be derived: for the in-unison case, i.e. $p = 1$, Eqs. (6.26) gives,

$$D23_{[i]s_2}^{\pm} : \begin{cases} U_2^2 = U_{[i]s_2}^2 + \eta_{[i]s_2} U_3^2, \\ \omega_r^2 = \omega_{[i]s_2}^2 + \frac{3}{4} \gamma_{[i]s_2} U_3^2, \end{cases} \quad (6.28a)$$

or

$$D23_{[i]s_3}^{\pm} : \begin{cases} U_3^2 = U_{[i]s_3}^2 + \eta_{[i]s_3} U_2^2, \\ \omega_r^2 = \omega_{[i]s_3}^2 + \frac{3}{4} \gamma_{[i]s_3} U_2^2, \end{cases} \quad (6.28b)$$

and for the out-of-unison case, i.e. $p = -1$, we obtain

$$D23_{[o]s_2}^{\pm} : \begin{cases} U_2^2 = U_{[o]s_2}^2 + \eta_{[o]s_2} U_3^2, \\ \omega_r^2 = \omega_{[o]s_2}^2 + \frac{1}{4} \gamma_{[o]s_2} U_3^2, \end{cases} \quad (6.29a)$$

or

$$D23_{[o]s_3}^{\pm} : \begin{cases} U_3^2 = U_{[o]s_3}^2 + \eta_{[o]s_3} U_2^2, \\ \omega_r^2 = \omega_{[o]s_3}^2 + \frac{1}{4} \gamma_{[o]s_3} U_2^2, \end{cases} \quad (6.29b)$$

where the second subscript of the backbone curve label denotes where the corresponding backbone curve bifurcates from, the coefficients, U^2 , ω^2 , η and γ are time-invariant and the calculated expressions are listed in Table 6.3.

Furthermore, it is also possible to have solutions where only Mode I and II are present. Eqs. (6.26) with the substitution $U_3 = 0$ becomes

$$\omega_{r1}^2 = \omega_{n1}^2 + \frac{3}{4} \alpha_1^I U_1^2 + \frac{1}{2} \alpha_2^I U_2^2, \quad (6.30a)$$

$$\omega_{r2}^2 = \omega_{n2}^2 + \frac{3}{4} \alpha_2^{II} U_2^2 + \frac{1}{2} \alpha_1^{II} U_1^2. \quad (6.30b)$$

In Eqs. (6.30), since all the nonlinear terms retained are unconditionally resonant, no phase condition is imposed, i.e. phase-unlocking, and the modal response frequency ratio can be arbitrary. Similarly, the same result is found when only Mode I and III are present, i.e.

$$\omega_{r1}^2 = \omega_{n1}^2 + \frac{3}{4} \alpha_1^I U_1^2 + \frac{1}{2} \alpha_3^I U_3^2, \quad (6.31a)$$

BP	D23 _[i]		D23 _[o]	
	S2	S3	S2	S3
$U_{[tr]s_n}^2$	$\frac{4}{3} \frac{\omega_{n3}^2 - \omega_{n2}^2}{\alpha_2^{\text{II}} - \alpha_2^{\text{III}}}$	$\frac{4}{3} \frac{\omega_{n3}^2 - \omega_{n2}^2}{\alpha_3^{\text{II}} - \alpha_3^{\text{III}}}$	$\frac{4(\omega_{n3}^2 - \omega_{n2}^2)}{3\alpha_2^{\text{II}} - \alpha_2^{\text{III}}}$	$\frac{4(\omega_{n3}^2 - \omega_{n2}^2)}{\alpha_2^{\text{II}} - 3\alpha_3^{\text{III}}}$
$\omega_{[tr]s_n}^2$	$\frac{\alpha_2^{\text{II}} \omega_{n3}^2 - \alpha_2^{\text{III}} \omega_{n2}^2}{\alpha_2^{\text{II}} - \alpha_2^{\text{III}}}$	$\frac{\alpha_3^{\text{II}} \omega_{n3}^2 - \alpha_3^{\text{III}} \omega_{n2}^2}{\alpha_3^{\text{II}} - \alpha_3^{\text{III}}}$	$\frac{3\alpha_2^{\text{II}} \omega_{n3}^2 - \alpha_2^{\text{III}} \omega_{n2}^2}{3\alpha_2^{\text{II}} - \alpha_2^{\text{III}}}$	$\frac{\alpha_3^{\text{II}} \omega_{n3}^2 - 3\alpha_3^{\text{III}} \omega_{n2}^2}{\alpha_3^{\text{II}} - 3\alpha_3^{\text{III}}}$
$\eta_{[tr]s_n}$	$\frac{\alpha_3^{\text{III}} - \alpha_3^{\text{II}}}{\alpha_2^{\text{II}} - \alpha_2^{\text{III}}}$	$\frac{\alpha_2^{\text{III}} - \alpha_2^{\text{II}}}{\alpha_3^{\text{II}} - \alpha_3^{\text{III}}}$	$\frac{3\alpha_3^{\text{III}} - \alpha_3^{\text{II}}}{3\alpha_2^{\text{II}} - \alpha_2^{\text{III}}}$	$\frac{\alpha_2^{\text{III}} - 3\alpha_2^{\text{II}}}{\alpha_3^{\text{II}} - 3\alpha_3^{\text{III}}}$
$\gamma_{[tr]s_n}$	$\frac{\alpha_2^{\text{II}} \alpha_3^{\text{III}} - \alpha_2^{\text{III}} \alpha_3^{\text{II}}}{\alpha_2^{\text{II}} - \alpha_2^{\text{III}}}$	$\frac{\alpha_3^{\text{II}} \alpha_2^{\text{III}} - \alpha_3^{\text{III}} \alpha_2^{\text{II}}}{\alpha_3^{\text{II}} - \alpha_3^{\text{III}}}$	$\frac{9\alpha_2^{\text{II}} \alpha_3^{\text{III}} - \alpha_2^{\text{III}} \alpha_3^{\text{II}}}{3\alpha_2^{\text{II}} - \alpha_2^{\text{III}}}$	$\frac{\alpha_3^{\text{II}} \alpha_2^{\text{III}} - 9\alpha_2^{\text{II}} \alpha_3^{\text{III}}}{\alpha_3^{\text{II}} - \alpha_3^{\text{III}}}$

Table 6.3 Expressions of the parameters in the descriptions of the double-mode backbone curves of the example plate. In the subscripts of the parameter labels, ‘ s_n ’ = ‘ s_2 ’ or ‘ s_3 ’ indicates the position of the double-mode backbone curves bifurcating from, i.e. either S2 or S3, and ‘ tr ’ = ‘ i ’ or ‘ o ’ stands for the type of interaction, i.e. either *in-unison* or *out-of-unison*. BP is short for bifurcation position.

$$\omega_{r3}^2 = \omega_{n3}^2 + \frac{3}{4} \alpha_3^{\text{III}} U_3^2 + \frac{1}{2} \alpha_1^{\text{III}} U_1^2. \quad (6.31b)$$

Therefore, the solutions of Eqs. (6.30) and (6.31) are not resonant and may be impossible for the single-frequency-single-mode-forced situation. Mode I is considered to be non-resonant to Mode II and III. The details about the influence of phase-locking on internal resonance can be found in [34].

When considering the situation of multi-frequency-multi-mode excitation, the solutions of Eqs. (6.30) and (6.31) may be valid. For example, the non-resonant Mode I is activated by external forcing and responding sinusoidally at a frequency other than the commensurable one of Mode II or III, e.g. $3\omega_{r1} = \omega_{r2,r3}$ or $\omega_{r1} = \omega_{r2,r3}$, to avoid resonance. Rearranging Eq. (6.30b) and Eq. (6.31b) results in modified backbone curve solutions, \hat{S}_2 and \hat{S}_3

$$\hat{S}_2: \quad \omega_{r2}^2 = \hat{\omega}_{n2}^2 + \frac{3}{4} \alpha_2^{\text{II}} U_2^2, \quad (6.32a)$$

$$\hat{S}_3: \quad \omega_{r3}^2 = \hat{\omega}_{n3}^2 + \frac{3}{4} \alpha_3^{\text{III}} U_3^2, \quad (6.32b)$$

where

$$\hat{\omega}_{n2}^2 = \omega_{n2}^2 + \frac{1}{2} \alpha_1^{\text{II}} U_1^2, \quad (6.33a)$$

$$\hat{\omega}_{n3}^2 = \omega_{n3}^2 + \frac{1}{2}\alpha_1^{\text{III}}U_1^2, \quad (6.33b)$$

and the hat symbol ‘ $\hat{\cdot}$ ’ denotes the solutions with consideration of the effect of Mode I for distinction. Similarly, the expressions of double-mode backbone curves are adjusted to be,

$$\hat{D}23_{[i]s_2}^{\pm} : \begin{cases} U_2^2 = \hat{U}_{[i]s_2}^2 + \eta_{[i]s_2}U_3^2, \\ \omega_r^2 = \hat{\omega}_{[i]s_2}^2 + \frac{3}{4}\gamma_{[i]s_2}U_3^2, \end{cases} \quad (6.34a)$$

or

$$\hat{D}23_{[i]s_3}^{\pm} : \begin{cases} U_3^2 = \hat{U}_{[i]s_3}^2 + \eta_{[i]s_3}U_2^2, \\ \omega_r^2 = \hat{\omega}_{[i]s_3}^2 + \frac{3}{4}\gamma_{[i]s_3}U_2^2, \end{cases} \quad (6.34b)$$

and,

$$\hat{D}23_{[o]s_2}^{\pm} : \begin{cases} U_2^2 = \hat{U}_{[o]s_2}^2 + \eta_{[o]s_2}U_3^2, \\ \omega_r^2 = \hat{\omega}_{[o]s_2}^2 + \frac{1}{4}\gamma_{[o]s_2}U_3^2, \end{cases} \quad (6.35a)$$

or

$$\hat{D}23_{[o]s_3}^{\pm} : \begin{cases} U_3^2 = \hat{U}_{[o]s_3}^2 + \eta_{[o]s_3}U_2^2, \\ \omega_r^2 = \hat{\omega}_{[o]s_3}^2 + \frac{1}{4}\gamma_{[o]s_3}U_2^2, \end{cases} \quad (6.35b)$$

where,

$$\hat{U}_{[tr]s_n}^2 = U_{[tr]s_n}^2 + \mu_{[tr]s_n}U_1^2, \quad (6.36a)$$

$$\hat{\omega}_{[tr]s_n}^2 = \omega_{[tr]s_n}^2 + \frac{1}{2}\nu_{[tr]s_n}U_1^2. \quad (6.36b)$$

The calculated expressions of the additive coefficients, i.e. μ and ν in Eq. (6.36), are listed in Table 6.4.

Comparing modified backbone solutions of Mode II and III, Eqs. (6.32a), (6.32b), (6.34) and (6.35), with the original ones, Eqs. (6.27b), (6.27c), (6.28) and (6.29), it can be seen that their base structures are identical. While, considering Eq. (6.33) for the modified single-mode backbone solutions, the ‘effective’ natural frequencies, $\hat{\omega}_{ni}$, increases with the response amplitude of Mode I (refer $\alpha_1^{\text{II}} > 0$ and $\alpha_1^{\text{III}} > 0$). This further results in the increment of the resonant response frequencies of Mode II and III, i.e. ω_{ri} . This explains

	$\hat{D}23_{[i]}$		$\hat{D}23_{[o]}$	
<i>BP</i>	<i>S2</i>	<i>S3</i>	<i>S2</i>	<i>S3</i>
$\mu_{[tr]s_n}$	$\frac{2\alpha_1^{\text{III}} - \alpha_1^{\text{II}}}{3\alpha_2^{\text{II}} - \alpha_2^{\text{III}}}$	$\frac{2\alpha_1^{\text{III}} - \alpha_1^{\text{II}}}{3\alpha_3^{\text{II}} - \alpha_3^{\text{III}}}$	$\frac{2(\alpha_1^{\text{III}} - \alpha_1^{\text{II}})}{3\alpha_2^{\text{II}} - \alpha_2^{\text{III}}}$	$\frac{2(\alpha_1^{\text{III}} - \alpha_1^{\text{II}})}{\alpha_3^{\text{II}} - 3\alpha_3^{\text{III}}}$
$\nu_{[tr]s_n}$	$\frac{\alpha_2^{\text{II}}\alpha_1^{\text{III}} - \alpha_1^{\text{II}}\alpha_2^{\text{III}}}{\alpha_2^{\text{II}} - \alpha_2^{\text{III}}}$	$\frac{\alpha_3^{\text{II}}\alpha_1^{\text{III}} - \alpha_1^{\text{II}}\alpha_3^{\text{III}}}{\alpha_3^{\text{II}} - \alpha_3^{\text{III}}}$	$\frac{3\alpha_2^{\text{II}}\alpha_1^{\text{III}} - \alpha_1^{\text{II}}\alpha_2^{\text{III}}}{3\alpha_2^{\text{II}} - \alpha_2^{\text{III}}}$	$\frac{\alpha_3^{\text{II}}\alpha_1^{\text{III}} - 3\alpha_1^{\text{II}}\alpha_3^{\text{III}}}{\alpha_3^{\text{II}} - 3\alpha_3^{\text{III}}}$

Table 6.4 Expressions of the extra parameters in the descriptions of the double-mode backbone curves of the example plate depicted, with non-resonant interactions considered.

the frequency-shift phenomenon caused by the nonlinear mixed-mode terms observed in spectrum results. A similar phenomenon can be observed in the double-mode backbone solution. In Eqs. (6.36), $\hat{\omega}_{[tr]s_n}$ is the function of U_1 , thus the resonant frequencies, ω_r , are also affected by the response amplitude of Mode I, see Eqs. (6.34) and (6.35).

Furthermore, to investigate the bilateral feature of this modal interaction, the effect of the presence of non-resonant modes to Mode I, i.e. Mode II and III, on the backbone curve $S1$ is considered. Simply rearranging Eq. (6.26a) gives the updated expression of $S1$, such that,

$$\hat{S}1 : \quad \omega_{r1}^2 = \hat{\omega}_{n1}^2 + \frac{3}{4}\alpha_1^{\text{I}}U_1^2, \quad (6.37)$$

where

$$\hat{\omega}_{n1}^2 = \omega_{n1}^2 + \frac{1}{2}\alpha_2^{\text{I}}U_2^2 + \frac{1}{2}\alpha_3^{\text{I}}U_3^2. \quad (6.38)$$

From this, we could predict that if Mode II and III are non-resonantly present, the value of the resonant frequency of the backbone curve $S1$ will be larger, corresponding to a right-forward shift in the frequency spectrum. Different from the modal interactions investigated in Chapter 4 and Chapter 5, the interaction between Mode I and Mode II and III considered here is not limited to the commensurable response frequencies and also does not cause resonance; therefore it is denoted as non-resonant modal interaction.

6.4.2 Backbone curves and forced response results

Now, the coefficients values are substituted into Eqs. (6.34) and (6.35) to compute the backbone curves of Mode II and III of the example plate. Then the numerically computed forced responses for the multi-frequency-multi-mode-forced situation are compared with the backbone curves to illustrate the effect of mixed-mode terms on frequency shift.

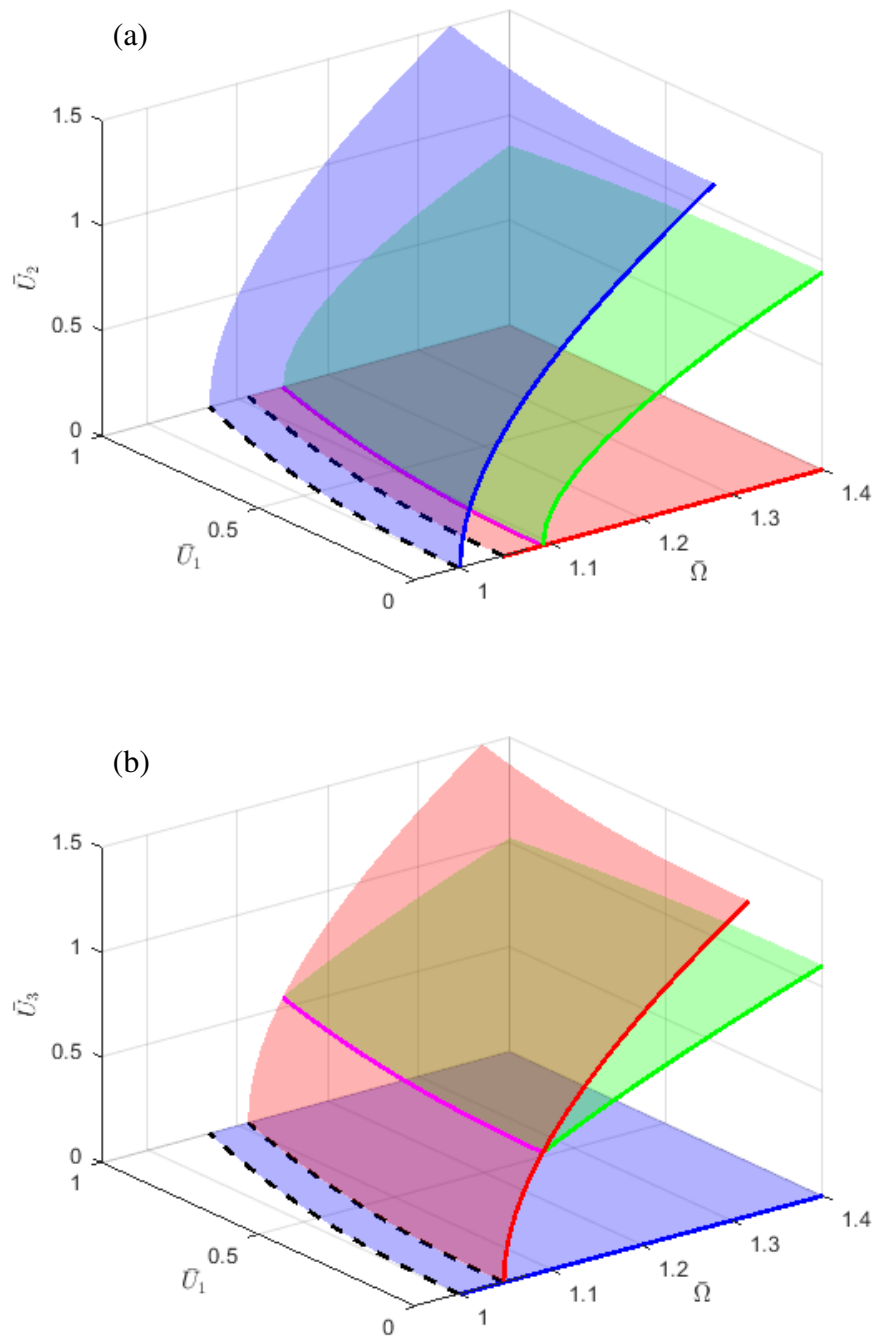


Fig. 6.9 The backbone curves of Mode II and III, of the plate depicted in Fig. 6.1 with considering the effect of the non-resonant modal interaction with Mode I. The single-mode backbone curves $\hat{S}2$ and $\hat{S}3$ are shaded in blue and red respectively, and the double-mode backbone curves, $\hat{D}23_{[i]}^{\pm}$, are in green. The black dash lines indicate the ‘effective’ natural frequencies described by Eq. (6.33) and magenta lines indicate the ‘effective’ bifurcation points described by Eq. (6.36). The blue, red and green lines represent the backbone curves $S2$, $S3$ and $D23_{[i]}^{\pm}$ respectively.

Fig. 6.9 shows backbone curves results projected onto a three-dimensional space of the resonant frequency, $\bar{\omega}_r$, against the fundamental response amplitude of Mode II or Mode III, \bar{U}_2 or \bar{U}_3 , against the fundamental response amplitude of Mode I, \bar{U}_1 . Here for the better illustration, the coordinates are scaled using $\bar{U}_i = U_i/h$ and $\bar{\omega}_r = \omega_r/\omega_{n2}$. Note that due to the inexistence of valid solution of Eqs. (6.35), there is no out-of-unison double-mode backbone curve for this case. From the results, it can be seen that the ‘effective’ natural frequencies of single-mode backbone curves (the black dash lines) and bifurcation points of double-mode backbone curves (solid magenta lines) are increasing with the response amplitude of Mode I, i.e. bending to the right viewing from negative z -direction. Meanwhile, the resonant frequencies of all the backbone curves related to Mode II and III have shifted to a higher value because of the appearance of \bar{U}_1 just as expected. The backbone curve results demonstrate that the presence of non-resonant modes may make the other vibration modes of the plate system appear stiffer.

Then the multi-frequency-multi-mode-forced responses of the example plate are computed. Firstly, a somewhat artificial situation is considered: the forcing of Mode I is such that the resonant response of this mode, U_1 , is at a constant amplitude, Mode II is left unexcited and Mode III is directly forced at a constant amplitude but a series of frequencies near its linear natural frequency. Here the forcing amplitude is chosen to be big enough such that the resonant modal interaction between Mode II and III can be triggered. The mathematical expression of this forced situation, which is also the equation used in the continuation simulation, is,

$$\begin{aligned} q_1 &= U_1 \cos(\omega_{r1}t + \phi_1), \\ \ddot{q}_2 + 2\zeta\omega_{n2}\dot{q}_2 + \omega_{n2}^2q_2 + \alpha_1^{\text{II}}q_1^2q_2 + \alpha_2^{\text{II}}q_2^3 + \alpha_3^{\text{II}}q_2q_3^2 &= 0, \\ \ddot{q}_3 + 2\zeta\omega_{n3}\dot{q}_2 + \omega_{n3}^2q_3 + \alpha_1^{\text{III}}q_1^2q_3 + \alpha_2^{\text{III}}q_2^2q_3 + \alpha_3^{\text{III}}q_3^3 &= F \cos(\Omega t). \end{aligned} \quad (6.39)$$

Fig. 6.10 shows the responses of the plate regarding the response amplitude of Mode II and Mode III in the same three-dimension projection space of Fig. 6.9. To aid comparison, the backbone curves are also shown, shaded in grey. In this plot, the single-mode and double-mode forced responses for different response amplitudes of Mode I are shown to surround their corresponding backbone curves. It can be seen that the maximum response points of each response branch are close to the backbone surfaces, which shows a frequency shift trend due to the presence of Mode I. Likewise, we can note that the amplitude of the peak response (either single-mode or double-mode) is also increased due to the increased frequency at which the peak response occurs.

Finally, a more realistic excitation case is considered in which Mode I is forced at a fixed frequency, Ω_c , and a constant amplitude, F_c , Mode III is still directly forced and Mode II is left unexcited, i.e.,

$$\begin{aligned} \ddot{q}_1 + 2\zeta\omega_{n1}\dot{q}_1 + \omega_{n1}^2q_1 + \alpha_1^I q_1^3 + \alpha_2^I q_1q_2^2 + \alpha_3^I q_1q_3^2 &= F_c \cos(\Omega_c t + \phi_1) \\ \ddot{q}_2 + 2\zeta\omega_{n2}\dot{q}_2 + \omega_{n2}^2q_2 + \alpha_1^{II} q_1^2q_2 + \alpha_2^{II} q_2^3 + \alpha_3^{II} q_2q_3^2 &= 0, \\ \ddot{q}_3 + 2\zeta\omega_{n3}\dot{q}_3 + \omega_{n3}^2q_3 + \alpha_1^{III} q_1^2q_3 + \alpha_2^{III} q_2^2q_3 + \alpha_3^{III} q_3^3 &= F \cos(\Omega t). \end{aligned} \quad (6.40)$$

The numerical results for this case are shown in Fig. 6.11. It can be seen that due to the interactions between Mode I and Mode III, the stiffening effect varies with excitation frequency due to the variance of the response amplitudes. For this case, the backbone curves still capture the nonlinear dynamic features of the forced-response curves, e.g. peak amplitude points, bifurcations and resonant frequency shift.

The backbone curve and forced-response results indicate that when the system is under multi-mode excitation, the associated modes, either resonant or non-resonant, must be considered together to give an accurate nonlinear response prediction, i.e. resonant frequency and bifurcation positions. Furthermore, the non-resonant modal interaction also highlights the importance of the inclusion of mixed-mode terms for nonlinear model selection.

6.5 Summary

In this chapter, we have observed the shifting phenomenon of resonant frequencies in a thin plate due to the geometrical nonlinearity of the multi-mode-forced situation. This phenomenon has been demonstrated by the dynamic responses of a thin rectangular plate with an ideal edge-pinned constraint. The response data in the time-domain were simulated using the implicit integrator on a ‘full-order’ finite element model which includes the geometrically nonlinear effect. Contrary to the finding in the previous chapters that there exists no interaction between non-resonant modes for the single-mode-single-frequency excitation case, the simulation results have demonstrated that the non-resonant modes do affect each other when multiple modes are activated simultaneously.

To investigate the interactions between non-resonant modes, the nonlinear reduced-order model has been developed by decomposing the nonlinear partial differential equation governing the motion of the plate using the Galerkin method. The resulting reduced-order model consists of both single-mode and mixed-mode nonlinear terms in the EoM of each mode. Based on the knowledge that only the mixed-mode nonlinear terms can cause the

influences between modes, two four-mode truncated nonlinear reduced-order models, one with both single- and mixed-mode terms and the other one only with single-mode terms, have been considered. They have been used to generate the dynamic response for comparison with each other and with FE results, to investigate the effect of mixed-mode terms. Although the NROM results are unable to be exactly matched with FE results due to the issue of shear locking in thin shell elements, i.e. finite element solutions of thin shell elements become stiffer from those predicted by Kirchhoff's theory [9], the qualitative comparison has shown the 'full' NROM can better catch the nonlinear frequency shifting behaviour for more forced situations. The NROM mutual comparison has also demonstrated the energy transfer between modes is due to the existence of the mixed-mode terms.

For understanding the mechanism of how mixed-mode terms affect the response frequency, the direct normal form method has been applied to estimate the backbone curves of the NROM of the plate under consideration. However, different from the standard process in previous chapters where the assumption that only single mode or multiple modes responding at commensurable frequencies is made when approximate the backbone curves, all modes have been regarded to be activated as multi-mode excitation considered. This leaves an open question as to whether an energy analysis for the plate with random input would explain what is happening. From the updated backbone curves of a three-mode NROM, consisting of Mode I, II and III, we have seen that due to the presence of non-resonant Mode I, both single- and double-mode- backbone curves of resonantly interactive Mode II and III have shifted. More specifically, the 'effective' natural frequencies and bifurcation positions have shifted. The forced response results have also been computed for the multi-mode-forced situation, which has once again proved the interaction between non-resonant modes. It is noteworthy that this non-resonant modal interaction could also occur in discrete systems, see the example in Appendix B.

In the following chapter, an approach for nonlinear system identification is introduced. The understanding of the non-resonant modal interactions that have been gained here inspires using the expressions describing backbone curves as a parametric model for multi-mode parameters estimation.

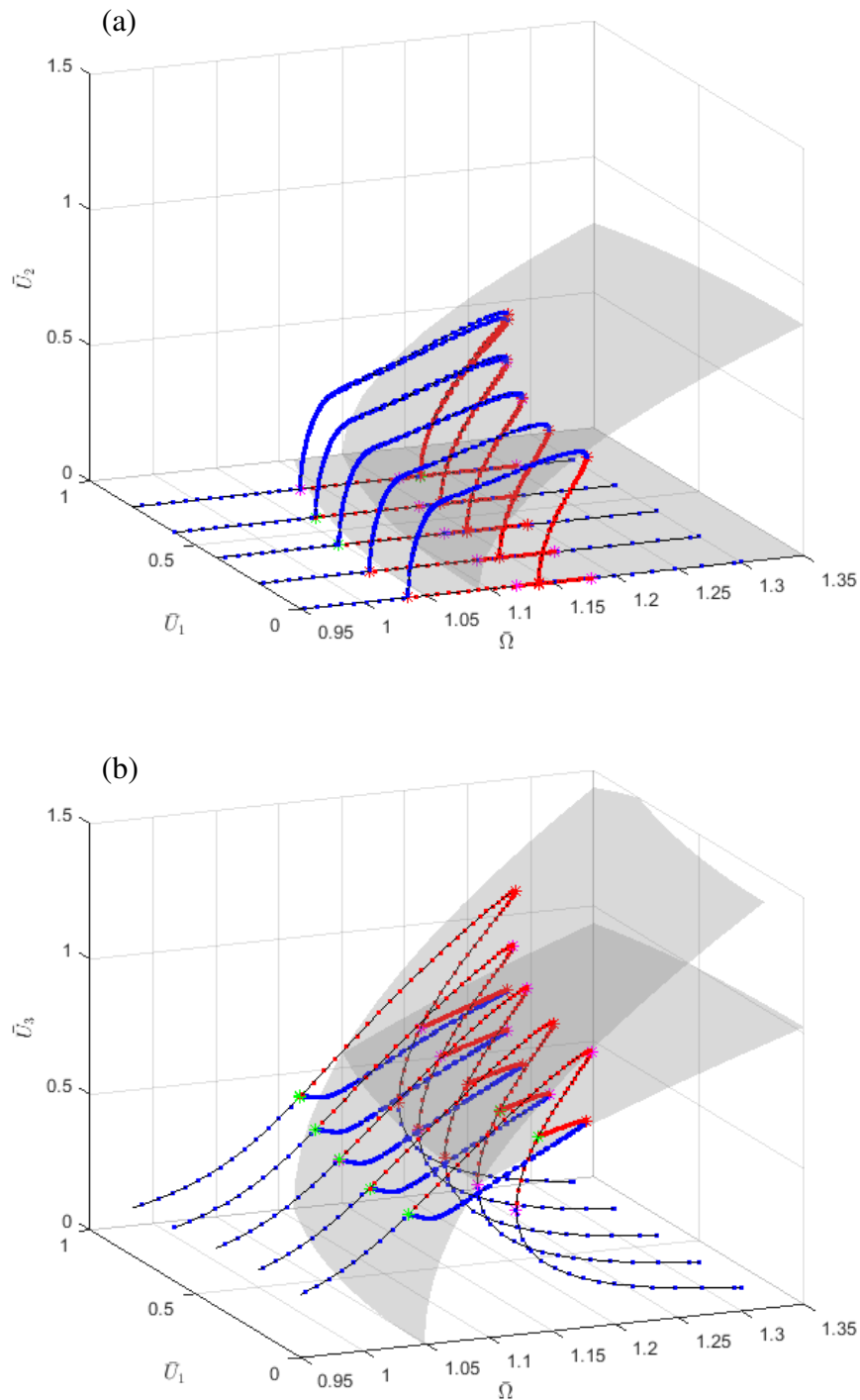


Fig. 6.10 The forced response curves of Mode II and III of the plate depicted in Fig. 6.1 for an artificial excitation case where Mode I is forced to response at a constant amplitude and Mode III is harmonically forced. The black lines denote the forced response curves, blue and red dots denote the stable and unstable sectors respectively, and green dots indicate the bifurcation positions. The grey surfaces denote the backbone curves.

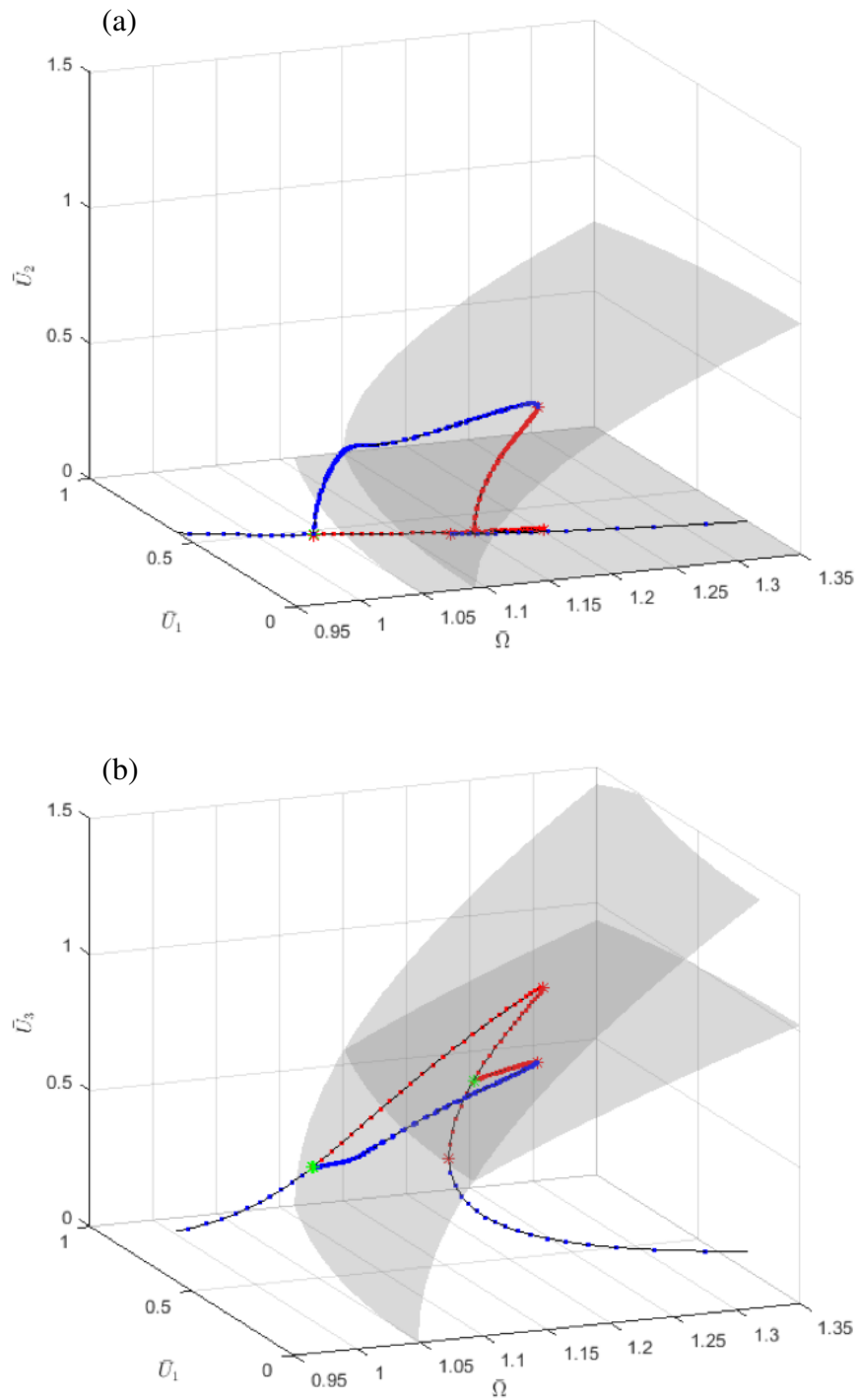


Fig. 6.11 The forced response curves of Mode II and III of the plate depicted in Fig. 6.1 for an artificial excitation case where Mode I is harmonically excited at constant amplitude and frequency and Mode III are harmonically forced at varying frequencies. The denotations are the same as those of Fig. 6.10.

Chapter 7

System identification based on backbone curve models

In this chapter we:

- Show how the backbone curve model can be used, alongside experimental measurements, to estimate nonlinear parameters, especially for those of nonlinear terms coupling non-resonant modes.
- Employ a short-time Fourier transform technique with size-varying windows to measure the backbone curves from the free-decay response comprising the contributions of multiple modes of the nonlinear system.
- Adopt a self-adaptive evolution algorithm to estimate the linear and nonlinear parameters of the backbone curve model of the nonlinear system.
- Demonstrate the ability of the proposed technique to estimate the parameters of nonlinear systems of multiple degrees of freedom by its application to an example plate.

7.1 Introduction

In the previous chapters, we have seen how the direct normal form technique may be used to derive time-invariant equations describing the backbone curves of nonlinear systems. All the applications of backbone curves in the previous examples are focused on the nonlinear dynamic behaviour prediction and interpretation of systems with known structural parameters under specific excitation circumstances. However, when considering the problem inversely,

if the response of a system is given, can we use the knowledge of backbone curves to determine the system parameters? This process is known as system identification, a technique to obtain a mathematical description of a system.

The identification of linear systems has been studied in depth for decades. There are plenty of successful applications, and their techniques are very mature, see for example [23]. However, the identification of nonlinear characteristics still needs development. Many existing identification approaches based on backbone curves or NNM tend to simply consider single-mode excitation situation [33, 54], which means that their results will lose efficacy for more complex situations, e.g. multi-mode excitation and random excitation. Other approaches, such as NARMAX methods [4] and machine learning [24], are versatile and able to identify nonlinear dynamic behaviour efficiently, but their resulting models give limited insight into the underlying physics.

In this chapter, we will show how the analytical descriptions of the backbone curves obtained by the direct normal form technique work as a computationally-cheap model of the dynamic behaviour of a nonlinear system. The main advantages of this proposed approach are (a) the parameters of multiple modes of the nonlinear system can be determined given a single experimental test and (b) the parameters of nonlinear mixed-mode terms contributing to the non-resonant interaction can be determined. The parameter estimation technique presented here consists of three main steps: (i) the measurement of the backbone curves of the structure of interest, (ii) the assumption of the mathematical model and the derivation of the corresponding backbone curves and (iii) the estimation of the parameters of the assumed model by fitting the model expressions to the measured data.

The literature [54] points out that as long as the damping of an unforced system is weak, the decaying response tends to fall to the closest point on backbone curves and then closely follow it. Based on this idea, an approach of approximating the measurement of backbone curves from the nonlinear system decaying response is introduced in §7.2. Firstly, for the determination of mixed-mode terms, the decay data is required to comprise the responses of multiple modes of interest. Therefore, these modes have to be activated initially, which means that a multi-mode excitation scenario is needed. Here we adopt a naive approach, i.e. using broadband excitation. When a broadband force is applied at the proper position of the structure for sufficient time, all the modes under consideration can be activated and then free decay after the forcing removed. This leads to an extra benefit of our system identification approach that no excitation frequency tuning process is required. For the technique in [33, 54], the specific system mode under consideration is required to reach or get close to its resonance before free decay. However, because of the nonlinear feature of

the amplitude-dependent resonant frequency, a careful excitation frequency tuning process is needed, which significantly increases the application complexity of their approach.

As the free-decay response contains the contribution of several modes, i.e. components of different fundamental response frequencies, the short-time Fourier transform, with the ability of the modal decomposition, is employed for the backbone curve measurement. Furthermore, the size of the window imposed is allowed to vary with time to track the temporal evolution of the instantaneous frequencies of nonlinear systems. Besides, as multiple modes contribute to the response, the modeshapes are required to be known in advance. Here the methods outlined in [100] or the linear modal analysis in any commercial finite element software can be used to estimate the modeshapes of the underlying linear system.

Based on the features of the measured backbone curves, a proper mathematical model must be selected that may be able to describe the nonlinear behaviour of the structure under consideration (where the parameters of that model are to be estimated). Furthermore, the expressions describing backbone curves of the assumed model must be formulated (the derivations are in previous chapters). Then, from the data found using the short-time Fourier transform, the self-adaptive differential evolution algorithm, introduced in §7.3, is employed to estimate the parameters of the model, based on the backbone curve expressions.

To demonstrate the application of the proposed system identification technique, the plate considered in Chapter 6 is considered. The estimated results are compared with the ‘true’ values of parameters to validate the performance of our technique using the criteria of relative difference. The results are found to have a reasonable level of accuracy.

7.2 Backbone curve measurement from transient free-decay data

To measure the backbone curves from the response data consisting of components of different fundamental frequencies, the normally used resonant decay method, an experimental technique for measuring the backbone curves from a fundamentally single-frequency response data, no longer works. So a technique with the ability of the mode decomposition, e.g. the Hilbert transform and empirical mode decomposition (EMP), must be used. Here the short-time Fourier transform with size-varied windows is adopted due to its utility when applied to nonlinear response with the characteristic of the amplitude-dependent response frequency.

7.2.1 Short-time Fourier transform with size-varying windows

Let the free-decay response of a nonlinear mechanical system in the time domain be denoted as $x(t)$, where t is time. The experimental data is measured in the period of T in which $N + 1$ data points are evenly spaced, such that the time increment $\Delta = T/N$. This means that there are $N + 1$ discretized measurements x_0, x_1, \dots, x_N , where $x_n = x(n\Delta)$. For the short-time Fourier transform (STFT), a window function, $w(t - \tau)$, is used which moves along the time axis with discrete time shifts $\tau = m\Delta$. The discretized window is sampled at the same $N + 1$ points in the period T , denoted as $w_{m,0}, w_{m,1}, \dots, w_{m,N}$, where $w_{m,n} = w((n - m)\Delta)$. Here the ‘effective’ period of the window function, where $t \in (m\Delta, m\Delta + T_w)$ then $w_m(t) > 0$, is chosen to be much shorter than the measurement period, i.e. $T_w \ll T$, so that T_w may be also called the window period. Hence, after the application of windows, the Fourier transform can be taken for different sections of the signal $x(t)$ and then the average frequency content in the applied window period, T_w , may be measured. Due to the smallness of T_w , it may allow us to assume the average result to be the instantaneous one at the time point of the corresponding window centre, i.e. $t_{w,m} = \Delta m + T_w/2$.

Mathematically, the discrete Fourier transform with the windowed signal is described as,

$$X(k, m) = \sum_{n=0}^N x_n w_{m,n} e^{-i2\pi k \frac{n}{N}}, \quad (7.1)$$

defined at discrete frequencies,

$$\omega(k) = \frac{2\pi k}{T}, \quad \text{for } k = 1, 2, \dots. \quad (7.2)$$

However, one of the issues with STFT is that its accuracy and resolution of the spectrum results are dominated by the effective period of the window function, T_w , e.g. when the window period is too large, the frequency of the signal will be poorly averaged. Conversely, when the window period is too small, then the poor frequency resolution makes it difficult to approximate the instantaneous frequency. For a linear system with a linearly scalable FRF, a fixed optimal window period may be found for processing the data of a specific structure under consideration. While for a nonlinear system whose response amplitude dictates the response frequency, the fixed window scenario may be ineffective.

To circumvent the trade-off issue of the conventional STFT, we may allow the window period of STFT to change as it moves along the time axis, e.g. the window period T_w is the function of the time instant, m . The ability to either expand or contract the window size helps produce an STFT with the better averaging and resolution. Hence, the mathematical

expression of the modified STFT with size-varying windows (STFT-SVW) is updated to be,

$$X(k, m) = \sum_{n=0}^N x_n w_{m,n}(m) e^{-i2\pi k \frac{n}{N}}. \quad (7.3)$$

Based on $X(k, m)$, the Fourier series coefficients approximation of $x(t)$ is,

$$\hat{X}(k, m) = \frac{2X(k, m)}{\sum_{n=0}^N w_{m,n}(m)}. \quad (7.4)$$

The instant at the centre of the window also becomes,

$$t_{w,m} = \frac{mT}{N} + \frac{T_w(m)}{2}. \quad (7.5)$$

7.2.2 Estimation of the instantaneous frequencies and amplitudes

In this section, an approach to estimate the instantaneous frequencies and amplitudes from the STFT results is introduced. Based on the modal superposition assumption, the free-decay data of the nonlinear system under light damping is allowed to be described as a summation of the response of P harmonic oscillators (i.e. linear normal modes), such that

$$x(t) = \sum_{i=1}^P \Phi_i U_i \cos \theta_i, \quad (7.6)$$

where Φ_i is the i^{th} modeshape of the underlying linear system, U_i and θ_i are the instantaneous response amplitude and the phase of each harmonic components respectively. Therefore, U_i and θ_i are functions of time, such as

$$U_i(t) = U_{i,0} \exp(-\zeta_i \omega_i t), \quad (7.7)$$

$$\theta_i(t) = \omega_{i,d} t + \theta_{i,0}. \quad (7.8)$$

Similar to the notations of the free response of a linear underdamped oscillator, $U_{i,0} = U_i(0)$ and $\theta_{i,0} = \theta_i(0)$ are the initial response amplitude and phase respectively, ζ_i is the damping ratio and ω_i and $\omega_{i,d}$ are the undamped and damped natural frequencies respectively, i.e. $\omega_{i,d} = \omega_i \sqrt{1 - \zeta_i^2}$. While contrary to those of linear systems, the damping ratio, ζ_i , and response frequency, ω_i , may not be invariant but be dependent on the magnitude of the response amplitudes, $U_i(t)$. Therefore, they are also functions of time, i.e. $\zeta_i(t)$ and $\omega_i(t)$.

Now, the time-dependent frequencies and damping ratios can be estimated from the

STFT results via using a simple peak-picking method. Assuming that the damping is small and there exists no modal resonant interaction in the free decay, it allows us to write the free-decay data in the form of Eq. (7.6). Hence, it is reasonable for us to believe that the damped response frequency occurs where there is a maximum absolute value of the Fourier coefficient within a user-defined frequency range of the spectrum of each windowed response. The values of these maximum absolute Fourier coefficients are the corresponding response amplitudes of each of the harmonic components at the time point of the applied window centre, i.e. $t_{w,m}$. The details of the process to fit the frequency, $\omega_i(t)$, damping ratio, $\zeta_i(t)$, and response amplitude, $U_{i,0}$, is described as below.

Firstly, considering the collection of the STFT data processing with the j^{th} ($j = 1, 2, \dots, m$) window with a centre time, $t_{w,j}$, i.e. $\hat{X}(k, j)$ and $\omega(k)$, a maximum amplitude of the Fourier coefficients within each N subsets of frequency range defined by the set $[k_{i,\min} k_{i,\max}]$ ($i = 1, \dots, N$) to be the instantaneous response amplitude of the i^{th} harmonic function, which can be mathematically expressed as,

$$U_i(t_{w,j}) = \frac{\max_{k \in [k_{i,\min} k_{i,\max}]} (|\hat{X}(k, j)|)}{\Phi_i}, \quad (7.9)$$

and the damped frequency of corresponding peak is

$$\omega_{i,d}(t_{w,j}) = \frac{2\pi k_{i,\hat{X}_{j,\max}}}{T}, \quad (7.10)$$

where $k_{i,\hat{X}_{j,\max}}$ denotes the value of k_i where $\hat{X}(k, j)$ has its maximum absolute value within the i^{th} subset of k_i . Note that the i^{th} subset of k_i is determined using Eq. (7.2) with the pre-estimating frequency range of i^{th} harmonic components, e.g. $\pm 15\%$ of i^{th} linear frequency.

Once a series of discrete $U_i(t)$ and $\omega_{i,d}(t)$ at $t_{w,j}$ are estimated, the instantaneous damping ratio may be estimated. There are two assumptions made and used here: (i) the damping and response periods are considered to be invariant during two window time points and equal to that at the first time point, i.e. $\zeta_i = \zeta_i(t_{w,j})$ and $\omega_i = \omega_i(t_{w,j})$ when $t_{w,j} \leq t < t_{w,j+1}$, and (ii) the decay rate at the closed end of the windowed response has decayed to a linear response amplitude, so that this allows us to regard $\beta_i(t_{w,m-1}) = \beta_i(t_{w,m})$. The second assumption is reasonable as the response amplitude is small so that the system is behaving almost linearly. Therefore, using Eq. (7.7), the relation between the response amplitude at two window time points is

$$U_i(t_{w,j-1}) = U_i(t_{w,j}) \exp(-\zeta_i(t_{w,j})\omega_i(t_{w,j})(t_{w,j} - t_{w,j-1})), \quad (7.11)$$

where the instantaneous damping rate, $\beta_i(t_{w,j}) = \zeta_i(t_{w,j})\omega_i(t_{w,j})$, at discrete times may be computed from

$$\beta_i(t_{w,j}) = \frac{1}{t_{w,j} - t_{w,j-1}} \ln \left(\frac{U_i(t_{w,j})}{U_i(t_{w,j-1})} \right). \quad (7.12)$$

Referring the relationship between damped and undamped response frequencies as

$$\omega_{i,d}(t_{w,j}) = \omega_i(t_{w,j}) \sqrt{1 - \zeta_i^2(t_{w,j})} t_{w,j}, \quad (7.13)$$

the instantaneous undamped frequency is estimated using Eq. (7.12), written as

$$\omega_i(t_{w,j}) = \sqrt{\omega_{i,d}^2(t_{w,j}) + \beta_i^2(t_{w,j})}. \quad (7.14)$$

Lastly, the instantaneous damping ratio is approximated using

$$\zeta_i(t_{w,j}) = \frac{\beta_i(t_{w,j})}{\omega_i(t_{w,j})}. \quad (7.15)$$

Now, with the collection of instantaneous response amplitudes U_i and frequencies ω_i , the backbone curves, U_i vs. ω_i , can be estimated.

7.2.3 Application

Now we consider the application of the STFT-SVW technique to the example plate structure in Chapter 6. Firstly, it is applied to the free-decay data simulated by the coupled nonlinear reduced-order model developed in §6.3 and the estimation results are compared with the real parameter values used. Secondly, the data generated using the ‘full-order’ nonlinear FE model is used to demonstrate the application of this technique to real-life nonlinear structures.

Nonlinear reduced-order model case

Firstly, the coupled truncated four-mode based NROM is used. Eq. (6.20b) is restated here again for clarity as,

$$\ddot{\mathbf{q}} + \mathbf{C}\dot{\mathbf{q}} + \mathbf{\Lambda}\mathbf{q} + \mathbf{N}_q(\mathbf{q}) = \mathbf{F}_m(t),$$

with

$$\mathbf{N}_q(\mathbf{q}) = \begin{pmatrix} \alpha_1^I q_1^3 + \alpha_2^I q_1 q_2^2 + \alpha_3^I q_1 q_3^2 + \alpha_4^I q_1 q_4^2 + \alpha_5^I q_2 q_3 q_4 \\ \alpha_1^{II} q_1^2 q_2 + \alpha_2^{II} q_2^3 + \alpha_3^{II} q_2 q_3^2 + \alpha_4^{II} q_2 q_4^2 + \alpha_5^{II} q_1 q_3 q_4 \\ \alpha_1^{III} q_1^2 q_3 + \alpha_2^{III} q_2^2 q_3 + \alpha_3^{III} q_3^3 + \alpha_4^{III} q_3 q_4^2 + \alpha_5^{III} q_1 q_2 q_4 \\ \alpha_4^{IV} q_1^2 q_4 + \alpha_2^{IV} q_2^2 q_4 + \alpha_3^{IV} q_3^2 q_4 + \alpha_4^{IV} q_4^3 + \alpha_5^{IV} q_1 q_2 q_3 \end{pmatrix}.$$

In order to generate the transient free-decay data comprising of the response components of multiple modes, Mode I and III are chosen to be randomly forced for a period of time, e.g. $T_f = 20$ s in our simulation. Then the force is removed to let the system free decay till a small response magnitude reaches, e.g. $T = 100$ s in our simulation. Again, the displacement response at the centre of the top-right square is considered, i.e. $x_c(t) = \frac{1}{2}q_1(t) - \frac{\sqrt{2}}{2}q_2(t) - \frac{\sqrt{2}}{2}q_3(t) + q_4(t)$, see Eqs. (6.4). The same integration operator, i.e. fourth-order Runge-Kutta, with the same time interval, $t_{RK} = 10^{-4}$ s, in §6.3.2 is used to simulate all the time-series response. In Fig. 7.1, a free-decay time-series data of the NROM is shown. It can be seen that the initial response amplitude of the metric point is close to two times of the plate thickness, which ensures the occurrence of the nonlinear behaviour. Note that the maximum initial response amplitude of the whole plate may be even larger.

Now a population of windows with the increasing length are applied on the ring-down data. For the modified STFT, a variety of window functions are available to be used, e.g. Rectangle, Hamming, *et al.*. The type of window chosen depends on the specific problem considered and the application of interest. Here, the size-varying Hanning window is used throughout the work and its discretized function is given as

$$w_{n,m} = \begin{cases} \frac{1}{2} \left[1 - \cos \left(\frac{2\pi(n-m)T}{T_w(m)N} \right) \right] & \text{if } 0 \leq (n-m)\frac{T}{N} \leq T_w(m), \\ 0 & \text{if } (n-m)\frac{T}{N} \geq T_w(m) \text{ or } (n-m)\frac{T}{N} < 0. \end{cases} \quad (7.16)$$

It is noteworthy that the other windows have also been tried and they can also provide satisfactory results for the case considered. The used size-varying Hanning window is shown in Fig. 7.2 and the window period is chosen to be increasing along the time axis due to the stiffening property of the example plate.

For the Fourier transformation, the sampling frequency, $f_s = 100$ Hz, is used which may be sufficient for covering the response frequency range of the considered modes. Fig. 7.3 shows the Fourier transform frequency content results. From the plot, we can see that there are two obvious populations of peaks located where their frequencies are slight bigger than the natural frequencies of Mode I and III respectively.

Through the peak-picking process, a series of the instantaneous response amplitudes and

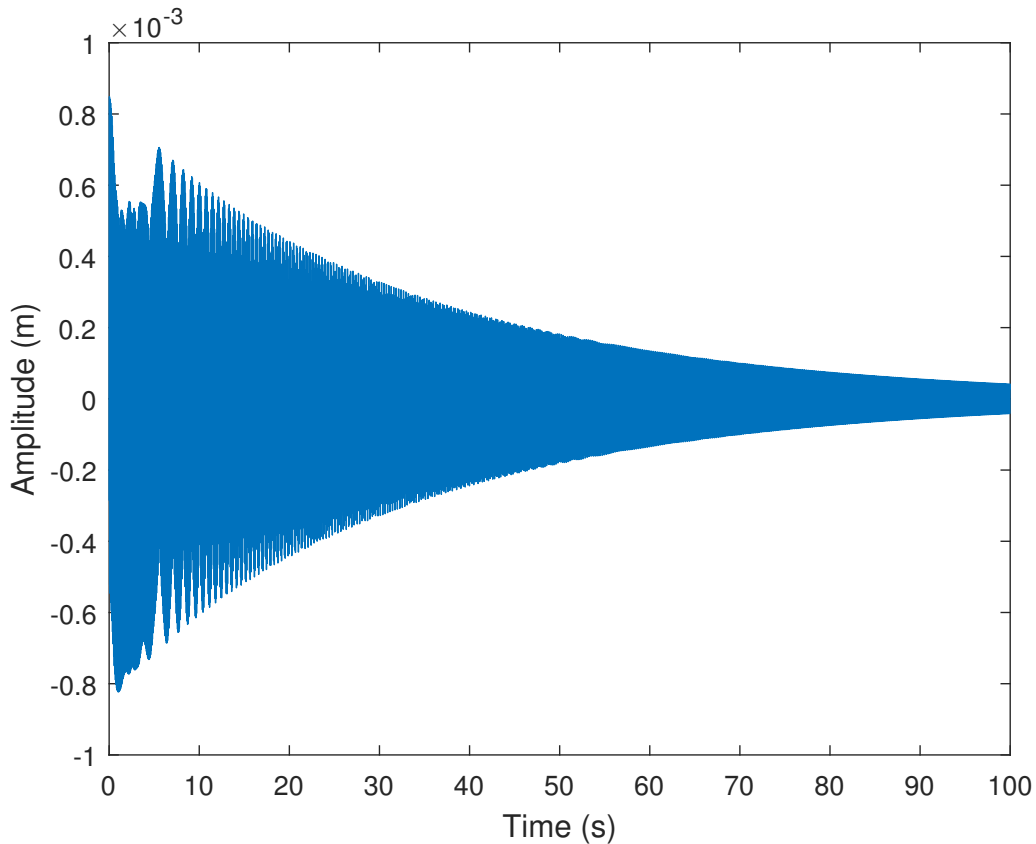


Fig. 7.1 A schematic representation of a free-decay displacement response of the example plate depicted in Fig. 6.1. This data is simulated using the NROM described by Eq. (6.20b) where Mode I and III of the plate are initially forced. The displacement response is acquired at the centre of the top-right square of the plate.

frequencies of each component are obtained. These results plotted against the corresponding time points of the applied windows, $t_{w,m}$, are shown in Fig. 7.4. It can be seen that both the response frequencies and amplitudes decrease with time, which matches the expectation of the system nonlinearity. Note that the results of instantaneous response amplitude, in Fig. 7.4, are scaled using $|\bar{q}_i| = |q_i|/h$.

Finally, the backbone curves are constructed using the instantaneous response frequency and amplitude results, shown in Fig. 7.5. For reference purposes, the analytical backbone curves approximated by the direct normal form technique for the case without considering the non-resonant interaction, see Eqs. (6.27a) and (6.27c), are also plotted. Through comparison, it can be seen that the measured backbone curve of Mode III has apparently deformed: the measured response frequencies are larger than the analytically estimated ones given the same amplitudes. This demonstrates that the response of Mode III has been af-

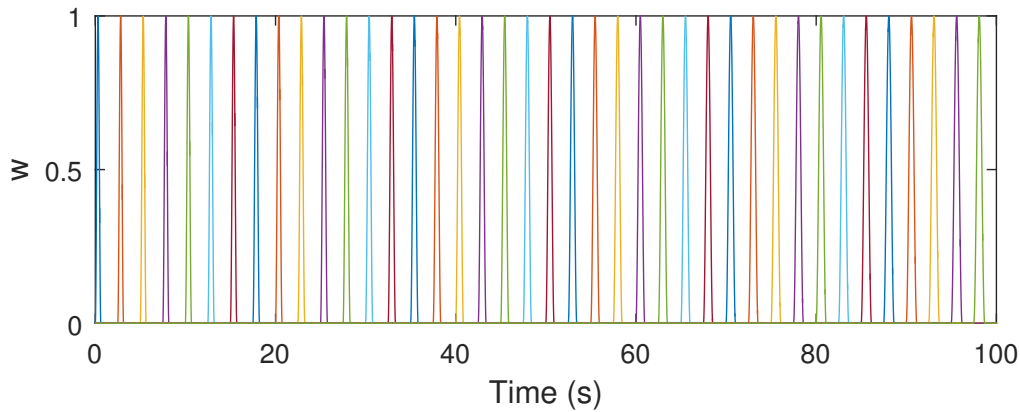


Fig. 7.2 A schematic representation of the Hanning windows of a varying size with time. These windows are applied to the data shown in Fig. 7.1 during the STFT process. Note that every 20 windows used are plotted for a better demonstration purpose.

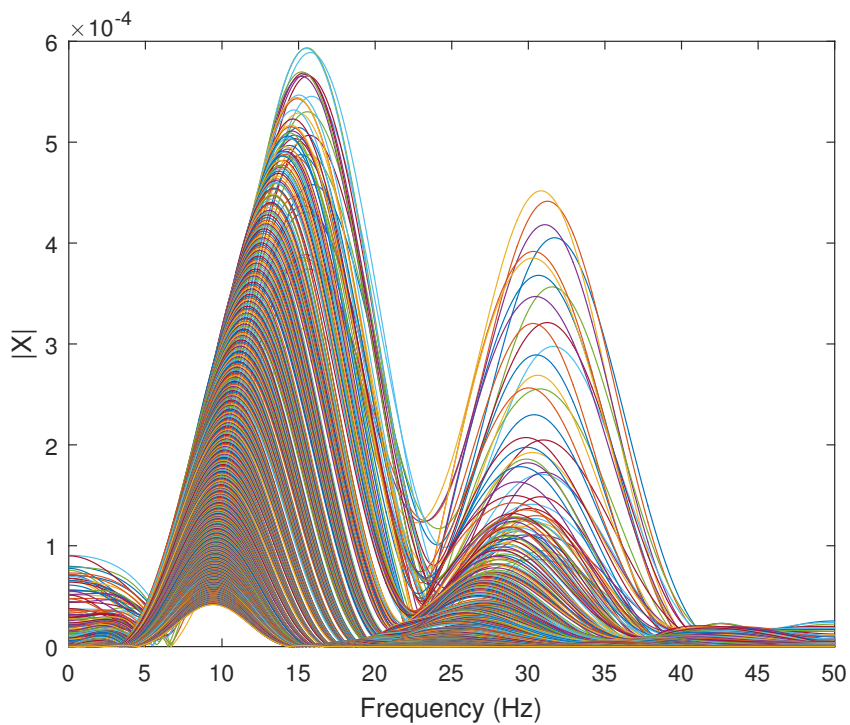


Fig. 7.3 A schematic representation of the Fourier transfer coefficient results of the free-decay response of the example plate depicted in Fig. 6.1. This result is obtained using response data in Fig. 7.1 pre-processed by the windows depicted in Fig. 7.2.

ected by the appearance of Mode I, i.e. the non-resonant modal interaction. However, the effect of Mode III on Mode I is not significant. Besides, when the response amplitudes are small, the response frequencies of both modes drop back to their corresponding linear

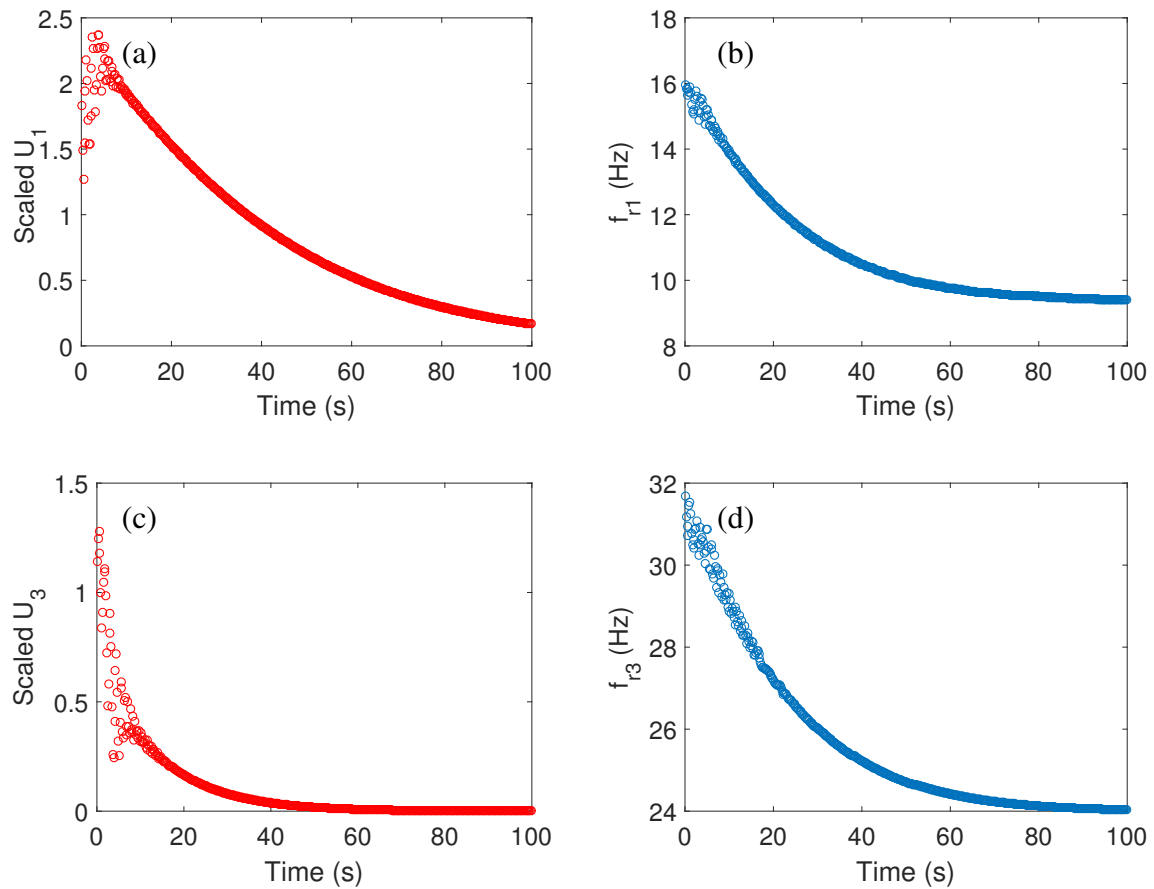


Fig. 7.4 A schematic representation of instantaneous response amplitudes and frequencies of Mode I and III of the plate depicted in Fig. 6.1. This result is obtained through the peak-picking process of the data in Fig. 7.3. (a) U_1 , (b) f_{r1} , (c) $|U_3|$, and (d) f_{r3} .

natural frequencies, i.e. ω_{ni} .

‘Full-order’ FE model

Now the application of the modified STFT technique to the FE simulation results is considered. The force pattern applied here is expected to be ‘identical’ to that used in the NROM simulation, i.e. Mode I and III are directly forced and Mode II and III are left unexcited. Therefore, the response of the plate under the excitation of the configuration shown in Fig. 7.6(a) is simulated using Abaqus[®]. Here, all the simulation settings, i.e. boundary condition, types of elements, mesh density, damping and minimum simulation time interval, are identical to those described in §6.2.

Unlike the NROM case that the actual values of parameters underestimation are already

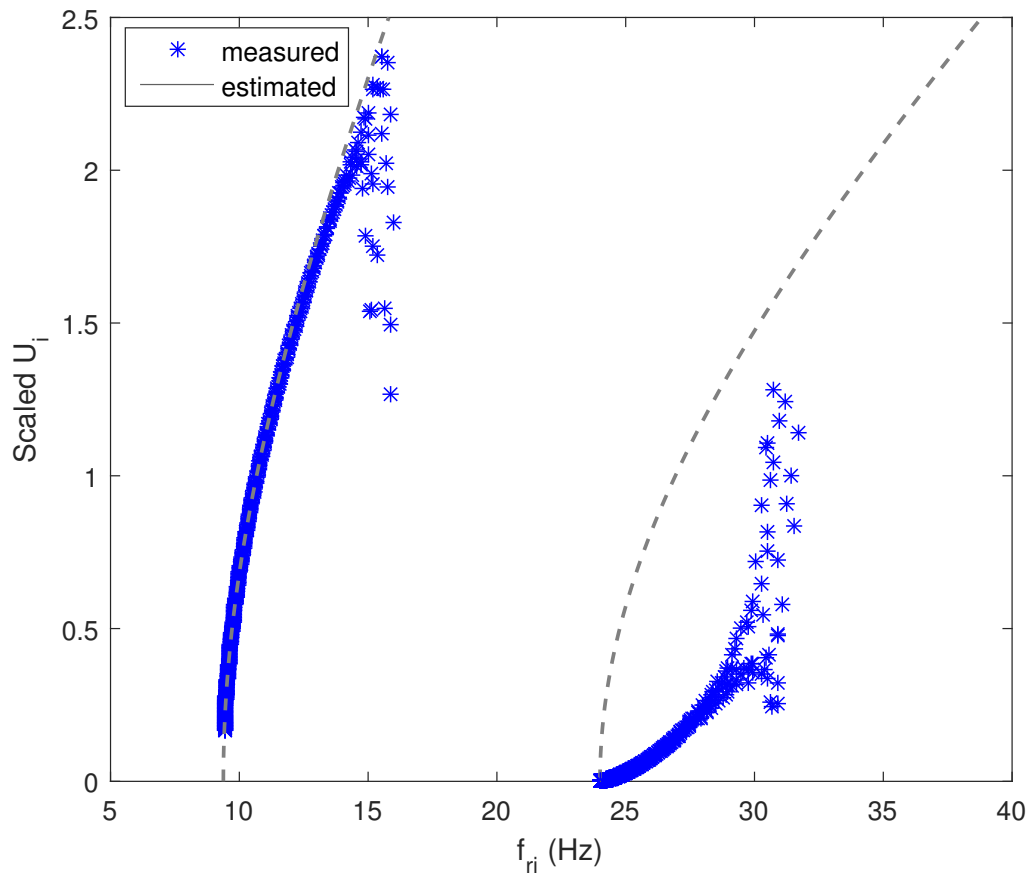


Fig. 7.5 The backbone curves of Mode I and III of the example plate depicted in Fig. 6.1, measured from NROM simulation data. The blue dots denote the measured backbone curves. The dashed-grey lines indicate the analytically approximated backbone curves computed using Eqs. (6.27a) and (6.27c) and the coefficient values in Table 6.2.

known for validation in the next section, the real parameter values of the mathematical model for FE case are unknown. Therefore, two more simulations that a single mode is initially excited are conducted, and their data are also processed with the STFT procedure. The force configurations for the single-mode FE simulation are shown in Fig. 7.6(b) and Fig. 7.6(c), which corresponds to the cases of only Mode I and only Mode III being initially forced respectively. Then the estimated backbone curves can be used to approximate the stiffness parameters of the corresponding modes, i.e. ω_{n1} & α_1^I and ω_{n3} & α_3^{III} .

Fig. 7.7 shows the backbone curves measured from the FE simulation data. The results based on single-mode simulation data are similar to that of a hardening Duffing oscillator. As a comparison, the shape deformation of the double-mode results is similar to that of the NROM results.

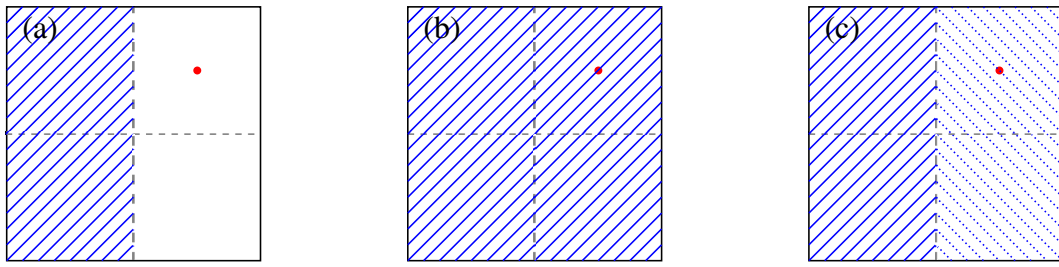


Fig. 7.6 The force configurations used for FE simulations of the example plate depicted in Fig. 6.1. The blue shades denote the areas when the excitation is applied and the opposite shade direction represents the opposite forcing direction. The red dots denote the position where the displacement response is considered. (a) Both Mode I and III are directly excited, (b) Only Mode I is directly excited, and (c) Only Mode III is directly excited.

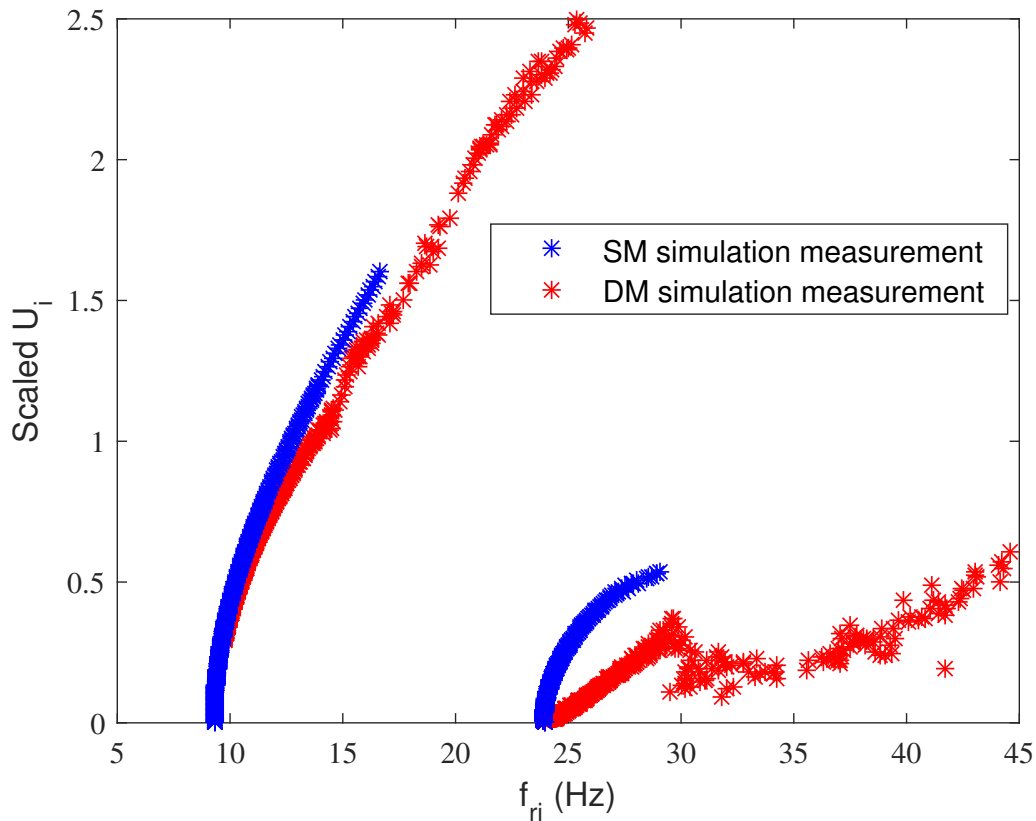


Fig. 7.7 The backbone curves of Mode I and III of the example plate depicted in Fig. 6.1, measured from FE simulation data. The red and blue dots denote the measurements from the simulation data for multi-mode- and single-mode-forced situations respectively.

The parameters values approximation based on these estimated backbone curves of the NROM and FE simulations will be shown in the application in the following section.

7.3 Stiffness parameters identification

To determine the system parameters using the backbone curves measured via the STFT process, a proper parametric model is required. Considering that the system underdetermination initially suffers a multi-mode disturbance, multiple modes of interest are activated simultaneously during the free-decay process. Therefore, the candidate backbone curve model must include the effect of potential non-resonant modal interactions, e.g. the one described by Eqs. (6.32) of the example plate.

Once the structure of the candidate model is decided, the model parameters, i.e. ω_{ni} and $\alpha_{\ell}^{[i]}$, can be estimated via a data fitting procedure. There is a number of parameter estimation techniques available for solving the problem here, e.g. quasi-Newton method and nonlinear regression method. In this section, the self-adaptive differential evolution (SaDE) algorithm is chosen to be used due to its excellent performance and easy usage.

7.3.1 Differential evolution algorithm

The differential evolution (DE) algorithm [91] is a simple but powerful population-based stochastic search technique for solving global optimisation problems. It has been proven to be applicable in many fields, such as pattern recognition [91], communication [38] and mechanical engineering [90]. The details of the DE algorithm are as follows:

Let \mathbf{p} be a $\{1 \times n\}$ vector of parameters of the problem under consideration and $\mathbf{S} \subset \mathbb{R}^n$ be the search space, where n is the number of parameters underdetermination. The whole process of DE involves N_G evolution generations. Within each generation, a population of N_P different n -dimensional target vectors is evolved. These individual vectors are the solution candidates, such as $\mathbf{X}_i^{[G]} = \{x_{i,1}^{[G]}, \dots, x_{i,n}^{[G]}\} \in \mathbf{S}$ where $i = 1, \dots, N_P$, and $G = 1, \dots, N_G$.

Firstly, an initial population of candidate vectors, i.e. $\mathbf{X}_1^{[1]}, \dots, \mathbf{X}_{N_P}^{[1]}$, is generated whose element values should ideally be randomly and uniformly distributed among the prescribed range of its corresponding parameters, i.e. $[p_j^{min}, p_j^{max}]$ ($j = 1, \dots, n$). Then two kinds of operations, i.e. mutation and crossover, are employed to produce a trial vector $\mathbf{U}_i^{[G]}$ for each target vector $\mathbf{X}_i^{[G]}$ in the current population. The candidate vectors of the subsequent generation, i.e. $\mathbf{X}_i^{[G+1]}$, is chosen from either $\mathbf{X}_i^{[G]}$ or $\mathbf{U}_i^{[G]}$ through a selection operation. The details of the three operations are:

Mutation operation

At the generation G , an associated mutant vector $\mathbf{V}_i^{[G]} = \{v_{i,1}^{[G]}, \dots, v_{i,n}^{[G]}\}$ for the corresponding target vector $\mathbf{X}_i^{[G]}$ are generated via one of the following 5 strategies as shown in the online available codes:

$$\begin{aligned}
 \text{"DE/rand/1"} : \quad \mathbf{V}_i^{[G]} &= \mathbf{X}_{r_1}^{[G]} + F \cdot (\mathbf{X}_{r_2}^{[G]} - \mathbf{X}_{r_3}^{[G]}), \\
 \text{"DE/best/1"} : \quad \mathbf{V}_i^{[G]} &= \mathbf{X}_b^{[G]} + F \cdot (\mathbf{X}_{r_1}^{[G]} - \mathbf{X}_{r_2}^{[G]}), \\
 \text{"DE/current to best/1"} : \quad \mathbf{V}_i^{[G]} &= \mathbf{X}_{r_1}^{[G]} + F \cdot (\mathbf{X}_b^{[G]} - \mathbf{X}_i^{[G]}) + F \cdot (\mathbf{X}_{r_1}^{[G]} - \mathbf{X}_{r_2}^{[G]}), \quad (7.17) \\
 \text{"DE/best/2"} : \quad \mathbf{V}_i^{[G]} &= \mathbf{X}_b^{[G]} + F \cdot (\mathbf{X}_{r_1}^{[G]} - \mathbf{X}_{r_2}^{[G]}) + F \cdot (\mathbf{X}_{r_3}^{[G]} - \mathbf{X}_{r_4}^{[G]}), \\
 \text{"DE/rand/2"} : \quad \mathbf{V}_i^{[G]} &= \mathbf{X}_{r_1}^{[G]} + F \cdot (\mathbf{X}_{r_2}^{[G]} - \mathbf{X}_{r_3}^{[G]}) + F \cdot (\mathbf{X}_{r_4}^{[G]} - \mathbf{X}_{r_5}^{[G]}),
 \end{aligned}$$

where r_1, \dots, r_5 are random integers within $[1, N_p]$ which $r_j \neq r_k$ and $r_j \neq i$ (where $j, k = 1, \dots, 5$) to ensure $\mathbf{X}_{r_j}^{[G]}$ be different from the current target vector $\mathbf{X}_i^{[G]}$, F is a factor chosen from the range $[0, 2]$ for scaling differential vectors and $\mathbf{X}_b^{[G]}$ is the individual vector with the best fitness value in its population at the current generation G .

Crossover operation

After the mutation phase, an associated trial vector, $\mathbf{U}_i^{[G]} = \{u_{i,1}^{[G]}, \dots, u_{i,n}^{[G]}\}$, is generated via a ‘binominal’ crossover operation. The values of individuals of trial vector, $u_{i,j}^{[G]}$, are randomly chosen to be equal either that of the mutant vector, $v_{i,j}^{[G]}$, or that of the target vector, $x_{i,j}^{[G]}$. The process of the crossover operation is mathematically expressed as,

$$u_{i,j}^{[G]} = \begin{cases} v_{i,j}^{[G]}, & \text{if } \mathfrak{R}([0, 1])_j \leq CR \text{ or } j = j_{\mathfrak{R}}, \\ x_{i,j}^{[G]}, & \text{otherwise,} \end{cases} \quad (7.18)$$

where $\mathfrak{R}(\bullet)$ is a random operator which generates a value in a defined range, CR is a constant within $[0, 1)$ specified by users and $j_{\mathfrak{R}}$ is a randomly chosen integer in $[1, NP]$ which is to ensure that the trial vector $\mathbf{U}_i^{[G]}$ is different from its corresponding target vector $\mathbf{X}_i^{[G]}$ by, at least, one element.

Selection operation

From Eqs. (7.17) and (7.18), it can be seen that some elements of trial vectors, $u_{i,j}^{[G]}$, may exceed the pre-specified range of the corresponding parameter under determination. For this case, the exceeding individuals need to be re-initialised via a random and uniform re-selection process within its search range before evaluating the fitness of the trial vectors. Then, a selection operation is performed to produce the target vectors of the next generation by comparing the fitness value (e.g. the value of a specific cost function) of each trial vector with that of its corresponding target vector, in the current population. For example, the (either trial or target) vector of a smaller fitness value will enter the population of the next generation for a minimisation problem, i.e.

$$\mathbf{X}_i^{[G+1]} = \begin{cases} \mathbf{U}_i^{[G]}, & \text{if } f(\mathbf{U}_i^{[G]}) \leq f(\mathbf{X}_i^{[G]}) \\ \mathbf{X}_i^{[G]}, & \text{otherwise} \end{cases} . \quad (7.19)$$

The above three operations are repeated generation after generation until specific termination criteria is satisfied, e.g. the user-specified generation number, N_G , is reached. Finally, the target vector of the last population with the smallest fitness value is regarded as the final solution. The schematic diagram of the DE algorithm is concluded in Fig. 7.8.

7.3.2 Self-adaptive differential evolution algorithm

From the typical process of the DE algorithm mentioned previously, we can see that for a specific problem three critical control parameters F , CR and N_p need to be specified by the user, and the most suitable learning strategy out of all available ones are expected to be used. It is believed that the parameters and strategy setting have a significant effect on the algorithm performance [26, 81]. For example, the value of F affects the convergence speed of the algorithm, and CR is sensitive to the nature and complexity of the problem. Although, the most suitable control parameters and strategy could be found for a specific problem via the process of trial and error. However, the searching process is significantly time-consuming and more importantly, the most suitable parameters and strategy may vary during different evolution stages as the preference of the global and local search capability may vary through the evolution process. Therefore, Qin and Suganthan [75] introduced a new DE algorithm that can automatically adapt the learning strategies and the parameter setting during the evolution.

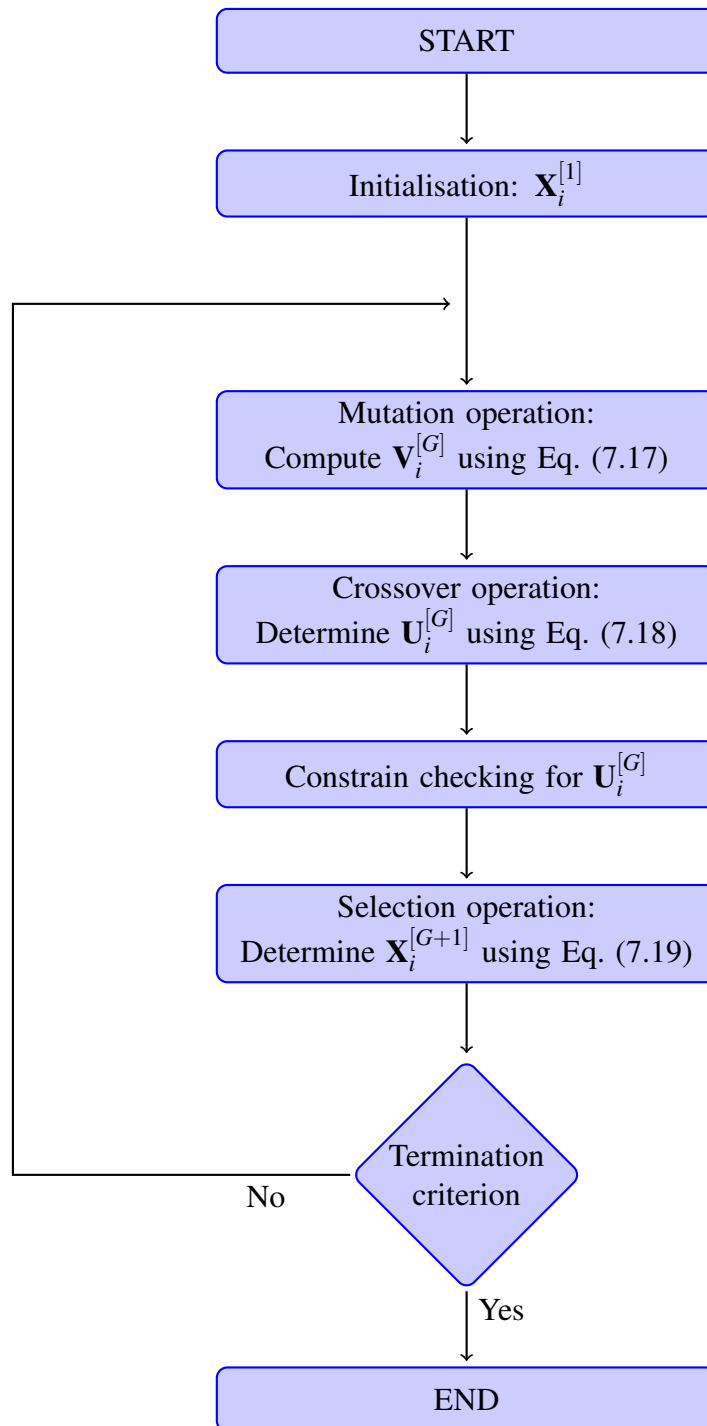


Fig. 7.8 A schematic diagram of the DE algorithm.

Learning strategy adaptation

The learning strategy adaptation of SaDE is to probabilistically select a learning strategy out of the candidates pool to apply to the current population. Firstly, a strategies pool including N_s learning strategies needs to be confirmed. Then, the probability of applying each learning strategy, p_s ($s = 1, \dots, N_s$ and $\sum_1^{N_s} p_s = 1$), needs to be determined. At the start of the evolution process, the probability of applying each candidate strategy needs to be initialized for the first population. Normally, the initial probabilities are set to be equal, i.e. $p_{s,0} = \frac{1}{N_s}$, which ensures that all the candidate strategies have the equal chance to be applied for the initial population. Then, an N_p -dimensional vector, \mathbf{R} , is generated whose elements are uniformly and randomly chosen from the range $[0, 1)$, i.e. $\mathbf{R} = \{\gamma_1, \dots, \gamma_{N_p}\}$ and $\gamma_j \in [0, 1)$. If the value of the j^{th} element of \mathbf{R} is bigger than the sum of the applied probability of the first $s - 1$ strategies but less than that of the first s strategies, then the j^{th} trial vector in the current population will be generated using the s^{th} strategy, i.e.

$$\text{Apply} \begin{cases} 1^{\text{st}} \text{ strategy,} & \text{if } 0 \leq \gamma_j < p_1, \\ s^{\text{th}} \text{ strategy,} & \text{if } \sum_1^{s-1} p_s \leq \gamma_j < \sum_1^s p_s, \text{ when } 2 \leq s \leq N_s. \end{cases} \quad (7.20)$$

After performing the selection operation, the numbers of trial vectors successfully and unsuccessfully entering the next generation while generated by the s^{th} strategy are recorded as $n_s^{\{s\}}$ and $n_s^{\{f\}}$ respectively. These two groups of numbers are accumulated during the learning period (a user-specified number of generations). Then, the applying probability of each strategy is updated to be

$$p_s = \frac{n_s^{\{s\}} \sum_{i=1}^{N_s} (1 - \delta_{si}) n_i^{\{c\}}}{\sum_{j=1}^{N_s} \left\{ n_j^{\{s\}} \sum_{i=1}^{N_s} (1 - \delta_{si}) n_i^{\{c\}} \right\}}, \quad (7.21)$$

where $n_i^{\{c\}} = n_i^{\{s\}} + n_i^{\{f\}}$ and δ_{ij} is the Dirac delta function. Eq. (7.21) represents the percentage of the success rate of the trial vectors generated by the s^{th} strategy during the learning period. Finally, the most suitable learning strategy of the highest applying probability can be selected for the problem under consideration.

Control parameters adaptation

For the conventional DE algorithm, there are three critical user-specified control parameters, i.e. N_p , F and CR , whose values will affect the result of the problem under consideration. The parameter of the population size, N_p , is related to the dimension of the problem consid-

ered. Therefore, in SaDE, the value of N_p is still kept to be user-specified. So for the new DE algorithm, the parameters F and CR are automatically adapted.

It is found that the F value will affect the ability of the DE algorithm for searching good mutant vectors throughout the evolution process, i.e. small and large F values correspond to local and global search ability respectively [75]. Although the choice of F is very flexible, it still falls within the preferred range of $(0, 1]$. Therefore, in SaDE, a population of N_p different F is randomly generated within the range $(0, 2]$ under the normal distribution of mean 0.5 and standard deviation 0.3 for the current generation.

The idea of the parameter CR adaptation is based on: (i) a proper choice of CR may lead to good performance under several learning strategies; while a poor choice of CR may result in performance deterioration under any learning strategy, and (ii) the good CR parameter value falls within a small range, with which the algorithm can perform consistently well on a complex problem [75]. In SaDE, the CR values are assumed to fall in the normal distribution with mean CR_m and a small specific standard deviation, e.g. 0.1. The initial value of CR_m is set to be 0.5. A set of N_p different CR values is randomly generated under the assumed normal distribution to evaluate their corresponding mutant vectors for several generations, i.e. n_{CR} . Then a new population of CR is generated under the same distribution for the evaluation process, which is repeated for n_ℓ times. After that, the mean of the normal distribution of CR is updated with the mean of the CR values corresponding to trial vectors successfully entering the next generation during the $n_\ell \cdot n_{CR}$ generations evolved. The above procedure is repeated with the updated normal distribution and the same standard deviation to let the algorithm learn an optimal CR value range that best suits the problem under consideration.

7.3.3 Application

In this section, the results of the backbone curves of Mode I and III of the example plate measured in §7.2.3 are used to determine the parameters of the corresponding modes using the SaDE algorithm. The first step, as described previously, is to choose a proper model that is sufficiently accurate to describe the relation between the modal response amplitudes and frequencies. Let's restate the approximated backbone curve expressions without and with consideration of the non-resonant interaction again here, i.e.

$$\omega_{r1}^2 = \omega_{n1}^2 + \frac{3}{4}\alpha_1^I U_1^2, \quad (7.22a)$$

$$\omega_{r3}^2 = \omega_{n3}^2 + \frac{3}{4}\alpha_3^{III} U_3^2, \quad (7.22b)$$

and,

$$\omega_{r1}^2 = \omega_{n1}^2 + \frac{3}{4}\alpha_1^I U_1^2 + \frac{1}{2}\alpha_3^I U_3^2, \quad (7.23a)$$

$$\omega_{r3}^2 = \omega_{n3}^2 + \frac{3}{4}\alpha_3^{III} U_3^2 + \frac{1}{2}\alpha_1^{III} U_1^2. \quad (7.23b)$$

Simply examining the backbone curve estimations in Fig. 7.5, the model of Eqs. (7.22) is found to be obviously inaccurate for the results of Mode III (note that the grey dash lines in Fig. 7.5 are the backbone curves computed using Eq. (7.22)). It has also been demonstrated in Chapter 6 that the NROM with mixed-mode terms is better at predicting the system response for the multi-mode-forced situation as it includes the effect of non-resonant modal interactions. Therefore, it allows us to reasonably assume that Eqs. (7.23) may be proper for the multi-active-modes free-decay response data.

Writing the right side of Eqs. (7.23) in the form of a function gives,

$$f_1(U_1, U_3) = \omega_{n1}^2 + \frac{3}{4}\alpha_1^I U_1^2 + \frac{1}{2}\alpha_3^I U_3^2, \quad (7.24a)$$

$$f_3(U_1, U_3) = \omega_{n3}^2 + \frac{3}{4}\alpha_3^{III} U_3^2 + \frac{1}{2}\alpha_1^{III} U_1^2, \quad (7.24b)$$

which are our candidate model for the SaDE algorithm. Therefore, the vectors of the parameters under determination are $\mathbf{p}_1 = [\omega_{n1}, \alpha_1^I, \alpha_3^I]$ and $\mathbf{p}_2 = [\omega_{n3}, \alpha_3^{III}, \alpha_1^{III}]$. Note that as the parameters of Mode I and Mode III are independent when considering each individual backbone curve, \mathbf{p}_1 and \mathbf{p}_2 are determined separately here. To have an objective measure of the goodness of fit, the normalised mean-square error (MSE) is used as the cost function to find the ‘best’ population of parameters, whose expression is,

$$MSE(f_n) = \frac{100}{N\sigma_{\omega_n}^2} \sum_{i=1}^N (f_{n,i} - \omega_{n,i}^2)^2, \quad (7.25)$$

where,

$$f_{n,i} = f_n(U_{1,i}, U_{3,i}), \quad (7.26)$$

the subscript $n = 1$ or 3 denotes the index of the model function member, the subscript i denotes the i^{th} input data and N is the number of data points. In our application, $N = m$ where m is the window number of STFT as no data cleaning process is applied. Experience shows that an MSE of less than 5.0 indicates good fit [99], which will also be used to examine the performance of our model. Note that when considering the FE based backbone curves data for the single-mode-forced situation, as only one mode is assumed to be activated,

i.e. the non-resonant modal interaction is assumed to not occur, the backbone curve model, Eqs. (7.22), is applied, written in functional form as,

$$\hat{f}_1(U_1) = \omega_{n1}^2 + \frac{3}{4}\alpha_1^I U_1^2, \quad (7.27a)$$

$$\hat{f}_3(U_3) = \omega_{n3}^2 + \frac{3}{4}\alpha_3^{III} U_3^2, \quad (7.27b)$$

During the determination of each group of parameters, the SaDE algorithm is repeated 10 times, and the values of the ‘best’ run are chosen to be the final result. The settings of the SaDE algorithm are: size of the population is $N_p = 30$ (10 times of parameters number), the value of crossover ratio, CR , are updated after 10 generations and the learning period of the strategy adaptation is also 10 generations. Besides, a group of test runs are conducted to find the converged features related to the number of the generation, N_G . Fig. 7.9 and Fig. 7.10 show the convergence maps of the SaDE algorithm applied to the model, Eq. (7.24), for the NROM and FE results respectively. From the convergence maps, $N_G = 200$ is found to be sufficient for both cases.

The ‘best’ determination results are shown in Table 7.1 and Table 7.2 for those using the NROM simulation data, in Fig. 7.5, and the FE model simulation data, in Fig. 7.7, respectively.

	True ($\times 10^9$)	Est. ($\times 10^9$)	Diff. (%)	MSE
ω_{n1}	58.9	58.823	0.13	
α_1^I	5.45	5.5773	2.34	0.068
α_3^I	22.7	20.560	9.43	
ω_{n3}	150.8	150.953	0.10	
α_1^{III}	22.7	21.036	7.33	2.800
α_3^{III}	31.4	32.715	1.06	

Table 7.1 The true and estimated values of the linear natural frequencies and nonlinear parameters of the example plate, using nonlinear NROM simulation data.

From Table 7.1, it can be seen that the MSE value for the case of either Mode I or Mode III is less than 5. This demonstrates that our backbone curve model provides a good fit with the measured backbone curve data. Besides, for all the parameters underdetermination, the relative differences between the real and estimated values are below 10%. Especially, the

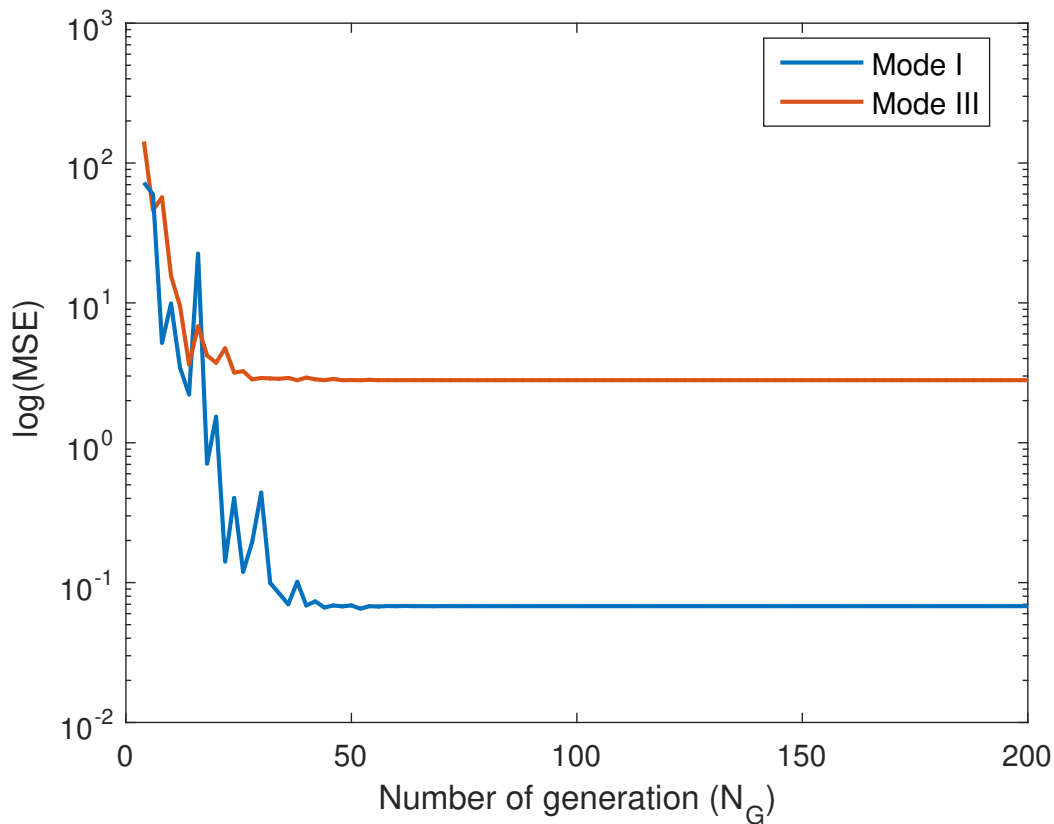


Fig. 7.9 A schematic representation of the convergence map of the SaDE algorithm processing NROM simulation data: MSE against the number of generation adopted. The result shown is for processing the data in Fig. 7.5 with using the functions described in Eqs. (7.24). The blue and red lines denote results for determining the coefficients associated to Mode I and III respectively.

estimated natural frequencies and parameters of single-mode nonlinear terms are surprisingly close to the corresponding real values. Therefore, it can be concluded that our system identification approach using the backbone curve model can give sufficiently accurate results.

For the FE simulation case, the performance assessment of our technique may be limited to the linear natural frequencies and parameters of single-mode nonlinear terms, as the mixed-mode parameters between non-resonant modes cannot be determined from the single-mode-forced simulation. From Table 7.2, a promising result can still be seen, i.e. the MSE values are all under 5 and the relative differences for all the estimated parameters are significantly small.

Furthermore, the estimated coefficients values are substituted into the backbone curves

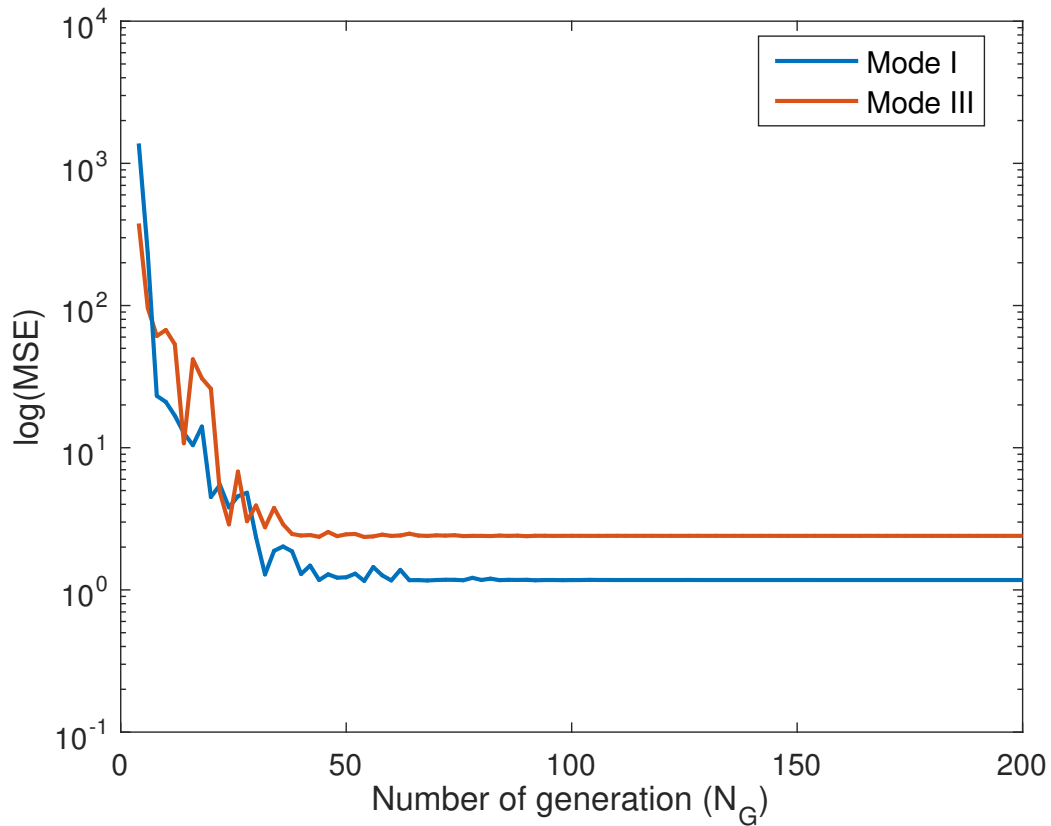


Fig. 7.10 A schematic representation of the convergence map of the SaDE algorithm processing FE simulation data. The result shown is for processing the data of the multi-mode-forced case in Fig. 7.7 with using the function described in Eqs. (7.24).

	SM est. ($\times 10^{10}$)	MSE	DM est. ($\times 10^{10}$)	MSE	Diff. (%)
ω_{n1}	58.737		58.678		0.10
α_1^I	1.008	0.247	1.038	1.174	2.98
α_3^I	n/a		5.901		n/a
ω_{n3}	150.164		150.571		0.27
α_1^{III}	n/a	2.379	21.036	2.400	n/a
α_3^{III}	15.947		14.352		9.83

Table 7.2 The estimated values of the linear natural frequencies and nonlinear parameters of the example plate, using FE simulation data.

expressions, Eqs. (6.26a) and (6.26c), and the results are plotted on top of those calculated using real values, see Fig. 7.11 and Fig. 7.12. As expected, the ‘real’ and estimated results for both cases are very close to each other.

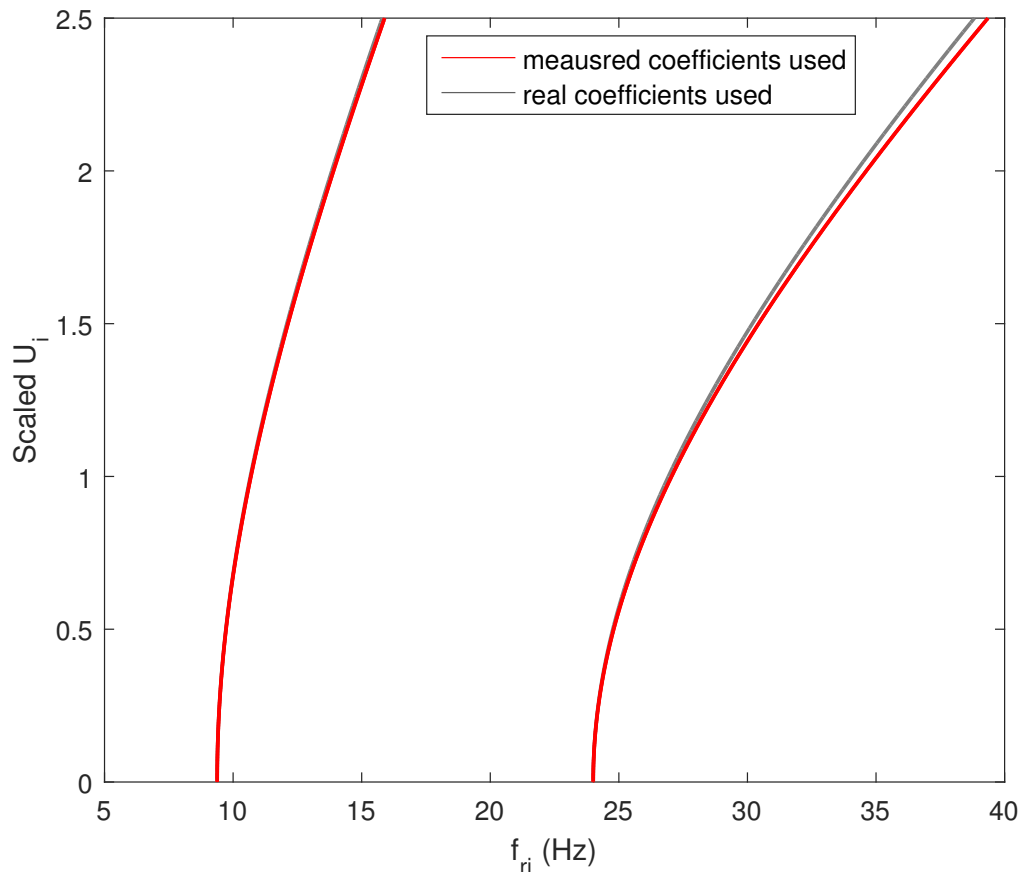


Fig. 7.11 A comparison between the true and estimated backbone curves of Mode I and III of the example plate depicted in Fig. 6.1, using NROM simulation data. The solid-red and dashed-grey lines indicate the backbone curves calculated by Eqs. (6.27a) and (6.27c) using the estimated parameters in Table 7.1 and the true parameters in Table 6.2 respectively.

7.4 Summary

In this chapter, we have introduced an approach for estimating the parameters of a nonlinear system using the backbone curves expressions. Compared with the existing parameter estimation methods based on backbone curves, the main advantages of the proposed technique is the ability to estimate the parameters of mixed-mode nonlinear terms related to non-

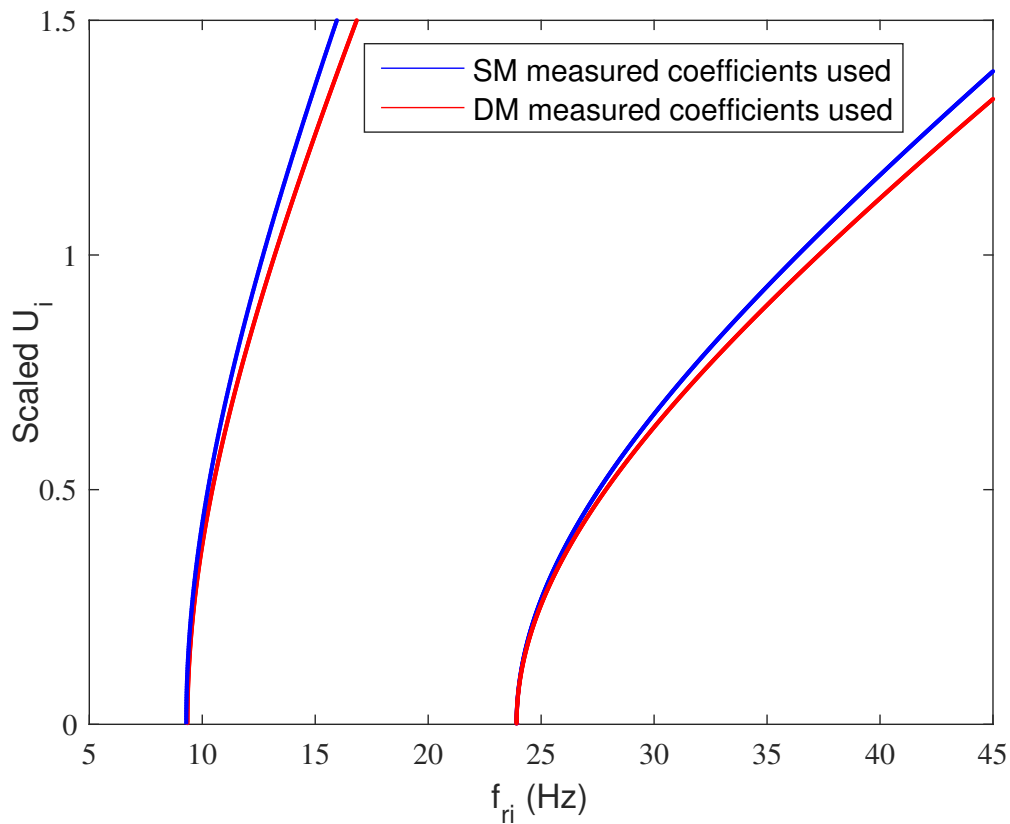


Fig. 7.12 A comparison between the estimated backbone curves of Mode I and III of the example plate depicted in Fig. 6.1, using FE simulation data for the single-mode- and double-mode-forced situations. The blue and red lines indicate the backbone curves calculated by Eqs. (6.27a) and (6.27c) using the parameters of single-mode and double-mode estimations in Table 7.2 respectively.

resonant modes, and identify parameters of multiple modes using the experimental data of a single test. Besides, the other benefits may also be that no excitation frequency tuning process is required and also the random input is easier to be generated compared with the sine waves, which means that the ambient vibrations may be potentially employed for the system identification by using our technique. Here the approach has been demonstrated using a thin, rectangular plate with edges simply supported, whose dynamic behaviour has been simulated using either a four-mode nonlinear reduced-order model or a ‘full-order’ finite element model. The estimation results from the experimental simulation data of both models are promising, which shows that the expressions describing the set of non-resonant coupled backbone curves represents a useful parametric model that can be used for efficient and easily applicable parameters estimation.

During the backbone curves measurement process of the introduced approach, as the free-decay response in the time-domain consists of contributions of multiple activated modes, the short-time Fourier transfer method with the ability of modal decomposition has been adopted. To improve the application performance of this technique on nonlinear systems with the amplitude-dependent-frequency features, the short-time Fourier transfer technique is modified to allow the size of the applied windows to vary with time to enhance its spectrum resolution without sacrificing the accuracy.

When choosing the mathematical model structure for the system under consideration, the one only considering the single-mode contribution is apparently unfit for the measured backbone curve data. Instead, the model with the consideration of effects of non-resonant modal interactions seems to be valid and has been used. With the candidate parametric model and experimentally measured backbone curves, the modified differential evolution algorithm, the self-adaptive differential evolution algorithm, has been used to estimate the values of model parameters. The advantages of using SaDE are no need of choosing learning strategies and less number of the user-specific control parameters. The only control parameters for the algorithm is the generation number which can decide with simple convergence test simulations. The use of SaDe makes the introduced system identification approach more powerful for even more complex cases, e.g. numerous parameters underdetermination.

Chapter 8

Conclusion and future work

8.1 Conclusions

Nonlinear analysis tools

In Chapter 3, three primary tools for analytically investigating the dynamics of nonlinear mechanical structures in this thesis were introduced: the direct normal form technique, the solution stability assessment technique and the backbone curve. The direct normal form technique was first derived: the process of its application to a damped and externally forced system of multiple degrees of freedom with nonlinearities of a polynomial form in the stiffness, damping and external forcing was introduced. It was shown that compared with other nonlinear analytical approximation techniques, the normal form technique is inherently able to consider the nonlinear multi-degree-of-freedom systems. Contrary to the first-order normal form variation, the direct normal technique is readily applied to systems whose motion is described by second-order differential equations which are the natural form of most of the dynamic problems in mechanical systems.

The other significant advantage of this technique is its easy application into a computer program due to its vectorised parameters. In the derivation process of the direct normal form technique, some limitations resulted from its application assumptions were identified. The first one is that the nonlinear terms must be (approximately) expressed in the polynomial form. Secondly, the nonlinear terms and linear damping terms must be small compared with the linear inertial terms, and the differences of the fundamental response frequencies from the linear natural frequencies must be small as well. Additionally, the approximated solutions must be steady state and periodic. Along with these limitations, the direct normal form technique was demonstrated to be sufficiently accurate, by comparison with numerical

results, for the works in this thesis.

A companion technique for assessing the stability of the approximated solutions was then derived. As this method is based on the direct normal form technique, it is readily applicable to the normal form solutions. Finally, the backbone curve, which is a locus of the steady-state free responses of the underlying conservative system of the nonlinear structures, was introduced. The process of backbone curve computation for the nonlinear multi-degree-of-freedom system with no damping and forcing terms using the direct normal form technique was derived. This process was demonstrated to be a simplified version of the ‘full’ direct normal form application.

All these techniques were applied to a single-degree-of-freedom nonlinear Duffing oscillator to find its steady-state resonant forced response, stability and backbone curve respectively. The results demonstrate the suitability of these techniques for the analytical study of the dynamic behaviours of nonlinear mechanical systems.

In conclusion, in Chapter 3 it was shown that:

- The analytical approximation framework based on the direct normal form technique can be applied to the (conservative and non-conservative) multi-degree-of-freedom systems with polynomial nonlinearities to study their dynamic responses at a sufficiently accurate level.
- The backbone curves can be used as a simplified tool for the investigation of the dynamic behaviours of nonlinear single-degree-of-freedom systems.

$N - i$ modal interaction of nonlinear multi-degree-of-freedom systems

In Chapter 4, the resonant modal interaction involving a subset of modes of nonlinear multi-degree-of-freedom systems was investigated. This was demonstrated by considering an in-line, bilaterally symmetric 3-degree-of-freedom oscillator with cubic nonlinear springs. Due to the symmetry of the linear structure of the example system, one of its oscillating modes is linearly independent, and the other two modes are nonlinearly coupled. Firstly, the direct normal form technique was used to derive the analytical description of the resonant forced response of the example system. However, it was shown that the solutions of these expressions were difficult to find due to the existence of nonlinearly coupled terms in the equations of the corresponding modes. Therefore, the forcing and damping related terms were removed to solve the expressions of backbone curves which govern the relationship between the modal fundamental response amplitudes, frequencies, and phase differences.

The simple backbone curve solutions including the contribution of one of the underlying modes correspond to single-mode backbone curves. It was observed that the response on these backbone curves tended to that of the equivalent linear system as the response amplitude tends to zero, which suggests that these single-mode solutions are the nonlinear extension of their linear counterparts. Due to the existence of nonlinear terms coupling two nonlinear modes with similar natural frequencies, it was found that double-mode backbone curve solutions may exist caused by the one-to-one modal interaction. This resonant modal interaction was found to result in two main types of double-mode backbone curves with different modal phase differences: the in-unison backbone curves when the phase difference between the two coupled modes is 0 or π and out-of-unison backbone curves when the phase difference is $\pm\pi/2$. However, the occurrence of this resonant modal interaction was demonstrated to be affected by the nonlinear stiffness: no double-mode backbone curve exists for our example system when its nonlinearity is hardening,

The relationship between the single- and double-mode backbone curves was investigated by considering their analytical expressions. The double-mode backbone curves were found to emanate from the points on the single-mode backbone curves. Furthermore, a stability analysis of the backbone curves was conducted to find that primary single-mode backbone curves lost their stability at the positions of those points where the double-mode backbone curves bifurcate. This finding again demonstrated the resonant modal interaction.

Finally, the numerically computed forced-response results were compared with the backbone curves for validation. It was shown that either the single- or double-mode forced-response curves could find their corresponding backbone curves at which their maximum-amplitude forced-response points almost locate. The comparison results have demonstrated that the backbone curves could interpret the complex dynamic behaviour of forced nonlinear multi-degree-of-freedom systems even when the modal interaction occurs. Furthermore, using the stability information of primary forced-response curves determined by the technique outlined in §3.3, backbone curves were shown to be able to predict the occurrence of modal interactions for a specific forcing situation.

In conclusion, in Chapter 4 it was shown that:

- In a nonlinear system of multiple degrees of freedom, it is possible that only a subset of its nonlinearly coupled modes can resonantly interact due to the specific system structure, for which case the subsystems comprising those associated modes could be considered to investigate the system responses.
- Modal interaction involving the same nonlinear modes can cause different kinds of

resonances with different phase differences, which causes the dynamic behaviour of nonlinear systems to be far more complicated than that of linear systems.

- Backbone curves can give insight to the modal interaction of the nonlinear systems of multiple degrees of freedom including its occurrence conditions and effects on the system forced responses.

***N* modal interaction of nonlinear multi-degree-of-freedom systems**

Chapter 5 began by deriving the expressions describing the relationship between the modal fundamental response amplitudes and frequencies for the generic conservative 3-degree-of-freedom oscillator with cubic nonlinear springs by using the direct normal form technique. These descriptions were used to find the backbone curve solutions of two example systems for investigating the resonant modal interaction involving all modes of nonlinear systems of multiple degrees of freedom. In the derivation process, a symbolised coefficient matrix and a third-power polynomial terms vector were defined to express the nonlinear terms in modal coordinates. Consequently, the origin of the resonant terms retained in the final expressions can be traced, and then a specific nonlinear behaviour caused by these nonlinear terms can also be analysed. It was found that the nonlinear terms retained in the final resonant equations of motion can be classified into two types based on their relationship with the modal response frequencies: the unconditional and condition resonant nonlinear terms. The later would lead to the phase terms in the time-invariant equations for finding backbone curve solutions, which are the reason for the existence of multiple mixed-mode backbone curves involving the same modes and also an essential condition for the occurrence of resonant modal interactions discussed in Chapter 6.

Secondly, a specially designed example 3-degree-of-freedom oscillator was considered to investigate the one-to-one-to-one resonant modal interaction using its backbone curves. It was found that some of the single-mode backbone curves did not exist and the double-mode backbone curves related to these modes would directly emanate from the no-motion trivial solution. This phenomenon was demonstrated to be because the single-mode response associated with these modes loses its stability as soon as one of the modes is activated. Additionally, the existence of the triple-mode backbone curves was analysed. As three modes are involved in the one-to-one-to-one internal interaction, there exist four groups of triple-mode backbone curves in theory classified by the modal phase differences which are 0 , π and $\pm\pi/2$ which is similar to that of the example system in Chapter 4. However, it was proved that only two groups might exist for our system because the phase condition could

not be satisfied for the others. These existing triple-mode backbone curves were observed to be able to emanate from the bifurcation points on either single- or double-mode backbone curves. The unique former case was explained in the same manner as that of double-mode backbone curves bifurcating from the no-motion solution. The system forced responses were numerically computed to compare with the backbone curves to better demonstrate those multi-mode internal interactions. It was shown that the forced responses of the system under a single-mode excitation exhibit those unique dynamic features of the backbone curves.

Finally, the auto-parametric modal interaction involving multiple modes was considered. The linear stiffness ratio of the grounding and coupling springs of the other example 3-degree-of-freedom system was tuned to have approximated commensurable linear natural frequencies, i.e. $\omega_{n1} : \omega_{n2} : \omega_{n3} \approx 1 : 2 : 3$, and, also, its three underlying modes are nonlinearly coupled. Therefore, a one-to-two-to-three modal interaction could happen within this system. The backbone curve results have demonstrated an interesting finding of the multi-mode auto-parametric interaction that the modes, which are unexpected to get internal resonance, may also resonantly interact when some extra modes are considered.

In conclusion, Chapter 5 has shown that:

- For nonlinear multi-degree-of-freedom systems, the modal interaction may cause the disappearance of the responses only comprising that of some specific modes for any forcing situation as those responses lose their stability immediately when they appear.
- When the internal interaction involves multiple modes of a nonlinear system, some non-resonant modes when considering fewer modes may also resonate, which suggests that it is essential to consider all the nonlinearly coupled modes simultaneously to capture these types of multi-mode resonant interactions.

Resonant frequency shift

In Chapter 6, a thin rectangular plate, with its all edges simply supported, was introduced. The nonlinearity of the example plate was the result of membrane stress when its transverse displacement response is large compared with its thickness. The nonlinear dynamic behaviour of this plate under multi-mode excitation was demonstrated by the power spectral density results simulated by its finite element model. It was shown that when the example plate was randomly forced at high amplitude, the resonant frequencies of all its modes under consideration had shifted from their corresponding linear natural frequencies. This phenomenon demonstrates that the nonlinearity due to the large-amplitude response causes the

resonant frequency shift. Additionally, when the plate was permitted to be mildly and randomly excited with one of its modes vigorously and harmonically forced, the other modes under consideration have been observed to exhibit a frequency-shift behaviour. This observation implies that there exist modal interactions affecting the response frequency.

To investigate the mechanism of nonlinearity affecting the resonant response frequencies for the multi-mode-forced situation, the nonlinear mathematical model, i.e. nonlinear reduced-order model, was considered. The mathematical model was developed by decomposing the partial differential equation governing the motion of the example plate using linear modeshapes. This governing equation of motion is nonlinear and captures the effect of large-amplitude displacement response. In the resulting model, there exist two types of nonlinear terms: single-mode and mixed-mode terms. To investigate the modal interaction, two nonlinear reduced-order models, the coupled one and uncoupled one, were used for simulating the system response for the same excitation situations considered in the finite element analysis simulations. Through the comparison with the finite element results, the coupled model including mixed-mode terms was demonstrated to be able to more accurately describe the nonlinear behaviour of the example plate, especially for the hybrid excitation situation.

The nonlinear reduced-order model simulation results have shown that both the single-mode and mixed-mode nonlinear terms could contribute to the resonant frequency shift when multiple modes are directly excited. However, it was found that only the mixed-mode nonlinear terms could cause the effects of the frequency shift between nonlinear modes. Additionally, a further group of simulations was conducted to eliminate the possibility that the frequency shift associated with the mixed-mode nonlinear terms is caused by the resonant modal interaction. This suggested that for the multi-mode-forced situation, there must exist another kind of modal interaction which is not limited to the nonlinearly coupled modes with commensurable response frequencies.

Finally, backbone curves were employed to investigate the mechanism of the mixed-mode nonlinear terms affecting modal response frequencies. It was found that when multiple modes are activated simultaneously by the external forcing, they may affect each other if they are nonlinearly coupled via the mixed-mode terms even they do share a commensurable response frequencies relationship. This kind of modal interaction is termed as non-resonant interaction.

In conclusion, in Chapter 6 it was shown that:

- An underlying low-order model, e.g. reduced-order model, can be sufficiently accurate to explain the nonlinear dynamic behaviours, e.g. resonant frequency shift, of the

‘full-order’ system.

- When nonlinear multi-degree-of-freedom systems are under a multi-mode excitation, a modal interaction can occur between its nonlinearly coupled modes without the commensurable response frequencies relationship.
- The backbone curve model can be used to interpret the complex dynamic behaviours of nonlinear system under a multi-mode-multi-frequency excitation, e.g. the resonant frequency shift due to the non-resonant modal interaction under a random forcing.

System identification based on backbone curve models

In Chapter 7, an approach for the identification of nonlinear systems was introduced, employing the analytical descriptions of the backbone curves to estimate the nonlinear parameters along with the linear natural frequencies. It was demonstrated that the advantages of this approach compared with other system identification techniques using backbone curves include the estimation of the parameters of multiple modes of the system simultaneously using test data, the determination of the parameters of coupled-mode nonlinear terms related to non-resonant modes and no more need of the excitation frequency tuning operation. The benefits of the introduced system identification approach are from the consideration of non-resonant modal interactions in the analytical expressions of backbone curves derived using the direct normal form technique. The application of this technique was demonstrated using the example nonlinear plate introduced in Chapter 6, and its nonlinear reduced-order model was employed to derive the backbone curve model. Our approach was applied to the ‘experiment’ data simulated using both nonlinear reduced-order model and finite element model. For both cases, the estimates of the linear natural frequencies were found to be remarkably accurate, and that of the cubic parameters was at a sufficient level.

In our nonlinear system identification approach, the idea of the resonant decay method was first employed to obtain the measurement of backbone curves. The modes of interest of the nonlinear system under consideration are initially forced by a multi-mode excitation, e.g. the random excitation of a specific forcing configuration. Then the external force is removed to let the system free decay, and the backbone curves can be measured from the free-decay response data. Because the free-decay response includes the contributions of multiple modes, the short-time Fourier transform with the ability of modal decomposition is used to estimate the frequency content of the data. To address the trade-off issue of the short-time Fourier transform, the length of its windows is allowed to vary with time. Finally, a

simple peak-picking process is applied to find populations of instantaneous modal response frequencies and amplitudes, which are then used to form the backbone curves.

To estimate the parameter value using the backbone curve measurements, the self-adapted differential evolution algorithm is adopted. The most significant advantage of using the differential evolution algorithm is its ease of use. Compared with the conventional differential evolution algorithm, the learning strategy and some of the control parameters of the self-adapted differential evolution algorithm do not need to be specified by users, which makes it even more easy to be applied.

In conclusion, in Chapter 7 it was shown that:

- When the non-resonant modal interaction is considered, the system identification approach will not be limited to the identification of single-mode parameters like other approaches based on backbone curves.
- As multiple modes are allowed to be activated simultaneously in the experimental data of our introduced approach, some easily-generated excitation scenarios, e.g. even the ambient vibration, can be employed for the system identification.
- In our approach, the backbone curve model including the effect of non-resonant modal interactions can first be used to identify the parameters of mixed-mode nonlinear terms associated with non-resonant modes.

8.2 Suggestions for potential future work

- As discussed in Chapter 3, the direct normal form technique is limited to the systems of weak nonlinearity, e.g. the detuning of the response frequencies from the linear natural frequencies is small. However, a number of mechanical applications are strongly nonlinear. e.g. the nonlinear energy sink studied in [27]. Therefore, the future work will concentrate on how to relax the smallness assumption of the direct normal form technique to make it adaptable to the application of strongly nonlinear systems.
- In the forced-response results shown in Chapter 4 and Chapter 5, it can be seen that the nonlinear systems may exhibit quasi-periodic responses in the frequency ranges where no stable steady-state response exists. But the results show that our recent backbone curve analysis framework fails to provide any information about this nonlinear behaviour due to the limitation of the normal form technique. Therefore, we believe

that some ‘new’ backbone curves approximated using direct normal form technique can address this limitation.

- For the resonant modal interaction occurring situation, our investigation about the relationship between backbone curves and system forced responses is limited to the single-mode forcing scenario. However, real-life mechanical systems are often under more complex excitations. Therefore, using the backbone curves to predict and interpret the forced responses of nonlinear systems under a multi-mode excitation is a vital issue for the future research.
- In Chapter 5, the investigation of the multi-mode auto-parametric interaction has stopped with the backbone curve analysis due to a lack of proper system parameters. Future work will be kept on seeking better parameters or system structures to study the effect of this modal interaction on the forced system responses.
- The current direct normal form technique cannot be used to approximate the responses of a nonlinear system under a multi-frequency excitation. For example, in Chapter 6, the backbone curves approximated by the direct normal form technique can only indirectly interpret the occurrence and effect of non-resonant modal interaction for the multi-frequency-multi-mode-forced situation. Therefore, a promising future work will be carried out in the investigation of the application of the direct normal form technique to the multi-frequency forcing situation.
- For our nonlinear system identification approach, the resonant modal interaction is not considered in our backbone curve model. However, it can happen during the system free-decay progress that causes unexpected modes to be activated, in which case our approach may give incorrect identification results. For this issue, we suggest that further research should be undertaken in: (i) identifying the occurrence of the resonant modal interaction during the free-decay period so that the corresponding test data can be get rid of and (ii) improving our approach to be adaptable to the resonant modal interaction case by employing new backbone curve measurement technique and including the effect of resonant interaction in our backbone curve model.
- The parametric model of our nonlinear system identification approach does not consider the effect of noise which is inevitable in real experimental data. Further work needs to be carried out to include the noise components to make our approach noise-robust.

References

- [1] Nicholas A Alexander and Frank Schilder. Exploring the performance of a nonlinear tuned mass damper. *Journal of Sound and Vibration*, 319(1):445–462, 2009.
- [2] Vladimir Igorevich Arnol'd. *Geometrical methods in the theory of ordinary differential equations*, volume 250. Springer Science & Business Media, 2012.
- [3] Everett Minnich Baily. *Steady-state harmonic analysis of nonlinear networks*. PhD thesis, Department of Electrical Engineering, Stanford University., 1968.
- [4] Stephen A Billings. *Nonlinear system identification: NARMAX methods in the time, frequency, and spatio-temporal domains*. John Wiley & Sons, 2013.
- [5] Robert D Blevins and R Plunkett. Formulas for natural frequency and mode shape. *Journal of Applied Mechanics*, 47:461, 1980.
- [6] A Cammarano, TL Hill, SA Neild, and DJ Wagg. Bifurcations of backbone curves for systems of coupled nonlinear two mass oscillator. *Nonlinear Dynamics*, 77(1-2): 311–320, 2014.
- [7] A Cammarano, SA Neild, SG Burrow, DJ Wagg, and DJ Inman. Optimum resistive loads for vibration-based electromagnetic energy harvesters with a stiffening nonlinearity. *Journal of Intelligent Material Systems and Structures*, page 1045389X14523854, 2014.
- [8] Matthew Cartmell and MP Cartmell. *Introduction to linear, parametric and nonlinear vibrations*. Chapman and Hall London, 1990.
- [9] Dominique Chapelle and Klaus-Jurgen Bathe. *The finite element analysis of shells-fundamentals*. Springer Science & Business Media, 2010.
- [10] Chuen-Yuan Chia. *Nonlinear analysis of plates*. McGraw-Hill International Book Company, 1980.
- [11] Roy Craig and Mervyn Bampton. Coupling of substructures for dynamic analyses. *AIAA journal*, 6(7):1313–1319, 1968.
- [12] Edward F Crawley and Allan C Aubert. Identification of nonlinear structural elements by force-state mapping. *AIAA journal*, 24(1):155–162, 1986.
- [13] Edward F Crawley and Kevin J O'Donnell. Identification of nonlinear system parameters in joints using the force-state mapping technique. *AIAA Paper*, 86(1013): 659–667, 1986.

- [14] Harry Dankowicz and Frank Schilder. *Recipes for continuation*. SIAM, 2013.
- [15] Thibaut Detroux, Ludovic Renson, Luc Masset, and Gaëtan Kerschen. The harmonic balance method for bifurcation analysis of large-scale nonlinear mechanical systems. *Computer Methods in Applied Mechanics and Engineering*, 296:18–38, 2015.
- [16] Annick Dhooge, Willy Govaerts, and Yu A Kuznetsov. Matcont: a matlab package for numerical bifurcation analysis of odes. *ACM Transactions on Mathematical Software (TOMS)*, 29(2):141–164, 2003.
- [17] Annick Dhooge, Willy Govaerts, Yu A Kuznetsov, Hil Gaëtan Ellart Meijer, and Bart Sautois. New features of the software matcont for bifurcation analysis of dynamical systems. *Mathematical and Computer Modelling of Dynamical Systems*, 14(2):147–175, 2008.
- [18] Annick Dhooge, Willy Govaerts, Yu A Kuznetsov, Hil Gaëtan Ellart Meijer, and Bart Sautois. Matcont: numerical bifurcation analysis toolbox in matlab. Available at <https://sourceforge.net/projects/matcont/>, 2017.
- [19] Andrew J Dick, Balakumar Balachandran, and C Daniel Mote Jr. Nonlinear vibration modes in micro-resonator arrays. In *Proceedings of SPIE, the International Society for Optical Engineering*, pages 61660N–1. Society of Photo-Optical Instrumentation Engineers, 2006.
- [20] Scott W Doebbling, Charles R Farrar, Michael B Prime, and Daniel W Shevitz. Damage identification and health monitoring of structural and mechanical systems from changes in their vibration characteristics: a literature review. 1996.
- [21] Eusebius J Doedel. Auto: A program for the automatic bifurcation analysis of autonomous systems. *Congr. Numer*, 30:265–284, 1981.
- [22] Eusebius J Doedel, Alan R Champneys, Thomas F Fairgrieve, Yuri A Kuznetsov, B E Oldeman, R C Paffenroth, B Sandstede, X J Wang, and C Zhang. Auto-07p: Continuation and bifurcation software for ordinary differential equations. Available at <http://cmvl.cs.concordia.ca/auto>, 2017.
- [23] DJ Ewins. *Modal testing: theory, practice and application (mechanical engineering research studies: engineering dynamics series)*. 2003.
- [24] Charles R Farrar and Keith Worden. *Structural health monitoring: a machine learning perspective*. John Wiley & Sons, 2012.
- [25] MI Friswell, EI Saavedra Flores, and Y Xia. Vibration isolation using nonlinear springs. In *Proceedings of ISMA*, pages 2333–2342, 2012.
- [26] Roger Gämperle, Sibylle D Müller, and Petros Koumoutsakos. A parameter study for differential evolution. *Advances in intelligent systems, fuzzy systems, evolutionary computation*, 10:293–298, 2002. SaDE.
- [27] Oleg Gendelman, LI Manevitch, Alexander F Vakakis, and R M’closkey. Energy pumping in nonlinear mechanical oscillators: Part i—dynamics of the underlying hamiltonian systems. *Journal of Applied Mechanics*, 68(1):34–41, 2001.

- [28] A Gonzalez-Buelga, SA Neild, DJ Wagg, and JHG Macdonald. Modal stability of inclined cables subjected to vertical support excitation. *Journal of Sound and Vibration*, 318(3):565–579, 2008.
- [29] Emmanuel Gourdon, Nicholas A Alexander, Colin A Taylor, Claude-Henri Lamarque, and Stéphane Pernot. Nonlinear energy pumping under transient forcing with strongly nonlinear coupling: Theoretical and experimental results. *Journal of sound and vibration*, 300(3):522–551, 2007.
- [30] Jack K Hale. *Oscillations in nonlinear systems*. McGraw-Hill, 1963.
- [31] Thomas L Hill. *Modal interactions in nonlinear systems*. PhD thesis, University of Bristol, 2016.
- [32] TL Hill, A Cammarano, SA Neild, and DJ Wagg. An analytical method for the optimisation of weakly nonlinear systems. *Proceedings of EURO DYN 2014*, pages 1981–1988, 2014.
- [33] TL Hill, PL Green, A Cammarano, and SA Neild. Fast bayesian identification of a class of elastic weakly nonlinear systems using backbone curves. *Journal of Sound and Vibration*, 360:156–170, 2016.
- [34] TL Hill, SA Neild, A Cammarano, and DJ Wagg. The influence of phase-locking on internal resonance from a nonlinear normal mode perspective. *Journal of Sound and Vibration*, 379:135–149, 2016.
- [35] Tom L Hill, Andrea Cammarano, Simon A Neild, and David J Wagg. Out-of-unison resonance in weakly nonlinear coupled oscillators. In *Proceedings of the Royal Society of London A: Mathematical, Physical and Engineering Sciences*, volume 471, page 20140659. The Royal Society, 2015.
- [36] Joseph J Hollkamp and Robert W Gordon. Reduced-order models for nonlinear response prediction: Implicit condensation and expansion. *Journal of Sound and Vibration*, 318(4):1139–1153, 2008.
- [37] RA Ibrahim. Recent advances in nonlinear passive vibration isolators. *Journal of sound and vibration*, 314(3):371–452, 2008.
- [38] Jarmo Ilonen, Joni-Kristian Kamarainen, and Jouni Lampinen. Differential evolution training algorithm for feed-forward neural networks. *Neural Processing Letters*, 17(1):93–105, 2003. SaDE.
- [39] Gérard Iooss and Daniel D Joseph. *Elementary stability and bifurcation theory*. New York, 1990.
- [40] Louis Jezequel and Claude-Henri Lamarque. Analysis of non-linear dynamical systems by the normal form theory. *Journal of sound and vibration*, 149(3):429–459, 1991.
- [41] Xiaoi Jiang, D Michael McFarland, Lawrence A Bergman, and Alexander F Vakakis. Steady state passive nonlinear energy pumping in coupled oscillators: theoretical and experimental results. *Nonlinear Dynamics*, 33(1):87–102, 2003.

- [42] Gaëtan Kerschen, J-C Golinval, and K Worden. Theoretical and experimental identification of a non-linear beam. *Journal of Sound and vibration*, 244(4):597–613, 2001.
- [43] Gaëtan Kerschen, Young Sup Lee, Alexander F Vakakis, D Michael McFarland, and Lawrence A Bergman. Irreversible passive energy transfer in coupled oscillators with essential nonlinearity. *SIAM Journal on Applied Mathematics*, 66(2):648–679, 2005.
- [44] Gaëtan Kerschen, Jeffrey J Kowtko, D Michael McFarland, Lawrence A Bergman, and Alexander F Vakakis. Theoretical and experimental study of multimodal targeted energy transfer in a system of coupled oscillators. *Nonlinear Dynamics*, 47(1-3):285–309, 2007.
- [45] Gaëtan Kerschen, Maxime Peeters, Jean-Claude Golinval, and Alexander F Vakakis. Nonlinear normal modes, part i: A useful framework for the structural dynamicist. *Mechanical Systems and Signal Processing*, 23(1):170–194, 2009.
- [46] Gaëtan Kerschen, Maxime Peeters, Jean Claude Golinval, and Cyrille Stéphan. Non-linear modal analysis of a full-scale aircraft. *Journal of Aircraft*, 2013.
- [47] Hamed Haddad Khodaparast, Hadi Madinei, Michael I Friswell, Sondipon Adhikari, Simon Coggon, and Jonathan E Cooper. An extended harmonic balance method based on incremental nonlinear control parameters. *Mechanical Systems and Signal Processing*, 85:716–729, 2017.
- [48] Ivana Kovacic and Michael J Brennan. *The Duffing equation: Nonlinear oscillators and their behaviour*. John Wiley & Sons, 2011.
- [49] Mehmet Kurt, Ilya Slavkin, Melih Eriten, D Michael McFarland, Oleg V Gendelman, Lawrence A Bergman, and Alexander F Vakakis. Effect of 1: 3 resonance on the steady-state dynamics of a forced strongly nonlinear oscillator with a linear light attachment. *Archive of Applied Mechanics*, 84(8):1189–1203, 2014.
- [50] Young Sup Lee, Gaëtan Kerschen, Alexander F Vakakis, Panagiotis Panagopoulos, Lawrence Bergman, and D Michael McFarland. Complicated dynamics of a linear oscillator with a light, essentially nonlinear attachment. *Physica D: Nonlinear Phenomena*, 204(1):41–69, 2005.
- [51] IJ Leontaritis and Stephen A Billings. Input-output parametric models for non-linear systems part i: deterministic non-linear systems. *International journal of control*, 41(2):303–328, 1985.
- [52] IJ Leontaritis and Stephen A Billings. Input-output parametric models for non-linear systems part i: deterministic non-linear systems. *International journal of control*, 41(2):303–328, 1985.
- [53] JOHN C Lindenlaub. An approach for finding the sinusoidal steady state response of nonlinear systems. In *Proc. 7th Ann. Allerton Conf. Circuit and System Theory*. Univ. Illinois, 1969.

- [54] Julián M Londoño, Simon A Neild, and Jonathan E Cooper. Identification of backbone curves of nonlinear systems from resonance decay responses. *Journal of Sound and Vibration*, 348:224–238, 2015.
- [55] LI Manevich and Iu V Mikhlin. On periodic solutions close to rectilinear normal vibration modes. *Journal of Applied Mathematics and Mechanics*, 36(6):988–994, 1972.
- [56] Jerrold E Marsden and Marjorie McCracken. *The Hopf bifurcation and its applications*, volume 19. Springer-Verlag, 1976.
- [57] SF Masri and ToK Caughey. A nonparametric identification technique for nonlinear dynamic problems. *Journal of Applied Mechanics*, 46(2):433–447, 1979.
- [58] MATLAB[®]. *version 8.5.0 (r2015a)*. Natick, Massachusetts: The Mathworks, Inc., 2015.
- [59] MI McEwan, Jan R Wright, Jonathan E Cooper, and Andrew Yee Tak Leung. A combined modal/finite element analysis technique for the dynamic response of a nonlinear beam to harmonic excitation. *Journal of Sound and Vibration*, 243(4):601–624, 2001.
- [60] MI McEwan, JR Wright, JE Cooper, and AYT Leung. A finite element/modal technique for nonlinear plate and stiffened panel response prediction. In *Proceedings of the 42nd AIAA/ASME/ASCE/AHS/ASC Structures, Structural Dynamics, and Materials Conference and Exhibit Technical Papers*, pages 3061–3070, 2001.
- [61] Kenneth Meyer, Glen Hall, and Dan Offin. *Introduction to Hamiltonian Dynamical Systems and the N-Body Problem: A Mechanised Logic of Computation*, volume 90. Springer Science & Business Media, 2008.
- [62] Marc P Mignolet, Adam Przekop, Stephen A Rizzi, and S Michael Spottswood. A review of indirect/non-intrusive reduced order modeling of nonlinear geometric structures. *Journal of Sound and Vibration*, 332(10):2437–2460, 2013.
- [63] Alexander A Muravyov and Stephen A Rizzi. Determination of nonlinear stiffness with application to random vibration of geometrically nonlinear structures. *Computers & Structures*, 81(15):1513–1523, 2003.
- [64] Malcolm Nash. *Nonlinear structural dynamics by finite element model synthesis*. PhD thesis, Imperial College London (University of London), 1978.
- [65] Ali H Nayfeh and Balakumar Balachandran. *Applied nonlinear dynamics: analytical, computational and experimental methods*. John Wiley & Sons, 2008.
- [66] Ali H Nayfeh and Dean T Mook. *Nonlinear oscillations*. John Wiley & Sons, 2008.
- [67] Ali Hasan Nayfeh. *Nonlinear interactions: analytical, computational and experimental methods*. Wiley, 2000.
- [68] TA Nayfeh, W Asrar, and AH Nayfeh. Three-mode interactions in harmonically excited systems with quadratic nonlinearities. *Nonlinear Dynamics*, 3(5):385–410, 1992.

- [69] Steven Naylor, Michael F Platten, Jan R Wright, and Jonathan E Cooper. Identification of multi-degree of freedom systems with nonproportional damping using the resonant decay method. *Journal of vibration and acoustics*, 126(2):298–306, 2004.
- [70] SA Neild and DJ Wagg. A generalized frequency detuning method for multidegree-of-freedom oscillators with nonlinear stiffness. *Nonlinear Dynamics*, 73:1–15, 2013.
- [71] Simon A Neild and David J Wagg. Applying the method of normal forms to second-order nonlinear vibration problems. *Proceedings of the Royal Society A: Mathematical, Physical and Engineering Science*, 467(2128):1141–1163, 2011.
- [72] M Peeters, L Renson, , and G Kerschen. Nnmcont: A matlab package for the continuation of nonlinear normal modes. Available at <http://www.ltas-vis.ulg.ac.be/cmsms/index.php?page=nnm>, 2016.
- [73] Maxime Peeters, Régis Vigié, Guillaume Sérandour, Gaëtan Kerschen, and J-C Golinval. Nonlinear normal modes, part ii: Toward a practical computation using numerical continuation techniques. *Mechanical systems and signal processing*, 23(1):195–216, 2009.
- [74] EP Petrov and DJ Ewins. Analytical formulation of friction interface elements for analysis of nonlinear multi-harmonic vibrations of bladed discs. In *ASME Turbo Expo 2002: Power for Land, Sea, and Air*, pages 899–908. American Society of Mechanical Engineers, 2002.
- [75] A Kai Qin and Ponnuthurai N Suganthan. Self-adaptive differential evolution algorithm for numerical optimization. In *Evolutionary Computation, 2005. The 2005 IEEE Congress on*, volume 2, pages 1785–1791. IEEE, 2005. SaDE.
- [76] Richard H Rand. A higher order approximation for non-linear normal modes in two degree of freedom systems. *International Journal of Non-Linear Mechanics*, 6(4):545–547, 1971.
- [77] L Renson, A Gonzalez-Buelga, DAW Barton, and SA Neild. Robust identification of backbone curves using control-based continuation. *Journal of Sound and Vibration*, 367:145–158, 2016.
- [78] Ludovic Renson, Jean-Philippe Noël, and Gaëtan Kerschen. Complex dynamics of a nonlinear aerospace structure: numerical continuation and normal modes. *Nonlinear Dynamics*, 79(2):1293–1309, 2015.
- [79] EI Rivin. Passive vibration isolation. *Applied Mechanics Reviews*, 57:B31, 2004.
- [80] Robert E Roberson. Synthesis of a nonlinear dynamic vibration absorber. *Journal of the Franklin Institute*, 254(3):205–220, 1952.
- [81] T Rogalsky, S Kocabiyik, and RW Derksen. Differential evolution in aerodynamic optimization. *Canadian Aeronautics and Space Journal*, 46(4):183–190, 2000. SaDE.
- [82] Reinhardt Mathias Rosenberg. Normal modes of nonlinear dual-mode systems. *Journal of Applied Mechanics*, 27(2):263–268, 1960.

- [83] Jan A Sanders, Ferdinand Verhulst, and James A Murdock. *Averaging methods in nonlinear dynamical systems*, volume 59. Springer, 2007.
- [84] Frank Schilder and Harry Dankowicz. Continuation core and toolboxes (coco). Available at <https://sourceforge.net/projects/cocotools/>, 2017.
- [85] Sanjiv Sharma, Etienne B Coetzee, Mark H Lowenberg, Simon A Neild, and Bernd Krauskopf. Numerical continuation and bifurcation analysis in aircraft design: an industrial perspective. *Phil. Trans. R. Soc. A*, 373(2051):20140406, 2015.
- [86] AD Shaw, SA Neild, and DJ Wagg. Dynamic analysis of high static low dynamic stiffness vibration isolation mounts. *Journal of Sound and Vibration*, 332:1437–1455, 2012.
- [87] AD Shaw, TL Hill, SA Neild, and MI Friswell. Periodic responses of a structure with 3: 1 internal resonance. *Mechanical Systems and Signal Processing*, 81:19–34, 2016.
- [88] Steven W Shaw and Christophe Pierre. Normal modes for non-linear vibratory systems. *Journal of sound and vibration*, 164(1):85–124, 1993.
- [89] Y Shi and C Mei. A finite element time domain modal formulation for large amplitude free vibrations of beams and plates. *Journal of Sound and Vibration*, 193(2):453–464, 1996.
- [90] Rainer Storn. Differential evolution design of an iir-filter. In *Evolutionary Computation, 1996., Proceedings of IEEE International Conference on*, pages 268–273. IEEE, 1996. SaDE.
- [91] Rainer Storn and Kenneth Price. Differential evolution—a simple and efficient heuristic for global optimization over continuous spaces. *Journal of global optimization*, 11(4):341–359, 1997. SaDE.
- [92] Minoru Urabe. *Nonlinear autonomous oscillations: Analytical theory*, volume 34. Academic Press, 1967.
- [93] A. F. Vakakis and O. Gendelman. Energy pumping in nonlinear mechanical oscillators: Part ii—resonance capture. *Journal of Applied Mechanics*, 68(1):42–48, 05 2001.
- [94] Alexander F Vakakis. *Analysis and identification of linear and nonlinear normal modes in vibrating systems*. PhD thesis, California Institute of Technology, 1991.
- [95] Alexander F Vakakis, D Michael McFarland, Lawrence Bergman, Leonid Manevitch, and Oleg Gendelman. Passive vibration control by nonlinear energy pumping. In *IUTAM Symposium on Chaotic Dynamics and Control of Systems and Processes in Mechanics*, pages 451–458. Springer, 2005.
- [96] Ferdinand Verhulst. *Nonlinear differential equations and dynamical systems*. Springer Science & Business Media, 2006.
- [97] Gotz Von Groll and David J Ewins. The harmonic balance method with arc-length continuation in rotor/stator contact problems. *Journal of sound and vibration*, 241(2):223–233, 2001.

-
- [98] David Wagg and Simon Neild. *Nonlinear Vibration with Control: For Flexible and Adaptive Structures*. Springer-Verlag, Berlin, Germany, 2014.
- [99] Keith Worden and Geoffrey R Tomlinson. *Nonlinearity in structural dynamics: detection, identification and modelling*. CRC Press, 2000.
- [100] JR Wright, JE Cooper, and MJ Desforges. Normal-mode force appropriation—theory and application. *Mechanical Systems and Signal Processing*, 13(2):217–240, 1999.
- [101] JR Wright, MF Platten, JE Cooper, and M Sarmast. Identification of multi-degree-of-freedom weakly non-linear systems using a model based in modal space. In *Proceedings of the International Conference on Structural System Identification, Kassel*, pages 49–68, 2001.
- [102] ZF Xin, SA Neild, DJ Wagg, and ZX Zuo. Resonant response functions for nonlinear oscillators with polynomial type nonlinearities. *Journal of Sound and Vibration*, 332(7):1777–1788, 2013.

Appendix A

Order selection criteria for AR modelling

A.1 AR modelling

For the autoregressive (AR) modelling, a time series, $x[n]$, may be expressed as,

$$x[n] = \sum_{k=1}^p a_k x[n-k] + e[n], \quad (\text{A.1})$$

where a_k are the AR coefficients or characteristic polynomials of the AR model, p is the number of a_k or order of the AR model and $e[n]$ is a purely stationary white noise with zero mean and finite variance σ^2 . Eq. (A.1) means that the current value of the series, $x[n]$, can be expressed as a linear function of its p previous values, i.e. $\sum_{k=1}^p a_k x[n-k]$, plus an error term, i.e. $e[n]$. There are four methods for estimating the AR coefficients, such as Yule-Walker method, Burg method, covariance method and modified covariance method. Then, the power spectrum of the time series signal, x , can be estimated from the a_k coefficients of the AR model, such that

$$P_{AR}(f) = \frac{\sigma^2 T}{\left| 1 + \sum_{k=1}^p a_k e^{-j2\pi f k T} \right|^2}, \quad (\text{A.2})$$

where $P_{AR}(f)$ is the AR power spectral estimation, and T is the sample period.

A.2 Order selection criteria

The main issue for the application of the AR-model-based power spectrum estimation is the determination of the AR order. The true AR order of a given signal is normally unknown

so that many methods of order selection criteria have been developed for the estimation of the AR order. The most established methods include the Final Prediction Error (FPE), Akaike Information Criterion (AIC), Rissanen's Minimum Description Length (MDL) estimator and Parzen's Criterion AR Transfer (CAT) Function. The expressions for these order selection criteria are

$$FPE(k) = \frac{N+k+1}{N-k-1} \sigma(k)^2, \quad (\text{A.3})$$

$$AIC(K) = \ln(\sigma(k)^2) + \frac{2k+1}{N}, \quad (\text{A.4})$$

$$MDL(k) = \sigma(k)^2 \left[1 + \left(\frac{p+1}{N} \right) \ln(N) \right], \quad (\text{A.5})$$

$$CAT(k) = \left[\frac{1}{N} \sum_{j=1}^k \frac{N-j}{N\sigma(j)^2} \right] - \frac{N-k}{N\sigma(k)^2}, \quad (\text{A.6})$$

where N is the sample size of $x[n]$, k is the AR model order, σ^2 is the variance of the prediction error for the given model order, such that

$$\sigma(k)^2 = \frac{1}{N-p} \sum_{n=p+1}^N \left\{ x(n) + \sum_{i=1}^p a_i x(n-i) \right\}^2. \quad (\text{A.7})$$

The process of estimating the true optimal AR order of a given signal via using the criteria mentioned above is:

1. Choose a maximum order, K , which the optimum order would not exceed.
2. Compute the variance $\sigma(k)^2$ of the prediction error for the scanning orders.
3. Calculate the criterion values for each specific criterion.
4. Choose the one with the minimum criterion value as the optimum order.

Ideally, all the criteria should suggest the same true order, but it may not always be true. For that case, the optimum order suggested by the majority of the criteria is regarded as the 'true' order, which is also partly why four criteria have been used here.

Appendix B

An example system with resonant and non-resonant modal interactions

For the nonlinear system depicted in Fig. 5.7, when the stiffness constants of its linear springs are $k = 0.85$ and $\bar{k} = 0.15$, its linear natural frequencies are $\omega_{n1} = 0.4906$, $\omega_{n2} = 1$ and $\omega_{n3} = 1.0292$, thus $\omega_{n1} : \omega_{n2} : \omega_{n3} \approx 1 : 2 : 2$. The linear modeshape matrix, Φ , is

$$\Phi = \begin{bmatrix} 1 & 1 & 1 \\ 5.0618 & 0 & -0.3951 \\ 1 & -1 & 1 \end{bmatrix}, \quad (\text{B.1})$$

and the coefficient matrix of nonlinear stiffness terms in modal coordinates is

$$\mathbf{n}_q^T = \kappa \begin{bmatrix} 0.0724 + 19.7151\lambda & 0 & 0.9276 - 86.7275\lambda \\ 0.2172 + 3.58494\lambda & 0 & 2.7828 - 15.7703\lambda \\ 0.2172 + 6.97739\lambda & 0 & 2.7828 - 30.6939\lambda \\ 0 & 3 + 49.4947\lambda & 0 \\ 0 & 1 + \lambda & 0 \\ 0 & 3 + 5.83891\lambda & 0 \\ 0.2172 - 20.3145\lambda & 0 & 2.7828 + 89.3645\lambda \\ 0.2172 - 1.23132\lambda & 0 & 2.7828 + 5.41662\lambda \\ 0.0724 - 0.79884\lambda & 0 & 0.9276 + 3.51413\lambda \\ 0 & 6 - 33.9997\lambda & 0 \end{bmatrix}, \quad (\text{B.2})$$

where $\lambda = \bar{\kappa}/\kappa$. Due to the specific linear natural frequencies relationship, it is possible to assume the response frequency ratio to be $r = 2$ and $\bar{r} = 2$. These are used to find the

time-invariant equations, written as

$$\left[\omega_{n1}^2 - \omega_{r1}^2 + \frac{1}{4} \left\{ 3\alpha_1^{[1]} U_1^2 + 2\alpha_2^{[1]} U_2^2 + 2\alpha_3^{[1]} U_3^2 \right\} \right] U_1 = 0, \quad (\text{B.3a})$$

$$\left[\omega_{n2}^2 - \omega_{r2}^2 + \frac{1}{4} \left\{ 2\alpha_4^{[2]} U_1^2 + 3\alpha_5^{[2]} U_2^2 + (2+p)\alpha_6^{[2]} U_3^2 \right\} \right] U_2 = 0, \quad (\text{B.3b})$$

$$\left[\omega_{n3}^2 - \omega_{r3}^2 + \frac{1}{4} \left\{ 2\alpha_7^{[3]} U_1^2 + (2+p)\alpha_8^{[3]} U_2^2 + 3\alpha_9^{[3]} U_3^2 \right\} \right] U_3 = 0, \quad (\text{B.3c})$$

where $p = e^{i2(|\phi_2 - \phi_3|)}$.

B.1 Resonant modal interaction

Using Eqs. (B.3), the expressions of the single-mode backbone curves may be obtained, written as

$$S1 : U_1 \neq 0, U_2 = U_3 = 0, \quad \omega_{r1}^2 = \omega_{n1}^2 + \frac{3}{4} \alpha_1^{[1]} U_1^2, \quad (\text{B.4a})$$

$$S2 : U_2 \neq 0, U_1 = U_3 = 0, \quad \omega_{r2}^2 = \omega_{n2}^2 + \frac{3}{4} \alpha_5^{[2]} U_2^2, \quad (\text{B.4b})$$

$$S3 : U_3 \neq 0, U_1 = U_2 = 0, \quad \omega_{r3}^2 = \omega_{n3}^2 + \frac{3}{4} \alpha_9^{[3]} U_3^2. \quad (\text{B.4c})$$

Besides, as the linear natural frequencies of the second and third modes are close, there exist 1 : 1 resonant double-mode backbone curves, $D23$. The expressions of the in-unison backbone curves $D23_{[i]}^{\pm}$ are

$$D23_{[i]}^{\pm} : \begin{cases} U_2^2 = [U_{D23_{[i]}^{S2}}] ^2 + \eta_{D23_{[i]}^{S2}} U_3^2, \\ \Omega^2 = [\omega_{D23_{[i]}^{S2}}] ^2 + \frac{3}{4} \gamma_{D23_{[i]}^{S2}} U_3^2, \end{cases} \quad \text{or} \quad \begin{cases} U_3^2 = [U_{D23_{[i]}^{S3}}] ^2 + \eta_{D23_{[i]}^{S3}} U_2^2, \\ \Omega^2 = [\omega_{D23_{[i]}^{S3}}] ^2 + \frac{3}{4} \gamma_{D23_{[i]}^{S3}} U_2^2, \end{cases} \quad (\text{B.5})$$

where $U_{D23[i]}^{Sn}$, $\eta_{D23[i]}^{Sn}$, $\omega_{D23[i]}^{Sn}$, $\gamma_{D23[i]}^{Sn}$ are constants whose values can be computed using the expressions

$$\begin{aligned}
[U_{D23[i]}^{S2}]^2 &= \frac{4\omega_{n3}^2 - \omega_{n2}^2}{3\alpha_5^{[2]} - \alpha_8^{[3]}}, & [U_{D23[i]}^{S3}]^2 &= \frac{4\omega_{n3}^2 - \omega_{n2}^2}{3\alpha_6^{[2]} - \alpha_9^{[3]}}, \\
[\omega_{D23[i]}^{S2}]^2 &= \frac{\alpha_5^{[2]}\omega_{n3}^2 - \alpha_8^{[3]}\omega_{n2}^2}{\alpha_5^{[2]} - \alpha_8^{[3]}}, & [\omega_{D23[i]}^{S3}]^2 &= \frac{\alpha_6^{[2]}\omega_{n3}^2 - \alpha_9^{[3]}\omega_{n2}^2}{\alpha_6^{[2]} - \alpha_9^{[3]}}, \\
\eta_{D23[i]}^{S3} &= \frac{\alpha_9^{[3]} - \alpha_6^{[2]}}{\alpha_5^{[2]} - \alpha_8^{[3]}}, & \eta_{D23[i]}^{S3} &= \frac{\alpha_8^{[3]} - \alpha_5^{[2]}}{\alpha_6^{[2]} - \alpha_9^{[3]}}, \\
\gamma_{D23[i]}^{S3} &= \frac{\alpha_5^{[2]}\alpha_9^{[3]} - \alpha_6^{[2]}\alpha_8^{[3]}}{\alpha_5^{[2]} - \alpha_8^{[3]}}, & \gamma_{D23[i]}^{S3} &= \frac{\alpha_6^{[2]}\alpha_8^{[3]} - \alpha_5^{[2]}\alpha_9^{[3]}}{\alpha_6^{[2]} - \alpha_9^{[3]}}.
\end{aligned} \tag{B.6}$$

Similarly, the governing expressions for the out-of-unison backbone curves $D23_{[o]}^{\pm}$ are

$$D23_{[o]}^{\pm} : \begin{cases} U_2^2 = [U_{D23[o]}^{S2}]^2 + \eta_{D23[o]}^{S2} U_3^2, \\ \Omega^2 = [\omega_{D23[o]}^{S2}]^2 + \frac{3}{4}\gamma_{D23[o]}^{S2} U_3^2, \end{cases} \text{ or } \begin{cases} U_3^2 = [U_{D23[o]}^{S3}]^2 + \eta_{D23[o]}^{S3} U_2^2, \\ \Omega^2 = [\omega_{D23[o]}^{S3}]^2 + \frac{3}{4}\gamma_{D23[o]}^{S3} U_2^2, \end{cases} \tag{B.7}$$

where

$$\begin{aligned}
[U_{D23[o]}^{S2}]^2 &= 4\frac{\omega_{n3}^2 - \omega_{n2}^2}{3\alpha_5^{[2]} - \alpha_8^{[3]}}, & [U_{D23[o]}^{S3}]^2 &= 4\frac{\omega_{n3}^2 - \omega_{n2}^2}{\alpha_6^{[2]} - 3\alpha_9^{[3]}}, \\
[\omega_{D23[o]}^{S2}]^2 &= \frac{3\alpha_5^{[2]}\omega_{n3}^2 - \alpha_8^{[3]}\omega_{n2}^2}{3\alpha_5^{[2]} - \alpha_8^{[3]}}, & [\omega_{D23[o]}^{S3}]^2 &= \frac{\alpha_6^{[2]}\omega_{n3}^2 - 3\alpha_9^{[3]}\omega_{n2}^2}{\alpha_6^{[2]} - 3\alpha_9^{[3]}}, \\
\eta_{D23[o]}^{S2} &= \frac{3\alpha_9^{[3]} - \alpha_6^{[2]}}{3\alpha_5^{[2]} - \alpha_8^{[3]}}, & \eta_{D23[o]}^{S3} &= \frac{\alpha_8^{[3]} - 3\alpha_5^{[2]}}{\alpha_6^{[2]} - 3\alpha_9^{[3]}}, \\
\gamma_{D23[o]}^{S2} &= \frac{1}{4}\frac{9\alpha_5^{[2]}\alpha_9^{[3]} - \alpha_6^{[2]}\alpha_8^{[3]}}{3\alpha_5^{[2]} - \alpha_8^{[3]}}, & \gamma_{D23[o]}^{S3} &= \frac{1}{4}\frac{\alpha_6^{[2]}\alpha_8^{[3]} - 9\alpha_5^{[2]}\alpha_9^{[3]}}{\alpha_6^{[2]} - 3\alpha_9^{[3]}}.
\end{aligned} \tag{B.8}$$

B.1.1 Hardening nonlinearity

Now the nonlinearity of this system is assumed to be hardening. Fig. B.1 shows the backbone curves of this system with the nonlinear stiffness parameters $\kappa = 0.04$ and $\bar{\kappa} = 0.02$. All panels show the backbone curves in the projection of the response frequency against a displacement. The first column shows the amplitudes of the fundamental displacement response in modal coordinates, i.e. U_1 , U_2 and U_3 , and the second column represents those of the three lumped masses, i.e. X_1 , X_2 and X_3 . Note that the results within frequency

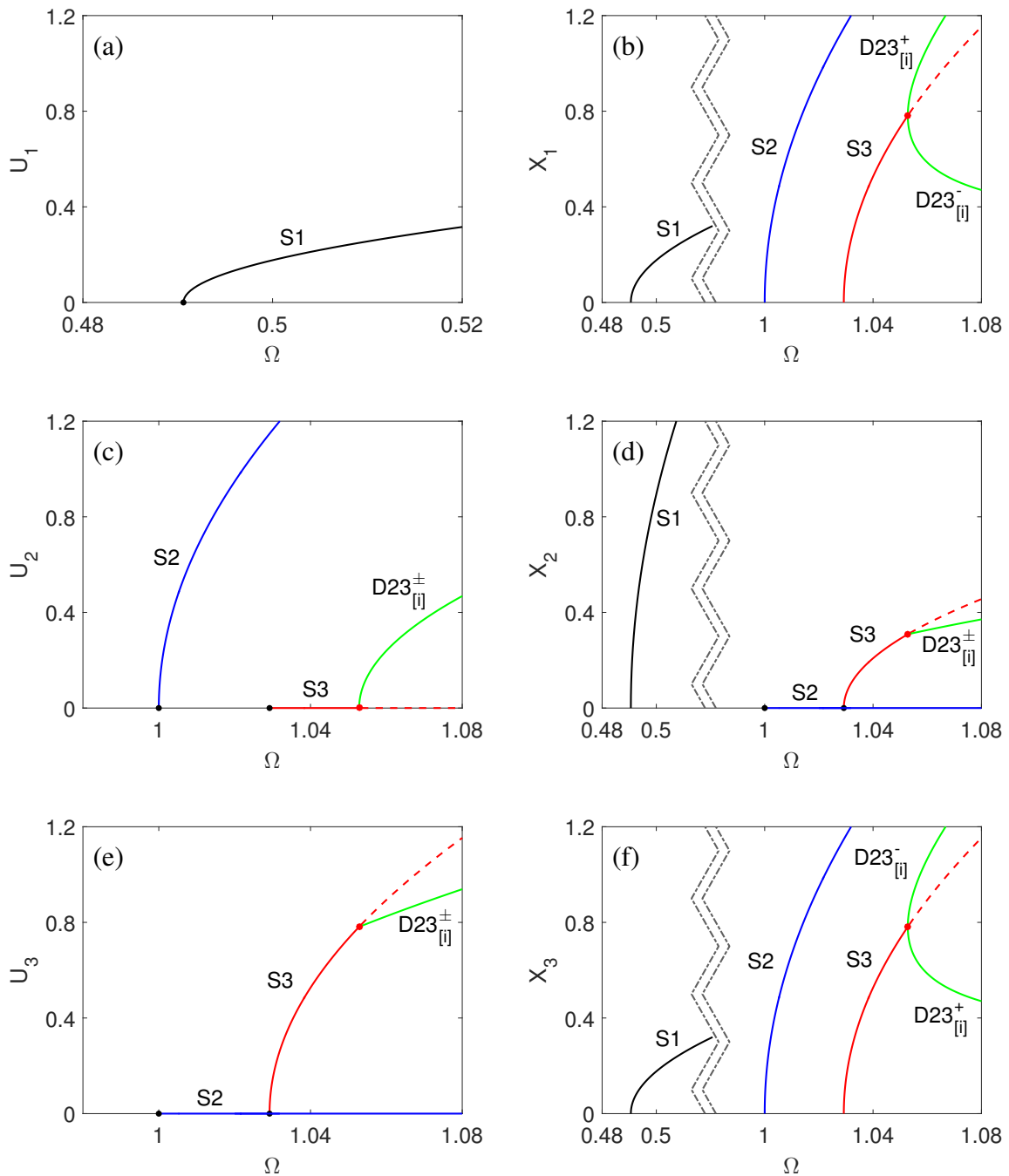


Fig. B.1 The backbone curves of the 3-DoF system depicted in Fig. 5.8 with the physical parameters $m = 1$, $k = 0.85$, $\bar{k} = 0.15$, $\kappa = 0.04$ and $\bar{\kappa} = 0.02$. The panels in the first and second columns show the modal and physical results respectively. Specific backbone curves are labelled respectively, and the bifurcation points are denoted by red dots. Stable and unstable solutions are represented by solid and dashed lines respectively.

bandwidth far away from the resonant frequencies or the parametric ones are not plotted. The labelled $S1$, $S2$ and $S3$ branches are the single-mode backbone curves and $D23_{[i]}^{\pm}$ are in-unison double-mode backbone curves.

From Fig. B.1, it can be seen that the branches $S1$, $S2$ and $S3$ are curves bending to the frequency increasing side (right) which indicates that all modes of the system have hardening nonlinearities. The branches $D23_{[i]}^{\pm}$ bifurcate from $S3$, while $D23_{[o]}^{\pm}$ do not exist here since there is no valid solution for Eqs. (B.7).

B.1.2 Softening nonlinearity

Now the system with softening nonlinearities is considered. Fig. B.2 shows the backbone curves for the case where $\kappa = -0.04$ and $\bar{\kappa} = -0.08$. Both types of double-mode backbone curves $D23_{[i]}^{\pm}$ and $D23_{[o]}^{\pm}$ exist for the softening case. The branches $D23_{[i]}^{\pm}$ emanate from $S2$ instead of $S3$ for the hardening nonlinearity. An interesting phenomenon of the softening nonlinearity result is that the branches $D23_{[o]}^{\pm}$ appear from $S3$ and end at $S2$ (or describing the other way around). This type of bifurcation behaviour has also been shown in the results of the system considered in Chapter 4. However, the difference is that $D23_{[o]}^{\pm}$ are not straightly vertical here.

For both results in Fig. B.1 and Fig. B.2, it shows that there is no resonance between the first mode and the rest two modes for both hardening and softening cases. This is because that there is no corresponding nonlinear term to the 1 : 2 auto-parametric resonance in the equations of associated modes, e.g. the quadratic terms.

B.2 Non-resonant modal interaction

When the non-resonant modal interaction between the first mode with the second and third modes is considered, the expressions of the backbone curves may be changed. For the single-mode backbone curve of the first mode, substituting with $U_1 \neq 0$, $U_2 \neq 0$ and $U_3 \neq 0$ into Eq. (B.3a) and then rearranging gives

$$\hat{S}1 : \quad \hat{\omega}_{r1}^2 = \hat{\omega}_{n1}^2 + \frac{3}{4}\alpha_1^{[1]}U_1^2, \quad (\text{B.9})$$

where the ‘effective’ natural frequency is

$$\hat{\omega}_{n1}^2 = \omega_{n1}^2 + \frac{1}{2}\alpha_2^{[1]}U_2^2 + \frac{1}{2}\alpha_3^{[1]}U_3^2. \quad (\text{B.10})$$

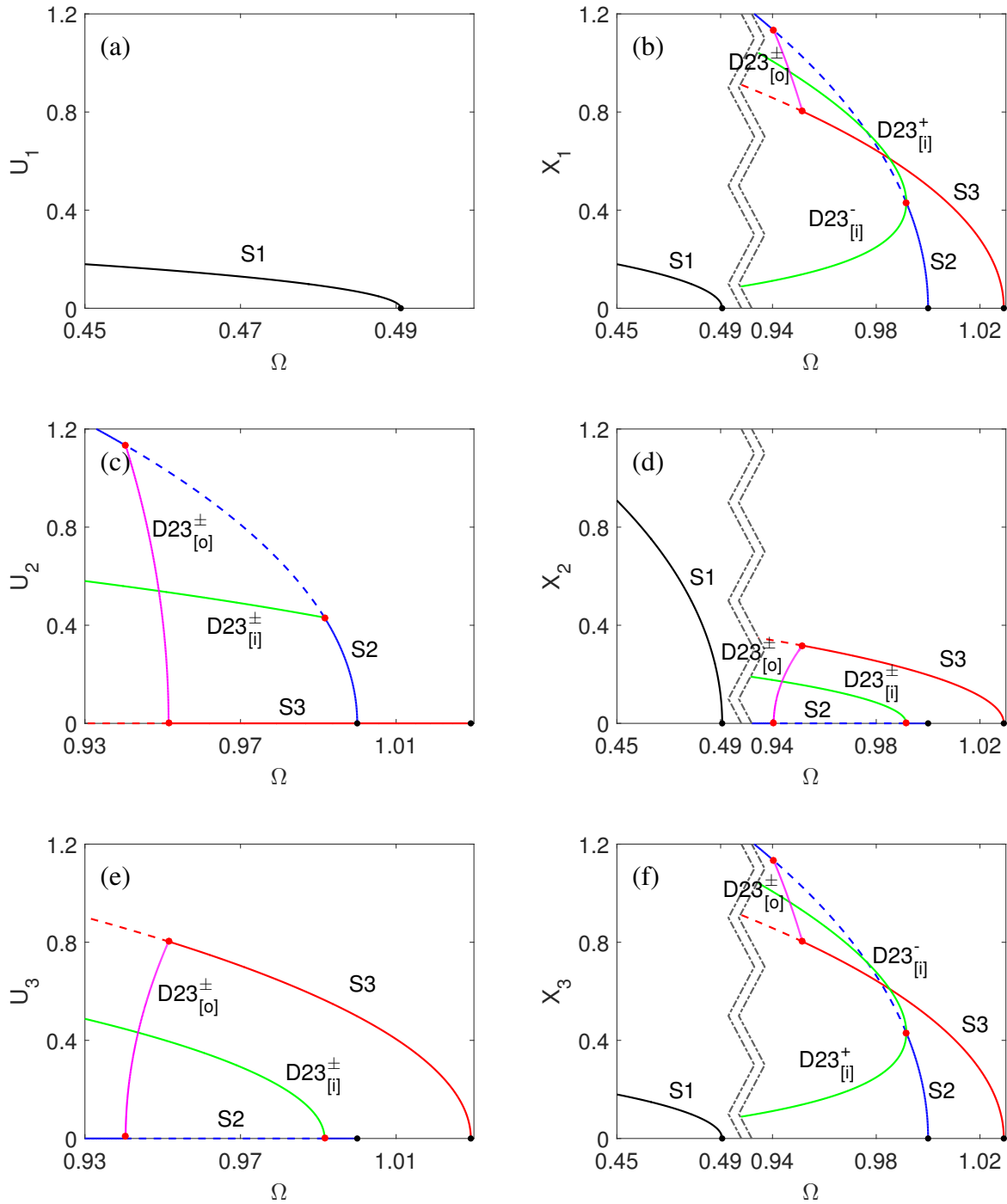


Fig. B.2 The backbone curves of the 3-DoF system depicted in Fig. 5.8 with the physical parameters $m = 1$, $k = 0.85$, $\bar{k} = 0.15$, $\kappa = -0.04$ and $\bar{\kappa} = -0.08$. The denotations are the same as those of Fig. B.1.

Similarly the descriptions of single-mode backbone curves S2 and S3 are updated to be

$$\hat{S}2 : \quad \hat{\omega}_{r2}^2 = \hat{\omega}_{n2}^2 + \frac{3}{4} \alpha_5^{[2]} U_2^2, \quad (\text{B.11a})$$

$$\hat{S}3 : \quad \hat{\omega}_{r3}^2 = \hat{\omega}_{n3}^2 + \frac{3}{4} \alpha_9^{[3]} U_3^2, \quad (\text{B.11b})$$

where

$$\hat{\omega}_{n2}^2 = \omega_{n2}^2 + \frac{1}{2} \alpha_4^{[2]} U_1^2, \quad (\text{B.12a})$$

$$\hat{\omega}_{n3}^2 = \omega_{n3}^2 + \frac{1}{2} \alpha_7^{[3]} U_1^2. \quad (\text{B.12b})$$

From Eqs. (B.10) and (B.12), it can be seen that due to the non-resonant modal interaction, the effective natural frequencies may vary with the response amplitude of the non-resonant modes.

For double-mode backbone curves, the expressions of in-unison ones, $\hat{D}23_{[i]}^{\pm}$, are updated to be

$$\hat{D}23_{[i]}^{\pm} : \quad \begin{cases} U_2^2 = [\hat{U}_{D23_{[i]}^{S2}}]^2 + \eta_{D23_{[i]}^{S2}} U_3^2, \\ \Omega^2 = [\hat{\omega}_{D23_{[i]}^{S2}}]^2 + \frac{3}{4} \gamma_{D23_{[i]}^{S2}} U_3^2, \end{cases} \quad \text{or} \quad \begin{cases} U_3^2 = [\hat{U}_{D23_{[i]}^{S3}}]^2 + \eta_{D23_{[i]}^{S3}} U_2^2, \\ \Omega^2 = [\hat{\omega}_{D23_{[i]}^{S3}}]^2 + \frac{3}{4} \gamma_{D23_{[i]}^{S3}} U_2^2, \end{cases} \quad (\text{B.13})$$

and the modified out-of-unison backbone curves, $\hat{D}23_{[o]}^{\pm}$, to be

$$\hat{D}23_{[o]}^{\pm} : \quad \begin{cases} U_2^2 = [\hat{U}_{D23_{[o]}^{S2}}]^2 + \eta_{D23_{[o]}^{S2}} U_3^2, \\ \Omega^2 = [\hat{\omega}_{D23_{[o]}^{S2}}]^2 + \frac{3}{4} \gamma_{D23_{[o]}^{S2}} U_3^2, \end{cases} \quad \text{or} \quad \begin{cases} U_3^2 = [\hat{U}_{D23_{[o]}^{S3}}]^2 + \eta_{D23_{[o]}^{S3}} U_2^2, \\ \Omega^2 = [\hat{\omega}_{D23_{[o]}^{S3}}]^2 + \frac{3}{4} \gamma_{D23_{[o]}^{S3}} U_2^2, \end{cases} \quad (\text{B.14})$$

where

$$\begin{aligned} [\hat{U}_{D23_{[tr]}^{Sn}}]^2 &= [U_{D23_{[tr]}^{Sn}}]^2 + \mu_{D23_{[tr]}^{Sn}} U_1^2, \\ [\hat{\omega}_{D23_{[tr]}^{Sn}}]^2 &= [\omega_{D23_{[tr]}^{Sn}}]^2 + \frac{1}{2} \nu_{D23_{[tr]}^{Sn}} U_1^2, \end{aligned} \quad (\text{B.15})$$

and

$$\begin{aligned} \mu_{D23_{[i]}^{S2}} &= \frac{2 \alpha_7^{[3]} - \alpha_4^{[2]}}{3 \alpha_5^{[2]} - \alpha_8^{[3]}}, & \mu_{D23_{[i]}^{S3}} &= \frac{2 \alpha_7^{[3]} - \alpha_4^{[2]}}{3 \alpha_6^{[2]} - \alpha_9^{[3]}}, \\ \nu_{D23_{[i]}^{S2}} &= \frac{\alpha_5^{[2]} \alpha_7^{[3]} - \alpha_4^{[2]} \alpha_8^{[3]}}{\alpha_5^{[2]} - \alpha_8^{[3]}}, & \nu_{D23_{[i]}^{S3}} &= \frac{\alpha_6^{[2]} \alpha_7^{[3]} - \alpha_4^{[2]} \alpha_9^{[3]}}{\alpha_6^{[2]} - \alpha_9^{[3]}}, \end{aligned} \quad \text{and} \quad (\text{B.16})$$

and

$$\begin{aligned} \mu_{D23[o]}^{S2} &= 2 \frac{\alpha_7^{[3]} - \alpha_4^{[2]}}{3\alpha_5^{[2]} - \alpha_8^{[3]}}, & \mu_{D23[o]}^{S3} &= 2 \frac{\alpha_7^{[3]} - \alpha_4^{[2]}}{\alpha_6^{[2]} - 3\alpha_9^{[3]}}, \\ \nu_{D23[o]}^{S2} &= \frac{3\alpha_5^{[2]} \alpha_7^{[3]} - \alpha_4^{[2]} \alpha_8^{[3]}}{3\alpha_5^{[2]} - \alpha_8^{[3]}}, & \nu_{D23[o]}^{S3} &= \frac{\alpha_6^{[2]} \alpha_7^{[3]} - 3\alpha_4^{[2]} \alpha_9^{[3]}}{\alpha_6^{[2]} - 3\alpha_9^{[3]}}. \end{aligned} \quad (\text{B.17})$$

From the modified backbone curve expressions, we can see that the bifurcation position, i.e. the amplitude, $\hat{U}_{D23[x]}^{Sn}$, and frequency, $\hat{\omega}_{D23[x]}^{Sn}$, of the double-mode backbone curves may also vary with the response amplitude of the non-resonant interacted mode, i.e. U_1 . This further affects the shapes of these mixed-mode backbone curves.